

Big, small, but no medium-sized
carnivorous dinosaurs pp. 871 & 941

Probing the fine structure
of partial waves pp. 886 & 936

N_2O_5 uptake into aqueous
aerosols p. 921

Science

\$15
26 FEBRUARY 2021
sciencemag.org

AAAS

RADAR REVOLUTION

Satellite eyes watch Earth's
subtle shifts p. 876



Consistently Devoted to Neuromodulation!

- **2000**, Initiation of the development of the PINS neuromodulation devices
- **2009**, First implantation of the PINS DBS (deep brain stimulation) device
- **2012**, First implantation of the PINS rechargeable DBS device
Establishment of National Engineering Laboratory for Neuromodulation
- **2014**, First implantation of the PINS VNS (vagus nerve stimulation) device
- **2015**, First implantation of the variable frequency DBS device
First implantation of the 3-Tesla MRI compatible DBS device
First clinical research of the PINS DBS device with the function of simultaneous stimulation and recording
- **2016**, Receiving the CE Mark for DBS devices
Co-sponsorship of *Science* & PINS Prize for Neuromodulation with *Science*
First implantation of the PINS SNM (sacral nerve neuromodulation) device
- **2017**, First remote DBS programming across different continents
- **2018**, First prize winner of the 2018 National Science and Technology Progress Award
- **2019**, First implantation of the PINS SCS (spinal cord stimulation) device
- **2020**, First implantation of the PINS DBS device supporting simultaneous stimulation and recording with Bluetooth connection for Brain-Machine Interface

Beijing PINS Medical Co., Ltd. focuses on the development and innovation of neuromodulation technologies, aiming to provide more comprehensive and professional solutions for patients suffering from neurological disorders.

CONTENTS

871 & 941

26 FEBRUARY 2021 • VOLUME 371 • ISSUE 6532

NEWS

IN BRIEF

868 News at a glance

IN DEPTH

870 Perseverance will explore history of ancient lake

Newly arrived Mars rover will probe rocks to reveal how wet planet was—and for how long
By P. Voosen

871 Hungry teen dinosaurs crowded out competitors

Study explains why ancient carnivores were tiny or huge, not medium-size
By G. Vogel
REPORT p. 941

872 Rare cosmic neutrino traced to star-shredding black hole

Particle points to black hole jets as high-energy accelerators
By D. Cleary

873 Hunt for renewable plastics clears a hurdle

Solving alkalinity problem may help make plastics from CO₂, water, and electricity
By R. F. Service

874 Vaccine trials ramp up in children and adolescents

Doctors stress need to vaccinate young people once shots are available
By J. Couzin-Frankel

875 New U.K. funding agency aims to tackle innovative research

Like ARPA in the United States, ARIA will fund risky ideas. But some worry that fledgling agency lacks a focus
By C. O'Grady

FEATURES

876 Shifting ground

Fleets of radar satellites are measuring movements on Earth like never before
By J. Rosen
PODCAST

INSIGHTS

PERSPECTIVES

882 Illuminating tremors in the deep

Telecommunication cables on the seafloor monitor seismic activity
By W. Wilcock
REPORT p. 931

884 SARS-CoV-2 dependence on host pathways

A drug that inhibits host protein synthesis shows antiviral activity against SARS-CoV-2
By J. P. Wong and B. Damania
RESEARCH ARTICLE p. 926

886 Transition states and spin-orbit structure

Spin-orbit coupling is required to explain a set of scattering resonances in the F + HD reaction
By T. P. Rakitzis
REPORT p. 936

887 In the zone for liver proliferation

Distinct liver compartments contribute to hepatocyte homeostasis versus regeneration
By E. R. Andersson
RESEARCH ARTICLES pp. 905 & 906

889 High-speed harvesting of random numbers

A broad-area multimode laser can be made into a powerful random number generator
By I. Fischer and D. J. Gauthier
REPORT p. 948

890 Optimizing age-specific vaccination

Vaccination strategies are not one-size-fits-all
By M. C. Fitzpatrick and A. P. Galvani
RESEARCH ARTICLE p. 916



Where
Science
Gets
Social.

AAAS.ORG/COMMUNITY



AAAS' Member Community is a one-stop destination for scientists and STEM enthusiasts alike. It's "Where Science Gets Social": a community where facts matter, ideas are big and there's always a reason to come hang out, share, discuss and explore.

**Member
COMMUNITY**
AAAS

AMERICAN ASSOCIATION FOR THE ADVANCEMENT OF SCIENCE

892 Paul J. Crutzen (1933–2021)

Father of modern atmospheric chemistry
By S. Solomon

POLICY FORUM**893 Was “science” on the ballot?**

Labeling dissent as “anti-science”
is bad social science and bad politics
By S. Hilgartner et al.

**BOOKS ET AL.****895 Evolution on other worlds**

Bound by finite natural laws, alien life may be
more familiar than we imagine By A. Woolfson

896 The soul and its shell

A neurosurgeon's audacious experiments
raised ire from animal rights activists
and interest from the Vatican By S. E. Lederer

LETTERS**897 Holistic environmental risk assessment for bees**

By C. J. Topping et al.

897 U.S. immigration reform for STEM doctorates

By J. Geng

898 Brazil's political upset threatens Amazonia

By L. Ferrante and P. M. Fearnside

898 Technical Comment abstracts**RESEARCH****IN BRIEF****901 From Science and other journals****REVIEW****904 Neurodegeneration**

Tau: Enabler of diverse brain disorders
and target of rapidly evolving therapeutic
strategies C.-W. Chang et al.

REVIEW SUMMARY; FOR FULL TEXT:
DOI.ORG/10.1126/SCIENCE.ABB8255

RESEARCH ARTICLES**Lineage tracing**

905 Proliferation tracing reveals regional
hepatocyte generation in liver
homeostasis and repair L. He et al.

RESEARCH ARTICLE SUMMARY; FOR FULL
TEXT: DOI.ORG/10.1126/SCIENCE.ABC4346

906 Liver homeostasis is maintained by
midlobular zone 2 hepatocytes Y. Wei et al.

RESEARCH ARTICLE SUMMARY; FOR FULL
TEXT: DOI.ORG/10.1126/SCIENCE.ABB1625

PERSPECTIVE p. 887

907 Coronavirus

Afucosylated IgG characterizes enveloped
viral responses and correlates with COVID-19
severity M. D. Larsen et al.

RESEARCH ARTICLE SUMMARY; FOR FULL TEXT:
DOI.ORG/10.1126/SCIENCE.ABC8378

908 3D genomics

In situ genome sequencing resolves DNA
sequence and structure in intact biological
samples A. C. Payne et al.

RESEARCH ARTICLE SUMMARY; FOR FULL TEXT:
DOI.ORG/10.1126/SCIENCE.AAY3446

909 Cancer genomics

Single-cell lineages reveal the rates, routes,
and drivers of metastasis in cancer xenografts
J. J. Quinn et al.

RESEARCH ARTICLE SUMMARY; FOR FULL TEXT:
DOI.ORG/10.1126/SCIENCE.ABC1944

910 Molecular motors

Shulin packages axonemal outer dynein arms
for ciliary targeting G. R. Mali et al.

916 Coronavirus

Model-informed COVID-19 vaccine
prioritization strategies by age and serostatus
K. M. Bubar et al.

PERSPECTIVE p. 890

921 Atmospheric chemistry

Reactive uptake of N₂O₅ by atmospheric
aerosol is dominated by interfacial processes
M. Galib and D. T. Limmer

926 Coronavirus

Plitidepsin has potent preclinical efficacy
against SARS-CoV-2 by targeting the host
protein eEF1A K. M. White et al.

PERSPECTIVE p. 884

REPORTS**931 Geophysics**

Optical polarization-based seismic and
water wave sensing on transoceanic cables
Z. Zhan et al.

PERSPECTIVE p. 882

936 Chemical dynamics

Quantum interference between spin-orbit
split partial waves in the F + HD → HF + D
reaction W. Chen et al.

PERSPECTIVE p. 886

941 Paleontology

The influence of juvenile dinosaurs
on community structure and diversity
K. Schroeder et al.

NEWS STORY p. 871; VIDEO

945 Nuclear astrophysics

¹²⁹I and ²⁴⁷Cm in meteorites constrain the
last astrophysical source of solar r-process
elements B. Côté et al.

948 Optoelectronics

Massively parallel ultrafast random
bit generation with a chip-scale laser
K. Kim et al.

PERSPECTIVE p. 889; PODCAST

DEPARTMENTS**867 Editorial**

Clarity on the crackdown
By Harvey Lodish et al.

958 Working Life

A perfect illusion By Naomi Dalchand

ON THE COVER

Flooding damage in the Bahamas, from
Hurricane Dorian in 2019, was remotely
assessed by NASA's Jet Propulsion
Laboratory and the Earth Observatory of
Singapore using synthetic aperture radar
(SAR) data from Europe's Sentinel-1 satel-
lites. By comparing SAR images acquired
before and after the hurricane, researchers
can see shifts in ground surface related to
flooding (yellow and red indicate increasingly
substantial surface change). A surge in SAR
data is enabling researchers to study changes
like these at finer scales and frequencies.



See page 876. Image:
ARIA, JPL-Caltech, Earth
Observatory of Singapore,
Nanyang Technological
University, NASA Earth
Applied Sciences Disasters
Program. Contains modi-
fied Copernicus Sentinel
data (2019)

Science Staff	866
AAAS News & Notes	900
Science Careers	953

SCIENCE (ISSN 0036-8075) is published weekly on Friday, except last week in December, by the American Association for the Advancement of Science, 1200 New York Avenue, NW, Washington, DC 20005. Periodicals mail postage (publication No. 484460) paid at Washington, DC, and additional mailing offices. Copyright © 2021 by the American Association for the Advancement of Science. The title SCIENCE is a registered trademark of the AAAS. Domestic individual membership, including subscription (12 months): \$165 (\$74 allocated to subscription). Domestic institutional subscription (51 issues): \$2148; Foreign postage extra: Air assist delivery: \$98. First class, airmail, student, and emeritus rates on request. Canadian rates with GST available upon request. GST #125488122. Publications Mail Agreement Number 1069624. Printed in the U.S.A.

Change of address: Allow 4 weeks, giving old and new addresses and 8-digit account number. **Postmaster:** Send change of address to AAAS, P.O. Box 96178, Washington, DC 20090-6178. **Single-copy sales:** \$15 each plus shipping and handling available from backissues.sciencemag.org; bulk rate on request. **Authorization to reproduce** material for internal or personal use under circumstances not falling within the fair use provisions of the Copyright Act can be obtained through the Copyright Clearance Center (CCC), www.copyright.com. The identification code for Science is 0036-8075. Science is indexed in the Reader's Guide to Periodical Literature and in several specialized indexes.

Editor-in-Chief Holden Thorp, hthorp@aaas.org

Executive Editor Monica M. Bradford

Editors, Research Valda Vinson, Jake S. Yeston Editor, Insights Lisa D. Chong

DEPUTY EDITORS Julia Fahrenkamp-Uppenbrink (UK), Stella M. Hurlley (UK), Phillip D. Szurmi, Sacha Vignieri SR. EDITORIAL FELLOW Andrew M. Sugden (UK) SR. EDITORS Gemma Alderton (UK), Caroline Ash (UK), Brent Grocholski, Pamela J. Hines, Di Jiang, Marc S. Lavine (Canada), Yevgeniya Nusinovich, Ian S. Osborne (UK), Beverly A. Purnell, L. Bryan Ray, H. Jesse Smith, Keith T. Smith (UK), Jelena Stajic, Peter Stern (UK), Valerie B. Thompson, Brad Wible, Laura M. Zahn ASSOCIATE EDITORS Michael A. Funk, Priscilla N. Kelly, Tage S. Rai, Seth Thomas Scanlon (UK), Yury V. Suleymanov LETTERS EDITOR Jennifer Sills LEAD CONTENT PRODUCTION EDITORS Harry Jach, Lauren Kmec CONTENT PRODUCTION EDITORS Amelia Beyna, Jeffrey E. Cook, Chris Filiatreau, Julia Katris, Nida Masiulis, Suzanne M. White SR. EDITORIAL COORDINATORS Carolyn Kyle, Beverly Shields EDITORIAL COORDINATORS Aneera Dobbins, Joi S. Granger, Jeffrey Hearn, Lisa Johnson, Maryrose Madrid, Ope Martins, Shannon McMahon, Jerry Richardson, Hilary Stewart (UK), Alana Warnke, Alice Whaley (UK), Anita Wynn PUBLICATIONS ASSISTANTS Jeremy Dow, Alexander Kief, Ronnel Navas, Brian White EXECUTIVE ASSISTANT Jessica Slater ASI DIRECTOR, OPERATIONS Janet Clements (UK) ASI SR. OFFICE ADMINISTRATOR Jessica Waldo (UK)

News Editor Tim Appenzeller

NEWS MANAGING EDITOR John Travis INTERNATIONAL EDITOR Martin Enserink DEPUTY NEWS EDITORS Elizabeth Culotta, Lila Guterman, David Grimm, Eric Hand (Europe), David Malakoff SR. CORRESPONDENTS Daniel Cley (UK), Jon Cohen, Jeffrey Mervis, Elizabeth Pennisi ASSOCIATE EDITORS Jeffrey Brainard, Catherine Maticic NEWS REPORTERS Adrian Cho, Jennifer Couzin-Frankel, Jocelyn Kaiser, Kelly Servick, Robert F. Service, Erik Stokstad, Paul Voosen, Meredith Wadman INTERNS Lucy Hicks, Cathleen O'Grady CONTRIBUTING CORRESPONDENTS Warren Cornwall, Andrew Curry (Berlin), Ann Gibbons, Sam Kean, Eli Kintisch, Kai Kupferschmidt (Berlin), Andrew Lawler, Mitch Leslie, Eliot Marshall, Virginia Morell, Dennis Normile (Shanghai), Elisabeth Pain (Careers), Charles Pillar, Michael Price, Tania Rabesandratana (Barcelona), Joshua Sokol, Emily Underwood, Gretchen Vogel (Berlin), Lizzie Wade (Mexico City) CAREERS Donisha Adams, Rachel Bernstein (Editor), Katie Langin (Associate Editor) COPY EDITORS Julia Cole (Senior Copy Editor), Cyra Master (Copy Chief) ADMINISTRATIVE SUPPORT Meagan Weiland

Creative Director Beth Rakouskas

DESIGN MANAGING EDITOR Marcy Atarod GRAPHICS MANAGING EDITOR Alberto Cuadra PHOTOGRAPHY MANAGING EDITOR William Douthitt WEB CONTENT STRATEGY MANAGER Kara Estelle-Powers DESIGN EDITOR Chrystal Smith DESIGNER Christina Aycock GRAPHICS EDITOR Nirja Desai INTERACTIVE GRAPHICS EDITOR Kelly Franklin SENIOR SCIENTIFIC ILLUSTRATORS Valerie Altounian, Chris Bickel SCIENTIFIC ILLUSTRATOR Alice Kitterman SENIOR GRAPHICS SPECIALISTS Holly Bishop, Nathalie Cary SENIOR PHOTO EDITOR Emily Petersen PHOTO EDITOR Kaitlyn Dolan WEB DESIGNER Jennie Pajeroski

Chief Executive Officer and Executive Publisher Sudip Parikh

Publisher, Science Family of Journals Bill Moran

DIRECTOR, BUSINESS SYSTEMS AND FINANCIAL ANALYSIS Randy Yi DIRECTOR, BUSINESS OPERATIONS & ANALYSIS Eric Knott DIRECTOR OF ANALYTICS Enrique Gonzales MANAGER, BUSINESS OPERATIONS Jessica Tierney SENIOR BUSINESS ANALYST Cory Lipman, Meron Kebede FINANCIAL ANALYST Alexander Lee ADVERTISING SYSTEM ADMINISTRATOR Tina Burks SENIOR SALES COORDINATOR Shirley Young DIGITAL/PRINT STRATEGY MANAGER Jason Hillman QUALITY TECHNICAL MANAGER Marcus Spiegler ASSISTANT MANAGER DIGITAL/PRINT Rebecca Doshi SENIOR CONTENT SPECIALISTS Steve Forrester, Jacob Hedrick, Antoinette Hodal, Lori Murphy PRODUCTION SPECIALIST Kristin Wolk DIGITAL PRODUCTION MANAGER Lisa Stanford CONTENT SPECIALIST Kimberley Oster ADVERTISING PRODUCTION OPERATIONS MANAGER Deborah Tompkins DESIGNER, CUSTOM PUBLISHING Jeremy Hunsinger SR. TRAFFIC ASSOCIATE Christine Hall SPECIAL PROJECTS ASSOCIATE Sarah Dhere

ASSOCIATE DIRECTOR, BUSINESS DEVELOPMENT Justin Sawyers GLOBAL MARKETING MANAGER Allison Pritchard DIGITAL MARKETING MANAGER Aimee Aponte JOURNALS MARKETING MANAGER Shawana Arnold MARKETING ASSOCIATES Tori Velasquez, Mike Romano, Ashley Hylton DIGITAL MARKETING SPECIALIST Asleigh Rojanavongse SENIOR DESIGNER Kim Huynh

DIRECTOR AND SENIOR EDITOR, CUSTOM PUBLISHING Sean Sanders ASSISTANT EDITOR, CUSTOM PUBLISHING Jackie Oberst

DIRECTOR, PRODUCT & PUBLISHING DEVELOPMENT Chris Reid DIRECTOR, BUSINESS STRATEGY AND PORTFOLIO MANAGEMENT Sarah Whalen ASSOCIATE DIRECTOR, PRODUCT MANAGEMENT Kris Bishop PRODUCT DEVELOPMENT MANAGER Scott Chernoff PUBLISHING TECHNOLOGY MANAGER Michael Di Natale SR. PRODUCT ASSOCIATE Robert Koepke SPJ ASSOCIATE Samantha Bruno Fuller

DIRECTOR, INSTITUTIONAL LICENSING Iquo Edim ASSOCIATE DIRECTOR, RESEARCH & DEVELOPMENT Elisabeth Leonard MARKETING MANAGER Kess Knight SENIOR INSTITUTIONAL LICENSING MANAGER Ryan Rexroth INSTITUTIONAL LICENSING MANAGER Marco Castellani MANAGER, AGENT RELATIONS & CUSTOMER SUCCESS Judy Lillibridge SENIOR OPERATIONS ANALYST Lana Guz FULFILLMENT COORDINATOR Melody Stringer SALES COORDINATOR Josh Haverlock

DIRECTOR, GLOBAL SALES Tracy Holmes US EAST COAST AND MID WEST SALES Stephanie O'Connor US WEST COAST SALES Lynne Stickrod US SALES MANAGER, SCIENCE CAREERS Claudia Paulsen-Young US SALES REP, SCIENCE CAREERS Tracy Anderson ASSOCIATE DIRECTOR, ROW ROWR Goncalves SALES REP, ROW Sarah Lelarge SALES ADMIN ASSISTANT, ROW Bryony Cousins DIRECTOR OF GLOBAL COLLABORATION AND ACADEMIC PUBLISHING RELATIONS, ASIA Xiaoying Chu ASSOCIATE DIRECTOR, INTERNATIONAL COLLABORATION Grace Yao SALES MANAGER Danny Zhao MARKETING MANAGER Kilo Lan ASCA CORPORATION, JAPAN Kaoru Sasaki (Tokyo), Miyuki Tani (Osaka) COLLABORATION/CUSTOM PUBLICATIONS/JAPAN Adarsh Sandhu

DIRECTOR, COPYRIGHT, LICENSING AND SPECIAL PROJECTS Emilie David RIGHTS AND LICENSING COORDINATOR Jessica Adams RIGHTS AND PERMISSIONS ASSOCIATE Elizabeth Sandler CONTRACTS AND LICENSING ASSOCIATE Lili Catlett

MAIN HEADQUARTERS

Science/AAAS
1200 New York Ave. NW
Washington, DC 20005

SCIENCE INTERNATIONAL

Clarendon House
Clarendon Road
Cambridge, CB2 8FH, UK

SCIENCE CHINA

Room 1004, Culture Square
No. 59 Zhongguancun St.
Haidian District, Beijing, 100872

SCIENCE JAPAN

ASCA Corporation
Sibaura TY Bldg. 4F, 1-14-5
Shibaura Minato-ku
Tokyo, 108-0073 Japan

EDITORIAL

science_editors@aaas.org

NEWS

science_news@aaas.org

INFORMATION FOR AUTHORS

sciencemag.org/authors/

science-information-authors

REPRINTS AND PERMISSIONS

sciencemag.org/help/

reprints-and-permissions

MEDIA CONTACTS

scipak@aaas.org

MULTIMEDIA CONTACTS

SciencePodcast@aaas.org

ScienceVideo@aaas.org

INSTITUTIONAL SALES

AND SITE LICENSES

sciencemag.org/librarian

PRODUCT ADVERTISING

& CUSTOM PUBLISHING

advertising.sciencemag.org/

products-services

science_advertising@aaas.org

CLASSIFIED ADVERTISING

advertising.sciencemag.org/

science-careers

advertise@sciencecareers.org

JOB POSTING CUSTOMER SERVICE

employers.sciencemag.org

support@sciencecareers.org

MEMBERSHIP AND INDIVIDUAL

SUBSCRIPTIONS

sciencemag.org/subscriptions

MEMBER BENEFITS

aaas.org/membercentral

AAAS BOARD OF DIRECTORS

CHAIR Steven Chu

PRESIDENT Claire M. Fraser

PRESIDENT-ELECT Susan G. Amara

TREASURER Carolyn N. Ainslie

CHIEF EXECUTIVE OFFICER

Sudip Parikh

BOARD Cynthia M. Beall

Rosina M. Bierbaum

Ann Bostrom

Stephen P.A. Fodor

S. James Gates, Jr.

Laura H. Greene

Kaye Husbands Fealing

Maria M. Klawe

Robert B. Millard

Alondra Nelson

William D. Provine

BOARD OF REVIEWING EDITORS (Statistics board members indicated with \$)

Takuzo Aida, U. of Tokyo

Leslie Aiello,

Wenner-Gren Foundation

Deji Akinwande, UT Austin

Judith Allen, U. of Manchester

Marcella Alsan, Harvard U.

Sebastian Amigorena,

Institut Curie

James Analytis, UC Berkeley

Trevor Archer, NIEHS, NIH

Paola Arlotto, Harvard U.

David Awschalom, U. of Chicago

Clare Baker, U. of Cambridge

Delia Baldassarri, NYU

Nenad Ban, ETH Zürich

Franz Bauer,

Pontificia U. Católica de Chile

Ray H. Baughman,

IST Dallas

Carlo Beenakker, Leiden U.

Yasmine Belkaid, NIAID, NIH

Philip Benfey, Duke U.

Kiros T. Berhane, Columbia U.

Bradley Bernstein,

Mass. General Hospital

Joseph J. Berry, NREL

Alessandra Biffi,

Harvard Med.

Chris Bowler,

École Normale Supérieure

Ian Boyd, U. of St. Andrews

Emily Brodsky, UC Santa Cruz

Ron Brookmeyer, UCLA (\$)

Christian Büchel, UKE Hamburg

Dennis Burton, Scripps Res.

Carter Tribble Butts, UC Irvine

György Buzsáki,

NYU School of Med.

Mariana Byndloss,

Vanderbilt U. Med. Ctr

Annmarie Carlton, UC Irvine

Nick Chater, U. of Warwick

Ling-Ling Chen, SIBCB, CAS

M. Keith Chen, UCLA

Zhijian Chen,

UT Southwestern Med. Ctr.

Ib Chorkendorff, Denmark TU

James J. Collins, MIT

Robert Cook-Deegan,

Arizona State U.

Virginia Cornish, Columbia U.

Carolyn Coyne, U. of Pitt.

Roberta Croce, VU Amsterdam

Ismail Dabo, Penn State U.

Jeff L. Dangl, UNC

Chiara Daraio, Caltech

Nicolas Dauphas, U. of Chicago

Christian Davenport,

U. of Michigan

Frans de Waal, Emory U.

Claude Desplan, NYU

Sandra Díaz,

U. Nacional de Córdoba

Ulrike Diebold, TU Wien

Stefanie Dimpfeler,

Goethe-U. Frankfurt

Hong Ding, Inst. of Physics, CAS

Dennis Discher, UPenn

Jennifer A. Doudna,

UC Berkeley

Ruth Drdlá-Schutting,

Med. U. Vienna

Raissa M. D'Souza, UC Davis

Bruce Dunn, UCLA

William Dunphy, Caltech

Scott Edwards, Harvard U.

Todd Ehlers, U. of Tübingen

Jennifer Eliseeff,

Johns Hopkins U.

Andrea Encalada,

U. San Francisco de Quito

Nader Engheta, U. of Penn.

Karen Ersche, U. of Cambridge

Beate Escher,

UFZ & U. of Tübingen

Barry Everitt, U. of Cambridge

Vanessa Ezenwa, U. of Georgia

Michael Feuer, GWU

Toren Finkel,

U. of Pitt. Med. Ctr.

Gwynn Flowers, Simon Fraser U.

Peter Fratzi,

Max Planck Inst. Potsdam

Elaine Fuchs, Rockefeller U.

Jay Gallagher, U. of Wisconsin

Daniel Gerschwind, UCLA

Ramon Gonzalez,

U. of South Florida

Sandra González-Bailón,

UPenn

Elizabeth Grove, U. of Chicago

Nicolas Gruber, ETH Zürich

Hua Guo, U. of New Mexico

Taejip Ha, Johns Hopkins U.

Sharon Hammes-Schiffer,

Yale U.

Wolf-Dietrich Hardt, ETH Zürich

Louise Harra, U. Coll. London

Jian He, Clemson U.

Carl-Philipp Heisenberg,

IST Austria

Ykä Helariutta, U. of Cambridge

Janet G. Hering, Eawag

Heather Hickman, NIAID, NIH

Hans Hilgenkamp, U. of Twente

Kai-Uwe Hinrichs, U. of Bremen

Deirdre Hollingsworth,

U. of Oxford

Randall Hulet, Rice U.

Auke Ijspeert, EPFL

Akiko Iwase, Yale U.

Stephen Jackson,

USGS & U. of Arizona

Erich Jarvis, Rockefeller U.

Peter Jonas, IST Austria

Matt Kaerlein,

U. of Wash.

William Kaelin Jr.,

Dana-Farber Cancer Inst.

Daniel Kammen, UC Berkeley

V. Narry Kim, Seoul Nat. U.

Robert Kingston,

Anuj Shah, U. of Chicago

Vladimir Shalae, Purdue U.

Jie Shan, Cornell U.

Beth Shapiro, UC Santa Cruz

Jay Shendure, U. of Wash.

Steve Sherwood,

U. of New South Wales

Brian Shiochet, UCSF

Robert Siliciano,

JHU School of Med.

Lucia Sivilotti, U. Coll. London

Alison Smith, John Innes Centre

Richard Smith,

UNC (\$)

Mark Smyth, QIMR Berghofer

John Speakman, U. of Aberdeen

Tara Spires-Jones,

U. of Edinburgh

Allan C. Spradling,

Carnegie Institution for Sci.

V. S. Subrahmanian,

Dartmouth

Ira Tabas, Columbia U.

Eriko Takano, U. of Manchester

Patrick Tan,

Duke-NUS Med. School

Sarah Teichmann,

Wellcome Sanger Inst.

Rocio Titiunik, Princeton U.

Shubha Tole,

Tata Inst. of Fundamental Res.

Kimani Toussaint, Brown U.

Wim van der Putten,

Netherlands Inst. of Ecology

Rheinilde Veugelers, KU Leuven

Clarity on the crackdown

Less than a month after his inauguration, U.S. President Biden moved to reverse policies that have deterred foreign students and high-skilled workers from coming to the United States. This is good news. The exchange of culture and knowledge drives innovation, which in turn builds the nation's economy and competitiveness on a global scale. But some countries, especially China, continue to present a dilemma when it comes to national security. In trying to strike a balance between preserving a culture of openness and protecting U.S. research, missteps can occur—and that can be detrimental to U.S. science.

In 2018, the U.S. Department of Justice established its China Initiative to crack down on espionage. Numerous scientists and engineers, mostly Chinese and Chinese American, have been accused or convicted of a wide range of acts, such as hiding their ties to China. Certainly, guilty individuals have been identified. But what is concerning are the prosecutorial methods wielded under the China Initiative. Many outstanding scientists, mostly Chinese American, are being investigated for not properly disclosing certain associations with China. Even routine responsibilities, such as recommending students for jobs and awards, or serving as a reviewer on grants, are being portrayed as crimes. Some professors and many trainees have had to leave their positions or training after the termination of grants from U.S. agencies. The scale and obscurity of these matters threaten to damage research and innovation in the United States as Chinese and Chinese American scientists find themselves under constant suspicion for activities that are routine in academic collaborations.

If this clampdown is to continue, then more effective efforts must be made to distinguish normal, constructive international collaboration from genuine acts of espionage and financial malfeasance. At the same time, U.S. citizens who come under scrutiny must be granted the same rights under the law as their fellow Americans, regardless of their ethnicity or country of origin. Toward this end, more clarity is needed from the federal government and from university administrators. For example, federal guidelines and enforcement of policies requiring U.S. academic scientists to report interac-

tions with foreign universities and organizations have changed substantially over the past few years. However, few universities have developed procedures to communicate these changes to their faculty. Nor have university grant administrative staff been trained to monitor and respond to the changes effectively. All federal agencies supporting unclassified research should present a single set of guidelines to the academic community, and host institutes should be audited to ensure that investigators have been informed of disclosure policies and best practices. If interactions with China are to be considered a special case, this should be made clear in federal guidelines as well, especially regarding collaborations and academic advising outside of federally supported programs.

It is particularly concerning that many scientists who are currently under investigation have been unfairly stripped of federal funding without due process. There should be a process wherein the actions of such individuals are considered relative to the guidelines of the federal agencies before termination of funding. The host university or institute could conduct an investigation in conjunction with the appropriate government agency, similar to the procedure in cases of scientific misconduct.

The scientific community, through organizations such as the U.S. National Academies of Sciences, Engineering, and Medicine and American Association for the Advancement of Science (AAAS, the publisher of *Science*), should also examine the history of engagement of U.S. scientists with international scientists and agencies, issuing reports on their societal benefits and risks. This study should include, but not be limited to, the current focus on China. To better monitor the impact of the China Initiative, the scientific community should keep a database of all scientists who have been, or are being, prosecuted or publicly investigated.

As the nation strives to reopen its doors to foreign students and scientists, it's important to remember that the strength of the U.S. scientific enterprise is its culture of academic openness to support discoveries that transform the country and the world. Let's not jeopardize that preeminence.

—Harvey Lodish, Jianzhu Chen, Phillip Sharp

Harvey Lodish, Jianzhu Chen, and Phillip Sharp are professors in the Department of Biology at the Massachusetts Institute of Technology, Cambridge, MA, USA. lodish@wi.mit.edu; jchen@mit.edu; sharp@mit.edu

“Even routine responsibilities... are being portrayed as crimes.”

A new German word meaning “exhausted with everything to do with the pandemic,” according to the Leibniz Institute for the German Language. It is one of more than 1200 recently created German words about COVID-19 compiled by the institute. A full list is at <http://scim.ag/2Nt4Us0>.



U.S. President Joe Biden (left), Vice President Kamala Harris (second from right), and their spouses honor the more than 500,000 Americans who have died from COVID-19.

IN BRIEF

Edited by Jeffrey Brainard

DISPATCHES FROM THE PANDEMIC

Fund for vaccine equity nears goal

COVID-19 | Efforts to equitably distribute COVID-19 vaccines around the globe received a crucial cash infusion last week. At a virtual meeting of the Group of Seven countries, several pledged more money through the COVID-19 Vaccines Global Access (COVAX) Facility's Advance Market Commitment, set up by the World Health Organization (WHO) and others to pay for vaccine doses for low- and middle-income countries. The United States pledged \$2 billion already appropriated by Congress, plus another \$2 billion contingent on others contributing. Germany offered €980 million and the European Union €500 million, bringing overall funding to \$6.3 billion—close to the \$7 billion WHO says is needed to pay for 2 billion doses by the end of this year. First doses of the AstraZeneca–University of Oxford and Pfizer vaccines are scheduled to be delivered through the COVAX Facility in coming weeks. But money alone isn't enough to help poor countries if wealthy ones continue to gobble up available vaccine supplies and

reduce the number of doses the COVAX Facility can buy, WHO Director-General Tedros Adhanom Ghebreyesus warned at a 22 February press conference.

U.S. sees drop in foreign students

GRADUATE EDUCATION | The number of international students starting U.S. graduate programs dropped steeply last fall, most likely because of travel restrictions from the pandemic. The Council of Graduate Schools reported last week that 26% fewer students from other countries began U.S. doctoral programs in 2020 compared with 2019, and 43% fewer started masters' programs. International students continued to favor U.S. institutions, filing 3% more applications than in 2019, despite fears that restrictive immigration policies would dampen interest.

Budget boost for NSF, NIST?

PANDEMIC RELIEF | The U.S. National Science Foundation (NSF) is in line for \$600 million as part of the massive coronavirus pandemic relief bill moving rapidly

through Congress. Both that amount and \$150 million for the National Institute of Standards and Technology were expected to be added to the \$1.9 trillion spending plan after *Science* went to press. The measure is designed to help the nation recover from the pandemic's devastating impacts, including damage to its science and technology enterprise. The bill already contains \$100 million for researchers to study effects on student learning. The NSF money could include support for early-career scientists.

U.K. board OKs 'challenge' trial

COVID-19 | A U.K. ethics board last week said a research team there can begin to intentionally infect volunteers with the pandemic coronavirus, in a world-first, hotly debated experiment intended to accelerate research on vaccines against the disease. As a first step, the “human challenge” experiment will determine the lowest dose of the virus needed to infect 90 healthy volunteers ages 18 to 30. The researchers then plan to give additional volunteers existing vaccines against the

virus and “challenge” them with the infectious dose, given into the nose. Scientists have said that despite the success of multiple vaccines in recent months, the trials could offer vital information about differences in their efficacies and the immune mechanisms behind protection. Critics contend the risk to the volunteers, who will be quarantined and paid for their time, isn’t worth the potential benefit because traditional vaccine efficacy trials can answer the most critical questions.

Pregnancy boosts infection rate

PUBLIC HEALTH | The pandemic coronavirus infected pregnant women in Washington state from March to June 2020 at a rate 70% higher than it did nonpregnant adults of the same age, a large retrospective study has found. When researchers excluded pregnant women who had no COVID-19 symptoms but tested positive for the virus during routine screening, the infection rate still exceeded the control group’s by 30%. Nonwhite women who were pregnant appeared to be markedly more susceptible. Previous research found an elevated risk of severe illness in pregnant women infected with the coronavirus, which combined with the new findings suggests U.S. authorities should prioritize them for COVID-19 vaccinations, wrote the authors of the study, published last week in the *American Journal of Obstetrics & Gynecology*. Also last week, manufacturers Pfizer and BioNTech launched a placebo-controlled clinical trial of their vaccine in pregnant women.

FDA warns of oximeter flaws

DIAGNOSTICS | Under pressure from physicians and lawmakers, the U.S. Food and Drug Administration (FDA) last week acknowledged that pulse oximeters—devices that measure oxygen levels and are common in COVID-19 care—are less accurate for people with darker skin. Research has long suggested racial bias in the devices, which attach to the fingertip and use light beams to estimate the oxygen saturation of blood. (A recent study found they were almost three times as likely to miss low blood oxygen in Black patients than in white ones.) In an alert, FDA did not refer specifically to racial bias but said factors such as skin pigmentation, thickness, and temperature could affect accuracy. It urged patients and caregivers to pay more attention to trends in readouts than individual measurements, and not to rely on oximeters alone to gauge health.

SCIENCEMAG.ORG/TAGS/CORONAVIRUS

Read *Science*’s online coverage of the pandemic.

CONSERVATION

Ferret cloned for restoration



Researchers have cloned one of the most endangered mammals in North America, which could boost the species’ genetic diversity and aid restoration efforts. The black-footed ferret clone (left), born in December 2020 and named Elizabeth Ann, is the first clone of an endangered animal native to North America. Members of other endangered species have been cloned, but few of the offspring have survived their first month and none has been reintroduced to the wild. (In August 2020, for example, San Diego Zoo Global announced the successful cloning of a Przewalski’s horse, an endangered species that went extinct in the wild but has been reintroduced in Mongolia using captive-bred animals.) Black-footed ferrets were thought to be extinct in North America until 1981, when a rancher in Wyoming found a small population. After captive breeding and reintroductions, several hundred of the ferrets now live in the wild—all descended from seven individuals. One of the original captured ferrets, named Willa, has no surviving offspring. Her cells had been frozen and were used to clone the new ferret, the U.S. Fish and Wildlife Service said last week.

Reef studies exclude locals

MARINE SCIENCE | Scientists from poor nations that hold many of the world’s tropical coral reefs are often excluded from research teams that “parachute” in for studies, concludes an analysis this week in *Current Biology*. The authors examined nearly 3700 studies published from 1969 to 2020. Many lead authors came from wealthier nations with few or no reefs, they found. In a subset of 305 studies from Indonesia, the Philippines, and Australia, they found that 40% of the Indonesian and the Philippine studies had no local co-authors, versus 22% for Australia. To help coral reefs, the authors say more equitable and numerous collaborations must become “the rule and not the exception.”

A push for a fusion power plant

ENERGY | If the United States wants to include fusion power in efforts to shift to low-carbon energy, it should accelerate a plan to build a prototype plant, an expert panel said last week. The plant, first proposed in 2018, would use the process that powers the Sun to generate electricity. It would advance beyond ITER, the huge international fusion experiment under construction in France that aims to produce more

energy than it consumes. But if utilities are going to embrace fusion, the United States should complete a demonstration plant by 2040, suggests the report by the National Academies of Sciences, Engineering, and Medicine. It says the U.S. Department of Energy should team with industry to develop multiple designs for a plant that generates at least 50 megawatts and costs no more than \$6 billion. U.S. fusion researchers embraced the pilot plant in a new long-range plan released in December 2020, but some nuclear specialists say the proposed timetable is unrealistic.

Europe picks radar satellites

EARTH SCIENCE | The European Space Agency (ESA) this week gave preliminary approval to the Harmony mission: two radar satellites that will monitor glacier flows, slip along earthquake faults, and tiny shifts in the ocean surface using a technique called interferometric synthetic aperture radar, or InSAR (see p. 876). The satellites will fly in tandem with ESA’s Sentinel-1 InSAR satellites, capturing their reflected beams along different angles and flight paths to sharpen the resolution of the data. The mission, expected to cost several hundred million euros, is expected to get final approval for construction by fall 2022.



A hovercraft captured the last moments of Perseverance's dramatic descent to Mars.

PLANETARY SCIENCE

Perseverance will explore history of ancient lake

Newly arrived Mars rover will probe rocks to reveal how wet planet was—and for how long

By **Paul Voosen**

Last week, NASA's \$2.7 billion Perseverance rover made a picture-perfect landing on the floor of Mars's Jezero crater, which scientists believe was filled to the brim with water 3.8 billion years ago. Two kilometers away looms the rover's primary target: a fossilized river delta, created as muddy water spilled into the crater—ideal for preserving signs of life.

But before Perseverance starts the long climb up into the delta, to drill samples that will eventually be returned to Earth, it will examine the rocks beneath its six aluminum wheels. The rover landed near outcrops of rock layers that may have originally been laid down before and after the lake and the delta. The NASA team will probe them for clues to the nature and timing of the brief period when water flowed—and life might have flourished. Even the first images returned to Earth, grainy and taken from the underneath the rover, left the team elated, says Katie Stack Morgan, the mission's deputy project scientist at NASA's Jet Propulsion Laboratory (JPL). "We have enough for the scientists to really sink their teeth into."

The rover's arrival at Mars was filled with nail-biting drama, even as the precise, autonomous descent unfolded like clockwork. After the spacecraft plunged by parachute through the thin air, a rocket-propelled hovercraft took over, seeking a boulder-free spot before lowering the rover from nylon cords. The final moments, captured in breathtaking detail by cam-

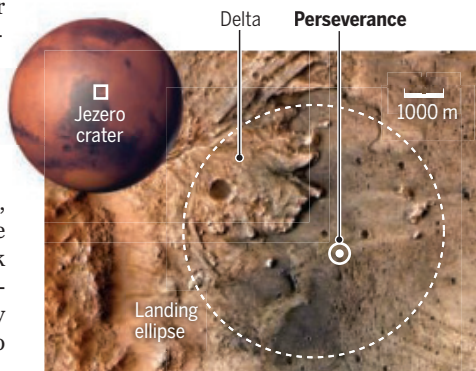
eras below the hovercraft, show the rover landing in a cloud of dust. "We did have a pretty clean run," says Allen Chen, head of the rover's landing team at JPL, in a dry understatement. "It did what it had to do." The touchdown marks NASA's ninth successful landing on the martian surface out of 10 tries.

After 3 days, the rover had executed 5000 commands and scientific instruments were certifying their health, says Jessica Samuels, an engineer and mission manager at JPL. "Everything is coming back exactly how we want it to." The rover raised its camera mast 2 meters above the surface to capture a panorama of its surroundings. After several days updating software, the team plans to wiggle the rover's wheels and conduct a short test drive. The rover will also extend its five-jointed, 2-meter-long robotic arm, which carries the rover's coring drill and several more cameras, and put it through some calisthenics. A second robotic arm, designed to manipulate a cache of dust and rock samples inside the rover, will be run through its paces.

Stored in 43 ultraclean tubes, those samples represent the start of a multibillion-dollar, multinational effort to collect mar-

A muddy target

Perseverance landed 2 kilometers away from the edge of a fossil river delta, a promising site for finding organic molecules and other signs of life.



tian rocks and return them for analysis on Earth; two follow-up missions to retrieve the samples are planned for later this decade (*Science*, 22 November 2019, p. 932). Within its first 2 years, the rover is expected to fill nearly half the tubes on its trek of more than 10 kilometers to the crater's rim. The rest will be filled in an extended mission, as the rover trundles beyond the crater to ancient highlands thought to have once held geothermal springs.

Perseverance's primary mission is to search for evidence of past life, captured in the delta mudstones and other rocks likely to preserve organic molecules—or even fossilized life. But interpreting this evidence will also require a better understanding of Mars's climatic past, from clues that can be collected right away by the rover.

The first opportunity to drill a sample could come within a few months, on the flat, pebble-strewn terrain where Perseverance landed. Some scientists believe these rocks are from an ancient lava flow that erupted long after the lake disappeared, arguing that they look the way Hawaiian flows might if bombarded by meteorites and whipped by winds for several billion years. But when Perseverance's predecessor, the Curiosity rover, explored similar rocks in Gale crater and its ancient lake, most of what scientists had thought were lava fields turned out to be sedimentary rocks: ground up volcanic bits ferried by water and deposited in layers, presumably in the vanished lake. The early pictures from Perseverance are difficult to interpret: Rocks riddled with holes could be pumice, porous from gas escaping from cooling lava, or they could be sedimentary rocks, perforated over time by water. Bigger boulders in the distance look like ancient volcanic rocks: dark and coated by a light-colored dust.

Fortunately, Perseverance's scientific instruments are designed to pin down the rocks' origin. Cameras on the mast could spy distinctive angular striped layers, called cross-bedding, that only form when deposited as sediments. A camera mounted on the end of the rover's robotic arm for microscopic views could capture the grain of minerals: Sedimentary rocks, for example, are typically rounded by their watery travels. Two other instruments on the arm will fire x-rays and ultraviolet laser light at rock samples, provoking reactions that could reveal chemical fingerprints of volcanic or sedimentary rocks.

It's a crucial distinction. If the rocks are volcanic—either lava deposits or, more likely, ash from a distant eruption—they'll contain trace radioactive elements that

decay at a certain rate, so when samples are returned to Earth, lab scientists could date the eruption and put a bound on the age of the lake. Any date will also help pin down the highly uncertain overall martian timeline, currently dated by counting the number of craters on a given terrain. (Older surfaces are pocked with more craters.) Sampling such a volcanic rock would “provide a critical anchor to the timing of events we are looking at,” says Ken Farley, the mission's project scientist and a geologist at the California Institute of Technology.

The rover's initial path is likely to cross another intriguing target just 250 meters away on the crater floor: outcrops that, from orbit, appear rich in both olivine, a volcanic mineral, and carbonates, which can form when olivine is exposed to water and carbon dioxide. If this layer is volcanic ash from an eruption that preceded the

Jezero lake, radioactive dates from it and the potential volcanic layer deposited on the lakebed should bracket the lake's existence in time. Moreover, isotopes of oxygen in the carbonates could reveal the temperature of the water that formed the mineral; balmy water would suggest Mars was once warm and wet for mil-

lions of years at a time, whereas water near freezing would argue for sporadic bursts of warmth. The carbonate might even contain gas bubbles—samples of the ancient martian atmosphere, which could allow scientists to see whether it held methane or other greenhouse gases that would have warmed early Mars. “That obviously would be game changing,” says Timothy Goudge, a planetary scientist at the University of Texas, Austin, who led the team that made the case for Jezero as a landing site.

There will be no drilling at the landing site itself. But there will be flying. After the monthlong commissioning phase is over, the team will find a nearby, flat spot to loose the 1.8-kilogram Ingenuity helicopter, which survived the landing attached to the rover's belly. With a fuselage the size of a tissue box, Ingenuity is a technology demonstration, a bid to fly a rotor-powered vehicle on another planet for the first time. After being dropped to the surface, the helicopter will furiously spin its rotors to ascend 3 meters in the air for 20 seconds. Four additional, higher flights could follow, over a total of 30 days, says MiMi Aung, Ingenuity's project manager at JPL. On later flights the helicopter could collect reconnaissance images for terrain off the rover's main path. “It will be truly a Wright brothers moment,” Aung says, “but on another planet.” ■

“Everything is coming back exactly how we want it to.”

Jessica Samuels,
Jet Propulsion Laboratory

PALEONTOLOGY

Hungry teen dinosaurs crowded out competitors

Study explains why ancient carnivores were tiny or huge, not medium-size

By **Gretchen Vogel**

Any parent of growing teenagers knows their appetites can reach gargantuan proportions. Now, imagine you had a young *T. rex* checking the fridge. The outsize appetites of growing dinosaurs reshaped food chains in their environment and squeezed out other carnivores, according to a new study on p. 941 of hundreds of dinosaurs of all sizes.

The “elegant study puts real numbers on something we’ve suspected for a while,” says Steve Brusatte, a paleontologist at the University of Edinburgh who was not involved with the study. There weren’t many mid-size meat eaters “because the juveniles and teenagers and subadults of the big beastly dinosaurs were hoarding those niches.”

Most groups of animals have many small species, somewhat fewer medium-size species, and even fewer large species. In contrast, the extinct dinosaurs—especially carnivores—had plenty of species no bigger than modern-day chickens and also many giant species, but few medium-size ones.

Paleontologists wondered whether juvenile dinosaurs crowded out medium-size adults by exploiting the habitats and food sources those species might have taken. To test the idea, Katlin Schroeder, a Ph.D. student at the University of New Mexico (UNM), Albuquerque, combed a global collection of fossil data called the Paleobiology Database to determine the size distribution of more than 550 dinosaur species in 43 ancient ecosystems across 136 million years and seven continents.

In most communities, herbivorous dinosaurs came in a range of sizes. But “carnivores are completely different,” she says. Carnivores between 100 and 1000 kilograms were consistently quite rare. “It’s as if you went to the savanna and saw nothing in size between a bat-eared fox and lion,”

Schroeder says. Patterns in all the dinosaur communities studied “are very similar, which is not what you’d expect from communities separated by 100 million years and half a globe,” she notes.

“They did this on a grand scale,” says Gregory Erickson, a paleontologist at Florida State University. “It’s very impressive, and very comprehensive. ... We saw the gap [in species’ sizes] for years, but never quantified it.”

To explore the reason, Schroeder and paleontologists Felisa Smith of UNM and Kathleen Lyons of the University of Nebraska, Lincoln, modeled the role that juvenile carnivores such as *Tyrannosaurus rex* might have played in ecosystems, based on their growth curves and the relative numbers of juveniles and adults found in “mass death” fossil beds. “We said, OK, if the juveniles are really using up this space, how many of them would you expect?” Smith says. Their calculations showed that “the teenagers fill the gap,” she says. “If you fill them in, then you get a community that looks like what you’d expect.”

The effect may be stronger in meat eaters because each carnivorous dinosaur species occupied a wide range of niches. They hatched from relatively small eggs; even the largest ones only weighed about 15 kilograms as hatchlings. Then they grew very quickly, changing diets and hunting methods to accommodate their new sizes and competing with a range of other species along the way, Erickson says.

The study’s emphasis on how animals’ niches can change as they grow offers fresh insights, says Mike Benton, a paleontologist at the University of Bristol. “It will make people look at predator-prey interactions in a different way.” ■



A *Tarbosaurus*—a cousin of *Tyrannosaurus rex*—grew mightily in size over its lifetime, as seen in these skulls from a 2-year-old, a teenager, and an adult.



Black holes can tear apart stars, feeding a particle jet.

PARTICLE ASTROPHYSICS

Rare cosmic neutrino traced to star-shredding black hole

Particle points to black hole jets as high-energy accelerators

By Daniel Clery

Neutrinos are everywhere, streaming through your body by the trillions every second. But the chargeless, nearly massless particles are notoriously hard to pin down, especially the rare high-energy ones from deep space. Only about a dozen cosmic neutrinos are detected annually, and only one had been linked to a source in the sky. Now, IceCube, the kilometer-wide neutrino detector nestled deep beneath the South Pole, has traced another one to its birthplace: a supermassive black hole tearing a star to pieces in a galaxy 750 million light-years away.

“It’s a very exciting story if this is correct,” says Tsvi Piran, a theorist at the Hebrew University of Jerusalem. The discovery suggests these rare tidal disruption events (TDEs) could be a major source of high-energy neutrinos and cosmic rays—other deep-space visitors whose origins have also been a mystery.

The only way to detect neutrinos is to wait for one to hit an atomic nucleus. The result is a shower of debris particles and a flash of light. The collisions are rare, however, so researchers need a huge volume of matter to detect them. IceCube uses 1 cubic kilometer of Antarctic ice, threaded with photon detectors. From the arrival time and brightness of the flash at each detector, researchers can calculate a neutrino’s direction and whether its source is nearby or in deep space.

In 2017, IceCube connected the first deep-space neutrino to a known source: a superbright galaxy known as a blazar. Blazars contain voracious supermassive black holes, which suck in matter and are thought to spurt out a jet of particles.

On 1 October 2019, a flash in the detector revealed another likely deep-space candidate. IceCube researchers sent out an alert so astronomers could scan the sky in the direction of the arriving neutrino. A California telescope, the Zwicky Transient Facility, swung into action and found that the apparent source was a known TDE, the team reported this week in *Nature Astronomy*. “When we saw it could be a TDE, we immediately went ‘Wow!’” says lead author Robert Stein of the DESY particle physics laboratory in Germany.

Based on less than 100 observed TDEs, researchers believe they occur when the gravity of a supermassive black hole rips up a star that has strayed too close. Half the mass is pulled into a disk around the black hole and the rest arcs outward in a long streamer. The new result suggests TDEs also produce a short-lived particle jet, like a blazar burp.

With two cosmic neutrinos now traced to them, jets are emerging as a primary explanation for deep-space neutrinos, edging ahead of neutron stars and stellar explosions. Jets could produce neutrinos much as particle physicists do on Earth: with a high-energy beam of protons that slams into surrounding material, says co-author Suvi Gezari of the Space Telescope Science Institute. “For TDEs to emerge as a likely site for neutrino production is very exciting,” she says.

They might also help explain the source of ultra-high-energy cosmic rays, particles like protons that zip across the cosmos and bombard Earth’s atmosphere daily. Making neutrinos requires accelerating protons to high energy, Piran says, so TDEs could be producing the cosmic rays at the same time.

IceCube’s pointing ability is poor, so Stein concedes the apparent match between the neutrino and the TDE could be a coincidence. “We will have to wait and see if there are additional events,” he says. ■

Hunt for renewable plastics clears a hurdle

Solving alkalinity problem may help make plastics from CO₂, water, and electricity

By Robert F. Service

Plastics are a climate problem. Making precursors for common plastics, such as ethylene and carbon monoxide (CO), consumes fossil fuels and releases plenty of carbon dioxide (CO₂). In recent years, chemists have devised bench-top reactors called electrochemical cells that aim to reverse the process, starting with water and waste CO₂ from industrial processes and using renewable electricity to turn them into feedstocks for plastics. But that green vision has a practical problem: The cells often consume highly alkaline additives that themselves take energy to make.

“This has been a very challenging scientific problem,” says Peidong Yang, a chemist at the University of California, Berkeley. Now, his team and a second group are reporting strides toward solving the alkalinity hurdle. One advance links two electrochemical cells in tandem to bypass the problem altogether, and another turns to an enzyme-like catalyst to generate a desired chemical without consuming alkaline additives. The plastics industry isn’t about to abandon fossil fuels for CO₂ and renewable electricity, but “the field is picking up steam,” says Feng Jiao, an electrochemist at the University of Delaware, Newark.

Companies currently make ethylene, a clear, sweet-smelling gas, by using superheated steam under pressure to “crack” the larger hydrocarbons in oil. Honed for decades, the process is extremely efficient, capable of producing ethylene for about \$1000 per ton. But its production generates about 200 million tons of CO₂ annually, 0.6% of the world’s emissions.

Electrochemical cells, which operate like batteries in reverse, offer a greener alternative. In contrast to batteries, which convert chemical energy into electricity, electrochemical cells feed electricity to catalysts that make chemicals.

Both kinds of devices rely on two electrodes separated by an electrolyte that ferries charged ions. In electrochemical cells designed to convert CO₂ to more valuable chemicals, the dissolved gas and water react at the cathode to form ethylene and other hydrocarbons. The electrolyte is typically spiked with potassium hydroxide, which allows the chemical conversions to

occur at a lower voltage, thereby boosting the overall energy efficiency. And it helps channel most of the added electricity toward creating hydrocarbons instead of hydrogen gas, a less valuable product.

But Matthew Kanan, an electrochemist at Stanford University, notes that the hydroxide carries an energy penalty of its own. The hydroxide ions react with CO₂ at the cathode, forming carbonate, which precipitates out of solution as a solid. As a result, the hydroxide must be continually replenished—and hydroxide itself takes energy to make, making the overall process an energy loser.

In 2019, Kanan and his colleagues reported a partial solution. In place of CO₂, they fed

renewable electricity. The CO flows into another electrochemical cell whose catalysts are tailored to favor the production of ethylene, a more widely used commodity chemical than acetate. The tandem reactor no longer consumes hydroxide and has an FE of 65% for energy stored in ethylene produced by the device, the researchers reported last week in *Joule*. “That’s a significant advance,” Jiao says.

In the December 2020 issue of *Nature Energy*, Yang and his colleagues reported a very different way to get around the alkalinity problem. In an alkaline electrochemical cell, they redesigned the catalyst to exclude water and hydroxide ions at the sites where it splits CO₂. The device can



Conventional polyethylene production, powered by fossil fuels, could one day be replaced by chemical reactors that rely on renewable energy and consume carbon dioxide.

their cell CO, which doesn’t react with hydroxide to form carbonate. The cell itself was highly efficient: Seventy-five percent of the electrons they fed their catalyst—a metric referred to as the faradaic efficiency (FE)—went to making acetate, a simple carbon-containing compound that can be used as a feedstock for industrial microbes. The trouble is that making CO normally requires fossil fuels, undoing some of the climate benefits of the scheme.

Now, a team led by Edward Sargent, a chemist at the University of Toronto, has taken this approach a step further. They started with a commercially available device called a solid oxide electrochemical cell, which uses high temperatures to convert CO₂ to CO and could be powered by

convert the gas into CO without generating carbonate, a major energy win. But this cell doesn’t yet convert that CO and hydrogen from water into ethylene and other hydrocarbons, Yang notes.

Better electrochemical cells aren’t the only force propelling the research. As wind and solar energy generation burgeons, renewable energy prices are plummeting. Those low energy prices mean that doubling of the overall energy efficiency of tandem electrochemical cells could make them cost competitive with the standard fossil fuel approach for manufacturing ethylene, Sargent and his colleagues report in a December 2020 paper in *ACS Energy Letters*. “We are trying to put that option in play,” Kanan says. ■



A teenager receives a shot in a clinical trial of the Pfizer-BioNTech COVID-19 vaccine.

COVID-19

Vaccine trials ramp up in children and adolescents

Doctors stress need to vaccinate young people once shots are available

By Jennifer Couzin-Frankel

As older adults, health care workers, firefighters, and others roll up their sleeves for a COVID-19 vaccine, there's a flurry of research to get shots to children, for whom no vaccine has yet been authorized. Even though young people are less likely to fall seriously ill, doctors and scientists agree that vaccinating them is crucial for their own protection and that of the broader population. And because companies already have solid data from adult trials, they are running smaller studies in children that focus on safety and immune responses to COVID-19 vaccines.

The first two vaccines to receive emergency use authorization in the United States for adults are now in clinical trials for young people, with initial results expected by summer. Pfizer and BioNTech have completed enrollment of more than 2200 volunteers ages 12 to 15, and Moderna is wrapping up recruitment of a planned 3000 volunteers with the same minimum age. Both vaccines are based on messenger RNA coding for the coronavirus spike protein, which prompts production of protective antibodies. Another three vaccines, which use a harmless virus to deliver a gene for the same protein, are also taking steps toward pediatric authorization. On 12 February, AstraZeneca and the Univer-

sity of Oxford announced they would begin to test their vaccine in 300 U.K. children ages 6 to 17. Johnson & Johnson, whose adult vaccine will be considered by U.S. regulators this week, says it's moving toward testing in young people, and Sinovac Biotech is testing its product on children in China ages 3 to 17.

Adult deaths from COVID-19 dwarf those in children: In the United States, for example, young people make up about 250 of 500,000 total deaths. But for children, COVID-19 is still "causing more deaths than influenza does in a typical season," says Douglas Diekema, a pediatrician and bioethicist at Seattle Children's Hospital. "Those are unnecessary deaths and should be prevented." In addition, more than 2000 children and teenagers have developed a severe inflammatory syndrome that can cause critical illness and damage organs (*Science*, 29 May 2020, p. 923). And some children report lingering symptoms such as intense fatigue, similar to the emerging "long COVID" in adults.

The hazards have convinced many doctors that children need access to vaccines before they can return to their pre-2020 routines. "I don't think anybody wants to keep kids wearing masks for the rest of their childhood," says Evan Anderson, a pediatric infectious disease specialist

at Children's Healthcare of Atlanta who helped lead adult clinical trials of Moderna's vaccine and has pressed for prioritizing pediatric studies. Furthermore, because children can transmit the virus to adults—for whom vaccination isn't 100% effective—protecting kids will be key to driving down infection rates.

For children and another special population, pregnant women, clinical trials are trending much smaller than the tens of thousands of participants in the adult trials that garnered initial authorization. Although these latest studies will, like their larger counterparts, track symptoms and count COVID-19 cases, they will primarily rely on immune markers as a proxy for vaccine effectiveness. One widely used marker is "neutralizing" antibodies to the virus as measured in the blood. Neutralizing antibodies stop viruses from entering cells and replicating. In Pfizer's and Moderna's adolescent trials, antibodies will be measured 1 month after the second dose of vaccine. The goal is to see whether in a younger crowd the vaccine spurs antibody levels that match those in adults, explains Robert French, who directs the Gamble Vaccine Research Center at Cincinnati Children's Hospital and is helping lead Pfizer's adolescent trial.

One sticking point is that scientists are unsure how high a level of neutralizing antibodies to look for. "We don't know the protective titer" of antibodies that someone needs to be shielded from illness, says John Moore, a vaccine researcher at Cornell University who isn't involved in running vaccine trials. Still, he continues, "We have a pretty good feel." If children produce somewhat fewer antibodies relative to adults

that's unlikely to be concerning, he says. But if "responses were down 50-fold, you'd be getting worried" that the vaccine wasn't protecting them. (In the adult trials, elderly people developed about half as many neutralizing antibodies as younger adults but were well-protected from illness.) The U.S. Food

and Drug Administration (FDA) would not comment about study designs, but in guidance to industry, it has indicated it's open to considering a COVID-19 vaccine's use based on immune responses that are "reasonably likely to predict clinical benefit."

There's precedent for focusing on these kinds of surrogate markers. Rabies vaccine studies, for example, relied on "indirect markers of protection," says Grace Lee, a pediatric infectious disease specialist at Stanford Children's Health who also sits on

Science's COVID-19 reporting is supported by the Heising-Simons Foundation.

the Advisory Committee on Immunization Practices (ACIP), which develops recommendations for U.S. vaccine use. “You can’t wait for people to get rabies” in a clinical trial. To craft vaccines against human papillomavirus, researchers initially examined their ability to prevent symptoms of infection and then used immunologic markers as trials shifted into younger age groups.

Like other physicians eager for results of trials on children 12 and up, Lee thinks it’s unlikely that efficacy of COVID-19 vaccines will falter markedly in adolescents, whose immune responses are similar to those of adults. “The main thing I’m looking for is safety,” she says. With some 200 million people vaccinated worldwide so far, the vaccines appear very safe in adults. Still, because the risk of harm from COVID-19 to children is much lower than to adults, physicians and parents want assurances of safety and evidence that neutralizing antibodies and other markers of immunity persist, a sign that the protection will be durable.

In kids and adolescents, Pfizer, Moderna, and AstraZeneca are testing the same dose adults receive. As more trials of younger children open, however, companies may experiment with different doses. With drugs, “You want to have a certain level in the bloodstream,” says Paul Offit, a vaccine researcher at the Children’s Hospital of Philadelphia who sits on a vaccine advisory committee for FDA. “So weight matters.” But for vaccines, which aim to trigger an immune response, the dose varies less—or not at all. The same dose of flu vaccine, for example, is generally given to 6-month-olds and 60-year-olds, and young children actually get a higher dose of diphtheria and pertussis vaccines than adults. At a January ACIP meeting, Emily Erbelding, an infectious diseases specialist at the National Institute of Allergy and Infectious Diseases, suggested half- and quarter-doses may be tried in infants and young children. “If you get the same immune response at a quarter of the dose and it decreases side effects, well then we would probably give a smaller dose,” French says.

In the meantime, pediatricians, parents, and others have to wait. Pfizer, for example, has announced plans to submit its data on adolescents to regulators by June; it also expects to open a trial in 5- to 11-year-olds within a couple of months, and in under 5-year-olds later this year. Diekema, a volunteer cross-country coach at the local high school, is getting ready to head back to the field for the first time in a year. Even if he does his best to enforce social distancing among the teens, he imagines them playfully high-fiving between runs. Children are “like magnets” when near one another, he says. “That’s why we need the vaccines.” ■

RESEARCH POLICY

New U.K. funding agency aims to tackle innovative research

Like ARPA in the United States, ARIA will fund risky ideas. But some worry that fledgling agency lacks a focus

By Cathleen O’Grady

The U.K. government has released its plans for emulating the storied high-risk, high-reward U.S. funding agency, the Advanced Research Projects Agency (ARPA). During the 2019 election campaign, the Conservative government promised to set up such an agency, and Prime Minister Boris Johnson’s former adviser Dominic Cummings pushed for it. Now, it has a name, the Advanced Research & Invention Agency (ARIA), and a confirmed budget. Business secretary Kwasi Kwarteng announced last week it would be funded by an initial £800 million over 4 years, and would begin to disburse grants by 2022.

Unlike ARPA, now known as DARPA because it specializes in defense-related research, ARIA so far lacks a focus, which concerns some experts. “The fabric of an ARPA organization is its mission,” says Anna Goldstein, a science policy researcher at the University of Massachusetts, Amherst, who provided evidence on ARPA to U.K. politicians. Without that, she says, “ARIA is a solution in search of a problem.”

The government will soon introduce legislation in Parliament to enshrine the agency in law, aiming to give it more permanence than pet political projects sometimes enjoy. It will sit within the Department for Business, Energy and Industrial Strategy, but remain independent from the main research funding agency, UK Research and Innovation. The new law may also allow ARIA to sidestep normal spending rules, audits, and even freedom of information requests. But those checks and balances don’t hinder risk taking, says James Wilsdon, a science policy researcher at the University of Sheffield. “You don’t have to be a scathing political critic of the government to raise a quizzical eyebrow about attempts to put chunks of the research budget in a place where they’re not subject to any of those checks and balances.”

DARPA, created as ARPA in 1958 after the Soviet Union launched the Sputnik satellite and the United States panicked about falling behind on military technology, is credited with innovations in the development of the internet, GPS, and robotics. Such is the power of the brand name that it has spawned spinoffs for intelligence (IARPA), homeland security (HSARPA), and energy technology (ARPA-E). Unlike traditional funding agencies, which hand out grants through peer review, DARPA and its ilk give program managers the freedom and budget to seek out promising work, fund it with no bureaucracy, and cut it off early at signs of failure.

Because of limited public data, DARPA’s triumphs can only be tracked through a series of anecdotal success stories, Goldstein says. But in 2020, Goldstein and her colleagues analyzed more comprehensive data from ARPA-E and found that projects it funded led to more patents than from those it rejected or comparable projects that found funding elsewhere—a hint that the agency has a knack for hitting on innovative research.

In announcing ARIA, Kwarteng nodded to two possible focuses: disease outbreaks and climate change. “Those would both be excellent choices,” Goldstein says. “Why not create two ARIAs and do both?” Recruitment for the agency’s leaders will begin in the next few weeks. But that is risky while the purpose of the agency remains uncertain, Wilsdon says, because different goals demand different leadership.

The new agency will likely only take up about 1% of the government’s total research funding, which Johnson’s government has pledged to increase drastically over the coming years. But the funds are a “reasonable starting point,” says Nancy Rothwell, president of the University of Manchester and co-chair of the government’s advisory Council for Science and Technology. It’s enough to do something useful, she says, but not a reckless gamble. “Time will tell whether or not [its budget] should increase.” ■

**“ARIA
is a solution
in search
of a problem.”**

Anna Goldstein,
University of
Massachusetts, Amherst

SHIFTING GROUND

Fleets of radar satellites are
measuring movements on Earth
like never before

By Julia Rosen

East Africa has been called the cradle of humanity. But the geologically active region has also given birth to dozens of volcanoes. Few have been monitored for warnings of a potential eruption, and until recently, most were believed to be dormant. Then, Juliet Biggs decided to take a closer look—or rather, a farther look.

Biggs, a geophysicist at the University of Bristol, uses a technique called interferometric synthetic aperture radar (InSAR) to detect tiny movements of Earth's surface from space. In a series of studies, she and her co-authors analyzed satellite data on the East African volcanoes. According to their latest results, which were published last month, 14 have been imperceptibly growing or shrinking in the past 5 years—a clue that magma or water is moving underground and that the volcanoes are not completely asleep. “It’s really changed the way these volcanoes are viewed, from something that’s kind of dormant to really very active systems,” Biggs says. After data showed that the Corbetti volcano, which abuts the fast-growing city of Hawassa, Ethiopia, is inflating steadily at a rate of 6.6 centimeters per year, Biggs’s Ethiopian colleagues included it in the country’s geological hazard monitoring network.

No other technology could produce such a comprehensive survey. Individual GPS stations can track surface movements of less than 1 millimeter, but InSAR can measure changes almost as subtle across a swath hundreds of kilometers wide. That has made it a vital tool for earth scientists studying the heaves and sighs of our restive planet. “We tend to think of the ground as this solid platform,” Biggs says, “and actually, it’s really not.”

With InSAR, scientists are tracking how ice streams flow, how faults slip in earthquakes, and how the ground moves as fluids are pumped in or out. “Everywhere you look on Earth, you see something new,” says Paul Rosen, an InSAR pioneer at NASA’s Jet

Propulsion Laboratory (JPL). “It’s a little bit like kids in a candy store.”

And the flood of InSAR data is growing fast. Since 2018, the number of civil and commercial SAR satellites in orbit has more than doubled. And at least a dozen more are set to launch this year, which would bring the total to more than 60. With the help of computing advances that make data processing easier, the satellite fleets may soon be able to detect daily or even hourly surface changes at just about every patch of ground on Earth.

As the technology grows more powerful

Organisation (ISRO). “I want it to become so socially relevant that they can’t go back to not having this data.”

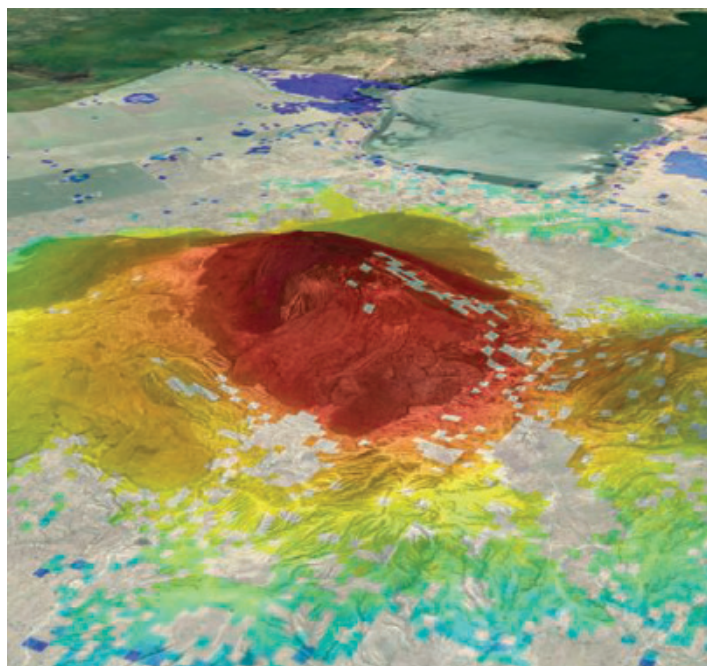
SYNTHETIC APERTURE RADAR, the “SAR” on which InSAR depends, originated in the 1950s as a tool for airborne military reconnaissance. Like traditional radar, SAR instruments captured images of the planet by sending out microwave pulses and recording the echoes. And like a traditional radar, the instruments could penetrate clouds and worked equally well at night. A

key difference was the “synthetic” aspect of SAR. Larger radar antennas, like larger apertures on a camera, collect more of the echoes and enable sharper pictures. But building a single antenna large enough to take a high-resolution image isn’t practical. Researchers realized they could instead create an artificially large aperture by combining the signals received on a much smaller antenna as it moved through space. Today, SAR satellites with antennas just a few meters across can produce images with pixel resolutions as sharp as half a meter—better than many satellite-borne cameras.

SAR images, on their own, suffice for many types of surveillance, from counterterrorism to tracking oil spills in the ocean. But InSAR goes further, by looking for differences between multiple SAR images.

The technique takes advantage of phase information in the returning microwaves—in other words, where a signal is in its sinusoidal path when it hits the antenna. Any phase difference in the signal between SAR images taken from the same position at different times means the round-trip distance has changed, and can reveal surface movements down to a few millimeters. “There’s nothing else that compares to it,” says Michelle Sneed, a hydrologist at the U.S. Geological Survey. “I’m still amazed by it after a couple of decades.”

The 1978 launch of Seasat, NASA’s first ocean-observing satellite, provided data for early InSAR efforts. Seasat operated for just 105 days before a power failure brought the mission to an untimely end. But in that time, it collected repeat images of California’s Imperial Valley taken over the course



The surface of Ethiopia's Corbetti volcano has been rising nearly 7 centimeters per year, a sign of underground activity. In this image, red shows the most cumulative inflation.

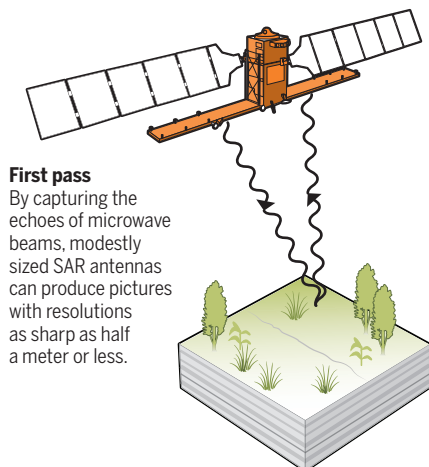
and ubiquitous, InSAR is spreading beyond the geosciences. With InSAR data, railroads are monitoring the condition of their tracks and cities are monitoring shifts in buildings caused by construction. “It’s popping up everywhere,” says Dáire Boyle, who follows trends in the space industry for Evenflow, a consulting firm in Brussels. Analysts value the SAR market at roughly \$4 billion, and expect that figure to nearly double over the next 5 years.

Many believe InSAR will eventually underpin our daily lives. From measuring the water stored in mountain snowpacks to enabling quick responses to natural disasters, InSAR data will prove invaluable to governments and industries, says Cathleen Jones, a science team leader for NISAR, an upcoming joint SAR mission from NASA and the Indian Space Research

Changes between radar images taken before and after 2019 earthquakes in Ridgecrest, California, reveal slip along perpendicular faults (lower left). Each color cycle represents 11.5 centimeters of ground motion.

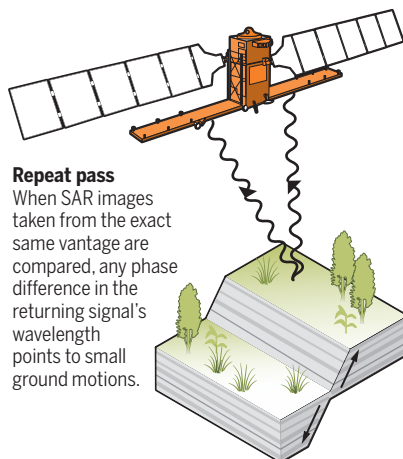
Rulers of Earth

A remote sensing technique called interferometric synthetic aperture radar (InSAR), first demonstrated more than 30 years ago, is reaching its heyday. By comparing radar imagery gathered over time, researchers can detect ground motions as small as a few millimeters.



First pass

By capturing the echoes of microwave beams, modestly sized SAR antennas can produce pictures with resolutions as sharp as half a meter or less.



Repeat pass

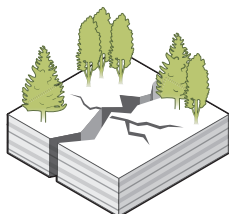
When SAR images taken from the exact same vantage are compared, any phase difference in the returning signal's wavelength points to small ground motions.

Moving targets

InSAR was first used in the geosciences, but the technique has also spread into a number of commercial applications. Analysts suggest a \$4 billion SAR market will nearly double in the next 5 years.

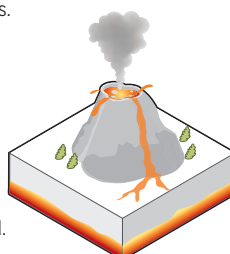
Earthquakes

Ground slippage can be measured—even for small, slow-moving tremors.



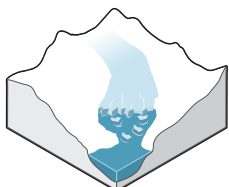
Volcanoes

Hazard can be monitored by how the surface rises and falls, a sign of magma or water moving underground.



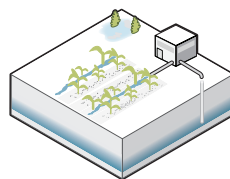
Glaciers

InSAR has shown how global warming has sped up glaciers, adding to sea-level rise.



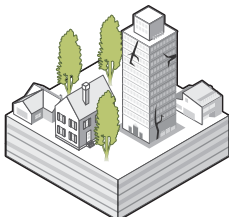
Water resources

Surface sinking can be used to track groundwater pumped from aquifers.



Infrastructure monitoring

Small shifts in buildings, railroads, dams, and pipelines can point to instabilities and guide maintenance.



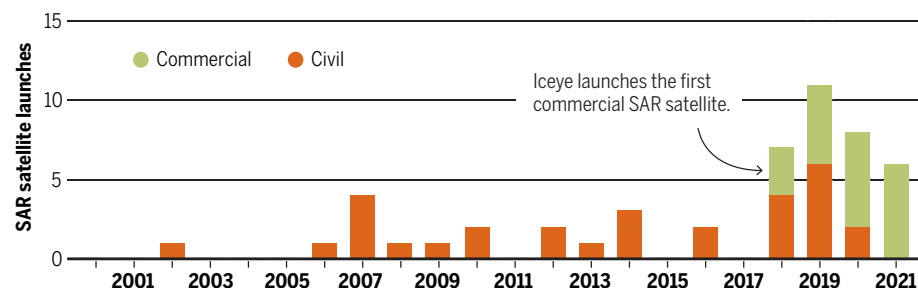
Natural disasters

Responders and insurers can assess damage from floods or fires by measuring the surface changes they cause.



A satellite surge

SAR satellites launched by private companies will soon eclipse the number of civil SAR satellites funded by national governments. Overall, nearly 50 are operational, more than double the number in 2018.*



of 12 days. Scientists at JPL later compared those images using InSAR to show the subtle swelling of fields as they soaked up irrigation water. “It is not hard to think of numerous applications for the type of instrument demonstrated,” the authors wrote in a 1989 paper. And they were right.

A classic InSAR study came in 1993, when a team of scientists in France used data from the SAR-enabled European Remote Sensing satellite to study a powerful earthquake that rocked Landers, California, the year before. By analyzing images taken before and after the quake, they calculated that the fault had slipped by up to 6 meters, which agreed with detailed field observations. The InSAR data also revealed how the ground buckled for kilometers around the fault—illustrating the full effects of the temblor at an unprecedented scale.

The paper inspired scientists like Sneed, who went on to use InSAR to study how groundwater extraction causes the ground to sink. During a drought in California’s San Joaquin Valley in the late 2000s, she and her colleagues discovered that the surface was subsiding as fast as 27 centimeters per year in places where farmers pumped the most groundwater. Irrigation canals were sagging as a result of uneven sinking, impeding water flow. “It’s a really expensive problem,” Sneed says. (Another recent InSAR study linked specific water-intensive crops—notably corn, cotton, and soy—to increased subsidence.)

Glaciologists adopted the technology, too. As a young researcher at JPL in the 1990s, Ian Joughin used InSAR—which tracks both vertical and horizontal movements—to measure the speed of polar ice streams. Some scientists thought flow rates would be relatively immune to climate change. But, sadly for the world, InSAR studies by Joughin and others proved those predictions wrong. “Especially in the early 2000s, we just saw all kinds of glaciers double their speed,” says Joughin, who now studies the fate of polar ice sheets and their contribution to sea-level rise at the University of Washington, Seattle.

By the 2000s, many earth scientists were using InSAR—and grappling with its limitations. There were few SAR satellites in orbit, and they tended to switch between instruments or imaging modes to accommodate different users’ needs, making the data hard to use for InSAR. The early missions collected the repeat images needed for InSAR only about once a month, and researchers often had to correct for their wobbly orbits. That meant that although scientists could study an event after it happened, they could rarely watch it unfold in real time.



A port explosion rocked Beirut in August 2020. Before-and-after radar images were used to identify areas (red) with surface changes due to damaged buildings.

Leaders at the European Space Agency (ESA) were convinced there was a better way.

MALCOLM DAVIDSON REMEMBERS the excitement and anxiety he felt on 3 April 2014, the day the first Sentinel-1 satellite launched. “All your life goes into a few minutes,” says Davidson, mission scientist for ESA’s flagship SAR program. He also remembers the relief when the satellite safely reached orbit, and the awe that came over him when he saw its first image, of ocean swells. “It was very convincing that the mission was going to do great things,” he says.

With Sentinel-1, the plan was simple: “We cut out all the experiments, and we said, ‘Look, this is a mapping machine.’” He and his colleagues chose a primary imaging mode to use over land—surveying a 250-kilometer swath at a resolution of 5 meters by 20 meters—that they hoped would satisfy most researchers, and made sure the orbits would overlap precisely, so all the data would be suitable for InSAR. The first satellite, Sentinel-1a, retraced its path every 12 days. Then, in 2016, ESA launched a clone that made repeat images available about every 6 days for many places on Earth.

SAR missions like Italy’s COSMO-SkyMed and Germany’s TerraSAR-X also support InSAR and can achieve even higher reso-

lutions. But they do not distribute data freely like Sentinel, which many credit for driving a transition from opportunistic experiments to what Davidson sees as “a more operational view of the world.” With Sentinel-1 data, Norway created a national deformation map that has helped identify rockslide hazards and revealed that parts of Oslo’s main train station were sinking. Water managers in California rely on the data to track groundwater use and subsidence. And in Belgium, it is used to monitor the structural integrity of bridges. “It can all be done remotely now, saving time, saving money,” Boyle says.

The large and growing body of InSAR data has also revealed small surface movements that were previously hidden by noise. As radar signals pass through the atmosphere, they slow down by an amount that depends on the weather, producing variability that can swamp tiny but important displacements. Thanks to long-term records from missions like Sentinel, researchers can now tease information from the noise, for example, helping them track movements of just a few millimeters per year in Earth’s crust—enough to strain faults and eventually cause earthquakes.

Such efforts would not have been possible without huge gains in computing

power. In the 1990s, stacking a single pair of SAR images could take days, Sneed says, and interpreting the results could take much longer. Now, researchers can process hundreds of images overnight, and they increasingly rely on artificial intelligence (AI) algorithms to make sense of the data. In one recent test, an AI algorithm was tasked with identifying small fault movements known as slow earthquakes. It correctly found simulated and historical events, including ones that had eluded human InSAR experts, says Bertrand Rouet-Leduc, a geophysicist at Los Alamos National Laboratory who presented preliminary results in December 2020 at the annual meeting of the American Geophysical Union.

Rouet-Leduc and his team now plan to monitor faults around the world using the same approach. He says it’s mostly a matter of exploiting the vast quantity of data that “sits on servers without being looked at,” because it’s simply too much for scientists to tackle. The researchers hope they will be able to answer questions like when and why slow earthquakes happen, and whether they can trigger big, damaging events by increasing stress on other parts of a fault.

Commercial users often lack the expertise to process InSAR data, so hundreds of companies have sprung up to help. One,



Norway's national deformation map, based on InSAR data from Sentinel-1 satellites, showed parts of Oslo's train station sinking (red dots) by more than 1 centimeter per year, perhaps because of nearby construction.

Dares Technology, monitors the ground for the construction, mining, and oil and gas industries. By tracking surface changes as fluids are injected or extracted from an oil reservoir, for example, Dares can help companies estimate pumping efficiency and prevent dangerous well failures.

In the beginning, convincing clients that InSAR data were useful and trustworthy was difficult, says Dares CEO Javier Duro. Now, he says, "Everybody wants to include InSAR in their operations." Duro is particularly interested in detecting precursors to accidents, for example, by looking for signs of instability in the walls of open-pit mines or in the dams used to store mine tailings. The company usually sends out several alerts per month to clients, who can take actions to avoid disasters. "Typically, InSAR data have been used for back analysis," Duro says. "Our mission is to focus on the present and the future, and try to predict what could happen."

THE SURGE IN SATELLITES promises to bring yet another InSAR revolution. Italy, Japan, Argentina, and China all plan to launch additional SAR satellites soon, and NISAR, the

NASA-ISRO mission, will take flight in late 2022 or early 2023. NISAR will image Earth's full land surface every 6 days, on average, says Rosen, the mission's project scientist. Its two radar sensors will help researchers track many things, including crop growth and changes in woody biomass—crucial for understanding the climate system. With a better view of Antarctica than other missions, NISAR can also monitor changes in ice.

Taken together, Sentinel-1, NISAR, and the other civil satellites will image most places on Earth at least every 12 hours, Rosen says. But the temporal resolution of InSAR will remain constrained by the revisit rate of the individual missions, because the technique can't be done with imagery from different missions. However, private companies with large constellations of microsatellites hope to vault the field into yet another realm, by radically increasing revisit frequencies.

On 24 January, a SpaceX Falcon 9 rocket blasted off from Cape Canaveral, Florida, carrying three satellites, each about the size of a minifridge and weighing less than 100 kilograms, from Iceye. The Finnish SAR startup has raised more than

\$150 million toward its audacious goal of imaging every square meter of Earth every hour.

The launch brought Iceye's commercial constellation to six, giving it an early lead over rival companies such as Capella Space—which had two satellites on the same rocket—and Umbra, both based in California. Iceye plans to add at least eight more satellites this year, allowing it to revisit most of the globe once a day. "That is groundbreaking," says Pekka Laurila, who co-founded Iceye as an undergraduate at Aalto University and now serves as the company's chief strategy officer.

Ultimately, Iceye hopes to assemble a constellation of as many as 100 satellites as it approaches its hourly monitoring objective. That would open up new applications, like tracking how buildings and dams expand during the heat of the day and contract at night—a clue to their structural integrity. Already, Iceye data have been used to guide ships through Arctic sea ice and to track illegal fishing vessels. "If you can work closer to real time, you can actually do something about it," Laurila says.

So far, though, Iceye has focused on flood monitoring, which can guide disaster response efforts. In fact, the company provided some of the first images of Grand Bahama after Hurricane Dorian devastated the island in 2019, Laurila says. Precise flood data are also valuable to insurers, who can use them to trigger automatic insurance payouts after an event instead of processing claims and sending out inspectors. Until now, Iceye has tracked floods using regular SAR data, but it hopes to start to apply InSAR as it increases its revisit frequencies, because the technique can measure the height and extent of inundation much more precisely.

And that's just the beginning of what Laurila hopes Iceye will do. His ultimate goal is to build a "new layer of digital infrastructure" that will provide a "real-time, always-available, objective view on the world," he says. He believes that, like modern GPS, reliable SAR and InSAR data will support myriad applications, many of which have yet to be imagined. "Nobody thought of your Uber and pizza delivery when they thought of GPS," Laurila says.

If Iceye and its peers succeed, they will expose the shifts and shudders of the planet, day in and day out. They will spy tilting buildings and slumping slopes, and they will witness the growth of crops and the flow of commodities around the world. If space-based imagery often portrays Earth as quiet and still, InSAR reveals the true restlessness of our living planet. ■

Julia Rosen is a journalist in Portland, Oregon.

2020 Winner
Christopher Zimmerman, Ph.D.
Princeton Neuroscience Institute
For research on thirst and drinking
behavior



Now It's Your Turn!

Application Deadline
June 15, 2021

Eppendorf & Science Prize for Neurobiology

The annual Eppendorf & Science Prize for Neurobiology is an international prize which honors young scientists for their outstanding contributions to neurobiological research based on methods of molecular and cell biology. The winner and finalists are selected by a committee of independent scientists, chaired by *Science's* Senior Editor, Dr. Peter Stern. If you are 35 years of age or younger and doing great research, now is the time to apply for this prize.

As the Grand Prize Winner, you could be next to receive

- > Prize money of US\$25,000
- > Publication of your work in *Science*
- > Full support to attend the Prize Ceremony held in conjunction with the Annual Meeting of the Society for Neuroscience in the USA
- > 10-year AAAS membership and online subscription to *Science*
- > Complimentary products worth US\$1,000 from Eppendorf
- > An invitation to visit Eppendorf in Hamburg, Germany

It's easy to apply! Write a 1,000-word essay and tell the world about your work. Learn more at:

eppendorf.com/prize

INSIGHTS

PERSPECTIVES



Yellow buoys indicate where fiber optic cable is being laid beneath the ocean. These telecommunication cables could be exploited to sense seismic waves.

GEOPHYSICS

Illuminating tremors in the deep

Telecommunication cables on the seafloor monitor seismic activity

By William Wilcock

The paucity of seismic stations in the ocean limits sustained seafloor seismic and pressure observations that are needed for rapid earthquake detection, early warning of damaging ground shaking, and tsunami prediction and verification. Because establishing infrastructure in the oceans is expensive,

there is a big advantage to methods that use undersea telecommunication cables. On page 931 of this issue, Zhan *et al.* (1) describe a new approach to monitor earthquakes, oceanic swell, and potential tsunamis. It relies on observing changes in the polarization of the light that is used to transmit data through the optical fibers in cables on the seafloor. This approach requires no new infrastructure or instrumentation, but

instead relies on utilizing observations already made to extract the telecommunication data received at the end of the cable. The finding should spur implementation of an array of cable sensing technologies for geophysical monitoring.

Polarized light is used to transmit data through telecommunication cables because it doubles the capacity of each optical fiber. Imperfections make fibers birefringent—that is,

light is refracted in two different directions, and polarized light travels at slightly different speeds depending on the orientation of polarization. As a result of birefringence, the orientation and degree of polarization, known as the state of polarization, change as light travels along an optical fiber. Because the birefringence of a fiber is sensitive to changes in temperature and mechanical stress from squeezing, bending, and stretching, the polarization of the light emerging

unanticipated later wave that traveled either in the ocean or as an interface wave along the seafloor. Polarization is not equally sensitive to earthquakes at all seismic frequencies, and the sensitivity appeared to vary with geographic location, suggesting a dependence on ocean depth or seafloor properties. For earthquakes in the Middle America Trench, the amplitudes of signals at 0.15 to 0.35 Hz increased with the predicted amplitude of ground motions. More work is required to

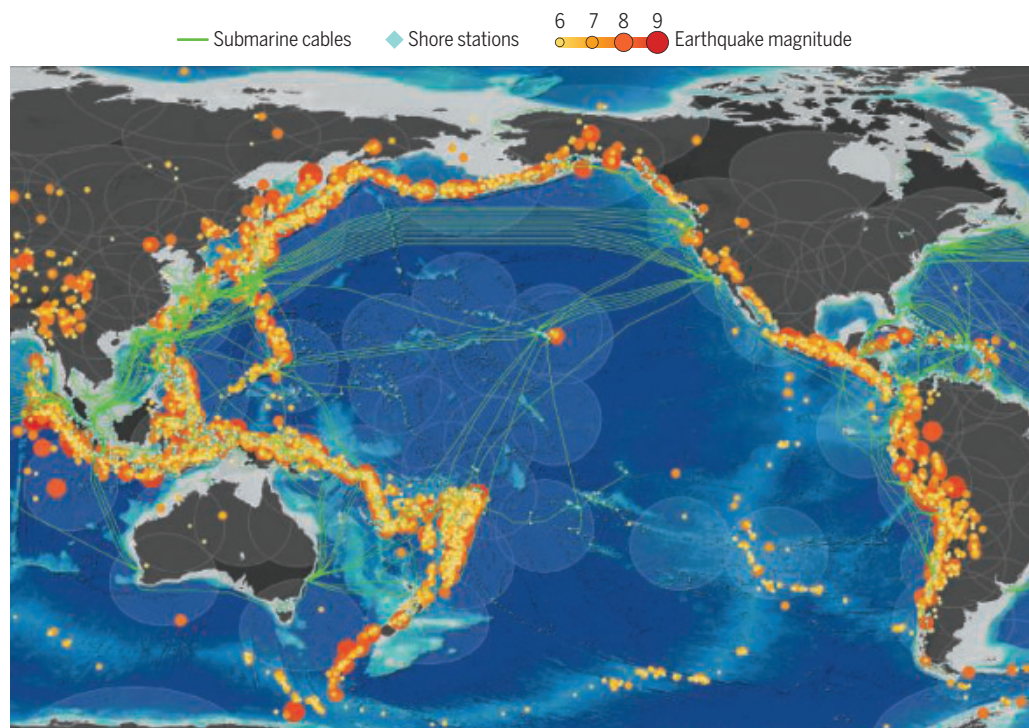
of damaging tsunamis in deep water, the technique has promise for this application. Future efforts to stabilize the environment of the shore stations, characterize the land segments of cable routes, and combine polarization measurements from the many communication channels (wavelengths) used in the typical submarine cable should improve signal-to-noise ratio and expand the bandwidth of observations.

Polarization monitoring adds to an exciting array of new technologies

that exploit submarine telecommunication cables for seismic and tsunami observations. Ultrastable laser interferometry senses the strains from seismic waves by measuring changes in the time it takes light to travel the full length of a fiber (2). Unlike polarization monitoring, it requires specialized equipment in the shore station, but has the advantage of localizing deformation of the cable if observations are made from both ends. Distributed acoustic sensing also measures changes in strain through the effect on backscattered light. It turns a dedicated optical fiber into a sensor somewhat akin to a line of closely spaced and very broadband horizontal seismometers that can extend up to about 100 km from the interrogating electronics (3). The scientific potential of this approach has been demonstrated in several submarine cables (4–6), and it is being adopted commercially to monitor the nearshore portions of cables to identify sections at risk of failure. Science Monitoring and

Seafloor cables and earthquakes

Map centered on the Pacific Ocean shows the distribution of earthquakes of magnitude ≥ 6 in the U.S. Geological Survey catalog from 1970 through 2021, the location of submarine cables from TeleGeography's telecom resources licensed under Creative Commons CC BY-NC-SA 3.0, and regions within 10° of stations in the Global Seismic Network (light transparent areas).



from a fiber changes with time. To extract the telecommunications signal, the receiver at the end of the cable continuously monitors the state of polarization. For cables on land, changes in the polarization are dominated by noise from temperature fluctuations, air flow, and anthropogenic activity.

Zhan *et al.* discovered that in the thermally stable setting of the seafloor, the state of polarization can be used to observe geophysical signals. Using data from a cable connecting Los Angeles, California, to Valparaiso, Chile, they detected the body waves generated by moderate- to larger-sized earthquakes with predicted maximum ground displacements as small as 0.1 mm. They also observed an

understand how the birefringence responds to seismic waves and how this response is reflected in the signal integrated along the cable's length. However, the findings of Zhan *et al.* show that polarization monitoring has the potential to characterize earthquake size.

Continuous signals were also detected at around 0.06 Hz, a frequency that correlates with the amplitude of storm-generated seismic noise at coastal stations. These signals, known as primary microseisms, are generated by the seafloor pressures from ocean swells on the shallow continental shelf near either end of the cable. The observations of Zhan *et al.* do not extend down to the frequencies of 0.001 Hz necessary to detect tsunamis, but given that the amplitude of seafloor pressure variations from coastal swells is similar to that

Reliable Telecommunications (SMART) cable systems would incorporate a package of conventional sensors, including accelerometers, seismometers, and pressure gauges, into the optical repeaters that are spaced 50 to 100 km apart along submarine cables (7). The concept was first proposed over a decade ago (8) and is now being planned for several locations, including a cable ring linking Portugal, the Azores, and Madeira. However, the approach is disruptive to established practices in the telecommunications industry and has yet to achieve traction on major transoceanic cables.

The current distribution of seafloor cables is not uniform but is quite well configured for monitoring the seismically active subduction zones that extend around the Pacific rim and along several other coastlines (see

School of Oceanography, University of Washington, Seattle, WA 98195-7940, USA. Email: wilcock@uw.edu

the figure). In regions where there are no cables, particularly the southern oceans, efforts to develop long-term autonomous seafloor seismometers (9), operate floating sensors (10), and deploy strategically placed arrays of temporary seismometers (11) are critical for improving the resolution of seismic images of the Earth's structure and the completeness of global earthquake catalogs. Where cables do cross ocean basins, they could transform academic seismology by providing new observations in regions that are presently poorly observed. Subduction zones are costly to instrument offshore with dedicated warning systems (12), but many of the most hazardous coincide with regions where telecommunication cables land. Here, distributed acoustic sensing could be supported by repurposing decommissioned commercial cables and by adding spare fibers to the nearshore portions of new installations. Polarization monitoring and ultrastable laser interferometry could extend observations further offshore using cables that run both perpendicular and parallel to coastlines. Incorporating fiber-sensing technologies into effective earthquake and tsunami warning systems will require that the signals are accurately quantified through extensive co-sited observations with conventional seismic and pressure sensors. Obviously, this can be most comprehensively achieved by making the new cables "SMART" with these sensors incorporated along their path where they would also contribute to warning. Given that SMART cables will also provide observations to constrain how climate change is affecting the temperature of the deep ocean, ocean circulation, and sea-level rise (7), it is time for cable suppliers and technology companies to step forward and work with scientists and governments to make them a reality. ■

REFERENCES AND NOTES

1. Z. Zhan *et al.*, *Science* **371**, 931 (2021).
2. G. Marra *et al.*, *Science* **361**, 486 (2018).
3. T. Parker *et al.*, *First Break* **32**, (2014).
4. E. F. Williams *et al.*, *Nat. Commun.* **10**, 5778 (2019).
5. N. J. Lindsey *et al.*, *Science* **366**, 1103 (2019).
6. A. Sladen *et al.*, *Nat. Commun.* **10**, 5777 (2019).
7. B. M. Howe *et al.*, *Front. Mar. Sci.* **6**, 10.3389/fmars.2019.00424 (2019).
8. Y. You, *Nature* **466**, 690 (2010).
9. M. D. Kohler *et al.*, *Seismol. Res. Lett.* **91**, 1343 (2020).
10. F. J. Simons *et al.*, *J. Geophys. Res. Solid Earth* **114**, B05307 (2009).
11. H. Kawakatsu *et al.*, in EGU General Assembly 2016 (2016; <http://adsabs.harvard.edu/abs/2016EGUGA.18.2514K>), vol. 18, pp. EPSC2016-2514.
12. S. Aoi *et al.*, *Earth Planets Space* **72**, 126 (2020).

ACKNOWLEDGMENTS

I thank J. Delaney, B. Howe, and D. Toomey for comments on this manuscript.

10.1126/science.abg4479

CORONAVIRUS

SARS-CoV-2 dependence on host pathways

A drug that inhibits host protein synthesis shows antiviral activity against SARS-CoV-2

By Jason P. Wong^{1,2} and Blossom Damania^{1,2}

Severe acute respiratory syndrome coronavirus 2 (SARS-CoV-2) first emerged in 2019, and its high pathogenicity, infectivity, and transmissibility have led to a global pandemic. Although several vaccines have been approved in different countries, most of the global population currently remains unvaccinated because of disparities in vaccine distribution and limited manufacturing capabilities (1). Owing to a lack of treatment options (particularly in low- and middle-income countries), the slow progression of vaccination, and the emergence of SARS-CoV-2 variants that elicit reduced responses to vaccines, there is an urgent need to identify therapeutics to reduce COVID-19 morbidity and mortality. On page 926 of this issue, White *et al.* (2) demonstrate that the small-molecule drug, plitidepsin, which is approved to treat relapsed and refractory multiple myeloma, possesses antiviral activity against SARS-CoV-2 and may be a promising drug candidate for treating COVID-19.

In broad terms, treatments for viral infections can target the virus, host, or underlying symptoms of infection. Antiviral treatments work by disrupting the viral life cycle. For SARS-CoV-2, the life cycle can be divided into three stages: host cell entry and trafficking, replication of the viral genome, and packaging and egress of new virions (3) (see the figure). Entry of SARS-CoV-2 into host cells occurs through receptor-mediated endocytosis or virion fusion with the cell membrane. Once in the cell, two polyproteins, pp1a and pp1ab, are translated from the RNA genome. These polyproteins are cleaved to generate nonstructural protein 1 (nsp1) to nsp16. The Nsps form the replication and transcription complex (RTC), which transcribes the viral genomic and subgenomic RNA (sgRNA). The sgRNAs encode structural and accessory proteins. Structural proteins traffic through the endoplasmic reticulum-to-Golgi secretory pathway, where viral genomes are packaged

to form budding vesicles, which are then released as new virions by exocytosis.

A common class of antivirals being tested in clinical trials against SARS-CoV-2 is nucleoside and nucleotide analogs, which inhibit viral replication when incorporated into the RNA by the RTC (3–5). Remdesivir is a nucleotide analog that is presently the only U.S. Food and Drug Administration (FDA)-approved antiviral for COVID-19 treatment and is recommended for use in patients requiring oxygen that is administered in a noninvasive manner (6). However, like other antivirals, it is most effective when administered early during infection, when individuals exhibit mild-to-moderate disease symptoms. Currently, remdesivir is given as an intravenous infusion, restricting its use to clinical settings. Hence, new antivirals with oral bioavailability, which are readily available and accessible to the general public, are needed to shorten the infectious phase and prevent further spread. Nucleotide or nucleoside analogs that can be administered orally, such as sofosbuvir (combined with either daclatasvir or ledipasvir), ribavirin, and favipiravir are being tested in clinical trials for treating COVID-19. Favipiravir has shown promise in a few open-label clinical trials for COVID-19, but more studies are needed to confirm its efficacy (3). Another way to disrupt viral genome replication is to prevent cleavage of the polyproteins that generate the RTC. Many clinical trials are examining if lopinavir and/or ritonavir, which target the SARS-CoV-2 3C-like protease that is responsible for cleaving the polyproteins (6), are effective. Other inhibitors in clinical trials include those that target viral entry and trafficking such as camostat mesilate and baricitinib (6).

An alternative antiviral approach is to target host cell pathways that are essential for virus replication, such as protein synthesis. Viruses are completely dependent on the host for translation and have evolved a variety of ways to exploit this machinery for their use (7). In human cells, translation can be divided into four phases: initiation, elongation, termination, and recycling of the ribosome. Translation is initiated by binding of the 5' cap on messenger RNA (mRNA) by the 43S preinitiation complex. This complex scans

¹Department of Microbiology and Immunology, University of North Carolina at Chapel Hill, Chapel Hill, NC 27599, USA. ²Lineberger Comprehensive Cancer Center, University of North Carolina at Chapel Hill, Chapel Hill, NC 27599, USA. Email: damania@med.unc.edu

the mRNA for the start codon and recruits the 60S ribosomal subunit to complete the assembly of the ribosome and begin elongation. Viruses can mimic host mRNAs, which contain a 5' cap, 3' polyadenylated tail, and untranslated regions (UTRs) flanking the 5' and 3' end, to utilize the host translation machinery (7, 8). The SARS-CoV-2 proteins, nsp10, nsp13, nsp14, and nsp16, cap the 5' end of viral RNA (3). Coronaviruses are known to down-regulate global host mRNA translation (8). SARS-CoV-2 nsp1 blocks entry of mRNAs into the ribosome, thereby preventing translation (9–11). Currently, it is unclear whether viral mRNAs are completely able to avoid suppression by nsp1 (10, 11). However, a reporter gene encoding a viral 5' UTR demonstrated a fivefold increase in gene expression in comparison to one encoding a host cell 5' UTR (10). Thus, SARS-CoV-2 commandeers the host translational machinery and is highly dependent on it to make its own viral proteins.

White *et al.* convincingly demonstrate that plitidepsin, which targets the host eukaryotic translation elongation factor 1 α (eEF1A), possesses antiviral activity against SARS-CoV-2. Treatment of mice with plitidepsin reduced viral lung titers and lung pathology upon infection to a similar degree as remdesivir. Expression of the structural protein, N, was also lower in plitidepsin-treated cells compared to remdesivir-treated cells despite similar amounts of N sgRNA in both cells. This is likely due to the inhibition of translation of N by plitidepsin. A concern and limitation of translation inhibitors are the potential toxicities arising from the systemic inhibition of host translation. However, the safety profile of plitidepsin is well studied as it has been tested in many cancer clinical trials (2). An open-label proof-of-concept clinical trial of plitidepsin, given intravenously, to treat COVID-19 has been completed (NCT04382066), and another translation inhibitor, zotatifin, is in clinical trials as an intravenous treatment for COVID-19 (NCT04632381). Zotatifin inhibits the eukaryotic translation initiation factor 4A

(eIF4A) (2). Both phase 1 clinical trials aim to evaluate the safety of these inhibitors for use in patients with mild or moderate COVID-19.

Another small molecule that modulates host translation is rapamycin, which is an orally administered drug that regulates kinases involved in host protein synthesis (12). Multiple clinical trials are underway to examine the efficacy of rapamycin in patients with

mild to moderate COVID-19. The study of White *et al.* suggests that translation inhibitors may have promise in treating patients with mild or moderate COVID-19. There are discernable advantages to targeting the host, which include creating a higher bar for viruses to develop resistance and a broader protection against diverse viral strains.

Despite the rollout of vaccines in several countries, discovering antivirals to treat SARS-CoV-2 continues to be important. There are already concerns about the emergence of SARS-CoV-2 variants that may be less susceptible to the current vaccines. Moreover, new antivirals are needed if remdesivir-resistant SARS-CoV-2 strains emerge. Recent data indicate that plitidepsin maintains potent antiviral activity against the B.1.1.7 SARS-CoV-2 variant (13). Furthermore, many viruses rely on similar host pathways for propagation, leading to some antivirals having a broad spectrum of activity against multiple viruses (3, 6). Remdesivir was originally identified for treating hepatitis C and respiratory syncytial virus, but was ineffective. It was repurposed for use against Ebola virus, and now against SARS-CoV-2. This suggests that antivirals discovered in the race to treat COVID-19 may be useful for future epidemics. ■

REFERENCES AND NOTES

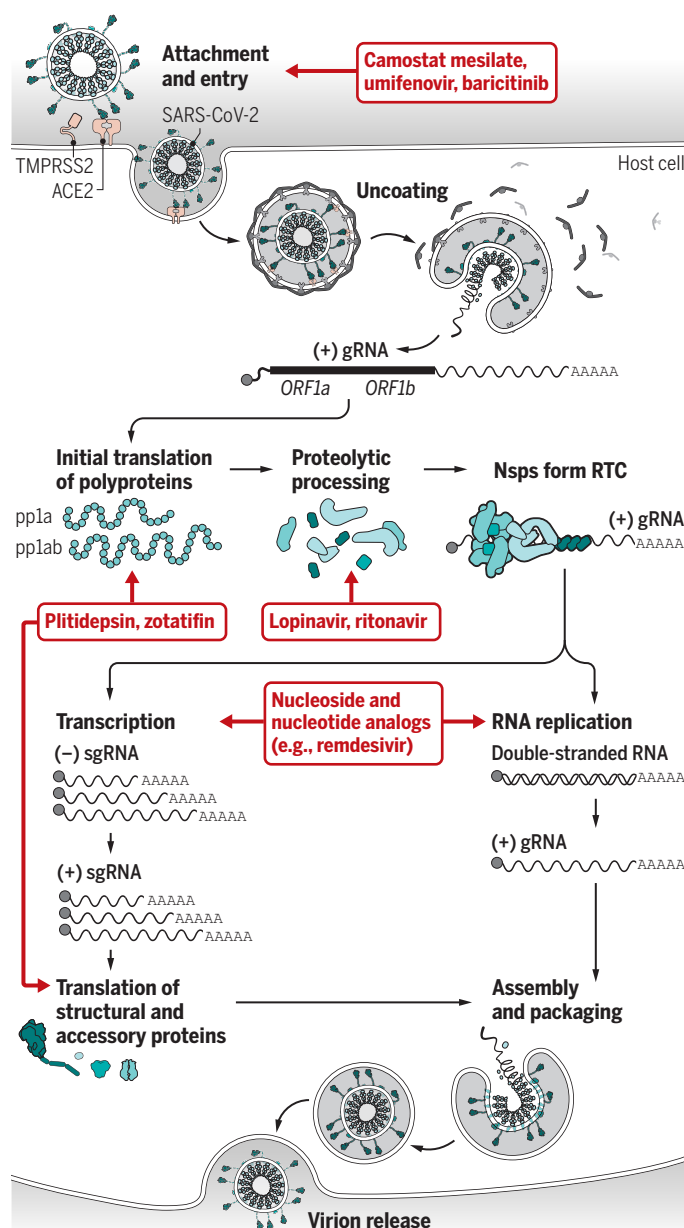
1. N. Basta *et al.*, (McGill COVID19 Vaccine Tracker Team, <https://covid19.trackvaccines.org/vaccines/>), vol. 2021.
2. K.M. White *et al.*, *Science* **371**, 926 (2021).
3. P.V. Kovski *et al.*, *Nat. Rev. Microbiol.* **10**, 1038/s41579-020-00468-6 (2020).
4. A.J. Puijssers *et al.*, *Cell Rep.* **32**, 107940 (2020).
5. T.P. Sheahan *et al.*, *Sci. Transl. Med.* **9**, eaal3653 (2017).
6. B. Hu *et al.*, *Nat. Rev. Microbiol.* **10**, 1038/s41579-020-00459-7 (2020).
7. Z.A. Jaafar, J.S. Kieft, *Nat. Rev. Microbiol.* **17**, 110 (2019).
8. K. Nakagawa, K.G. Lokugamage, S. Makino, *Adv. Virus Res.* **96**, 165 (2016).
9. M. Thoms *et al.*, *Science* **369**, 1249 (2020).
10. K. Schubert *et al.*, *Nat. Struct. Mol. Biol.* **27**, 959 (2020).
11. A.K. Banerjee *et al.*, *Cell* **183**, 1325 (2020).
12. N. Laham-Karam, G.P. Pinto, A. Poso, P. Kokkonen, *Front. Chem.* **8**, 276 (2020).
13. A.-K. Reusch *et al.*, *bioRxiv* 2021.01.24.427991 (2021).

ACKNOWLEDGMENTS

J.P.W. and B.D. are supported by National Institutes of Health grants CA096500, CA254564, CA019014, CA163217, and DE028211.

Targeting the viral life cycle

The SARS-CoV-2 life cycle begins with entry into the host cell, followed by generation of the RTC derived from pp1a translated from ORF1a, and pp1ab translated by ribosomal frameshifting to ORF1b. Then, the viral genome is replicated and packaged into new virions. Inhibitors (red) targeting viral and host factors that are important in the viral life cycle could prevent the spread of infection.



ACE2, angiotensin-converting enzyme 2; gRNA, genomic RNA; Nsp, nonstructural proteins; ORF1, open reading frame 1; pp1a, polyprotein 1a; RTC, replication and transcription complex; SARS-CoV-2, severe acute respiratory syndrome coronavirus 2; sgRNA, subgenomic RNA; TMPRSS2, transmembrane protease serine 2.

CHEMICAL DYNAMICS

Transition states and spin-orbit structure

Spin-orbit coupling is required to explain a set of scattering resonances in the F + HD reaction

By T. Peter Rakitzis

Transient intermediate structures between reactants and products in chemical reactions—transition states—can be probed by colliding the reactants at a well-defined collision energy E_{col} , and then observing the product scattering angle θ and product kinetic and internal energy. By varying E_{col} , sharp variations, or resonances, can be observed in the probability of forming the product at a particular scattering angle and internal energy. These resonances correspond to the energy-level structure of the transition state and have been investigated in the F + HD \rightarrow HF + D reaction for decades (1). On page 936 of this issue, Chen *et al.* (2), through scattering experiments with high resolution and sensitivity, have observed a distinct set of scattering resonances for F + H, which theory can only reproduce by including electronic spin and orbital angular momentum. Thus, the authors measure the transition-state structure with previously unattainable sensitivity.

The geometry and energetic structure of the transition region plays a crucial role in our understanding of chemical reactivity. However, the extremely short lifetime of the transition state (typically less than 10^{-12} s) does not allow the application of optical spectroscopy to probe its structure, so more indirect methods must be used. The energy of the electronic states of atoms and molecules is determined predominantly by the electrostatic attraction and repulsion among the negatively charged electrons and positively charged nuclei. Smaller but important contributions result from the magnetic interaction between the magnetic moments of the electron spins and the electronic orbital angular momentum, known as spin-orbit coupling. This coupling

of the spin angular momentum \mathbf{s} and the orbital angular momentum \mathbf{l} yields the total angular momentum \mathbf{j} , through vector addition, $\mathbf{j} = \mathbf{l} + \mathbf{s}$. Thus, the quantum number j can have multiple values, ranging, in integer steps, from $l + s$ when \mathbf{l} and \mathbf{s} are parallel to $|l - s|$ when they are antiparallel.

Each value of j corresponds to a different electronic state. For example, for halogen atoms (and H atoms in p orbitals), the quantum numbers $l = 1$ and $s = 1/2$ add

to yield $j = 3/2$ (the halogen-atom ground state) and subtract to give state $j = 1/2$ (note that the quantized angular momentum magnitude $|\mathbf{j}| = \sqrt{j(j+1)} \hbar$, where $\hbar = h/2\pi$, and h is Planck's constant). The relativistic spin-orbit energy splitting between these two states is very small for H(2p) atoms, at ~ 0.000045 eV (where the average electron orbital speed is about 1% of the speed of light). However, it increases strongly with atomic number to reach 0.05

eV for F atoms and 0.94 eV for I atoms (where average electron orbital speed is a large fraction of the speed of light), and the spin-orbit energy is about 10% of the electron binding energy. Thus, spin-orbit effects play an increasingly important role for the structure and reactivity of heavy atoms.

Until now, the theoretical treatments of the F + HD reaction needed to explain the extensive experimental measurements of the scattering distributions have not required the inclusion of spin-orbit effects in the transition state. Chen *et al.* selected a particular reactive resonance at a collision energy of 2.10 kcal/mol and identified a peculiar horseshoe-shaped feature in the scattering distribution (see the figure). This feature could not be well described by the standard theoretical treatment, which had errors of about 20 to 40% (red line in insets). However, when spin-orbit coupling is included (3), \mathbf{s} and \mathbf{l} are coupled to the nuclear orbital angular momentum \mathbf{L} , to yield four states, with total angular momentum quantum numbers $L \pm 1/2$ and $L \pm 3/2$. The inclusion of the interference between these four spin-orbit split resonance pathways (J17.5L17–, J17.5L19–, J18.5L17+ and J18.5L19+) in the calculations provides the accurate dynamical picture of this benchmark chemical reaction (green line in insets).

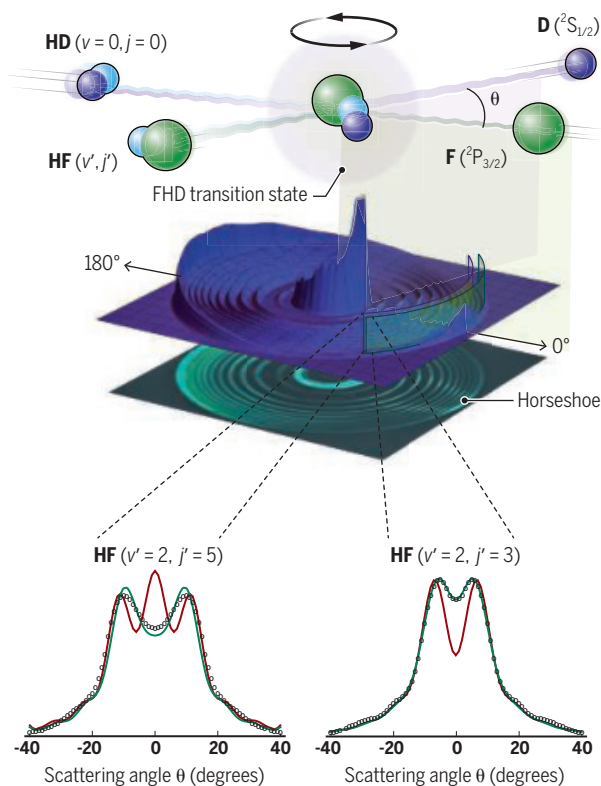
Through reactive scattering at a resonance, Chen *et al.* have identified a method for isolating and measuring the spin-orbit structure of the transition state. Given this result, it might seem that the im-

Explaining “horseshoe” scattering

The reactive collision of F atoms and ground-state HD molecules to form HF + D studied by Chen *et al.* revealed scattering resonances that could only be explained by including spin-orbit energy effects.

Collision and scattering

A quasi-bound resonance in the “asymmetric stretch” of the FHD transition state is formed (top). In the scattering profiles (bottom), measured at angle θ and speed (radius) of the D-atom products, each ring is a different vibrational state v' and rotational state j' of the HF product.



Spin-orbit transition-state structure

Theory must include electronic spin and orbital angular momentum in the transition state (green line; red line without) to explain the experimental horseshoe pattern (open circles).

Department of Physics, University of Crete, and IESL-FORTH (Institute of Electronic Structure and Laser, Foundation for Research and Technology Hellas), Heraklion, Greece. Email: ptr@iesl.forth.gr

pressive series of experiments on the F + HD reaction that test the theory of chemical reactions to new limits have reached their limit. For three-atom reactions, the end seems nearer than ever before. However, although the authors have controlled and measured the energy of the reactants and products with quantum-state precision, there is one final quantum number that is left to be controlled and measured: the magnetic quantum number m_{j_i} of each angular momentum j_i (where the subscript i can be F, HD, HF, or D), which is the projection of each j_i on a laboratory axis and determines the relative spatial orientation of the angular momenta of the reactants and products.

For example, selection of m_{j_F} can control whether the F-atom p orbital is preferentially parallel or perpendicular to the F velocity vector, and selection of $m_{j_{HD}}$ (for $j_{HD} > 0$) can control whether the HD bond is preferentially parallel or perpendicular to the HD velocity vector. Such control provides intuitive models of the reactive encounter, whereas the reduction in the averaging over all possible orientations will further amplify resonance effects and will test theory even more stringently. Methods for the control and measurement of the angular momentum orientation of HD, halogen atoms, HF, and D atoms have been demonstrated (4–7), opening the way for such m-state-resolved experiments.

Progression to experiments with larger systems is also an obvious next step. Recently, theory explained the cold HCl rotational distributions from the nine-atom $Cl + C_2H_6 \rightarrow HCl + C_2H_5$ reaction (8), resolving a nearly 25-year discrepancy with the experimental measurements. The close interplay between theory and experiment continues in the long quest to understand chemical reactivity and reactions of increasing complexity. ■

REFERENCES AND NOTES

1. T. Wang *et al.*, *Chem. Soc. Rev.* **47**, 6744 (2018).
2. W. Chen *et al.*, *Science* **371**, 936 (2021).
3. Z. Sun, D. H. Zhang, M. H. Alexander, *J. Chem. Phys.* **132**, 034308 (2010).
4. N. C. M. Bartlett *et al.*, *J. Chem. Phys.* **129**, 084312 (2008).
5. A. P. Clark, M. Brouard, F. Quadrini, C. Vallance, *Phys. Chem. Chem. Phys.* **8**, 5591 (2006).
6. A. Kvaran, O. F. Sigurbjornsson, H. S. Wang, *J. Mol. Struct.* **790**, 27 (2006).
7. B. M. Broderick *et al.*, *Rev. Sci. Instrum.* **85**, 053103 (2014).
8. D. Papp, V. Tajti, T. Györi, G. Czako, *J. Phys. Chem. Lett.* **11**, 4762 (2020).

ACKNOWLEDGMENTS

We gratefully acknowledge X. Yang for providing the data for the figure and G. Katsoprinakis for assistance in its preparation.

10.1126/science.abg3184

REGENERATION

In the zone for liver proliferation

Distinct liver compartments contribute to hepatocyte homeostasis versus regeneration

By Emma R. Andersson

In humans, the liver is the most regenerative solid organ, able to regrow to normal size after removal of up to 90% of the liver volume (1, 2). The liver is also distinct because it scales with body size, a characteristic that has been attributed to a “hepatostat” that adjusts liver size to the needs of the body (3). Identifying the cells contributing to liver homeostasis and repair could lead to therapies that can activate specific cellular compartments responsible for regeneration. On pages 906 and 905 of this issue, Wei *et al.* (4) and He *et al.* (5), respectively, find that, in mice, a subset of cells in a particular region of the liver, called midlobular zone 2, are the major contributors to hepatocyte proliferation during homeostasis and identify other hepatocyte subsets that contribute to regeneration after damage. This raises questions regarding the mechanisms that induce hepatocyte proliferation and the zonal division of labor with respect to the hepatostat.

At first glance, the liver appears to be composed of a “simple” repeating architectural element, the liver lobule. Conceptually, the liver lobule is a hexagonal unit with a central vein in the middle and a portal vein, hepatic artery, and bile duct (lined by biliary cells) at each of its six corners, separated by hepatocyte sinusoids and other cell types (see the figure). However, a strategic division of labor in the liver is achieved through specialization of cellular roles as a function of the architectural gradient (6–8) from the portal or central vein, spanning three zones from periportal to midlobular to pericentral. Most emphasis thus far has been placed on the specialization of the periportal zone (zone 1), which is enriched for gluconeogenesis and cholesterol and urea biosynthesis functions,

and the pericentral zone (zone 3), which is enriched for glycolysis and glutamine and bile acid biosynthesis functions. Less is known of the role of zone 2, which has largely been considered a transition zone, in addition to its function in the regulation of iron concentration in the blood (6).

Both hepatocytes (9, 10) and biliary cells (11–13) can contribute to regeneration of hepatocytes, depending on the context. Although a tendency toward repopulation from zone 2 had been noted, homeostatic proliferation has been suggested to be broadly and relatively equally distributed among different liver zones. The studies of Wei *et al.* and He *et al.* describe new tools to trace and identify proliferating cells in

liver. By indelibly labeling cells of interest at a given time point and examining their status at a later time point, it is possible to trace the lineages of cells derived from the original cells of interest to unravel principles of development, homeostasis, or pathology (14). The workhorse of genetic lineage tracing uses induction of permanent expression of a fluorophore, through excision of an upstream stop cassette by site-specific recombinases (SSRs), usually the

Cre-LoxP system. By directing SSR expression to specific cell types using cell type- or cell function-specific promoters, distinct cell types, or cells undergoing defined processes, can be followed over time.

Maintaining liver size in normal conditions, during homeostasis, requires repopulation of cells lost because of normal turnover. By contrast, in response to damage, cells must regenerate damaged tissue. To determine the competence of hepatocytes in different zones to repopulate or regenerate the liver, Wei *et al.* generated 11 new conditional Cre mouse strains that allow inducible fluorescent labeling of hepatocytes in different zones and performed lineage tracing with these and three other extant Cre strains under homeostatic or damaging conditions. To exclusively trace proliferat-

“By distributing proliferative potential widely across zones... the liver achieves a capacity to rapidly respond to damage with proliferation of the healthiest hepatocytes without the use of stem cells.”

Department of Cell and Molecular Biology, Karolinska Institutet, Stockholm, Sweden. Email: emma.andersson@ki.se

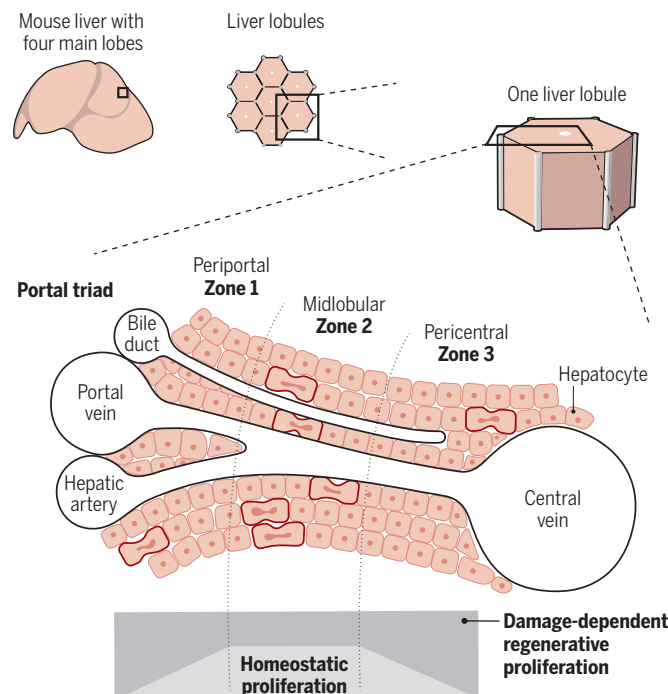
ing cells in a cell type-specific and inducible manner, He *et al.* developed a strategy to inducibly and permanently fluorescently label specific proliferating cells using combinatorial SSRs, dubbed ProTracer. Collectively, using these new tools and approaches demonstrated that zone 2 midlobular hepatocytes are the main source of repopulating hepatocytes during homeostasis but that regeneration of hepatocytes is dependent on where the liver injury occurs.

Random lineage tracing after liver injury has demonstrated that periportal and midlobular hepatocytes reconstitute liver after a pericentral injury, whereas pericentral and midlobular hepatocytes reconstitute liver after periportal injury (9). Although hepatocytes from all zones have the capacity to proliferate, Wei *et al.* show that during homeostasis, zone 1 hepatocytes diminish in number, whereas zone 3 hepatocytes remain steady in number. By contrast, zone 2 hepatocytes increase more than threefold over a year, suggesting that zone 2 hepatocytes are the main source of proliferating hepatocytes during homeostatic conditions, confirming previous work using random rainbow lineage tracing (9). Similar to previous findings, the response to periportal injury resulted in expansion of zone 3- and zone 2-traced hepatocytes, whereas pericentral injury resulted in expansion of zone 1- and zone 2-traced hepatocytes. It is thus now clear that the capacity of hepatocytes to proliferate is broadly spread among lobule zones but that predominantly zone 2 hepatocytes maintain homeostasis, whereas predominantly zone 1 and zone 3 hepatocytes respond to injury and repopulate the liver after injury to zones 3 and 1, respectively. Liver function and repair are thus maintained by hepatocytes in general and not by a rare stem cell population. Thanks to these newly developed mouse Cre strains, it will be possible to unravel exactly which hepatocytes and signaling mechanisms contribute to liver homeostasis, growth, repair, or cancer. It will also be interesting to investigate the sexual dimorphism of increased liver regeneration in females.

ProTracer is an interesting approach to tracing cells that have proliferated. This method allows inducible lineage tracing of

Hepatocyte repopulation and regeneration

Liver architecture is defined by repeating units, called liver lobules, which have a hexagonal structure with a central vein and a portal triad (portal vein, hepatic artery, and bile duct) at each corner, separated by hepatocytes. Hepatocytes exhibit specialized functions from the portal vein to the central vein, creating three zones. Zone 2 hepatocytes are the main contributors to homeostatic proliferation, whereas hepatocytes in zones 1 and 3 are capable of regenerating liver after damage to zones 3 and 1, respectively.



cells that proliferate from a specific time point. During homeostasis, continuous proliferation tracing using ProTracer showed that zone 2 hepatocytes proliferate twice as much as zone 1 hepatocytes and eight times more than zone 3 hepatocytes, further strengthening the concept that zone 2 hepatocytes are the main contributors to liver homeostasis. By contrast, regeneration after partial hepatectomy in which whole liver lobes are removed, and which induces enlargement of the remaining liver lobes, was first dominated by proliferation of zone 1 hepatocytes (at 40 hours), and by 7 days, zones 1 and 2 were 80% populated by hepatocytes that had undergone proliferation, whereas only half of zone 3 hepatocytes had undergone proliferation.

The ProTracer mouse model opens up the possibility of tracing cell proliferation from adult stages over longer time scales (several months) in a continuous manner, enabling the identification of slowly cycling cells and rare stem cells in various organs. This may unveil previously unknown stem cell populations. In the liver, regeneration after injury is usually maintained by cells with phenotypic fidelity: Typically, hepatocytes regenerate hepatocytes, and

biliary cells regenerate biliary cells. By distributing proliferative potential widely across zones, and soliciting recovery from the least-damaged regions, the liver achieves a capacity to rapidly respond to damage with proliferation of the healthiest hepatocytes without the use of stem cells. Whether specific hepatocyte zones are more or less important for regeneration and whether certain hepatotoxins are more damaging because they target important subsets of hepatocytes are questions that can be addressed with these new tools.

The studies of Wei *et al.* and He *et al.* raise several questions. Zone 1 hepatocytes proliferate far more than zone 3 hepatocytes, yet zone 1 hepatocyte numbers decline with time, whereas zone 3 numbers remain steady. Do hepatocytes have different life spans depending on their location? It is also unclear which molecular mechanisms induce zone-specific hepatocyte proliferation in response to distinct modes of injury; perhaps these can be leveraged therapeutically to induce or accelerate regeneration of hepatocytes.

Although hepatocytes can transdifferentiate to regenerate the biliary tree (15), it is not yet known whether transdifferentiation is a function of only a subset of hepatocytes and whether this also could be leveraged therapeutically to induce regeneration in biliary diseases. These questions and others can now begin to be addressed, building a foundation to approach liver disease therapeutically. ■

REFERENCES AND NOTES

1. A. P. Monaco, J. Hallgrímsson, W. V. McDermott Jr., *Ann. Surg.* **159**, 513 (1964).
2. B. Cady, M. Bonneval, H. R. Fender Jr., *Am. J. Surg.* **137**, 514 (1979).
3. G. K. Michalopoulos, B. Bhushan, *Nat. Rev. Gastroenterol. Hepatol.* **18**, 40 (2021).
4. Y. Wei *et al.*, *Science* **371**, eabb1625 (2021).
5. L. He *et al.*, *Science* **371**, eabc4346 (2021).
6. K. B. Halpern *et al.*, *Nature* **542**, 352 (2017).
7. K. B. Halpern *et al.*, *Nat. Biotechnol.* **36**, 962 (2018).
8. A. Braeuning *et al.*, *FEBS J.* **273**, 5051 (2006).
9. F. Chen *et al.*, *Cell Stem Cell* **26**, 27 (2020).
10. Y. Malato *et al.*, *J. Clin. Invest.* **121**, 4850 (2011).
11. A. Raven *et al.*, *Nature* **547**, 350 (2017).
12. X. Deng *et al.*, *Cell Stem Cell* **23**, 114 (2018).
13. J. O. Russell *et al.*, *Hepatology* **69**, 742 (2019).
14. C. S. Baron, A. van Oudenaarden, *Nat. Rev. Mol. Cell Biol.* **20**, 753 (2019).
15. J. R. Schaub *et al.*, *Nature* **557**, 247 (2018).

10.1126/science.abg4864

High-speed harvesting of random numbers

A broad-area multimode laser can be made into a powerful random number generator

By Ingo Fischer¹ and Daniel J. Gauthier²

Human-made physical random number generators (RNGs) can be traced back 5000 years or more. Early examples such as knucklebones, two-sided throwsticks, or dice have been found in the Middle East, India, and China. RNGs were used for fortune telling and games of chance, with the oldest known board games of similar age as those of the number generators. Today, RNGs are vital for services and state-of-the-art technologies such as cryptographically secured communication, blockchain technologies, and quantum key distribution. Moreover, RNGs are needed in machine learning and scientific applications such as Monte Carlo numerical methods. On page 948 of this issue, Kim *et al.* (1) demonstrate an ultrafast RNG based on a broad-area laser with a multispot beam that is analogous to generating random numbers by using many dice at once.

Random numbers are often generated by using a software algorithm running on a computer, called “pseudo”-random because the sequence eventually repeats. Moreover,

relations among the numbers can exist that reveal that the numbers are not uniformly random. Hence, true RNGs (TRNGs) are of great interest, providing random numbers based on physical measurements that involve some noisy or stochastic process. All TRNGs have some nonidealities, such as generating zeroes more frequently than ones for a binary-output device, which must be mitigated by carefully engineering the device and postprocessing the data to improve the randomness quality (2).

Some applications require generating random numbers at very high rates, such as encrypting data in cloud-computing data centers, high-speed communication networks, or massive simulations. Photonic devices are a natural fit for these applications because of their potential for high-speed operation, compact size for chip-scale devices, and low power consumption.

Recently, Marangon *et al.* (3) developed a TRNG that is based on interfering two different lasers on a beam splitter and detecting the resulting powers that emanate from its two output ports. The randomness comes about from quantum fluctuations in a laser due to a process known as spontaneous emission of photons. This process randomizes the phase of the light emitted by each laser, and this phase variation is converted to an intensity variation through the interference effect. Measuring which output port of the interferometer has the higher or lower intensity can be used to generate a one or

a zero, respectively, at random. A compact device can be realized by generating random numbers in real time at a rate of 8 Gb/s for days at a time, passing tests that are used to assess the quality of the bit stream.

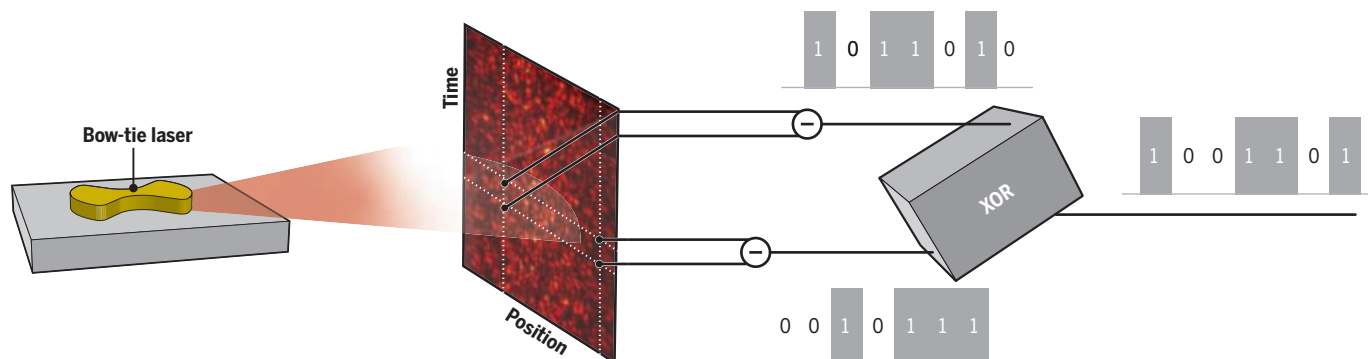
The bottleneck in reaching higher speeds is that the lasers are single-mode and only generate a Gaussian beam-like spot at a single frequency. Kim *et al.* overcome this bottleneck by using a broad-area laser that simultaneously emits a plethora of modes, resulting in a multispot beam. The patterns undergo a complex dance, writhing and growing bright and dim because of phase and amplitude variation of the light within the laser (see the figure). For a good TRNG, engineering the broad-area laser cavity is especially necessary so that spatial and temporal correlations are minimized. The authors do so, which is a major achievement.

Common broad-area lasers are known to exhibit irregular intensity pulsations in space and time because of the nonlinear interaction of light and the laser medium (4). Such instabilities result in correlations of their emission with characteristic spatial and temporal scales and are exceedingly difficult to avoid. This situation has plagued attempts to apply broad-area lasers more widely. Bittner *et al.* (5) showed that they could largely suppress the onset of spatiotemporal instabilities by using a cavity with a D shape, inspired by chaotic billiards; the balls on a D-shaped billiard table follow chaotic trajectories (6).

¹Instituto de Física Interdisciplinar y Sistemas Complejos (IFISC), Consejo Superior de Investigaciones Científicas–Universitat de les Illes Balears (CSIC–UIB), Campus Universitat de les Illes Balears, E-07122 Palma de Mallorca, Spain. ²Department of Physics, Ohio State University, Columbus, OH 43210, USA. Email: ingo@ifisc.uib-csic.es; gauthier.51@osu.edu

Creating bits with laser intensity

Ultrafast random bits are generated from a broad-area laser with a bow-tie cavity. In order to generate the random bits, first intensities separated by ~6 ps are subtracted from each other for the same positions on the detector. This creates bits of either ones or zeroes, which then undergo the exclusive-OR (XOR) logic operation with bits of another spot separated by half the width of the aperture. The XOR operation produces a one if the two inputs are different or a zero if the two inputs are the same. The broad-area laser allows for many different positions on the detector to be used simultaneously, allowing for fast generation of bits.



Kim *et al.* introduce another approach based on adapting the shape of the cavity. After performing extensive numerical modeling, the authors chose a bow-tie shape and precisely microfabricated a laser chip. The authors managed to boost the number of modes, avoiding their locking, and thereby substantially reduced the spatial and temporal correlation scales to 1.5 μm and 2.8 ps, respectively.

Another advantage of using the spatial degree of freedom of the special laser design is avoiding the two separate lasers and interference on an auxiliary beam splitter (3). Random numbers can be “harvested” from the complex emitted pattern by measuring the intensity at 254 spatial positions on ultrafast time scales (on the order of 1 ps) by using a special high-speed camera. This strategy is truly an ultrafast Demeter meeting chance.

Through this effort, they achieved a random bit generation rate of 250 Tb/s, which is much more than an order of magnitude greater than previous efforts. A full technical implementation of such an ultrafast TRNG still faces several challenges that need to be overcome. The high-speed camera could only capture data over a limited time (~ 2 ns), so they had to collect and concatenate multiple records to generate the more than 10^9 random numbers needed for the various statistical tests of randomness. Replacing the camera with a multitude of integrated photodetectors is yet to be achieved. Also, the required postprocessing of the measured intensities to ensure randomness is, at such speed, a task for the future.

Looking beyond, the innovative approach to tailor the spatial and temporal emission properties of broad-area lasers and manipulating the nonlinear interaction of light with the laser medium opens other applications that require many degrees of freedom. Several machine-learning approaches are based on a random mapping of low-dimensional input data onto a high-dimensional-state space, which might be accomplished by injecting a data-encoded beam into a tailored laser. Hence, broad-area lasers may become attractive photonic integrated circuits for ultrafast information processing (7, 8). ■

REFERENCES AND NOTES

1. K. Kim *et al.*, *Science* **371**, 948 (2021).
2. J. D. Hart *et al.*, *Appl. Phys. Lett. Photonics* **2**, 090901 (2017).
3. D. G. Marangon *et al.*, *J. Lightwave Technol.* **36**, 3778 (2018).
4. I. Fischer, O. Hess, W. Elsaßer, E. Göbel, *Europhys. Lett.* **35**, 579 (1996).
5. S. Bittner *et al.*, *Science* **361**, 1225 (2018).
6. H. Cao, J. Wiersig, *Rev. Mod. Phys.* **87**, 61 (2015).
7. P. R. Prucnal, B. J. Shastri, *Neuromorphic Photonics* (CRC Press, 2017).
8. D. Brunner, M. C. Soriano, G. Van der Sande, Eds., *Photonic Reservoir Computing* (De Gruyter, 2019).

10.1126/science.abg5445

CORONAVIRUS

Optimizing age-specific vaccination

Vaccination strategies are not one-size-fits-all

By Meagan C. Fitzpatrick^{1,2} and Alison P. Galvani²

Efficacious vaccines against severe acute respiratory syndrome coronavirus 2 (SARS-CoV-2) have been developed, tested, and approved for emergency use with unprecedented speed. Deployment of multiple vaccines was initiated in several countries less than 1 year after identification of the virus. Although vaccine production is being rapidly scaled up, demand will exceed supply for the next several months. Consequently, an urgent challenge is the optimization of vaccine allocation to maximize public health benefit. On page 916 of this issue, Bubar *et al.* (1) demonstrate that vaccination of older people is the optimal age-based strategy to alleviate the burden of COVID-19. Although vaccination of younger adults is projected to avert the greatest incidence, vaccinating older adults will most effectively reduce mortality. In addition, they assess targeted vaccination that was based on serological status, finding that vaccinating seronegative individuals improves efficiency especially in settings where seroprevalence is high.

Some have looked to influenza vaccination strategies for guidance, given that SARS-CoV-2 is a respiratory virus with similar modes of transmission (2). Until 2008, the U.S. Centers for Disease Control and Prevention (CDC) prioritized people aged 50 years and older for influenza vaccination because of their increased risk of mortality (3). To evaluate this long-standing policy, optimal influenza vaccine allocation was determined on the basis of a dynamic transmission model combined with optimization algorithms that facilitated the searching of wide ranges of parameter space across multiple dimensions concurrently (4). The dynamic model component simulates both the direct protection conferred to a vaccinated individual as well as the indirect protection for others that is attributable to reductions in onward trans-

mission. This modeling indicated that allocating scarce vaccines to school-age children and young adults achieves the most effective reduction in influenza burden whether measured in terms of incidence, hospitalizations, years of life lost, or economic cost (4). These insights prompted an expansion of recommendations to prioritize school-age children (5), which interrupts transmission for all ages and bolsters indirect protection against mortality. Bubar *et al.* extend the framework of transmission modeling combined with vaccine optimization developed for influenza (4) to explore SARS-CoV-2 vaccination strategies and, different from the optimal influenza vaccination strategy, they conclude that vaccinating older people most effectively mitigates mortality from COVID-19.

Although it may seem intuitive that the optimal strategies against influenza and COVID-19 would be identical, vaccine optimization is not one size fits all, even for apparently similar pathogens. Quantitative changes in the epidemiological landscape can lead to qualitative shifts in optimization (see the figure). The age-specific probability of infection is a key component of this landscape. As a result of contact patterns, older people are simultaneously less exposed to and less responsible for onward transmission of both influenza virus and SARS-CoV-2 (6). An awareness of their heightened risk for severe clinical outcomes from COVID-19 has further suppressed contacts of older people. By contrast, essential workers, who are more likely to be exposed to SARS-CoV-2, are usually younger adults. These behavioral factors point to reduced public health benefit from vaccination of older people, but there are other factors that must also be considered.

Vaccine efficacy also affects optimization. Vaccines that elicit more efficacious direct protection against infection concomitantly generate stronger indirect effects (7). Highly efficacious vaccines administered to younger people can efficiently interrupt transmission chains, whereas modestly efficacious vaccines do not. With everything else being equal, vaccine efficacy as high as so far reported for SARS-CoV-2 vaccines also favors prioritization of younger people (7, 8). A caveat is that clinical tri-

¹Center for Vaccine Development and Global Health, University of Maryland School of Medicine, Baltimore, MD, USA. ²Center for Infectious Disease Modeling and Analysis, Yale School of Public Health, New Haven, CT, USA. Email: alison.galvani@yale.edu

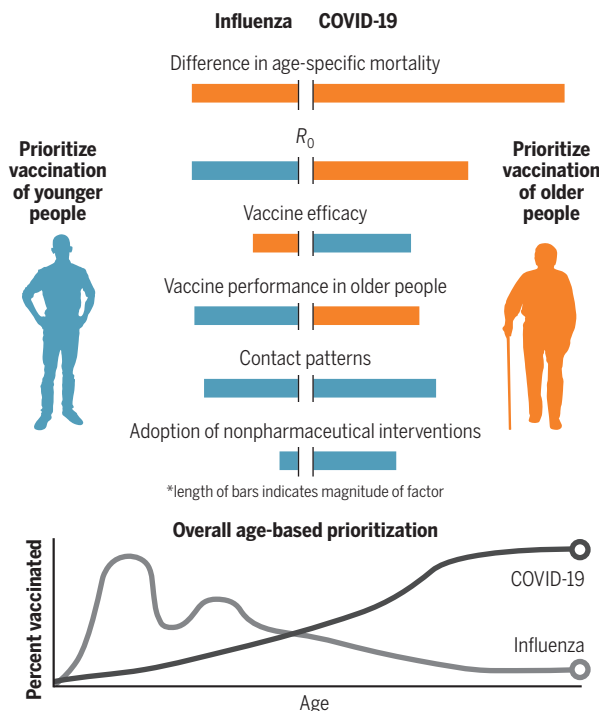
als for SARS-CoV-2 vaccines have measured protection against symptomatic disease, not necessarily infection. If these vaccines are less efficacious against infection and onward transmission, indirect protection would be diminished, and vaccination of older people would be consistently optimal.

However, the magnitude of two other elements counterbalances the influence of age-specific contact rates and high vaccine efficacy on optimal vaccination strategies: overall infectiousness and differences in case fatality according to age. Vaccines are less able to prevent death through indirect protection when infectiousness rises because the virus is able to infect more unvaccinated people. SARS-CoV-2 is highly contagious: Its reproductive number, R_0 (the average number of secondary infections arising from a single case when everyone is assumed to be susceptible), is typically double that of influenza virus (7, 9). Furthermore, age-based differences in case fatality are much larger for COVID-19 than for influenza. For example, hospitalized individuals aged 71 to 80 years have 46.2 times the risk of mortality compared with those aged 18 to 30 years, whereas this parameter is 9.3 times for seasonal influenza (10). Indirect effects from vaccinating younger people are unlikely to compensate for the amplified direct risk posed to older people by COVID-19. Beyond overall efficacy, vaccine characteristics can affect optimal vaccination strategies. Influenza vaccines have variable age-specific efficacy, with reduced protection for older people compared with younger individuals (7). Interim data from an ongoing phase III clinical trial of a SARS-CoV-2 vaccine do not indicate a comparable discrepancy because the vaccine appears to have similar efficacy across age groups (8).

An additional consideration relates to the age-specific effectiveness of nonpharmaceutical interventions (NPIs). Some measures, including masks and movement restrictions, reduce transmission risk regardless of symptom status. Others, such as temperature checks, are symptom-based and therefore miss asymptomatic infections. When the severity of symptoms correlates with age, such as for COVID-19 and influenza, there is a parallel correlation in the effectiveness of symptom-based interventions. Given that young people are more likely to be asymptomatic (11), infections

Key determinants of age-based vaccination

Epidemiological factors drive age-based vaccine optimization for influenza and COVID-19 with varying influence according to the mechanism and magnitude of the factor. When there are stark differences in mortality risk with age, or when the reproductive number R_0 is high, older people are more likely to be prioritized for vaccination. By contrast, high vaccine efficacy, the amount of social contact among younger people, and widespread adherence to nonpharmaceutical interventions can shift prioritization toward younger ages.



in this group are less likely to be contained by symptom-based control but are still able to be prevented by vaccination. Under these conditions, the delayed vaccination of young people would increase the ratio of asymptomatic to symptomatic infections. Such silent transmission has driven the widespread dissemination of SARS-CoV-2 (12). Although these considerations are unlikely to greatly alter prioritization for COVID-19 vaccines, public health officials should be mindful of these changing dynamics during the period when many older individuals are vaccinated and many younger people are not. It is imperative to maintain NPIs until high vaccination coverage is attained in all age classes.

The complexity of these epidemiological, clinical, behavioral, and vaccine-related relationships underscores the importance of pathogen-specific transmission modeling to inform vaccination strategies. Such models have guided vaccination policies for myriad diseases, including those caused by rubella virus, human papillomavirus, and varicella-zoster virus, which exhibit age-specific patterns in both transmission and severity. This framework can

also be applied to decisions about allocation that are not based on age but in which there are analogous dichotomies between mortality and transmission potential. At the same time, it is imperative to remain cognizant that model predictions are only as accurate as the data on which they are based. A particular limitation of modeling during an emerging disease outbreak is the sparsity of data (13). Current sources of imprecision for modeling the COVID-19 pandemic include evolving age-specific behavioral patterns as well as the temporal and geographical heterogeneity in adoption of NPIs. Also, a persistent pitfall for modeling is that analyses that galvanize action to avert crisis necessarily make themselves obsolete (13).

Bubar *et al.* elegantly synthesize the available data for COVID-19 within their model, concluding that the age-based strategy that saves the most lives is vaccination of older individuals. Both SARS-CoV-2 and influenza virus vaccination can be optimized within the overarching paradigm that balances the indirect risks of transmission against direct risks from mortality. Although vaccinating younger people prevents the most infections for both viruses, the

difference is that this strategy does not also avert the most deaths for COVID-19. To vanquish a pathogen that causes such steeply divergent case fatality rates as that of SARS-CoV-2, the optimal strategy is clear: Directly vaccinate those with greatest personal risk. ■

REFERENCES AND NOTES

1. K. M. Bubar *et al.*, *Science* **371**, 916 (2021).
2. K. Tingley, *New York Times*, 5 November 2020; www.nytimes.com/2020/11/05/magazine/who-gets-covid-vaccine.html.
3. A. E. Fiore *et al.*, *MMWR Recomm. Rep.* **57**, 1 (2008).
4. J. Medlock, A. P. Galvani, *Science* **325**, 1705 (2009).
5. A. E. Fiore *et al.*, *MMWR Recomm. Rep.* **59**, 1 (2010).
6. E. Zaghien *et al.*, *Am. J. Epidemiol.* **168**, 1082 (2008).
7. P. Sah, J. Medlock, M. C. Fitzpatrick, B. H. Singer, A. P. Galvani, *Proc. Natl. Acad. Sci. U.S.A.* **115**, 5151 (2018).
8. F. P. Polack *et al.*, *N. Engl. J. Med.* **10.1056/NEJMoa2034577** (2020).
9. J. Hilton, M. J. Keeling, *PLOS Comput. Biol.* **16**, e1008031 (2020).
10. L. Piroth *et al.*, *Lancet Respir. Med.* **10.1016/S2213-2600(20)30527-0** (2020).
11. N. G. Davies *et al.*, *Nat. Med.* **10.1038/s41591-020-0962-9** (2020).
12. S. M. Moghadas *et al.*, *Proc. Natl. Acad. Sci. U.S.A.* **10.1073/pnas.2008373117** (2020).
13. M. C. Fitzpatrick, C. T. Bauch, J. P. Townsend, A. P. Galvani, *Nat. Microbiol.* **4**, 1612 (2019).

Published online 26 January 2021
10.1126/science.abg2334

RETROSPECTIVE

Paul J. Crutzen (1933–2021)

Father of modern atmospheric chemistry

By Susan Solomon

Paul J. Crutzen, renowned atmospheric chemist and meteorologist, died on 28 January after a long illness. He was 87. During his inspired scientific career, he made breakthroughs that shed light on the ozone layer, air pollution, greenhouse gases, nuclear winter, and the effect of human activities on climate. Crutzen's towering academic achievements influenced environmental policies worldwide. Through it all, he maintained an open, joyful, and graceful disposition that endeared him to colleagues and students alike.

Born on 3 December 1933 to a working-class family in Amsterdam, Crutzen survived the Dutch famine of 1944–1945 (dubbed the “hunger winter”). In 1954, he earned a technical degree in civil engineering. Before leaving the Netherlands, he worked briefly as a bridge construction engineer and married the love of his life, Terttu Soininen. In 1959, an opportunity arose to move to Stockholm University and work as a computer programmer, giving Crutzen a chance to realize his long-held dream of an academic life. It did not take long for his talents to shine through, and he transitioned to the Department of Meteorology, where he earned his M.Sc. (filosofie kandidat degree) in 1963, his Ph.D. (filosofie licentiat degree) in meteorology in 1968, and his D.Sc. (filosofie doctor degree) in 1973, after completing a thesis on aircraft pollution in the stratosphere and troposphere.

With his background in meteorology, Crutzen adroitly spanned atmospheric chemistry and dynamics. His Ph.D. work at Stockholm University laid the basis for his blockbuster 1970 paper showing that catalytic chemistry involving nitric oxide (NO) is the dominant control on the distribution of stratospheric ozone. He and atmospheric chemist Harold Johnston independently pointed out that NO in the exhaust of supersonic aircraft flying at stratospheric altitudes might therefore threaten the ozone layer. Crutzen also drew attention to the potential role of NO from nitrous oxide generated by fertilizers as a mechanism for controlling stratospheric ozone. In the 1970s, he led the field in numerical modeling of processes in-

fluencing stratospheric ozone. His pioneering contributions to stratospheric chemistry ultimately resulted in his sharing the 1995 Nobel Prize in Chemistry with F. Sherwood Rowland and Mario Molina.

In the mid-1970s, Crutzen and his family moved to Boulder, Colorado, where he worked at the National Oceanic and Atmospheric Administration and, before long, became the director of the Atmospheric Chemistry Division at the National Center for Atmospheric Research. Crutzen's research extended from the stratosphere down into tropospheric ozone and pollution. He first identified the impact of biomass burning on pollutants, including carbon monoxide.



His interests also extended up into the mesosphere and lower thermosphere and into the world of climate. He is credited with suggesting that carbonyl sulfide makes major contributions to the amount of sulfuric acid aerosols in the stratosphere, which is important not only for stratospheric chemistry but also for climate. He showed that most tropospheric ozone is made in the lower atmosphere, not transported from the stratosphere. He also conducted leading work on the sources of methane, the second most important anthropogenic greenhouse gas.

I met Crutzen in 1977, when he took me under his wing as a graduate student to study the impact of solar proton events on atmospheric chemistry. His knowledge of every aspect of the chemistry that controls atmospheric ozone was breathtaking. He spent innumerable hours patiently teaching me how to analyze models and identify which chemical reaction produced which observable change in atmospheric gases. He was a skillful, supportive, and kind lifelong mentor

to me and dozens of others. When one colleague was having trouble getting his (later very influential) paper on the lifetime of atmospheric methane through review, Crutzen swooped in to convince the editor to publish it by agreeing to write a commentary himself. Another colleague was named to lead a chapter in an international scientific assessment for the Montreal Protocol and needlessly worried that Nobel laureate Crutzen—one of the chapter's authors—might have a hard time working as a team member rather than the leader. He quickly learned that Crutzen was always a constructive and thoughtful team player in any group effort.

A remarkable linguist, Crutzen could converse easily in multiple languages, including German, Swedish, and English. In 1980, Crutzen took a position in Mainz, Germany, as a director at the Max Planck Society. There, he and his colleague John Birks identified the problem of nuclear winter, a topic pioneered at about the same time by others, including Carl Sagan. Having lived through the devastation of World War II, Crutzen felt a deep connection to that work. He believed in the importance of scientific research to identify the risks of human conflict in the nuclear age.

A few years later, when the ozone hole was discovered, Crutzen showed that nitric acid clouds were vital to its chemistry (a discovery simultaneously and independently made by atmospheric scientist Brian Toon). Crutzen's incessant curiosity led him to contribute, together with climate physicist Veerabhadran Ramanathan and others, to our understanding of the role of black carbon as an important driver of climate change. That work also helped illuminate the health risks of black carbon, especially in the developing world.

Crutzen continuously churned out new and influential ideas. At a conference in 2000, he became annoyed by talk of the Holocene era as the current geological epoch, and he rose on the spot to declare that humanity had already had such a vast impact on the planet that we ought to be talking about the “Anthropocene” instead. He spent the last 20 years of his life expanding on and deepening the Anthropocene concept, which he entered into the common lexicon.

Crutzen was scientifically prolific, creative, and profoundly influential in the fields of atmospheric chemistry and climate science. He was also a person of great warmth, caring, deep humility, and genuine concern for his fellow humans as well as the future of the planet we all share. As we address the urgent challenges of pollution, climate change, and sustainability, the foundation he helped to build will support the many scientists and students who follow in his footsteps. ■

Department of Earth, Atmospheric and Planetary Sciences, Massachusetts Institute of Technology, Cambridge, MA, USA. Email: soloso@mit.edu

10.1126/science.abh0217

Was “science” on the ballot?

Labeling dissent as “anti-science” is bad
social science and bad politics

By **Stephen Hilgartner¹, J. Benjamin Hurlbut²,
Sheila Jasanoff³**

On 7 November 2020, moments before Kamala Harris and Joe Biden began their victory speeches, giant screens flanking the stage proclaimed, “The people have chosen science.” Yet, nearly 74 million Americans, almost half the voters, had cast their ballots for Donald Trump, thereby presumably not choosing science. Prominent scientists asserted that “science was on the ballot” and lamented that “a significant portion of America doesn’t want science” (1). But before despairing at the loss of trust in science, we should be sure we are worrying about the right problem. Was “science” really on the ballot? Is it useful to imagine U.S. citizens as divided into pro-science and anti-science camps? Does the label anti-science serve the purposes of deliberative democracy? The answer to these questions is plainly no. A correct diagnosis is essential to repairing the sorry state of science-society relations in the United States.

Campaign slogans notwithstanding, science was not on the ballot. If the election contested any aspect of science, it was not the worth of scientific knowledge but the authority of experts to decide how people should live their lives. What looks like an attack on science may simply be the pursuit of politics by other means. Americans are indeed divided, but the division is not between those who march for science and those who march against science. It is between competing understandings of how to balance collective responsibility and individual liberty. That division runs so deep that, for some, it even justifies violence and insurrection. Insisting on facts is not by itself an adequate response. Indeed, it fundamentally misconceives the role and power of science in modern democracies.

A PROXY WAR

The pandemic has seen much hand-wringing about Americans’ unwillingness to “accept science” and follow public health directives: wear a mask, obey lockdowns, accept job loss, homeschool children, let loved

ones die alone. Dissent from such mandates should not come as a surprise. Acceptance of intrusive public health policies, no matter how essential, depends on trust, not merely in “the facts” but also in the institutions that produce and evaluate evidence and weigh trade-offs. Epidemiological measures of deaths averted don’t capture other essential dimensions of life—economic, social, political, and even spiritual. Policies aimed primarily at reducing health risks are suspect to those who see other critical needs as being unjustifiably neglected.

In America, factual controversies in policy contexts are often less about the credibility of science than they are proxies for disagreements about competing ways of life. Policy stalemates about climate change, gun control, or mask wearing were not caused by citizens’ refusal to accept expert-certified facts. These disputes signal dissatisfaction with trade-offs that some citizens see as elevating expert values above their own.

It is tempting to treat matters of health, safety, and environmental policy as if they are primarily about facts, because this transforms intractable social disputes into seemingly answerable technical questions. But such moves are inimical to democracy. When the key issue is who decides, acting as if disagreements are mainly about evidence is bad politics and bad social science. It turns expertise into an object of distrust and exacerbates American culture’s tendency to alienate people from the perceived elitism of science (2). This creates fertile ground for alternative facts and conspiracy theories that reframe problems and relocate the focus of blame.

Science advice thus occupies a precarious position on the boundary between asserting facts and making policy. It faces the structural problem of being authoritative without becoming authoritarian. It divides power between scientists, who are mainly accountable to their peers, and authorized political representatives, who are accountable to the citizens they serve. This allocation of authority is fundamentally political, even constitutional. We should not be surprised if expert advisers find their claims being questioned, given their consequential role in contemporary governance.

PUBLIC HEALTH SOVEREIGNTY

For more than a century, Americans have agreed that safeguarding public health justifies granting health officials extraordinary powers to restrict liberty. This “public health sovereignty” (3) rests on a view of citizens as biological entities who must be protected or controlled to contain infection. But that reading sidelines the reality that citizens are also political subjects with individual rights. It downplays impacts on liberty, privacy, and solidarity unless institutional means are provided to let these considerations in.

The history of public health policy is full of controversies in which communities sought to rebalance their rights and interests against public safety. During the HIV-AIDS epidemic, for example, states debated whether to criminalize sexual behavior that spread the virus. It took a large, well-organized gay community to advocate for personal privacy, promote the value of open sexual expression, and challenge discrimination under the guise of public health protection. Where such communities existed, restraints tended to be weak. Elsewhere, public health sovereignty prevailed (4).

Restricting liberty in the name of public health becomes especially fraught when scientific knowledge is unsettled but policy responses are urgently needed. It is tempting to move fast, invoking expert authority to short-circuit deliberation. The challenge in such circumstances is not simply to persuade citizens to accept prepackaged expert judgments as fact; it is also to ensure that responsible institutions explicitly and visibly consider competing priorities when determining how to gather, interpret, and apply evidence. Labeling resistance as “anti-science” does little to further this goal. It separates experts from publics instead of building common ground.

AN ANTI-SCIENCE PUBLIC?

What stands in the way of improving science-society relationships during a public health emergency? The answer is certainly not that a substantial portion of America simply “doesn’t want science.” That diagnosis dangerously misses the mark. When decision-makers try to ground policy in scientific facts rather than in the trustworthiness of the essential (but fallible) institutions that produce them, any technical missteps make the policies more vulnerable. And missteps are inevitable when science is moving fast.

The “anti-science” label conflates normative dissent about which values matter with

¹Department of Science & Technology Studies, Cornell University, Ithaca, NY, USA. ²School of Life Sciences, Arizona State University, Tempe, AZ, USA. ³Harvard Kennedy School, Cambridge, MA, USA. Email: shh6@cornell.edu

epistemic dissent on matters of fact. It corrodes democracy and risks producing dissidents with contempt for experts. Instead of admonishing people to buy the science, we need a more robust politics of persuasion that requires experts to publicly address the competing values and interests at stake in setting policy agendas. When should protecting public health override individual freedom? Does the health risk of opening schools outweigh children's social needs? How should the power to decide be distributed among legislatures, courts, the executive, and scientific experts?

In our study of 16 countries' responses to COVID-19 (5), we found widely varying approaches based on the same evidence. In Sweden, Netherlands, and South Korea, citizens' priorities concerning what is essential for a good society substantially influenced the stringency of measures such as masking, lockdowns, and school closures. In Germany and Australia, opposing political parties came together to agree on policies serving a perceived national interest. In India, Japan, and the United Kingdom, dissent focused on the wisdom, efficacy, and motivations of government actions but not the seriousness of the disease or the need for decisive action. Only in the United States was policy disagreement consistently recast as being "for" or "against" science, as if all politics could be reduced to that simple litmus test.

Our study shows that policy preferences cannot be segregated into two distinct silos: informed versus ignorant, rational versus irrational, scientific versus anti-scientific. Yet, American public health discourse too often labels policies as either "evidence-based" or baseless. Decision-makers may find it expedient to shield themselves behind such characterizations, but hiding the value choices only inspires resistance and denialism (6).

REBUILDING THE POLITICS OF SCIENCE

How then can we build a more progressive politics of science? We must first recognize that trust cannot be produced on demand. It grows slowly out of strong social relationships. History shows that science fares best when it is responsive to skepticism, not insulated from it. Building a less paternalistic, more inclusive dialogue between science and citizens is crucial for informed, democratic governance. Three moves are essential: make science more attentive to citizens' real concerns, make citizens smarter about how science works in governance, and make spaces for deliberating different interpretations of science without polarizing conflicts.

President Biden has already taken praiseworthy steps toward the first goal. By nominating Eric Lander and Alondra Nelson, two prominent spokespersons for science in society, he laid the groundwork for a more intellectually diverse and socially inclusive channel of science advice at the highest levels of government. His nominees should now build a President's Council of Advisors on Science and Technology in Society, comprising not only scientists and engineers but also a more expansive range of experience to set the agenda for policy-relevant science. Expertise in advisory bodies should include, besides science, perspectives that



illuminate the social, historical, ethical, and political dimensions of technical decisions.

A second step is to bring society back into the curriculum of science education. Science and democracy harmonize best when both scientists and nonscientists learn how to participate in debates with technical components. Educational institutions must train all students—scientists included—to develop a wider imagination of the constitutional power of science to define the very terms in which we frame and debate social problems (7).

Expert elites who view the public as fully ignorant and irredeemably irrational need richer resources for understanding those who feel marginalized. Otherwise, like a self-fulfilling prophecy, policy institutions will tend to call forth the kinds of resistant citizens that they imagine they are addressing. When scientists or policy-makers insist that a policy is right because it is evidence-based, they should expect citizens to question: Who made that claim? On what authority? With what evidence? And subject to what oversight or opportunity for criticism? These are legitimate questions that enhance democracy, and our educational institutions

should teach scientists to respect them. Here, again, the president's advisers can help by placing science and society education high on the agenda.

Lastly, better dialogue between science and society requires forums where technical analysis and democratic deliberation can proceed in harmony. A wholesale appraisal of the role of such bodies in the U.S. government is long overdue, but one should note that before the present era of deregulation, government agencies consulted widely with civil society and tended to enjoy greater trust (8). Advisory bodies in both Europe and the United States have proved effective when they include a broad cross-section of the perspectives and priorities of citizens. Reviewing experience at home and abroad, the president's advisers should rebuild interactive fora where publics can freely question science, and science must give persuasive answers.

These three steps offer promise of creating common ground and achieving the legitimacy needed to guard against groundless and capricious dissent. To shore up the norms that support an enlightened society, we need to build better foundations for deliberation on the reliability and relevance of science for governance (9). In this time of national emergency, we must move beyond the distortions of the pro-science–anti-science frame and transition to more conversational relations

between science and society. It is a time for respectful partnership, not ill-informed division, between science and its publics. ■

REFERENCES AND NOTES

1. N. Florko, "Science was on the ballot: How can public health recover from a rebuke at the polls?," *STAT*, 4 November 2020.
2. S. Jasanoff, *Designs on Nature: Science & Democracy in Europe and the United States* (Princeton Univ. Press, 2005).
3. S. Jasanoff, *Droit, Sciences, Technologies* **11**, 125 (2020).
4. R. Bayer, A. Fairchild-Carrino, *Am. J. Public Health* **83**, 1471 (1993).
5. S. Jasanoff et al., "Comparative Covid response: Crisis, knowledge, politics," 12 January 2021; www.futuresforumonpreparedness.org/research.
6. S. Hilgartner, *Science on Stage: Expert Advice as Public Drama* (Stanford Univ. Press, 2000).
7. J. B. Hurlbut, *Experiments in Democracy: Human Embryo Research and the Politics of Bioethics* (Columbia Univ. Press, 2017).
8. D. P. Carpenter, *Reputation and Power: Organizational Image and Pharmaceutical Regulation at the FDA* (Princeton Univ. Press, 2010).
9. National Research Council, *Understanding Risk: Informing Decisions in a Democratic Society* (National Academies Press, 1996).

ACKNOWLEDGMENTS

We acknowledge funding from Schmidt Futures and the National Science Foundation (award nos. 2028567 and 2028585). The views expressed here are the authors' alone.

10.1126/science.abf8762

ASTROBIOLOGY

Evolution on other worlds

Bound by finite natural laws, alien life may be more familiar than we imagine

By **Adrian Woolfson**

The late Harvard biologist Stephen Jay Gould speculated that the history of life on Earth was deeply influenced by chance events (1). In a classic thought experiment, he imagined rewinding the “tape of life” back to its inception and allowing life’s history to play out again. The reemergence of humans, for example, was, in his view, a near impossibility.

Others have argued that life is more predictable and constrained. Evolution converges on the same solutions repeatedly, and its outcomes may have a certain inevitability (2). The eye, for example, has evolved multiple times in unrelated lineages.

Biologist Richard Lenski has turned Gould’s conceit into an experimental research paradigm. His artificial evolution “replay” experiments, in which identical populations of microbes are allowed to evolve in parallel for tens of thousands of generations, suggest that the truth lies somewhere in between (3).

In his entertaining and thought provoking *The Zoologist’s Guide to the Galaxy*, the Cambridge University zoologist and mathematical biologist Arik Kershenbaum—known principally for his studies of animal vocalizations—turns to astrobiology, a field concerned with the origins and persistence of life in the Universe, and provides readers with a tentative sketch of the nature of possible alien life on other potentially habitable planets. Kershenbaum assumes that evolution on other planets would likely play out in a manner recognizable to us earthlings because of the universality of the laws of physics, chemistry, and even biology and because there are a restricted number of behavioral imperatives to which all organisms are beholden. By focusing on behavior and prioritizing function over form, a generic

set of “biological rules” can be inferred. He argues that these can be universally applied to potential alien beings, because the laws should be relatively insensitive to biochemical and morphological specifics.

Like a modern-day Dr. Doolittle, Kershenbaum searches for clues about what aliens might look like and how they might communicate, by interrogating the shared strategies of the species surrounding us. While beetles, bats, and birds have different evolutionary origins and body plans, all have converged on flight as a common approach to locomotion. And while wolves and dolphins inhabit different ecological niches, both species rely on continuously varying vocalizations to avoid signal distortion when communicating across large distances.

Kershenbaum cautions against excessive anthropomorphism when attempting to evaluate potential alien communications. Human languages are impressively expressive, he concedes, but we should not assume that the electrical discharges of the South American knifefish or the disconsolate foot drumming of the kangaroo rat are not capable of encoding complex information.

Like their earthly counterparts, alien life-forms will face idiosyncratic evolutionary pressures that nevertheless channel their communication strategies in predictable directions. “On a dark, subterranean world, perhaps like the underground oceans of Enceladus, vision may be totally absent, and eyeless creatures could evolve a perfectly competent and rich communication using sound alone,” writes Kershenbaum. “Conversely,” he notes, “in the tenuous Martian atmosphere, acoustic communication just isn’t a good option.”

The fossilized bones and genome sequences of our relatives and ancient ancestors teach us that there are many different ways of being human. But if these extinct

Exotic earthbound creatures such as the short-beaked echidna offer hints about potential alien life.

species were alive today, would we afford them human rights? If yes, Kershenbaum argues, then we implicitly accept that “humans are a collection of different species.”

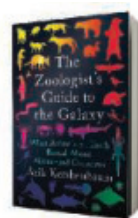
Defining a putative set of essential human features is, however, non-trivial. In situations where convergent evolution is marginalized by the imprint of historical contingency, alien morphology may deviate substantially from canonical human anatomy. Despite sharing many essential features with humans, such morphologically distinct aliens may not easily be recognizable as belonging to the extended human family.

The book’s key thesis rests on the notion that all complex life, regardless of its site of origin, is rooted in the immutable logic of evolution by natural selection. However, it does not account for the fact that there may be species that have learned to rewrite their own genomes. These species may, as such, be disconnected from their evolutionary history and less sensitive to the mandates of natural laws. In the presence of such ingenious beings, Kershenbaum’s guide might leave us lost in translation. But barring such a scenario, the author’s assertion that the unshakable prerogatives of physics, chemistry, and evolutionary biology, coupled with the omnipresent agency of convergent phenomena, offer a reasonable prospect of inferring the nature of distant alien species is compelling. ■

REFERENCES AND NOTES

1. S. J. Gould, *Wonderful Life: The Burgess Shale and the Nature of History* (Norton, 1989).
2. S. Conway Morris, *Life’s Solution: Inevitable Humans in a Lonely Universe* (Cambridge Univ. Press, 2003).
3. Z. D. Blount, R. E. Lenski, J. B. Losos, *Science* **362**, eaam5979 (2018).

10.1126/science.abe8625



The Zoologist’s Guide to the Galaxy
Arik Kershenbaum
Penguin Press,
2021. 368 pp.

HISTORY OF SCIENCE

The soul and its shell

A neurosurgeon's audacious experiments raised ire from animal rights activists and interest from the Vatican

By Susan E. Lederer

Historian Brandy Schillace's new book, *Mr. Humble and Dr. Butcher*—so titled to evoke Robert Louis Stevenson's Jekyll and Hyde—offers a probing and provocative portrait of the American neurosurgeon and neurophysiologist Robert J. White (1926–2010), whose life's ambition was to establish that the brain—the seat of consciousness, personhood, or, as a pious Catholic like White conceived of it, the human soul—could be separated from its bodily shell and even transferred to another body. Schillace, editor of BMJ's journal *Medical Humanities*, articulates the origins and outcome of White's obsession, his complex relationship with the media, and his service to several popes.

Between 1961 and his retirement from Case Western Reserve University in 1998, White oversaw the Brain Research Laboratory, where he and his colleagues pioneered techniques for isolating and maintaining the primate brain, cooling the brain for surgery, and surgically transplanting the head of the macaque monkey onto the body of another monkey. His publications in leading journals, including in *Science* in 1963 (1), earned him an international reputation and prompted fascinating collaborations and relationships.

White received visits and invitations to collaborate from Soviet researchers, including Vladimir Demikhov, whose recent work had included the surgical creation of two-headed dogs. Despite Cold War political tensions, White maintained close ties with Russian neurosurgeons and considered it a great honor to have been allowed to view Lenin's brain, preserved at the Moscow Brain Research Institute.

White liked to describe himself as a humble man. But "Humble Bob" was no

shrinking violet. In 1964, he gave his first interview to the *New York Times*, and throughout his career, he used the press to advance his ideas. In 1967, he agreed to be interviewed by Italian journalist Oriana Fallaci about his latest project, the "hot" isolation of the brain of a rhesus monkey—so called because it skipped the cooling step once considered essential to the procedure.

"The Dead Body and the Living Brain," which appeared in *Look* magazine on 28 November 1967, centered on the harrowing experience of one of White's subjects,



White's experiments took place during a shift in attitudes toward animal research.

a monkey that Fallaci named Libby, and cast White as a Frankenstein figure. White was not prepared for the firestorm that Fallaci's interview created, nor for the new nickname it would earn him—Dr. Butcher.

Schillace does a masterful job in charting the massive shift in attitudes toward animal experimentation and the emergence of animal rights in the 1960s and 1970s. But she reminds readers that White considered his experiments on monkeys to be mere rehearsals for his ultimate goal, to perform the surgery on a human being and thereby reduce human suffering.

White embraced comparisons with Mary Shelley's ambitious physician Victor Frankenstein, carrying a black doctor's bag emblazoned with the words "Dr. Frankenstein." He regarded the novel not as a cautionary tale but as a story of possibility and

Mr. Humble and Dr. Butcher: A Monkey's Head, the Pope's Neuroscientist, and the Quest to Transplant the Soul
Brandy Schillace
Simon and Schuster, 2021.
320 pp.



promise in which life might be preserved in gravely injured and catastrophically diseased human beings.

A lifelong Catholic who accepted the Church's teachings that limited ensoulment to human beings, White's professional interests intersected with the emerging debate over brain death in the late 1960s. He reasoned that the soul, being situated in the brain, was liberated in cases of brain death and thus that brain-dead individuals should be considered dead. In 1970, he was invited to Rome to advise the Pontifical Academy of Sciences and to a private audience with Pope Paul VI. He established

the Vatican's biomedical ethics commission in 1981, and the Church's stance on brain death soon shifted to be more in keeping with White's beliefs.

As White readied for retirement in the mid-1990s, he feared that he would miss his chance to complete the operation he had spent his entire career preparing for. Although he had long fantasized about performing a body transplant on Stephen Hawking, White found his "perfect patient" in Craig Vetovitz, a Cleveland man wheelchair-bound following an accident in 1971. The surgeon and his patient gave many interviews, but by this time, White no longer had

hospital privileges, nor did he have access to the funding and institutional support necessary for the extraordinary surgery or Vetovitz's rehabilitation. The much-hyped procedure would never become a reality.


White, who died in 2010 at the age of 84, did not live long enough to see the resurgence in interest in head transplantation that emerged in the past decade in the form of Italian surgeon Sergio Canavero, who promised to perform a human head transplant by 2020. As of this writing, he has not succeeded, but it may yet come true. For now, "The quest to transplant the soul continues on," writes Schillace. ■

REFERENCES AND NOTES

1. R. J. White, M. S. Albin, J. Verdura, *Science* **141**, 1060 (1963).

10.1126/science.abg1073

The reviewer is at the Department of Medical History and Bioethics, University of Wisconsin–Madison, Madison, WI 53706, USA. Email: susan.lederer@wisc.edu



The honey bee is not representative of less social bee species.

LETTERS

Edited by Jennifer Sills

Holistic environmental risk assessment for bees

In January, the European Food Safety Authority (EFSA) proposed a honey bee (*Apis mellifera*) pesticide risk assessment that uses a systems approach (1). The strategy accounts for multiple stressors and sub-lethal effects, unlike current assessments. We support this long-awaited paradigm shift for environmental risk assessment. However, the initial focus on honey bees alone is not enough to protect the majority of pollinators, nor will it help substantively address the plight of biodiversity. Therefore, EFSA should augment the approach to include more relevant species.

Although there are many socio-political, historical, and practical advantages for honey bees as a model, this bee species is an exceptional case in the bee world. Honey bee colonies are superorganisms whose social organization provides a highly resilient buffer against environmental stressors that solitary and less social bees lack. They are nurtured by beekeepers, who provide shelter, supplementary food, and disease

control. Honey bees are a good place to start, given how much we know about them and their place in the public eye, but they are simply not representative of most wild bee species that provide the bulk of pollination services. The overall bee-environment interaction would be better represented by extending the EFSA approach to more representative bee species.

Establishing which species are good analogs for modeling other, more vulnerable bee species should be prioritized. Knowledge should then be gathered for such species to allow modeling of other bee species, and ideally other non-target organisms. The environmental and toxicological context should also be modeled and monitored accurately to provide high-quality inputs to the species models. These steps would support a much more rigorous environmental risk assessment and would enhance this already long-awaited and necessary paradigm shift (2).

Christopher John Topping^{1*}, Mark Brown², Jordan Chetcuti³, Joachim R. de Miranda⁴, Francesco Nazzi⁵, Peter Neumann⁶, Robert J. Paxton^{7,8}, Maj Rundlöf⁹, Jane C. Stout³

¹Department of Bioscience, Kalø, Aarhus University, Denmark. ²Department of Biological Sciences, School of Life Sciences and the Environment, Royal Holloway, University of London, London,

UK. ³Department of Botany, School of Natural Sciences, Trinity College Dublin, Dublin, Ireland. ⁴Ekologikum, Swedish University of Agricultural Sciences, Uppsala, Sweden. ⁵Dipartimento di Scienze Agroalimentari, Ambientali e Animali, Università degli Studi di Udine, Udine, Italy. ⁶Institute of Bee Health, Vetsuisse Faculty, University of Bern, Bern, Switzerland. ⁷Institute for Biology, Martin-Luther-Universität Halle-Wittenberg, Halle (Saale), Germany. ⁸German Centre for Integrative Biodiversity Research (iDiv), Leipzig, Germany. ⁹Department of Biology, Lund University, Lund, Sweden.
*Corresponding author. Email: cjt@bios.au.dk

REFERENCES AND NOTES

1. EFSA, "Public consultation on the draft EFSA Scientific Committee Opinion on a systems-based approach to the environmental risk assessment of multiple stressors in honey bees" (2021); www.efsa.europa.eu/en/consultations/call/public-consultation-draft-efsa-scientific-committee-opinion-1.
2. C. J. Topping, A. Aldrich, P. Berry, *Science* **367**, 360 (2020).

COMPETING INTERESTS

C.J.T. is vice chair of the EFSA Panel on Plant Protection Products and their Residues, which is a scientific support to EFSA for regulatory issues for pesticides. All authors are affiliated with PoshBee (<https://poshbee.eu/>).

10.1126/science.abg9622

U.S. immigration reform for STEM doctorates

In their Policy Forum "Rethinking immigration policies for STEM doctorates" (22 January, p. 350), M. Roach and J. Skrentny suggest that U.S. immigration reform should provide an easier path to permanent residency for those who work in science, technology, engineering, and mathematics (STEM) fields and have Ph.D.s from U.S. universities. Before implementing the strategies they suggest, policy-makers should address such a program's unintended consequences.

Granting permanent residency to STEM doctorates upon graduation may stimulate educational institutions to seek STEM designations for their traditional non-STEM programs, such as business, management, and social sciences, to attract more foreign applicants. To counteract declining international applications (1), some business schools have already been working with the U.S. Department of Homeland Security to classify their MBA programs as STEM programs. This designation would make international students with F-1 visas eligible for an extended Optional Practical Training period (2), currently an extra benefit granted to STEM students only (3).

Indiscriminately expanding the scale of STEM designations could conversely result in chaotic consequences in the immigration system. Each year, there are approximately 140,000 employment-based immigrant visas made available to qualified applicants around the world (4). Granting green cards to all STEM doctorates, including those graduating from the nontraditional

STEM-designated programs such as business, management, and social science, could crowd out applicants who majored in science and engineering, potentially leading to unpredictable and long delays for all types of immigration applications. As a result, the U.S. Citizenship and Immigration Services may have to implement new rules to score and prioritize the extremely high volume of applications.

Permanent residency for STEM doctorates may also spur some universities to adopt new strategies. Of the 4034 U.S. postsecondary institutions in 2019, 736 were private for-profit institutions (5). These institutions may consider launching “accelerated” doctorate programs as a new revenue stream and lower the admission bar for students applying for these programs for the purposes of immigration. Proper oversight by accreditation agencies could ensure the continued integrity and rigor of the acceptance, supervision, and graduation of STEM doctoral students to prevent abuse of the system.

Scientific, technological, and engineering advancement is a critical foundation of U.S. competitiveness, and the talented, qualified STEM doctorates studying and working in this country are key to maintaining an edge in these fields. Thus, the proposed policy should be designed to primarily benefit those who are contributing to the traditional STEM disciplines after completing rigorous training.

Jiayang Geng

Bank of America Corporation, Jersey City, NJ 07311, USA and Whiting School of Engineering, Johns Hopkins University, Baltimore, MD 21218, USA. Email: derekgeng7@gmail.com

REFERENCES AND NOTES

1. C. Cutter, “Elite M.B.A. programs report steep drop in applications,” *Wall Street Journal* (2019).
2. U.S. Department of Homeland Security, STEM OPT Extension Overview (2016); <https://studyinthestates.dhs.gov/stem-opt-hub/stem-opt-extension-overview>.
3. M. Cheng, “Why MBA programs want to be classified as STEM studies,” QUART at WORK (2020).
4. U.S. Citizenship and Immigration Services, Permanent Workers (2020); www.uscis.gov/working-in-the-united-states/permanent-workers.
5. National Center for Education Statistics, “Number of degree-granting postsecondary institutions and enrollment in these institutions, by enrollment size, control, and classification of institution: Fall 2018” (2018); https://nces.ed.gov/ipeds/data/digest/d19/tables/dt19_31740.asp.

10.1126/science.abg8906

Brazil’s political upset threatens Amazonia

On 1 February, the Centrão coalition of political parties in Brazil, supported by President Jair Bolsonaro, gained control of

both houses of Brazil’s National Congress (1). Bolsonaro has a record of destructive environmental policies (2), but some of the pending bills that he supports were blocked by the former president of the Chamber of Deputies, Rodrigo Maia (3). Arthur Lira has now taken his position, and the legislature will now likely move to approve the bills that Maia had been blocking. This shift in power has ominous implications for Brazil’s environment and Indigenous peoples.

Shortly after the new presidents of the two houses of Congress took office, Bolsonaro sent them a list of 35 bills that he wants passed but that Maia had indicated he would block (4). Many of these bills threaten the environment. Among them is a notorious bill that would allow mining in Indigenous lands and in protected areas for biodiversity (PL 191/2020). Also included were bills to reduce environmental-licensing requirements (PL 3729/2004), offer public forest concessions to private initiatives (PL 5518/2020), reward land grabbers by promoting the legalization of illegal land claims (PL 2633/2020), and modify sharing arrangements to promote oil and gas extraction (PL 3178/2019).

Other bills on this list are likely to exacerbate Amazonian land conflicts and attacks on Indigenous and other traditional peoples. For example, PLC 119/2015 would alter the implementation of Indigenous people’s constitutional rights. PL 6438/2019 and PL 3723/2019 would further weaken gun-control laws. PL 6125/2019 would effectively give law-enforcement agents a “license to kill” by barring charges for excessive use of force.

These bills are expected to come up for a vote this year (5), at which point they are likely to pass. If they become law, they will exacerbate the effects of wood, mineral, meat, soy, natural gas, oil, and biofuel exports on deforestation in the Amazon and its associated loss of biodiversity and violation of Indigenous rights. Major importers of products from the Brazilian Amazon, such as the United States and China (6), cannot turn a blind eye to the impact of their trade with Brazil. President Bolsonaro and his supporters in the National Congress do not give much weight to the concerns of scientists and environmentalists, but they are very sensitive to international decisions that affect Brazil’s exports. Global partners should consider their trade policies accordingly.

L. Ferrante^{1*} and P. M. Fearnside²

¹National Institute for Research in the Amazon (INPA), Ecology Graduate Program, 69060-001,

Manaus, AM, Brazil. ²National Institute for Research in the Amazon (INPA), 69067-375 Manaus, AM, Brazil.

*Corresponding author.

Email: lucasferrante@hotmail.com

REFERENCES AND NOTES

1. M. Schreiber, “Arthur Lira eleito presidente da Câmara: como líder do Centrão se tornou aliado fundamental de Bolsonaro,” *BBC News Brasil* (2021). www.bbc.com/portuguese/brasil-55897146 [in Portuguese].
2. L. Ferrante, P. M. Fearnside, *Environ. Conserv.* **46**, 261 (2019).
3. A. Vital, “Maia diz a Raoni que não vai pautar projeto sobre mineração em terras indígenas,” *Câmara dos Deputados* (2019); www.camara.leg.br/noticias/590576-maia-diz-a-raoni-que-nao-vai-pautar-projeto-sobre-mineracao-em-terras-indigenas/ [in Portuguese].
4. R. Agostini, “Bolsonaro entrega a Pacheco e Lira lista com 35 projetos prioritários,” *CNN* (2021); www.cnnbrasil.com.br/politica/2021/02/03/bolsonaro-entrega-a-pacheco-e-lira-lista-com-35-projetos-prioritarios/ [in Portuguese].
5. D. Menegassi, “Mineração em Terras Indígenas, regularização fundiária e mais, entenda as prioridades de Bolsonaro para 2021,” *O Eco* (2021); www.oeco.org.br/noticias/mineracao-em-terras-indigenas-regularizacao-fundiaria-e-mais-entenda-as-prioridades-de-bolsonaro-para-2021/ [in Portuguese].
6. Trading Economics, Brazil Exports by Country (2021); <https://tradingeconomics.com/brazil/exports-by-country>.

10.1126/science.abg9786

TECHNICAL COMMENT ABSTRACTS

Comment on “Resolving spatial and energetic distributions of trap states in metal halide perovskite solar cells”

Sandheep Ravishankar, Thomas Unold, Thomas Kirchartz

Ni *et al.* (Research Articles, 20 March 2020, p. 1352) report bulk trap densities of 10^{11} cm^{-3} and an increase in interfacial trap densities by one to four orders of magnitude from drive-level capacitance profiling of lead halide perovskites. From electrostatic arguments, we show that the results are not trap densities but are a consequence of the geometrical capacitance and charge injection into the perovskite layer.

Full text: [dx.doi.org/10.1126/science.abd8014](https://doi.org/10.1126/science.abd8014)

Response to Comment on “Resolving spatial and energetic distributions of trap states in metal halide perovskite solar cells”

Zhenyi Ni, Shuang Xu, Jinsong Huang
Ravishankar *et al.* claimed that drive-level capacitance profiling (DLCP) cannot resolve trap density in perovskites of given thickness. We point out that the trap densities derived by DLCP are from the differential capacitance at different frequencies; thus, the background charges caused by diffusion and geometry capacitance have been subtracted. Even for the nondifferential doping analysis, the contribution from diffusion capacitance is negligible and that from geometry capacitance is excluded.

Full text: [dx.doi.org/10.1126/science.abd8598](https://doi.org/10.1126/science.abd8598)

PUT YOUR RESEARCH OUT IN FRONT

Submit your research:
[cts.ScienceMag.org](https://cts.sciencemag.org)

Shirley Malcom leads a sea change for STEM equity

AAAS initiative draws upon a wealth of experience in improving diversity in science

By **Andrea Korte**

As a growing chorus of voices calls for systemic change to address the systemic problems of sexism and racism in science, technology, engineering, mathematics, and medicine (STEMM), the SEA Change initiative at the American Association for the Advancement of Science aims to support educational institutions as they transform into diverse, equitable, and inclusive spaces.

SEA (STEMM Equity Achievement) Change was formally launched by AAAS in 2017 but is the culmination of a career's work in the making: that of the initiative's director, Shirley Malcom.

The initiative has its history in the Athena SWAN charter, established in the United Kingdom in 2005 to boost the ranks of women in science, but it also draws upon long-standing collaborations to diversify the scientific enterprise. When Paula Rayman was investigating a home in the United States for an adaptation of Athena SWAN, she knew that Shirley Malcom, with whom she had collaborated on diversity efforts since the 1980s, was the right person to oversee the effort.

"When Shirley decides to do something, it happens," said Rayman, who served as chair of the inaugural SEA Change Advisory Council.

Through a rigorous self-assessment process and an individualized action plan to break down barriers for marginalized people in STEMM, SEA Change "helps institutions begin to look at themselves honestly in ways that will allow them to reimagine what they are going to have to be in the 21st century in order to support all people who come to them," Malcom said.

Malcom noted that none of the institutions of higher education from which she earned degrees—University of Washington; University of California, Los Angeles; and Pennsylvania State University—set out to serve Black women. "How do you begin to identify and support people like me?" Malcom asked.

By providing a roadmap and a community, SEA Change helps institutions transform themselves to recruit, retain, and advance the full diversity of people who are captivated by science.

For Malcom, the Sputnik launch inspired her imagination as a girl growing up in Birmingham, Alabama. She was interested in science and excelled at it, but attending segregated, underresourced schools in the Jim Crow South left her underprepared for college courses at the University of Washington. She sought help from a teaching assistant—the only Black graduate student in the chemistry department—which led to improved exam scores. "I now knew that talent is developed," Malcom said in a 2020 conversation with the AAAS Member Community.

That understanding guides her work leading SEA Change today. "I'm trying to help make a way for others, not by saying there's anything wrong with them but by addressing the issues that we know to be problematic within the system itself," Malcom said.

She joined AAAS in 1975 as a research assistant inventorying programs around the country that were working to bring minorities into science. In cataloging those programs, she thought she

might find where all of the other Black women in science were, but instead she found a host of programs helping small numbers of individuals and "never rising to a level that would make a difference." Those intervention-based programs were not a long-term strategy, Malcom said, since they only focused on helping underrepresented individuals understand the system they were entering—a system that went unquestioned.

"That's one of the reasons that, now, this is so compelling to me at this stage in my career," she said. "After spending decades learning about these interventions and yearning for a systemic approach, finally there's the opportunity to help put one in place. And so that's what we have with SEA Change: something actually challenging the structure of the system itself."

Malcom went on to coauthor the first report related to women of color in STEM, published in 1976: "The Double Bind: The Price of Being a Minority Woman in Science."

The long-standing commitment at AAAS to the advancement of minority women in STEM, Malcom noted, is one reason why SEA Change broadened the Athena SWAN focus on gender to include race and intersectionality. Malcom headed the AAAS Office of Opportunities in Science between 1979 and 1989 and served as head of the AAAS Education and Human Resources directorate for nearly 30 years before becoming a AAAS adviser and director of SEA Change in 2018—a role that draws upon everything she has learned throughout her career and allows her to do what she has always wanted to do: support systemic change.

The work of changing systems is a long road, but there is much worth celebrating so far, Malcom said.

The community of SEA Change member institutions continues to grow. More and more resources are being made available, including the forthcoming launch of the Port of Call online hub for members. Three institutions earned SEA Change Bronze Awards in 2019 for the work they have already done to work toward sustainable, systemic change, and two more Institutional Bronze awardees were formally announced this month.

In a 2020 reflection on leading AAAS through social unrest in response to the continued impacts of racism and inequality, AAAS CEO Sudip Parikh called Malcom "a world-renowned leader in the conversation that we've been having for quite some time—but to which too few have paid sufficient attention."

Others are joining that conversation. Malcom sees greater visibility and awareness of the issue of sexism and racism in STEM and a steadily growing interest among decision-makers at colleges and universities in SEA Change as an avenue to effect systemic change in campus climate and culture.

She ultimately hopes to see hundreds of institutions involved, to see Bronze Award winners earn Silver and Gold Awards for higher levels of excellence, and for students and faculty to say that their institutions are truly supporting them.

"That's my dream," Malcom said.



Shirley Malcom speaks at the 2020 Emerging Researchers National Conference in Science, Technology, Engineering, and Mathematics in Washington, D.C.

RESEARCH

IN SCIENCE JOURNALS

Edited by Michael Funk



MOLECULAR MOTORS

Ciliary motors locked closed by Shulin

Motile cilia and flagella are vital cellular organelles with functions that include setting up the left-right body axis, clearing airways of mucus, and driving single-cell movements. Cilia beating is powered by arrays of dynein motors, the key force generators being the outer dynein arm (ODA) complexes. Using the protozoan *Tetrahymena*, Mali *et al.* identified a factor, which they name Shulin, that binds newly synthesized ODAs. Cryo-electron microscopy revealed how Shulin locks the dynein motors together by shutting off motor activity and facilitating delivery of ODAs from the cytoplasm to their final position in the cilia. —SMH *Science*, this issue p. 910

Scanning electron microscopy image of a freshwater ciliate, *Tetrahymena thermophila*, covered in motile cilia, which are beating cellular projections powered by the molecular motor dynein

CORONAVIRUS

Vaccine prioritization

There is likely to be high demand for the limited supplies of vaccine against severe acute respiratory syndrome coronavirus 2 (SARS-CoV-2), so how should vaccine distribution be prioritized? Bubar *et al.* modeled across countries

how uncertainty about a vaccine's characteristics affects prioritization strategies for reducing deaths and transmission (see the Perspective by Fitzpatrick and Galvani). In the model, vaccine efficacy and its ability to reduce disease and/or block transmission was accounted for in relation to age-related

variations in susceptibility, fatality rates, and immune decline. In almost all circumstances, reducing fatalities required distributing the vaccine to those who are most at risk of death, usually persons over 60 years of age and those with comorbidities. If a vaccine is leaky or poorly efficacious in older adults, then priority could

be given to younger age groups. To increase the available doses, further priority should be given to seronegative individuals. —CA

Science, this issue p. 916;
see also p. 890

ATMOSPHERIC CHEMISTRY

On the surface

The uptake and hydrolysis of N_2O_5 from the atmosphere by aqueous aerosols was long thought to occur by solvation and subsequent hydrolysis in the bulk of the aerosol. However, this mechanistic hypothesis was unverifiable because of the fast reaction kinetics. Galib *et al.* used molecular simulations to show instead that the mechanism is the inverse: Interfacial hydrolysis is followed by solvation into the interior. Their reactive uptake model is consistent with some existing experimental observations. —HJS

Science, this issue p. 921

PALEONTOLOGY

Not enough room

Modern carnivore communities include species that span a range of body sizes. For example, on the African savannah, there are small species (mongooses), medium species (wild dogs), and large species (lions). This variation reflects available prey sources that best suit each group. Carnivorous dinosaur communities, however, were missing species that fall into the middle, or mesocarnivore, group as adults. Schroeder *et al.* looked across communities, space, and time and found that this absence appears to have been driven by the distinctive biology of dinosaurs, in which giant adults start out as tiny hatchlings. Growing juvenile dinosaurs thus filled the other niches and limited trophic species diversity. —SNV

Science, this issue p. 941

GEOPHYSICS

Waiting for earthquakes to call

Instrumenting the vast ocean floor is difficult and expensive

but important for monitoring earthquakes and tsunamis. Zhan *et al.* used the polarization of regular telecommunication traffic to detect earthquakes and water swells in a 10,000-kilometer-long fiber-optic submarine cable (see the Perspective by Wilcock). The deep-water Curie cable is not as noisy as terrestrial counterparts, allowing the authors to detect strain from the cable. Results from the 9-month observation period showed how current submarine fiber-optic cables can also be used as a geophysical tool. —BG

Science, this issue p. 931;
see also p. 882

TRANSPLANTATION

A ratio to predict rejection

Current strategies to identify rejection of transplanted kidneys rely on invasive surveillance biopsies or have limited predictive value. Therefore, an early and noninvasive biomarker to predict rejection is needed. Cherukuri *et al.* characterized the ratio of interleukin-10 to tumor necrosis factor- α expressed by transitional B cells as a biomarker of early T cell-mediated allograft rejection. The authors found that this ratio predicted rejection at 3 months after transplantation in three patient cohorts, and it may be an effective biomarker that can be used clinically to tailor therapy based on risk of rejection. —CSM

Sci. Transl. Med. **13**, eabe4929 (2021).

NANO-OPTICAL WRITING

Toward next-generation optical disks

Subdiffraction information bits can be written using superresolution methods to achieve extremely high-density information storage. Using lanthanide-doped upconversion nanoparticles to locally reduce graphene oxide flakes through upconversion resonance energy transfer upon engineered illumination, Lamon *et al.* achieved an

estimated storage capacity of 700 terabytes on a 12-centimeter optical disk by nanoscale optical writing, comparable to a storage capacity of 28,000 single-layer Blu-ray disks. This technology offers an inexpensive solution for the next generation of high-capacity optical data storage and enables energy-efficient nanofabrication of flexible, graphene-based electronics. —LNL

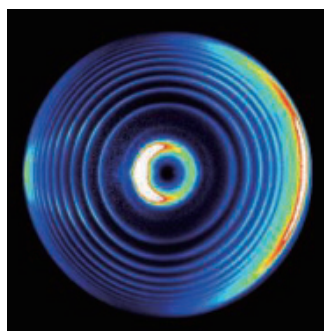
Sci. Adv. **10**, 1126/sciadv.abe2209 (2021).

CHEMICAL DYNAMICS

Intriguing dynamics pattern in F + HD

Despite decades of studies, the role of relativistic spin-orbit interactions in the dynamics of chemical reactions remains an intriguing topic. Using a high-resolution velocity map imaging crossed beams technique, Chen *et al.* observed an interesting pattern in the differential cross sections in the $F + HD \rightarrow HF + D$ reaction near the partial wave resonances (see the Perspective by Rakitzis). Further theoretical analysis showed that this pattern originates from quantum interference between spin-orbit split partial wave resonances with different total parities. The effect of the fine structure of the partial waves observed for this long known yet not completely explored three-atom system represents one more remarkable demonstration of the truly quantum nature of chemical reaction dynamics. —YS

Science, this issue p. 936;
see also p. 886



The scattering pattern for the F + HD reaction reveals the fine structure of partial waves.

IN OTHER JOURNALS

Edited by Caroline Ash
and Jesse Smith



POPULATION GENETICS

Linking phenotype with genotype

In humans, it is difficult to work out how natural selection affects phenotypic variation. With the accumulation of huge repositories of human genetic data and new computational methods, the impact of medical conditions and their evolutionary importance can be estimated. One challenge is that many complex diseases are linked to phenotypes with common and widely occurring genetic variants. Vy *et al.* predicted the overall number of deleterious genetic variants in coding proteins (known as the deleterious load) within individuals from the UK Biobank. Although overall deleterious load is not linked with any specific disease states, the authors found statistically significant associations between 27 traits and phenotypes associated with disease, including body mass, metabolic rate, and adiposity. Thus, the accumulative

effect of deleterious load might be a useful indicator for general health. —LMZ

PLoS Genet. **17**, e1009337 (2021).

EPIGENETICS

Inheriting female infertility

Polycystic ovary syndrome (PCOS) is a major cause of female infertility. It is characterized by hormonal and often metabolic dysfunction but little is understood about its etiology. For women with PCOS who do become pregnant, there is a high probability that their daughters will develop PCOS. This heritability has been proposed to arise, at least partially, if the embryos are exposed to abnormal levels of hormones. Mimouni *et al.* studied a mouse model of PCOS and found several differentially methylated genes in the ovaries of third-generation mice, indicating epigenetic-mediated heritability. Several of these genes were also differentially methylated in blood samples from mothers and



PERCEPTION

Feel the light

Octopuses have remarkable bodies that they stretch and reshape in response to the environment and to the animal's needs. How control over such flexibility is managed is an ongoing question.

Work in this area has shown that octopus arms exert a degree of individual control. Katz *et al.* found that octopus arms display a phototactic response to light, automatically withdrawing when the arm (especially the tip) is illuminated. Unlike previously described photoresponsive cells in the skin of the arms, this response appears to be both autonomic and channeled through the central nervous system. Perhaps, the authors suggest, this allows the arms to be protected from foraging predators during the day, but gives the octopus an override option during their own foraging bouts. —SNV

J. Exp. Biol. 10.1242/jeb.237529 (2021).

Each arm of an octopus is capable of an autonomous response to light to ensure that it remains hidden when predators are active.

daughters with PCOS, indicating the potential for methylation as a diagnostic biomarker. —GKA

Cell Metab.

10.1016/j.cmet.2021.01.004 (2021).

THIN FILMS

Ionic liquids assist in vacuum

Molecular layer deposition, an analog of atomic layer deposition, alternates self-limiting reactions to grow materials such as polymers. However, the vacuum conditions in practice generally limit the choices to polymers in which the barrier to reaction is low without solvent assistance, such as those with thionyl or acyl backbones. Shi and Bent show that an ionic liquid, 1-ethyl-3-methylimidazolium, can create a solvation environment for the Friedel-Crafts reaction in vacuum. This ionic liquid did not evaporate at reaction temperatures, wetted a silicon substrate, and formed a eutectic with the $AlCl_3$ catalyst. The authors alternated deposition of isophthaloyl

dichloride and diphenyl ether along with the catalyst to grow polyetherketoneketone thin films at a rate of about 5.5 angstroms per reaction cycle. —PDS

ACS Nano 10.1021/acsnano.0c09329 (2021).

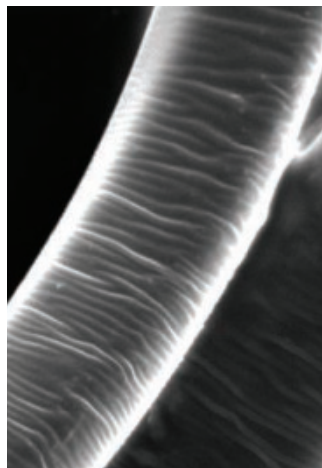
MATERIALS SCIENCE

Robust water-repellant fabrics

Materials that aggressively repel water are useful for protective fabrics and self-cleaning surfaces. However, it can be challenging to make coatings on woven fabrics that can resist rubbing and frequent washing cycles without using fluorinated molecules. Drawing inspiration from earthworms, which have wrinkled skins, Xu *et al.* created a similar surface texture on poly(ethylene terephthalate) fabric coating with poly(dimethylsiloxane) (PDMS). The PDMS is treated with an argon plasma, leading to the formation of cross links that have a graduated

depth concentration profile. This causes the PDMS surface to wrinkle, which leads to water repellence. The fabrics could survive hundreds of washing or rubbing cycles, and damage to the PDMS could be repaired using heat or further argon plasma treatment. —MSL

ACS Appl. Mat. Interfaces 13, 6758 (2021).



Wrinkled poly(ethylene terephthalate)-coated fibers can make durable, water-repellent fabrics.

WORKFORCE

The chemistry of inequality

More and more data on the issues surrounding diversity and inclusion in STEM are surfacing. Stockard *et al.* contribute to these data by providing evidence of inequities in experiences and career plans of doctoral students in chemistry. Using mixed-model regression analyses, they show that graduate students identifying as part of a traditionally underrepresented group were less likely to report supportive relationships with peers and postdocs. Women were less likely to (i) report supportive relationships with advisers, (ii) commit to remaining in chemistry, and (iii) aspire to academic research careers. Overall, the results suggest that the reality for traditionally underrepresented graduate students remains full of subtle obstacles, which are likely not specific to the chemistry field, that continue to impede efforts toward a diverse and inclusive scientific workforce. —MMc

Proc. Natl. Acad. Sci. U.S.A. 118, e2020508118 (2021).

SIGNAL TRANSDUCTION

Signaling for stress

Guanosine triphosphatase-activating protein-binding proteins called G3BP1 and G3BP2 function as a core component of stress granules. Stress granules are dynamic assemblages of ribonucleoproteins that form in distressed cells found in tumors or neurodegenerative disease states. G3BP1 also has an unexpected role in tethering the tuberous sclerosis complex (TSC) of proteins to lysosomes. At the lysosome, the TSC regulates a key metabolic regulator called mTORC1. Prentzell *et al.* detected G3BP1 in a screen for proteins that interact with mTORC1. If G3BP1 levels are low, then mTORC1 becomes hyperactive, stimulating cell motility in tumors or neuronal hyperactivity, which could be bad news for patients. —LBR

Cell 184, P655 (2021).

REVIEW SUMMARY

NEURODEGENERATION

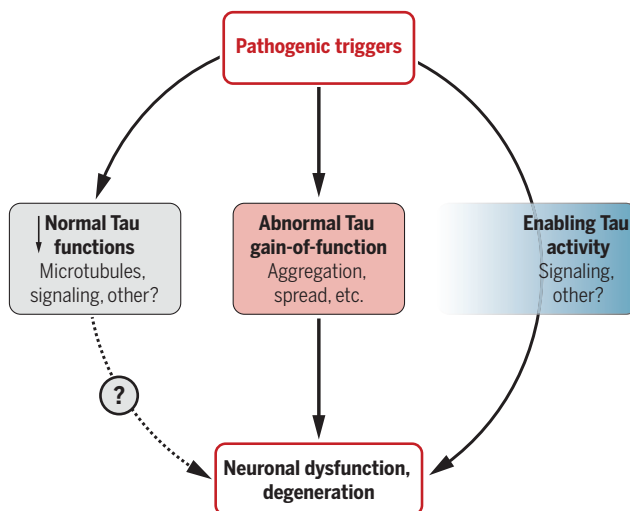
Tau: Enabler of diverse brain disorders and target of rapidly evolving therapeutic strategies

Che-Wei Chang, Eric Shao, Lennart Mucke*

BACKGROUND: The microtubule-associated protein tau has been implicated in the pathogenesis of Alzheimer's disease and a range of other neurodegenerative disorders (called "tauopathies"). As the number of people with tauopathies is rising in aging populations across the world, interest in the fundamental biology of this protein and in the development of tau-targeting treatments has been expanding rapidly. Recent insights into the complexity of this intrinsically disordered protein suggest that tau is a worthy but challenging target whose multifaceted nature will likely require a multi-pronged therapeutic approach. Derived from a single gene by alternative splicing, six major isoforms of tau have been identified in the human brain. In addition, tau is subject to many different posttranslational modifications, further indicating that it may be regulated by multiple processes and may participate in diverse functions.

ADVANCES: Tau is widely presumed to stabilize microtubules. However, the experimental reduction or ablation of tau in vivo does not alter many neural properties and processes that likely depend on microtubules, including neuronal integrity, axonal transport, synapse formation, and complex brain functions. Although tau reduction seems to have minimal effects on otherwise unmanipulated brains, it can prevent or diminish aberrant cell signaling, neural network dysfunctions (e.g., epileptic activity), and behavioral alterations caused by diverse disease processes, which suggests that tau activities are needed for other pathogenic triggers to cause these derangements. In addition to this "enabling bystander" role, tau's interactions with a large number of other proteins can cause adverse gains of function, which are associated with—and possibly caused by—the formation of abnormal tau structures and assemblies. Because abnormal forms of tau trigger a plethora of pathomechanisms, targeting individual downstream mechanisms may have limited ther-

apeutic impact, unless the relative pathogenic importance of the specific mechanism has been well established in experimental models that allow for conclusive validation of cause-and-effect relationships. Although much attention has focused on the abnormal aggregation of tau in tauopathies and on the ability of tau "seeds" to spread from neuron to neuron, internalization of propagating tau does not appear to impair neuronal survival or brain



Potential tau pathomechanisms. Developing effective tau-targeting therapeutics will require a better understanding of how exactly tau contributes to Alzheimer's disease and other disorders of the central nervous system. Potential mechanisms likely fall into the three broad categories shown. However, the relative pathogenic impact and overall importance of individual mechanisms have yet to be defined in truly disease-relevant contexts and may differ among diseases and even patients. The blue box on the right indicates tau activities that do not directly mediate but indirectly promote or facilitate pathogenic processes.

functions. Moreover, tau reduction prevents or diminishes neural network dysfunction and behavioral abnormalities also in disease models that do not have abnormal tau inclusions, which suggests that there is more to tau than aggregation and propagation. A promising diversification of tau-targeting therapeutic strategies is beginning to address this complexity. Lowering overall tau levels may have the greatest potential, as this strategy bypasses the unresolved questions of which forms of tau and which downstream

mechanisms are most detrimental in any given condition.

OUTLOOK: Many efforts to develop better treatments for neurodegenerative diseases have failed, in large part because of an inadequate understanding of disease mechanisms and, perhaps, because too many fundamental knowledge gaps, alternative interpretations of data, and methodological complexities did not receive the attention they deserved. This Review highlights important gaps in the understanding of tau and the methodological advances needed to fill them. It also pinpoints obstacles that could complicate the translation of tau-related scientific discoveries into better therapeutics and offers pragmatic strategies to overcome these challenges. Despite the extraordinary progress that has been made to date, the main physiological functions that tau fulfills in the adult and aging brain remain to be defined. Another critical objective is to develop better experimental models and technologies to rigorously compare different tau species and pathomechanisms, particularly their relative impacts on neuronal functions and survival in vivo. For the development of truly informative biomarkers and effective therapeutics, it will be critical to rigorously differentiate between associations and cause-and-effect relationships. Until the main drivers of neuronal dysfunction and demise have been identified for Alzheimer's disease and other conditions in which tau has a causal or enabling role, it seems prudent to focus on pragmatic strategies, such as overall tau reduction, while also expanding efforts to further validate the importance of more-specific targets and approaches. Investigational approaches to lower overall tau levels include tau-targeting antisense oligonucleotides, which have advanced into a clinical trial for early Alzheimer's disease, and the development of small-molecule drugs that can modulate the production or degradation of tau. The most desirable tau-targeting therapeutics would be efficacious across diverse tauopathies,

as well as affordable, easy to access, and well tolerated when administered over long periods of time to fragile groups of people who likely take multiple other medications. ■

The list of author affiliations is available in the full article online.

*Corresponding author. Email: lennart.mucke@gladstone.ucsf.edu

Cite this article as C.-W. Chang et al., *Science* 371, eabb8255 (2021). DOI: 10.1126/science.abb8255

S READ THE FULL ARTICLE AT
<https://doi.org/10.1126/science.abb8255>

RESEARCH ARTICLE SUMMARY

LINEAGE TRACING

Proliferation tracing reveals regional hepatocyte generation in liver homeostasis and repair

Lingjuan He*, Wenjuan Pu*, Xiuxiu Liu*, Zhenqian Zhang, Maoying Han, Yi Li, Xiuzhen Huang, Ximeng Han, Yan Li, Kuo Liu, Mengyang Shi, Liang Lai, Ruilin Sun, Qing-Dong Wang, Yong Ji, Jan S. Tchorz, Bin Zhou†

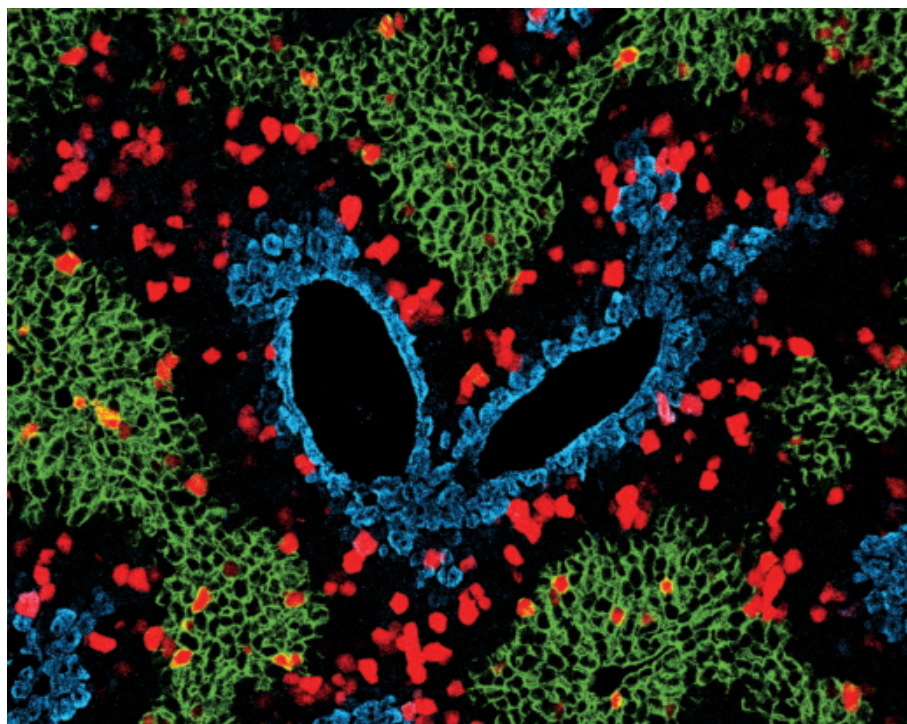
INTRODUCTION: Cell proliferation is a fundamental process in all multicellular organisms that is required to enable development, tissue homeostasis, tissue repair, and tissue regeneration. Disrupted proliferation is the pathogenic basis of many diseases. The ability to monitor cell proliferation has been essential for a myriad of studies in developmental biology, oncology, immunology, neuroscience, and regenerative medicine. The limitations of current approaches for measuring cell proliferation in vivo have left many fundamental questions in numerous life science fields insufficiently addressed. For example, decades of research have resulted in a controversial debate around zonal hepatocyte proliferation in liver homeostasis, repair, and regeneration.

RATIONALE: To provide a high-spatiotemporal resolution examination of in vivo cell proliferation,

we take advantage of two orthogonal, site-specific recombinases (Cre and Dre) to develop a genetic proliferation lineage tracing method—proliferation tracer (ProTracer). ProTracer enables the temporally continuous recording of cell proliferation events with high spatial resolution in specific cell lineages. Highlighting its capabilities, we provide insights into the regional proliferation of adult mouse hepatocytes, which are heterogeneous in gene expression and function. Previous conflicting studies identifying hepatocytes with superior proliferative capacity have mostly relied on the lineage tracing of a subset of cell populations, thereby introducing a potential selective bias. Whether a specific population of hepatocytes with increased proliferative capacity exists remains unclear. Rather than tracing only a subset of the whole hepatocyte population, an unbiased assessment of proliferation events in the entire hepatocyte pool over time is needed to address this fundamental question.

RESULTS: After an initial pulse treatment of tamoxifen, ProTracer permits the temporally continuous genetic recording of in vivo cell proliferation in diverse cell lineages over time in multiple organs and tissues. Using a hepatocyte-specific promoter, ProTracer could be primed to specifically record proliferation in hepatocytes—and not any other cell lineages—in the mouse liver. Furthermore, ProTracer enables noninvasive, long-term monitoring of hepatocyte proliferation over time in live animals. Cell proliferation tracing revealed that, at the whole hepatocyte-population level, more proliferation was detected in a subset of midzonal hepatocytes during liver homeostasis, with less proliferation in periportal hepatocytes and minimal proliferation in pericentral hepatocytes. Clonal analysis showed that most of the hepatocytes labeled by ProTracer have undergone cell division. Additionally, a highly regional and dynamic hepatocyte generation pattern was observed during repair and regeneration in response to several liver injuries, such as partial hepatectomy, bile duct ligation, and carbon tetrachloride-induced liver injury. Furthermore, genetic tracing of the proliferation of other cell lineages by ProTracer revealed distinct cell proliferation dynamics of macrophages, biliary epithelial cells, endothelial cells, and hepatic stellate cells after partial hepatectomy.

CONCLUSION: Our work provides a genetic system for the cumulative recording of cell type-specific proliferation in vivo. By genetically tracing the proliferation events of entire cell populations, ProTracer enables the unbiased detection of the specific cell population that mainly accounts for tissue homeostasis, repair, and regeneration. ProTracer reveals highly regional proliferation in midzonal hepatocytes, showing its greater contribution to maintaining the hepatocyte pool during liver homeostasis. Additionally, ProTracer revealed highly regional hepatocyte generation during liver repair and regeneration after injuries. Future applications and further iterations of ProTracer could substantially advance our understanding of cell generation and their dynamics in development, growth, regeneration, and diseases in multiple organs. ■



Highly regional hepatocyte generation in adult liver during tissue homeostasis. Immunostaining for E-cadherin (E-CAD) (green), glutamine synthetase (GS) (blue), and tdTomato (red; ProTracer signal) on liver sections of hepatocyte-specific ProTracer mice. Hepatocyte proliferation events (tdTomato⁺) genetically recorded by ProTracer are highly enriched in the E-CAD⁺GS[−] midlobular zone during liver homeostasis.

The list of author affiliations is available in the full article online.

*These authors contributed equally to this work.

†Corresponding author. Email: zhoubin@sibs.ac.cn

Cite this article as L. He *et al.*, *Science* 371, eabc4346 (2021). DOI: 10.1126/science.abc4346

S READ THE FULL ARTICLE AT
<https://doi.org/10.1126/science.abc4346>

RESEARCH ARTICLE SUMMARY

LINEAGE TRACING

Liver homeostasis is maintained by midlobular zone 2 hepatocytes

Yonglong Wei, Yunguan G. Wang, Yuemeng Jia, Lin Li, Jung Yoon, Shuyuan Zhang, Zixi Wang, Yu Zhang, Min Zhu, Tripti Sharma, Yu-Hsuan Lin, Meng-Hsiung Hsieh, Jeffrey H. Albrecht, Phuong T. Le, Clifford J. Rosen, Tao Wang, Hao Zhu*

INTRODUCTION: The liver's remarkable capacity to maintain proper tissue mass after injury has been known since ancient times. However, there has been considerable debate about the source of new liver cells that contribute to tissue growth, maintenance, and regeneration. Multiple studies have reported that disparate cell populations in the liver serve as rare stem cells, whereas others have proposed that most hepatocytes are similar in their regenerative activity regardless of position or function. Although hepatocytes appear histologically homogeneous, the liver lobule is actually organized into concentric zones, or rings, in which hepatocytes express different metabolic enzymes across the portal vein-to-central vein axis through which blood flows. Recently, single-cell profiling has enriched our understanding of the extraordinary diversity of hepatocytes, but this "zonal" heterogeneity has not been functionally interrogated in the context of tissue homeostasis, because the critical genetic labeling tools have not been available.

RATIONALE: Previous efforts to identify the most-regenerative hepatocytes have not definitively resolved fundamental questions about whether

regenerative activity is spatially restricted within particular zones or whether rare or common subsets of hepatocytes are responsible. This uncertainty was in part because fate mapping had only been performed on a few hepatocyte subsets and without side-by-side comparisons. We sought to systematically address fundamental questions about the source of new liver cells by generating a panel of 11 new *CreER* knock-in mouse models that label zonal subpopulations across the liver lobule. By using these tools in tandem with three existing *CreER* lines, tissue maintenance and regeneration as a function of zonal position were assessed.

RESULTS: In contrast to the idea that all hepatocytes across the lobule contribute equally to regeneration, we identified major differences between hepatocytes from different locations. During steady-state homeostasis, zone 1 cells near the portal vein decreased in number over time, as did zone 3 cells near the central vein on the opposite end of the lobule. However, midlobular zone 2 hepatocytes marked by the hepcidin antimicrobial peptide 2 (*Hamp2*) gene were in large part responsible for homeostatic repopulation. Zone 2 cells were also sheltered

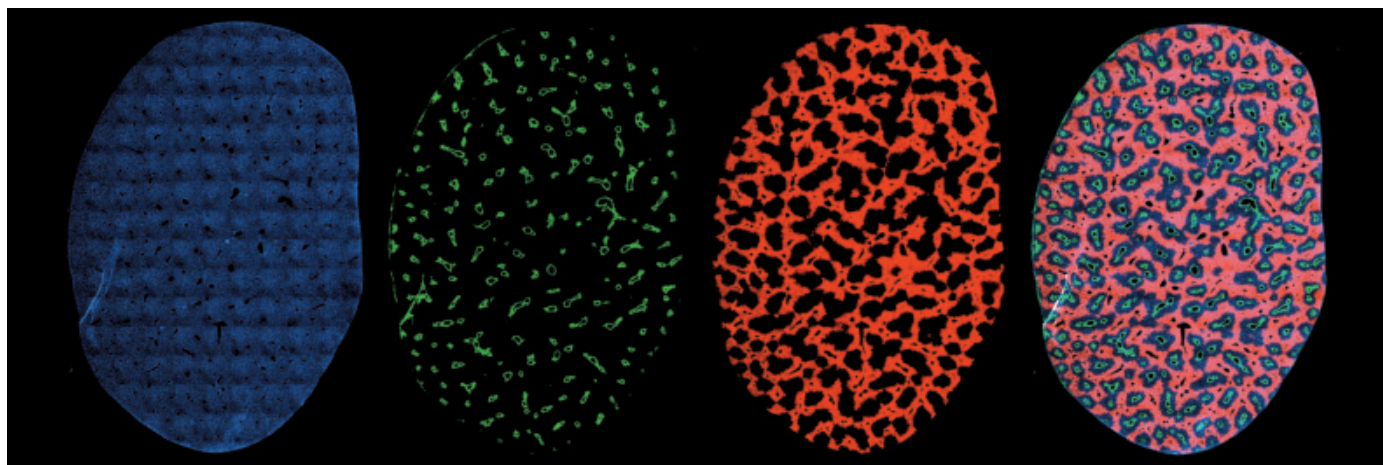
from toxic injuries affecting either end of the lobule and thus were well positioned to contribute to regeneration after these insults. To define the mechanistic basis of these lineage-tracing results, single-cell and bulk RNA sequencing transcriptomics were used to define genes that were specifically up- or down-regulated in zone 2. We then used in vivo CRISPR knock-out and activation screening to identify functionally important pathways that regulate zone 2 proliferation. These methods revealed that zone 2 repopulation is driven by the insulin-like growth factor binding protein 2-mechanistic target of rapamycin-cyclin D1 (IGFBP2-mTOR-CCND1) axis.

CONCLUSION: Different regions of the liver lobule exhibit differences in their contributions to hepatocyte turnover, and zone 2 is an important source of new hepatocytes during homeostasis and regeneration. These results challenge the idea that stem cells near the portal or central veins have the highest rates of liver repopulation, but they also support the principle that there are important zonal differences in hepatocyte biology. This study reconciles findings from multiple groups and offers a more unified view of hepatocyte repopulation. The identification of zone 2 hepatocytes as a regenerative population has far-reaching implications for the cellular basis of chronic disease pathogenesis, cancer development, and regenerative medicine strategies. ■

The list of author affiliations is available in the full article online.

*Corresponding author. Email: hao.zhu@utsouthwestern.edu
Cite this article as Y. Wei *et al.*, *Science* **371**, eabb1625 (2021). DOI: 10.1126/science.abb1625

S READ THE FULL ARTICLE AT
<https://doi.org/10.1126/science.abb1625>



Fate-mapping strains label different zones across the liver lobule. Cross-sectional images of a liver lobe from a glutaminase 2 (*Gls2*)-*CreER* reporter mouse in which hepatocytes from different metabolic zones are labeled. Panels from left to right: (i) 4',6-diamidino-2-phenylindole (DAPI) staining (blue) of cell nuclei, (ii) glutamine synthetase staining (green) of hepatocytes adjacent to central veins, (iii) Tomato fluorescence (red) that labels *Gls2*-expressing hepatocytes in zone 1, and (iv) a merged composite image of all three channels. This reporter strain is one of 14 used to track metabolically heterogeneous hepatocytes in the liver. Collectively, these strains were used to understand the regenerative capacity of different liver cell subtypes under homeostatic and injury conditions.

RESEARCH ARTICLE SUMMARY

CORONAVIRUS

Afucosylated IgG characterizes enveloped viral responses and correlates with COVID-19 severity

Mads Delbo Larsen*, Erik L. de Graaf*, Myrthe E. Sonneveld*, H. Rosina Plomp, Jan Nouta, Willianne Hoepel, Hung-Jen Chen, Federica Linty, Remco Visser, Maximilian Brinkhaus, Tonči Šuštić, Steven W. de Taeye, Arthur E. H. Bentlage, Suvi Toivonen, Carolien A. M. Koeleman, Susanna Sainio, Neeltje A. Kootstra, Philip J. M. Brouwer, Chiara Elisabeth Geyer, Ninotska I. L. Derksen, Gertjan Wolbink, Menno de Winther, Rogier W. Sanders, Marit J. van Gils, Sanne de Bruin, Alexander P. J. Vlaar, Amsterdam UMC COVID-19 biobank study group, Theo Rispens, Jeroen den Dunnen, Hans L. Zaaijer, Manfred Wuhrer, C. Ellen van der Schoot, Gestur Vidarsson†

INTRODUCTION: Antibody function is often considered static and mostly determined by isotype and subclass. The conserved N-linked glycan at position 297 in the Fc domain of immunoglobulin G (IgG) is essential for an antibody's effector functions. Moreover, this glycan is highly variable and functionally relevant, especially for the core fucose moiety. IgG lacking core fucosylation (afucosylated IgG) causes increased antibody-dependent cellular cytotoxicity (ADCC) through highly increased IgG-Fc receptor IIIa (FcγRIIIa) affinity. Despite constant levels of total plasma IgG-Fc fucosylation above 90%, specific IgG responses with

low core fucosylation have been sporadically reported. These are directed against alloantigens on blood cells and glycoproteins of HIV and dengue virus. In this study, we investigated the induction of afucosylated IgG to various antigens and delineated its dynamics and proinflammatory potential in COVID-19.

RATIONALE: Afucosylated IgG responses have only been found in various alloimmune responses against cellular blood groups and two enveloped viruses. Therefore, we tested the hypothesis that foreign surface-exposed, membrane-embedded proteins induce a spe-

cific B cell response that results in afucosylated IgG. We compared immune responses to natural infections by enveloped viruses and non-enveloped viruses, protein subunit vaccination, and live attenuated virus vaccinations. We also assessed the relation to the clinical outcome of such a response in COVID-19.

RESULTS: Analogous to blood cell alloantigens, the response to all enveloped viruses showed clear signatures of afucosylation of the antigen-specific IgG. By contrast, IgG against the non-enveloped virus, parvovirus B19, were highly fucosylated. The extent of afucosylated IgG responses varied, both between individuals and between antigens. The viral context was essential to induce afucosylated IgG because induction did not occur after subunit vaccination against hepatitis B virus. However, afucosylated IgG responses were found in response to attenuated viruses. Severe acute respiratory syndrome coronavirus 2 (SARS-CoV-2)-specific afucosylated IgG were also found in critically ill COVID-19 patients but not in individuals with mild symptoms. Over the 2 weeks after seroconversion, the amount of fucosylated anti-SARS-CoV-2 IgG increased markedly, in most reaching relative levels similar to those found in total IgG. Afucosylated IgG promoted interleukin-6 (IL-6) release in macrophages cultured in vitro, which is in line with an observed association of SARS-CoV-2-specific IgG afucosylation with IL-6 and C-reactive protein (CRP) in these patients.

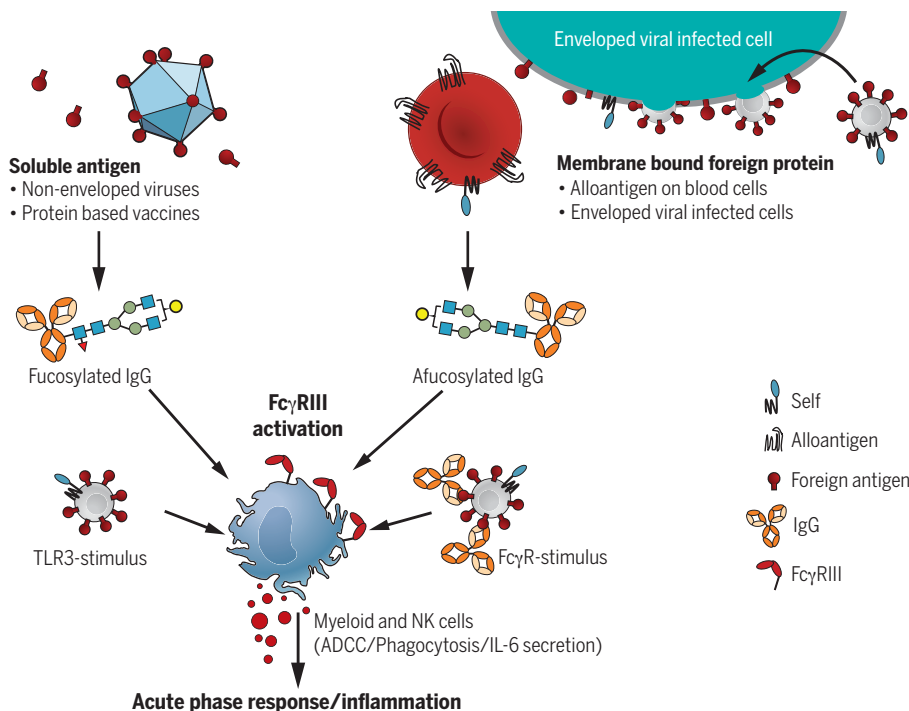
CONCLUSION: This work suggests that providing foreign B cell antigens in the context of host cells may be required to trigger an afucosylated IgG immune response. The strength of this response is highly variable for different antigens and between individuals. An afucosylated IgG response is a potent immune response, honed for the destruction of target cells by FcγRIII-expressing natural killer (NK) and myeloid cells. This may sometimes be desirable—for example, against HIV—and can be achieved in vaccines by providing the target as a surface protein, as is the case with attenuated viral vaccines or mRNA vaccines. However, for SARS-CoV-2, this afucosylated IgG response may promote the exacerbation of COVID-19 under conditions with high viral loads at the time of seroconversion. ■

The list of author affiliations is available in the full article online.
*These authors contributed equally to this work.

†Corresponding author. Email: g.vidarsson@sanquin.nl

This is an open-access article distributed under the terms of the Creative Commons Attribution license (<https://creativecommons.org/licenses/by/4.0/>), which permits unrestricted use, distribution, and reproduction in any medium, provided the original work is properly cited.
Cite this article as M. D. Larsen et al., *Science* 371, eabc8378 (2021). DOI: 10.1126/science.abc8378

READ THE FULL ARTICLE AT
<https://doi.org/10.1126/science.abc8378>



Afucosylated IgG response requires membrane context and results in strong FcγRIII-mediated activity.

Only membrane association on host cells endows foreign antigens to trigger the B cell receptor in the context of other self receptors, leading to an afucosylated IgG response. The elevated FcγRIII binding and activity of afucosylated IgG can in some cases be protective, but for SARS-CoV-2, this triggers excessive inflammation during a natural infection.

RESEARCH ARTICLE SUMMARY

3D GENOMICS

In situ genome sequencing resolves DNA sequence and structure in intact biological samples

Andrew C. Payne*, Zachary D. Chiang*, Paul L. Reginato*, Sarah M. Mangiameli, Evan M. Murray, Chun-Chen Yao, Styliani Markoulaki, Andrew S. Earl, Ajay S. Labade, Rudolf Jaenisch, George M. Church, Edward S. Boyden†‡, Jason D. Buenrostro†‡, Fei Chen†‡

INTRODUCTION: Genomes are spatially organized across length scales from single base pairs to whole chromosomes. This organization is thought to regulate gene expression and control cellular function and varies across cells within organisms. Current methods based on DNA sequencing achieve genome-wide coverage with base-pair resolution but lack spatial context. Alternatively, current methods based on imaging capture spatial context but are targeted and lack base-pair resolution. Thus, a method bridging sequencing and imaging modalities for mapping genome structure is lacking.

RATIONALE: Here, we describe in situ genome sequencing (IGS), a method for simultaneously sequencing and imaging genomes within intact biological samples. Sequencing enables parental alleles and repetitive elements to be distinguished and included in genomic analyses.

Further, imaging enables genome-wide study of spatial relationships within cells, such as association of genomic loci with nuclear structures, and between cells, such as structural similarities within cell lineages.

RESULTS: We applied IGS to cultured human fibroblasts and intact early mouse embryos at the pronuclear stage 4 zygote, late two-cell, and early four-cell stages of development, spatially localizing hundreds to thousands of DNA sequences in individual cells. In embryos, we integrated genotype information and immunostaining to identify and characterize parent-specific changes in genome structure between embryonic stages, including parental genome mixing, chromosome polarization, and nuclear lamina association. We further uncovered and characterized single-cell domain structures with lamina-distal boundaries and lamina-proximal interiors in paternal zygotic pronuclei. Finally,

we demonstrated epigenetic memory of global chromosome positioning within clonal cell lineages of individual embryos.

CONCLUSION: IGS unifies sequencing and imaging of genomes, offering a method that connects DNA sequences to their native spatial context within and between the cells of intact biological samples. The single-cell domain structures that we observed in zygotes open opportunities for further investigation, including addressing questions about how nuclear structures such as the lamina may modulate the epigenetic or intrinsic domain-forming behaviors of chromatin. Additionally, our observation of epigenetic memory of chromosome positioning highlights how genome organization during mitosis may influence genome structure at later stages of development. We anticipate that further development of IGS and integration with existing in situ molecular profiling technologies will provide increased resolution and enable multiomic measurements, creating new opportunities to study the structure and function of genomes across length scales and organisms. ■

The list of author affiliations is available in the full article online.

*These authors contributed equally to this work.

†These authors contributed equally to this work.

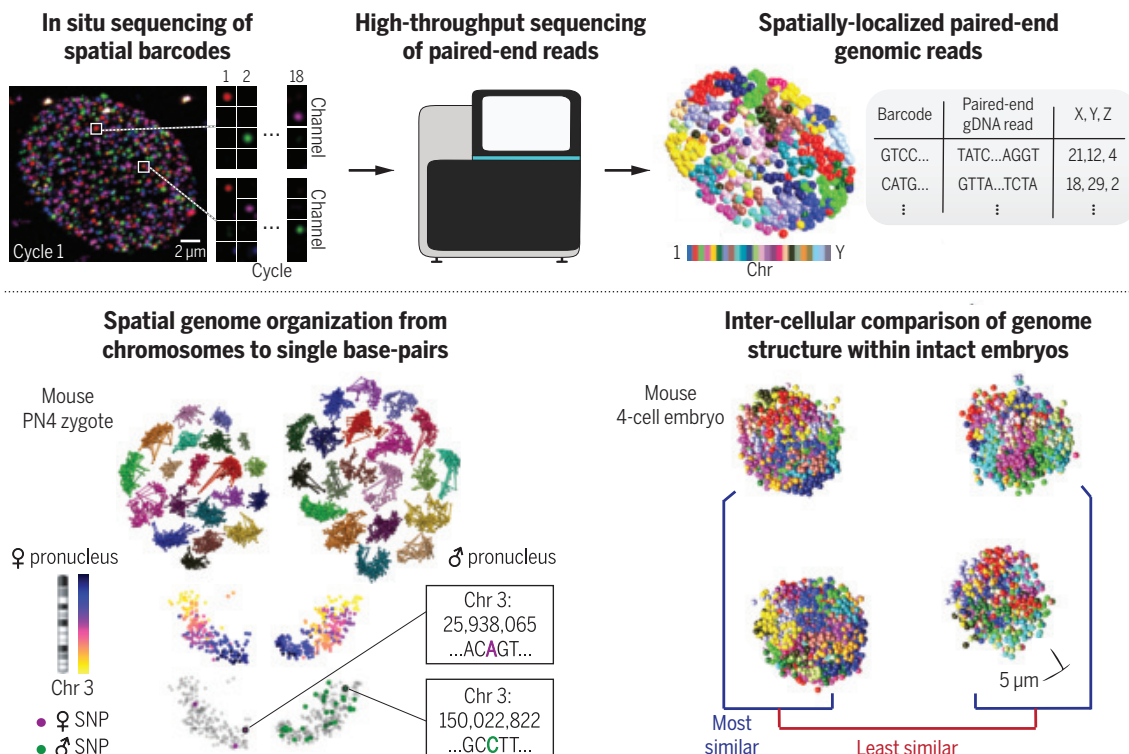
‡Corresponding author. Email: edboyden@mit.edu (E.S.B.); jason_buenrostro@harvard.edu (J.D.B.); chenf@broadinstitute.org (F.C.)

Cite this article as: A. C. Payne *et al.*, *Science* **371**, eaay3446 (2021). DOI: 10.1126/science.aay3446

READ THE FULL ARTICLE AT
<https://doi.org/10.1126/science.aay3446>

IGS unifies sequencing and imaging of genomes.

In situ sequencing of spatial barcodes within intact samples is followed by high-throughput paired-end sequencing. Data from the two modalities are computationally integrated, yielding spatially localized paired-end genomic reads. IGS in early mouse embryos enables the identification of chromosome territories that are assigned to parent-of-origin using base-pair-resolved genotype information. By preserving spatial organization in multicellular samples, IGS allows intercellular comparison of genome structure within individual embryos.



RESEARCH ARTICLE SUMMARY

CANCER GENOMICS

Single-cell lineages reveal the rates, routes, and drivers of metastasis in cancer xenografts

Jeffrey J. Quinn*, Matthew G. Jones*, Ross A. Okimoto, Shigeki Nanjo, Michelle M. Chan, Nir Yosef†, Trevor G. Bivona†, Jonathan S. Weissman†

INTRODUCTION: Cancer progression is fundamentally an evolutionary process, involving multiple distinct steps from oncogenic transformation to metastatic dissemination to development of therapeutic resistance. Defining the timing and molecular nature of each step in this process is critical to understanding cancer biology and to devising effective therapeutic strategies. Yet, it is challenging to directly observe these events because they unfold stochastically, in rare subpopulations of cells, and over long time scales.

RATIONALE: By reconstructing the phylogenetic relationships of tumor cells, it is possible to infer important features of these abstruse, past events, such as the timing or directionality of

metastatic dissemination. Advances in Cas9-based molecular recording technologies have now enabled the high-resolution mapping of subclonal cellular lineages that, when paired with single-cell RNA sequencing, can be used to infer distant events in a cell's past history and connect them to its present state.

RESULTS: We refined and applied our Cas9-based lineage recorder to study metastatic dissemination in implanted tumor cells in a mouse. These advances allowed us to resolve deep and accurate single-cell lineages for tens of thousands of metastatically disseminated cancer cells in a mouse over 2 months of growth.

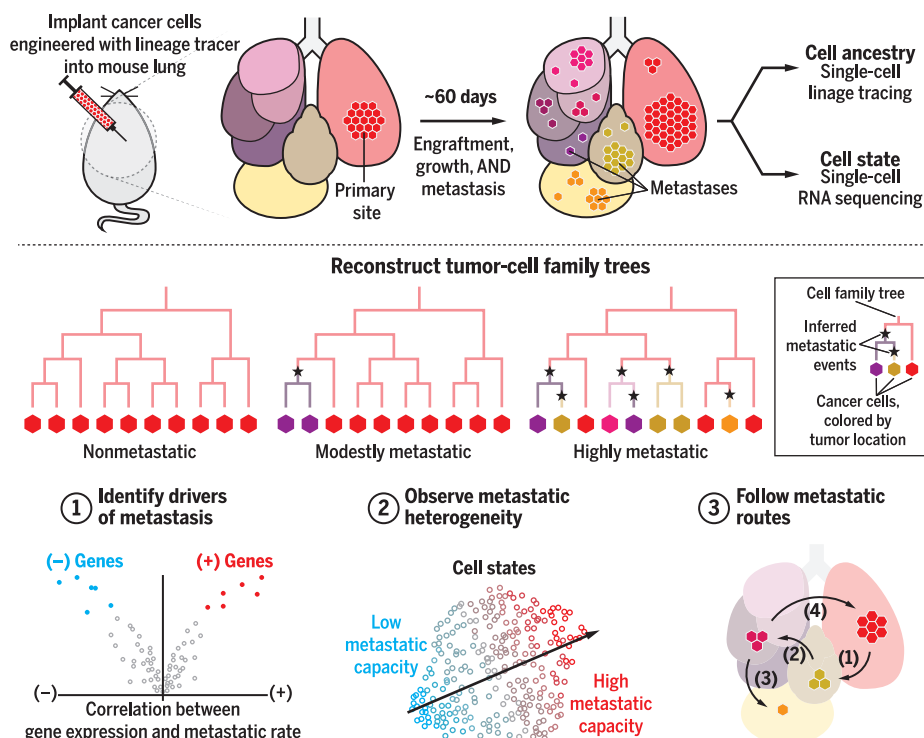
We leveraged the reconstructed phylogenetic trees to measure the frequency of metastatic

dissemination at single-cell resolution. Unexpectedly, we found that tumors arising from individual implanted cancer cells showed dramatic differences in their capacity to spread to distant tissues, ranging from completely non-metastatic (i.e., never leaving the primary site) to aggressively metastatic (i.e., frequently transiting between tissues). We paired this high-resolution lineage information with single-cell RNA sequencing to reveal characteristic sets of genes that underlie these divergent metastatic phenotypes. This analysis identified some genes that are known to modulate metastatic phenotype in lung cancers (such as *ID3* and *REG4*) and others that were unexpected (such as *KRT17*). Using CRISPR-based perturbations in two distinct lung cancer cell lines, we validated that over- or underexpression of genes identified by this analysis was sufficient to modulate cancer invasion phenotypes.

We then showed that the diversity of metastatic phenotypes observed in vivo stemmed from preexisting, heritable cellular states. Specifically, the heterogeneity in the expression of metastasis-associated genes existed before implantation into the mice, and cells with higher metastatic transcriptional signatures preimplantation went on to be more metastatic in vivo. Moreover, when cells from the same clone were implanted into different mice, they exhibited nearly identical metastatic behavior.

Finally, we traced the complex and multidirectional routes through which the metastases disseminated from tissue to tissue and identified the mediastinal lymphatic tissue as a transit hub for metastasis. We also found numerous examples of different seeding topologies, including reseeding (i.e., cancer cells returning to the primary tumor site from a metastasis) and seeding cascades (multistep metastatic seeding).

CONCLUSION: High-resolution lineage recording of tumor cells revealed a rich diversity of metastatic phenotypes and behaviors that would have otherwise been unobservable. This illuminated aspects of cancer biology that are essential to understanding disease progression, such as the rates, tissue routes, and transcriptional drivers of metastasis. We anticipate that our approach will be broadly applicable to future studies of other aspects of cancer biology, such as the evolution of drug resistance, and, more generally, of biological processes that unfold over many cell generations. ■



Exploring metastatic biology by tracing the lineages of engineered cancer cells implanted into mouse lungs. From cell ancestry information, we reconstructed high-resolution family trees of metastatically disseminated tumor cells and found populations with diverse metastatic behaviors. Pairing cell-state information with these lineages, we identified genes that drive metastatic capacity (1), observed heterogeneous metastatic states (2), and followed the tissue routes of metastatic dissemination (3).

The list of author affiliations is available in the full article online.
*These authors contributed equally to this work.

†Corresponding authors. Email: weissman@wi.mit.edu (J.S.W.); trever.bivona@ucsf.edu (T.G.B.); niriyosef@berkeley.edu (N.Y.)

Cite this article as J. J. Quinn et al., *Science* 371, eabc1944 (2021). DOI: 10.1126/science.abc1944

READ THE FULL ARTICLE AT
<https://doi.org/10.1126/science.abc1944>

RESEARCH ARTICLES

MOLECULAR MOTORS

Shulin packages axonemal outer dynein arms for ciliary targeting

Girish R. Mali^{1*}, Ferdos Abid Ali^{1*}, Clinton K. Lau^{1*}, Farida Begum¹, Jérôme Boulanger¹, Jonathan D. Howe¹, Zhuo A. Chen², Juri Rappsilber^{2,3}, Mark Skehel¹, Andrew P. Carter^{1†}

The main force generators in eukaryotic cilia and flagella are axonemal outer dynein arms (ODAs). During ciliogenesis, these ~1.8-megadalton complexes are assembled in the cytoplasm and targeted to cilia by an unknown mechanism. Here, we used the ciliate *Tetrahymena* to identify two factors (Q22YU3 and Q22MS1) that bind ODAs in the cytoplasm and are required for ODA delivery to cilia. Q22YU3, which we named Shulin, locked the ODA motor domains into a closed conformation and inhibited motor activity. Cryo-electron microscopy revealed how Shulin stabilized this compact form of ODAs by binding to the dynein tails. Our findings provide a molecular explanation for how newly assembled dyneins are packaged for delivery to the cilia.

Motile cilia play essential roles that range from setting up the left-right body axis to clearing mucus from the lungs (1). These slender cellular projections contain an axoneme built of microtubule doublets. Ciliary beating is powered by arrays of inner and outer dynein arm motors that

slide adjacent doublets past each other (2). The outer dynein arms (ODAs) are the main force generators in cilia and the most frequently mutated components in human motile ciliopathies (3). ODAs are multisubunit complexes (4), which are preassembled in the cytoplasm by a collection of nine dynein axo-

nemal assembly factors and associated chaperones (4, 5). After assembly, ODAs are targeted to cilia, where the intraflagellar transport (IFT) machinery carries them to their docking sites (6, 7). However, the mechanism of ODA delivery to the cilia and whether any additional factors are required for this process are both unclear.

ODAs assembled in the cell body are bound by Q22YU3 and Q22MS1

To identify potential ciliary targeting factors, we purified newly assembled ODAs from the cytoplasm of the protozoan ciliate *Tetrahymena thermophila*. We deciliated *Tetrahymena* to remove preexisting axonemes and trigger new ODA synthesis (8) (Fig. 1A). ODA complexes, containing a FLAG-tagged copy of the intermediate chain IC3 were extracted and separated from other assembly intermediates by size exclusion chromatography (SEC). Two factors coeluted with the new fully assembled ODAs and were identified by mass spectrometry (MS) as Q22MS1 and Q22YU3 (Fig. 1B and

¹MRC Laboratory of Molecular Biology, Francis Crick Avenue, Cambridge CB2 0QH, UK. ²Bioanalytics, Institute of Biotechnology, Technische Universität Berlin, 13355 Berlin, Germany. ³Wellcome Centre for Cell Biology, University of Edinburgh, Edinburgh EH9 3BF, UK.

*These authors contributed equally to this work.

†Corresponding author. Email: carter@mrc-lmb.cam.ac.uk

Fig. 1. Q22MS1 and Q22YU3 deliver ODAs from cytoplasm to cilia. (A) Scheme used to identify potential interactors of ODAs assembled in the cell body.

(B) SDS-PAGE of ODA purified from the cell body by IP-SEC showing coelution with Q22MS1 and Q22YU3. HC, heavy chains; IC, intermediate chains. (C) Cell swimming velocity comparing wild-type (WT $n = 108$) and mutant strains (Q22YU3Δ $n = 102$ and Q22MS1Δ $n = 110$). (D) Ratio of ODA/tubulin immunofluorescence intensity along individual cilia (WT $n = 118$, Q22YU3Δ $n = 104$, Q22MS1Δ $n = 129$, 3 to 10 cilia from 14 to 17 cells per genotype). (E) Representative cells showing immunofluorescence for ODA and tubulin [quantified in (D)]. Insets highlight reduced amount of ODA staining in mutant cilia compared to wild-type cilia. Scale bars, 10 μm. Error bars show standard deviation; **** $p \leq 0.0001$ (ANOVA with Tukey's test for multiple comparisons).

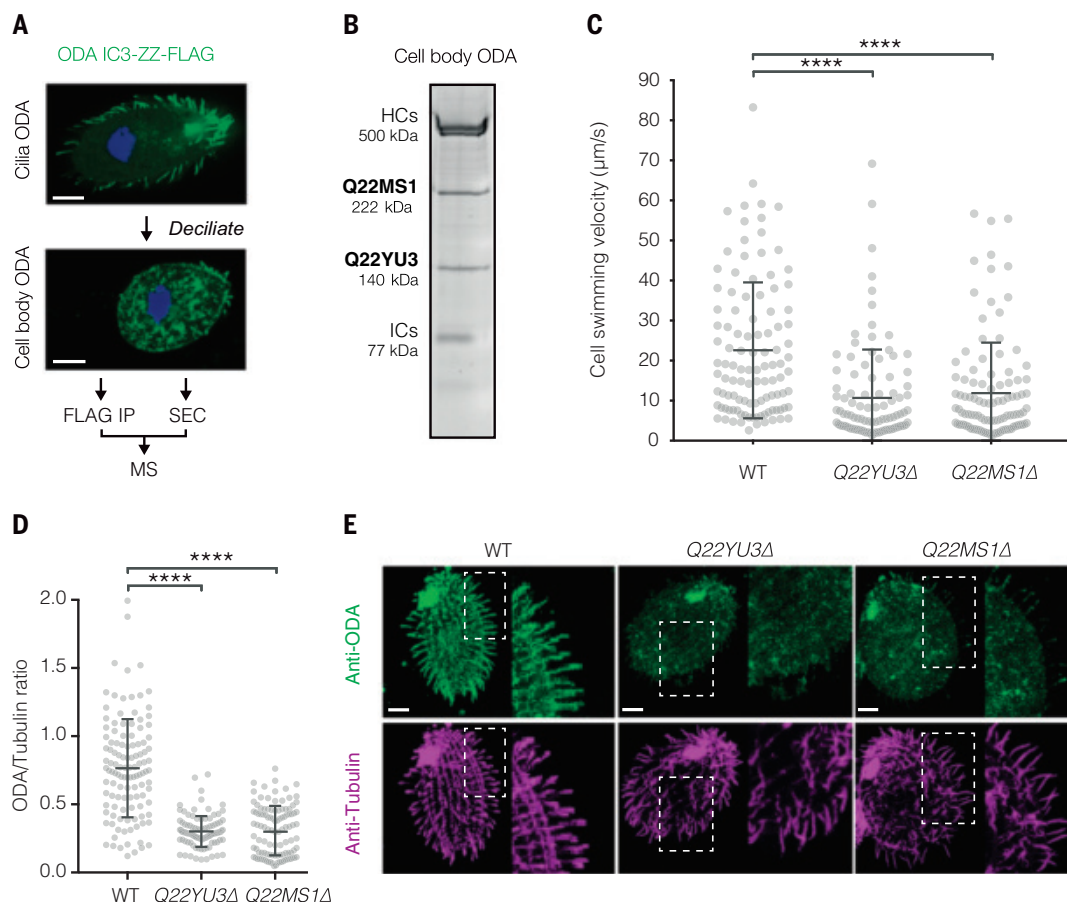


fig. S1A). We also performed label-free quantitative MS on the immunoprecipitated IC3 subunit and detected an equivalent-fold enrichment of both factors relative to other ODA subunits (fig. S1B and table S1). Taken together, these data suggest that Q22MS1 and Q22YU3 interact tightly with ODAs in the cell body.

Loss of Q22MS1 and Q22YU3 affects cilia motility

These ODA-associated factors lack known functions and have not previously been linked to motile cilia. Q22YU3 shares 24% identity to human C20ORF194 (fig. S2), whereas Q22MS1 has a unique domain architecture and no ortholog outside of *Tetrahymena*. To investigate their roles, we generated *Tetrahymena* knockout strains for each factor (fig. S3A). Both strains showed an approximately twofold decrease in swimming speed compared to wild-type (WT) (Q22YU3Δ, 10.6 ± 12 μm/s; Q22MS1Δ, 11.88 ± 12.6 μm/s; WT, 22.5 ± 16.9 μm/s; mean ± SD), suggesting defects in cilia movement (Fig. 1C). Mutants also had decreased accumulation of food vacuoles and a higher frequency of cytokinetic defects, which are hallmarks of defective cilia motility in *Tetrahymena* (9, 10)

(fig. S3, B and C). We found that the lengths and numbers of cilia in our knockouts were similar to those in the wild-type, suggesting that our observations were not attributable to defects in ciliogenesis (fig. S3, D and E). However, high-speed imaging showed that cilia in mutants beat slower than in wild-type cells (Q22YU3Δ = 7 ± 11 Hz, Q22MS1Δ = 4 ± 6 Hz, WT = 20 ± 12 Hz; mean ± SD) but at frequencies similar to those in an ODA temperature-sensitive mutant (11) (OADIC11 = 8 ± 11 Hz) (fig. S4 and movie S1). We therefore used immunofluorescence to test if loss of Q22YU3 and Q22MS1 affected ODA targeting to cilia. Staining with an antibody against ODAs showed marked reductions in their levels in cilia of mutant strains compared to the wild-type (Fig. 1, D and E, and fig. S3F). Thus, loss of Q22YU3 or Q22MS1 results in defective ciliary movement owing to reduced delivery of ODAs to the cilia.

Q22YU3 inhibits microtubule gliding by closing the ODAs

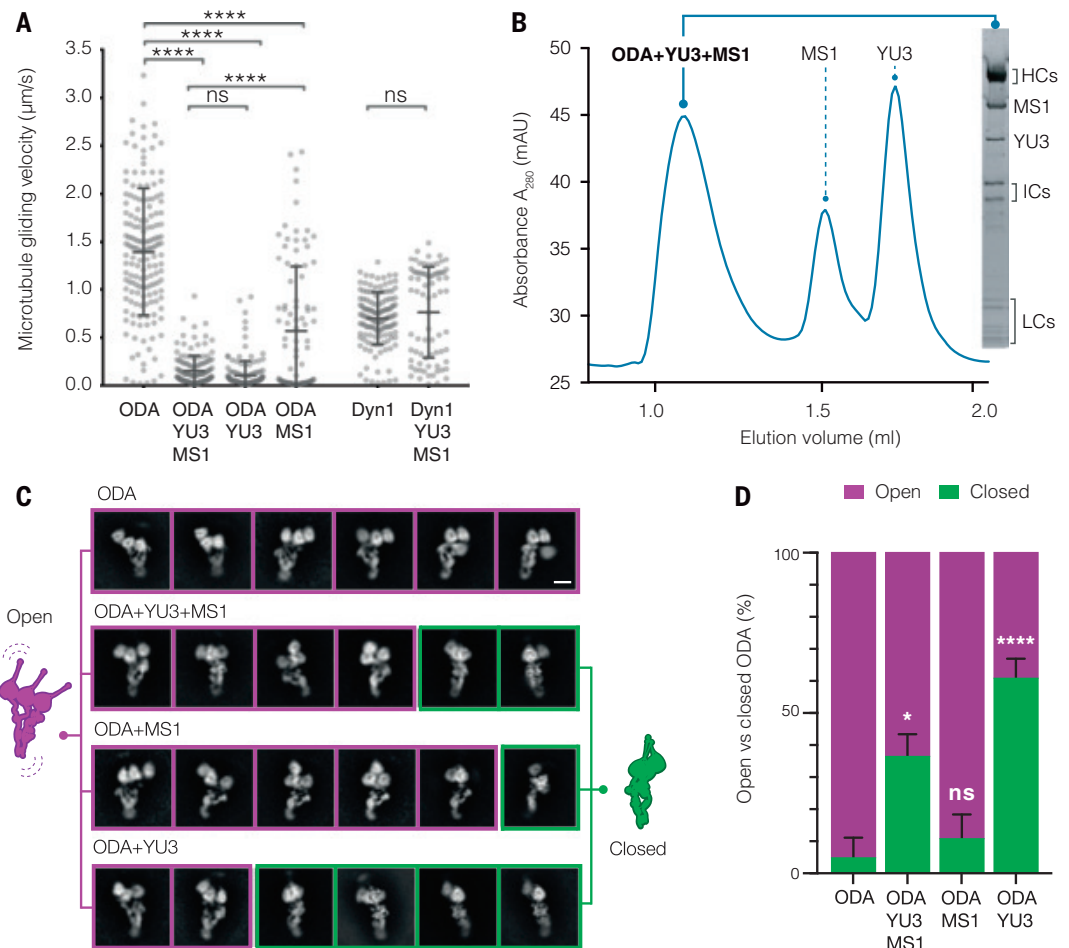
It has been proposed that ODAs need to be held in an inactive state during transport into the axoneme (4). We therefore tested whether

Q22YU3 and Q22MS1 inhibited dynein motor activity. We expressed both factors recombinantly and assayed their effect on the microtubule gliding activity of ODAs purified from axonemes (12) (Fig. 2A). In contrast to the cytoplasm-purified sample, these ODAs lacked Q22YU3 or Q22MS1. The axoneme-purified ODAs translocated microtubules at 1.39 ± 0.60 μm/s (mean ± SD). Gliding was severely compromised by the addition of both factors together (0.15 ± 0.15 μm/s) or with Q22YU3 alone (0.10 ± 0.15 μm/s). Q22MS1 reduced microtubule gliding velocities to a lesser extent (0.56 ± 0.76 μm/s). By contrast, addition of both factors to cytoplasmic dynein-1 did not significantly alter its microtubule gliding velocity (0.76 ± 0.47 μm/s for dynein-1 alone versus 0.69 ± 0.27 μm/s with both factors). Thus, Q22YU3 is sufficient to specifically inhibit ODA activity.

Tetrahymena ODAs contain three dynein heavy chains and, when purified from axonemes, show an open bouquet conformation with the heavy chain motor domains separated (13). However, when we used negative-stain electron microscopy (EM) to image ODAs purified from the cytoplasm, we noticed that ~40% of intact particles displayed a “closed”

Fig. 2. Q22YU3 binding inhibits ODAs by clustering motors.

(A) Microtubule gliding velocities. Individual gliding events from three technical replicates per sample are plotted (ODA *n* = 159, ODA+YU3+MS1 *n* = 136, ODA+YU3 *n* = 146, ODA+MS1 *n* = 94, Dyn1 *n* = 136, Dyn1+YU3+MS1 *n* = 76). YU3, Q22YU3; MS1, Q22MS1; Dyn1, human cytoplasmic dynein 1. Error bars show standard deviation; ns, not significantly different; *****p* ≤ 0.0001 (ANOVA with Tukey's test for multiple comparisons). (B) Axonemal-purified open ODA reconstituted with recombinant Q22YU3 and Q22MS1. SDS-PAGE gel of SEC peak fraction. (C) Representative 2D class averages showing the distribution of open (purple) and closed (green) ODA particles from ODAs alone and reconstituted with factors. Scale bar, 10 nm. (D) Quantification of closed and open particles from 18,000 particles per dataset (*n* = 3 technical replicates) represented as a percentage. Error bars show standard deviation. ns, not significantly different; **p* ≤ 0.01, *****p* ≤ 0.0001 (Kruskal Wallis test). Refer to fig. S6 and table S5.



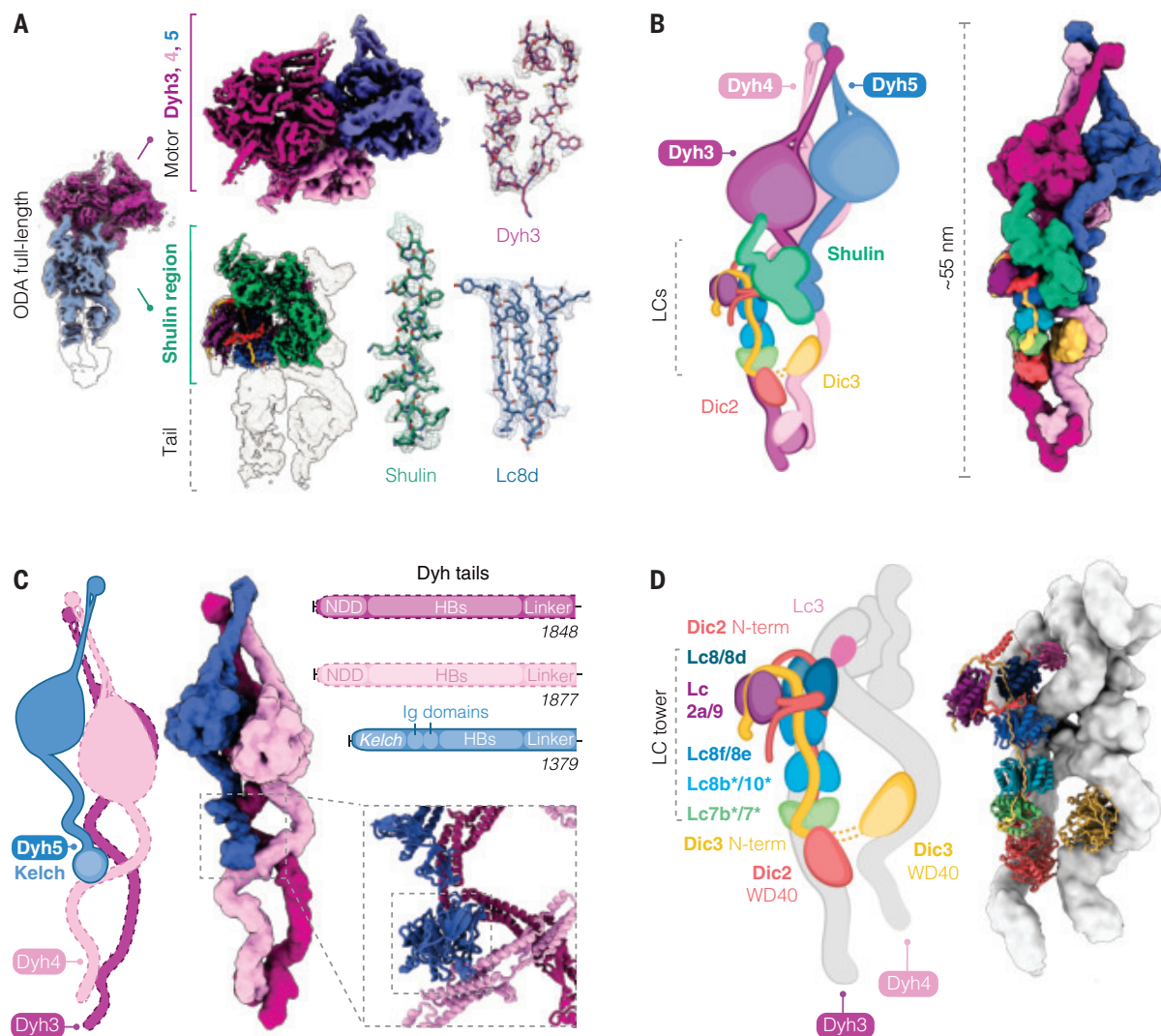


Fig. 3. Cryo-EM reconstruction shows architecture of closed ODA. (A) Overview of the closed ODA bound by Shulin with head (purple) and tail (blue) maps docked in an overall map (gray). Maps obtained after masked refinements are shown for the head region containing densities for Dyh3, 4, and 5 motor domains, and the ordered tail map contains a docked Shulin-region map (green). Representative cryo-EM densities are shown. The following contour levels (σ) are used: (right) ODA full-length structure, 0.000607; tail, 0.0026; motors, 0.01; (middle) ordered tail, 0.00448; Shulin region, 0.015; motors, Dyh3 0.01, Dyh4 0.015, Dyh5 0.015. Zoom insets showing side-chain densities were at contour level of 0.02. (B) Cartoon and filtered surface representation of all modeled subunits. (C) Dyh5 binds Dyh4 via its N-terminal Kelch domain (inset). HB, helical bundles; NDD, N-terminal dimerization domain. (D) DIC N-terminal extensions bind dimers of LCs, forming a LC tower and followed by globular WD40 domains that contact Dyh3 and Dyh4. Heterodimers of Lc7b/7 and Lc8b/Lc10 are tentatively assigned (*). Lc3 sits on Dyh4 and is not part of the LC tower.

Dyh5 0.015. Zoom insets showing side-chain densities were at contour level of 0.02. (B) Cartoon and filtered surface representation of all modeled subunits. (C) Dyh5 binds Dyh4 via its N-terminal Kelch domain (inset). HB, helical bundles; NDD, N-terminal dimerization domain. (D) DIC N-terminal extensions bind dimers of LCs, forming a LC tower and followed by globular WD40 domains that contact Dyh3 and Dyh4. Heterodimers of Lc7b/7 and Lc8b/Lc10 are tentatively assigned (*). Lc3 sits on Dyh4 and is not part of the LC tower.

conformation where the motor domains were clustered, and the tails were compacted (fig. S5). This closed conformation resembles a form previously observed only after cross-linking (13). To identify the factor responsible, we reconstituted axoneme-purified ODAs with recombinant Q22MS1 and Q22YU3. Both factors formed stable complexes with ODAs either together or individually (Fig. 2B, fig. S6, and table S5). Whereas ODAs on their own were mostly in the open conformation (Fig. 2, C and D), in the presence of both factors, $36 \pm 7\%$ (mean \pm SD) of particles were closed, similar to the fraction observed for ODAs purified from the cytoplasm. ODAs bound to Q22MS1

alone were closed only $11 \pm 8\%$ of the time. By contrast, in the presence of Q22YU3 alone, $61 \pm 6\%$ of ODAs were closed (Fig. 2, C and D; fig. S6; and table S5). Thus, Q22YU3 inhibits ODAs by holding the three heavy chains together in a closed conformation. We propose to name this protein Shulin (Sanskrit: one that holds the trident).

Cryo-EM structure shows molecular mechanism of ODA closure by Shulin (Q22YU3)

To elucidate how Shulin closes ODAs at a molecular level, we determined the structure of the reconstituted *Tetrahymena* ODA-Shulin

complex by cryo-EM. The resolution of our overall structure was limited to 8.8 Å owing to its flexibility (Fig. 3A and figs. S7 and S8). However, focused classification and local refinement produced a series of subregion maps ranging from 4.3 to 5.9 Å in global resolution (Fig. 3A and figs. S7 to S12). The central portion of the Shulin region map has a local resolution range of 3.5 to 4.2 Å (fig. S9), enabling de novo building of Shulin and its interactions (Fig. 3A and fig. S11A). In combination with MS to identify the ODA subunit composition (fig. S13), our maps allowed us to assign the positions of the three heavy chains (Dyh3, Dyh4, Dyh5), two essential intermediate chains

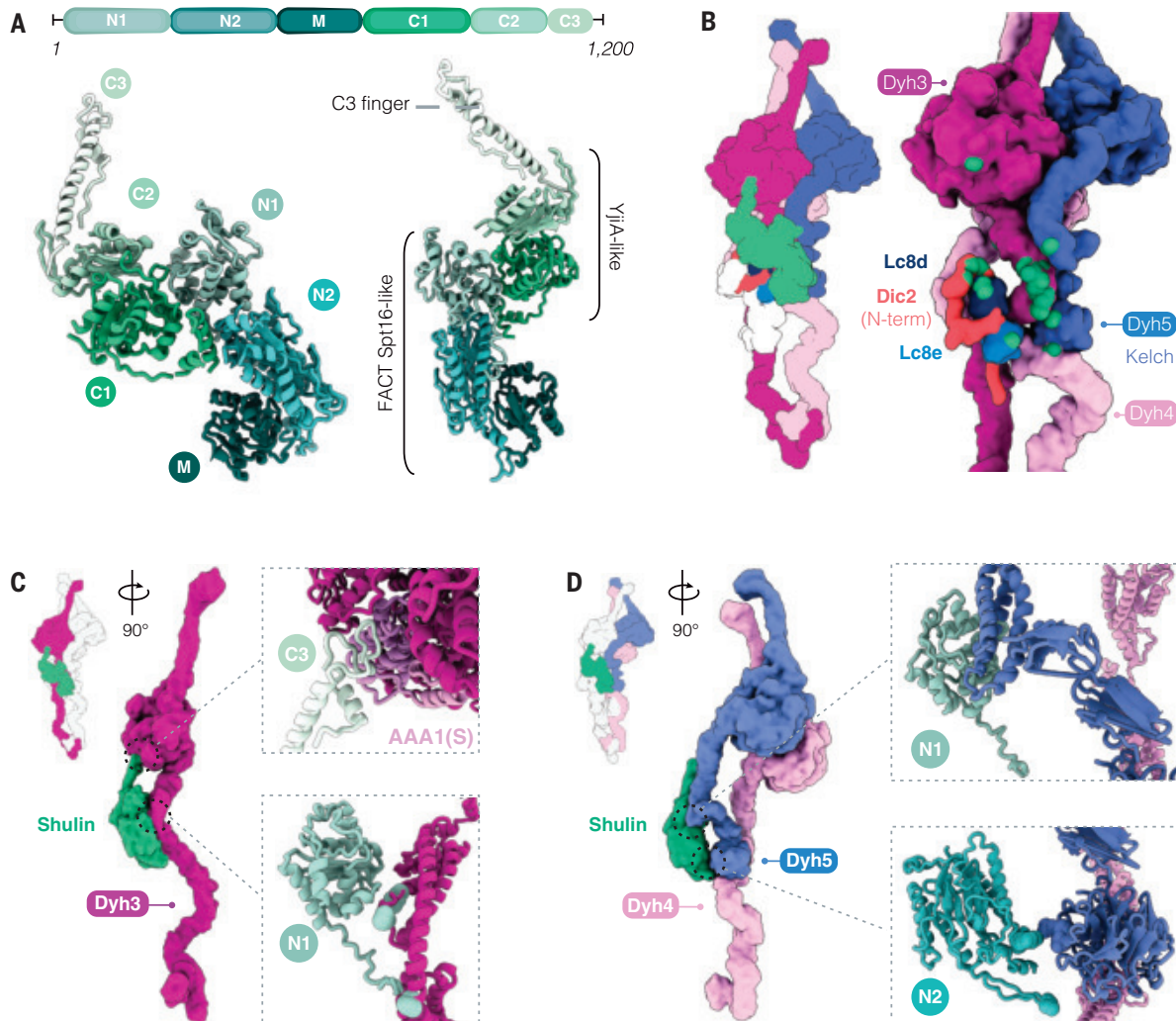


Fig. 4. Characterization of Shulin structure and its mechanism of ODA inhibition. (A) Domain architecture of Shulin. N-terminal (N1, N2) and middle (M) domains share a similar fold with the FACT complex core subunit Spt16. C-terminal (C1, C2) domains are similar to GTPase YjiA and are followed by a C-terminal finger (C3). (B) Cartoon and filtered surface representation with

main contacts between Shulin and ODA subunits highlighted in green spheres. (C) Shulin's N1 domain contacts helical bundles proximal to the linker in Dyh3 tail. The C3 finger projects out to contact Dyh3 AAA1(S) (insets). (D) Shulin's N1 domain contacts Dyh5 helical bundles, and its N2 domain touches the Kelch domain. Shulin contacts Dyh4 just below Dyh5 Kelch domain (insets).

(ICs: Dic2, Dic3), and 11 light chains (LCs) (Fig. 3B and figs. S8 to S12). We list the names and UniProt IDs of these subunits and provide names for the corresponding orthologs in *Chlamydomonas* and humans in table S2.

In our structure, the motor domains were clustered in a closed conformation (Fig. 3B) consistent with the negative-stain data. At the core of the structure are the Dyh3 (α -HC) and Dyh4 (β -HC) heavy chains, which are conserved across all eukaryotes with motile axonemes (14). They form a heterodimer held together by an N-terminal dimerization domain in an arrangement that is similar to cytoplasmic dyneins (15, 16). The third heavy chain, which is only found in ciliate and algal ODAs, is Dyh5 in *Tetrahymena* (γ -HC—equivalent to the α -HC in the alga *Chlamydomonas*, table S2). Our structure showed that Dyh5 is much shorter than the other heavy chains and is

anchored to Dyh4 halfway along its length. The N terminus of Dyh5 contains a Kelch-type β -propeller domain that sits on the helical bundles of Dyh4 (Fig. 3C). The peripheral attachment of this third heavy chain may explain why its loss in *Chlamydomonas* minimally affects flagellar motility (17).

In their tail regions, Dyh3 and Dyh4 wrap around the globular WD40 domains of the intermediate chains, with Dyh4 also binding to a small density consistent with the thioredoxin-like Lc3 light chain (Fig. 3D and fig. S14A). The intermediate chains have long N-terminal extensions, which are held together by a tower of light chains consisting of a Lc7/Lc7b heterodimer, three dimers of Lc8 orthologs and at the end, bent over to one side, a Tctex-like heterodimer of Lc2a/Lc9 (Fig. 3D and fig. S14B). On the basis of side-chain density, we assigned the positions of Lc8 and its orthologs: Lc8d,

Lc8e, and an unnamed Lc8-like protein (UniProt ID: Q22R86), which we called Lc8f. Our MS analysis on axoneme-purified ODAs showed the additional presence of two more Lc8 orthologs, Lc10 and Lc8b, which we tentatively assigned to the remaining two positions (fig. S13). The bent arrangement of the Lc2a/Lc9 heterodimer is stabilized by the Dic2 N terminus, which loops out from where it contacts Lc2a and wedges between Lc8d and Lc8e (fig. S14B).

Dynein motors comprise a ring of six AAA+ domains (AAA1 to AAA6), a force-producing linker, and a long coiled-coil stalk with the microtubule binding domain at the tip. In our structure, the motor regions of all three heavy chains were locked in the prepower stroke conformation of their catalytic cycle (18) with their linker domains bent through 90° (fig. S15, A and B). The density suggests that the stalks of each motor domain are angled to interact

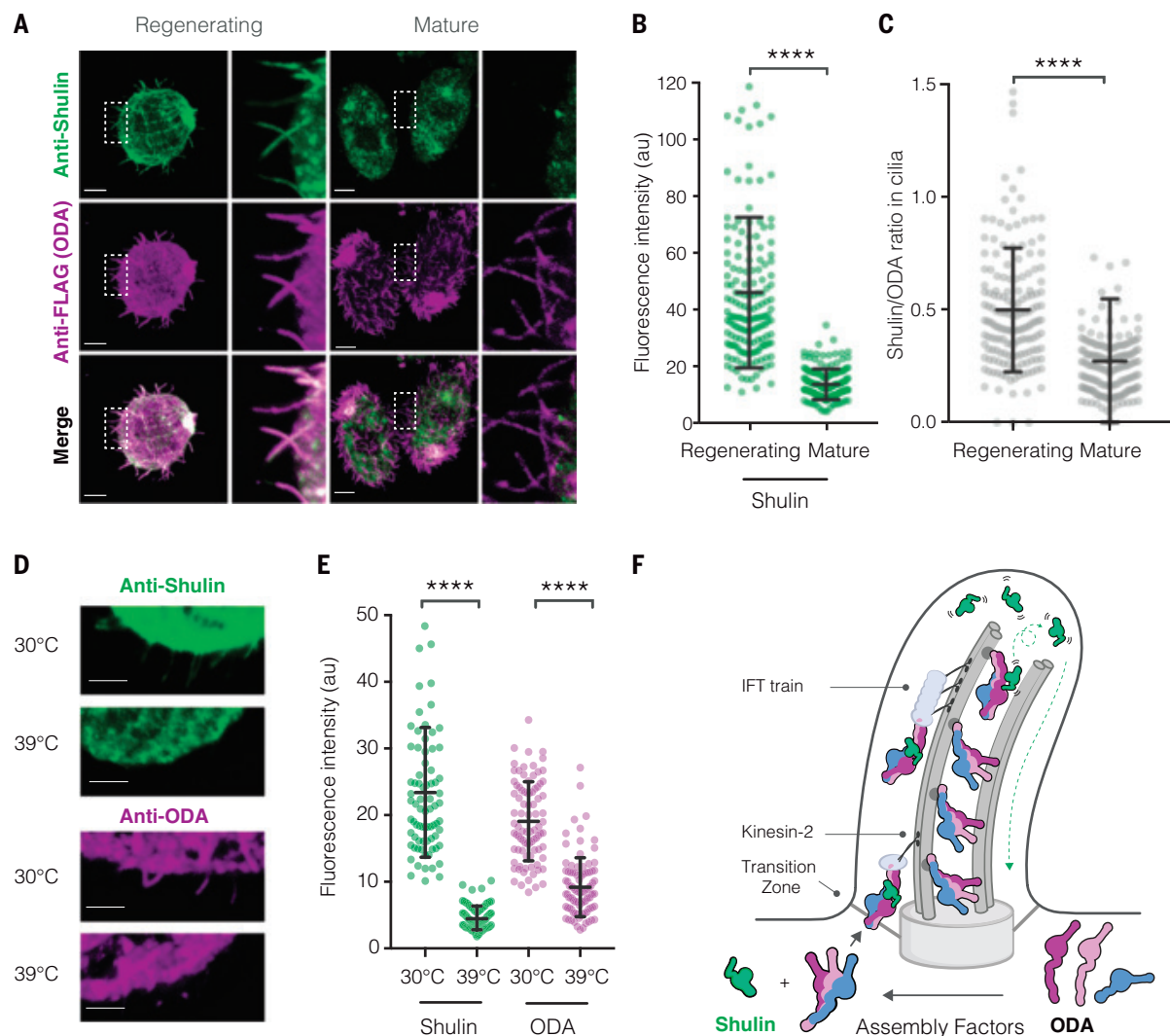


Fig. 5. Shulin delivers ODAs to regenerating cilia. (A) Coimmunostaining of ODAs (anti-FLAG) and Shulin in the IC3-FLAG strain. Representative cells regenerating cilia 30 min after deciliation and with mature cilia are shown; insets highlight differences in concentrations of Shulin and constant amounts of ODA in cilia in both conditions. (B and C) Quantification of Shulin concentrations in regenerating and mature cilia and ratios of per cilium fluorescence intensities for Shulin/ODA (regenerating $n = 160$, mature $n = 162$, 9 to 10 cilia from 16 cells per condition). (D and E) Immunostaining for Shulin and ODA (anti-ODA) in an

ODA temperature-sensitive mutant strain (*OAD1C11*) grown at permissive (30°C) and restrictive (39°C) temperatures for 16 hours (Shulin: 30°C $n = 78$, 39°C $n = 83$; ODA: 30°C $n = 87$, 39°C $n = 95$ cilia from 10 cells per condition). Scale bars, 10 μm . Error bars show standard deviation, **** $p \leq 0.0001$ (ANOVA). (F) Model for Shulin's role in delivering ODAs to cilia. Shulin locks ODAs in their closed state during IFT (intraflagellar transport) in regenerating cilia. Shulin is released after ODAs stably dock and leaves the ciliary compartment (green arrow).

with each other close to their microtubule-binding domains (Fig. 3, A and B, and fig. S15B). Clustering of motor domains is further stabilized by interactions between the Dyh3 and Dyh4 linkers, between the Dyh4 AAA4 and the elbow of the Dyh3 linker, and between the Dyh5 AAA3 and Dyh3 AAA4 (fig. S15, C and D). This clustered conformation is distinct from the one ODAs adopt upon docking onto ciliary doublets, where their motor domains are stacked parallel to each other and free to undergo their catalytic cycle (19, 20). Thus, the closed conformation may represent an inactive state of ODAs before their final incorporation into cilia.

Our Shulin structure shows that it contains N-terminal domains (N1, N2) that are related to the aminopeptidase P domain of Spt16, a core component of the histone chaperone FACT (Fig. 4A). We built the middle (M) domain de novo, revealing that it adopted a pleckstrin homology (PH) fold akin to the Spt16 C terminus. Thus, the whole N-terminal half of Shulin bears high structural homology to Spt16 (21). Unexpectedly, Shulin's C-terminal domains (C1 and C2) are structurally similar to the bacterial guanosine triphosphatase (GTPase) YjiA (22). C1 has a Ras-like fold, and C2 consists of a five-stranded β sheet. There is a nucleotide between C1 and C2, which plays a structural role holding

the two domains together (fig. S16A). Shulin ends in a long C-terminal finger with a helix-loop arrangement that projects away from the core of the molecule (C3) (Fig. 4A). Overall, the structure suggests that Shulin has evolved from a fusion of an ancestral Spt16 and a nucleotide-binding protein.

Shulin stabilizes the closed conformation of ODAs by binding all three heavy chains and the LC tower (Fig. 4B). It makes its most extensive interactions with Dyh3 (3216 \AA^2 surface area). Shulin's N1 domain contacts multiple sites in the Dyh3 tail, and its C3 finger binds the AAA1 small subdomain (AAA1S) in the Dyh3 motor domain (Fig. 4C). Residues at

these two sites are conserved among homologs of Dyh3 from multiple species (fig. S17, A and B) but not among other dynein heavy chains (fig. S17C). Our structure showed that Shulin bridges the Dyh3 tail and motor, holding them in a rigid conformation (fig. S16). It can only make these connections if the motor is in its prepower stroke state, suggesting that it directly locks Dyh3 into its closed conformation (fig. S15B). Truncation of Shulin to remove the motor-binding C3 finger abolished its ability to bind ODAs over gel filtration. Directly mixing the truncated Shulin with ODA also failed to induce closure in a negative-stain EM assay (fig. S18). Thus, bridging the Dyh3 tail and motor is key for stabilizing the closed state of ODAs.

Shulin holds the other two motor domains in their closed conformation indirectly by stabilizing the contacts they make with Dyh3 and each other. Its N2 domain makes a small connection (313 \AA^2) to Dyh4 close to where the Dyh5 Kelch domain is docked (Fig. 4D). This interaction holds Dyh3 and Dyh4 together and reinforces a contact between the helical bundles in their tail regions (fig. S16C). This, in turn, supports the connections, described above, between their motor domains (fig. S15). Shulin's connection to Dyh5, via its N1 domain, is also small (292 \AA^2) but is sufficient to stabilize the Dyh5 linker binding to the Dyh3 motor domain and motor-motor contacts between Dyh4 and Dyh5 (fig. S15E). In the light-chain tower, the M domain of Shulin contacts Lc8e and its C1 domain contacts Lc8d and an α helix in the Dic2 N terminus (fig. S16D). These contacts stabilize packing of the LC tower against the Dyh3 tail (fig. S16E). Thus, Shulin makes contacts with multiple ODA subunits and stabilizes the interactions between them that hold the motors in a closed conformation.

Q22MS1 dampens ODA activity by constraining the motors

Here, we identified two proteins, Q22MS1 and Shulin, which copurify with ODAs in the cytoplasm and are required for their delivery to cilia. Of these two proteins, the mechanism of the *Tetrahymena*-specific Q22MS1 is less clear. It is 222 kDa in size and contains a catalytically inactive nucleoside diphosphate kinase (NDK) domain. A homologous NDK domain is found in the recently identified *Xenopus* protein DAAP1 (23). DAAP1 has also been implicated in ODA delivery to cilia and localizes to membraneless organelles involved in dynein assembly. However, there is no sequence similarity between Q22MS1 and DAAP1 outside the NDK domain, and the mammalian orthologs of DAAP1 lack the NDK domain completely. Q22MS1 mildly reduces ODA motor activity in our microtubule gliding assays. To address how this could occur, we subclassified the open particles of ODAs alone and bound to Q22MS1. In

the presence of Q22MS1, we observed a significant increase in the number of particles with their motor domains constrained in a triangular conformation (fig. S19A). Cross-linking MS showed that Q22MS1 predominantly interacts with the tails of Dyh3, Dyh4, and Dyh5 on the opposite side of the complex from the Shulin-binding interface (fig. S19B). We thus propose that Q22MS1 binds the ODA tails and corrals the heads into a clustered triangular conformation, which causes a mild dampening of motor activity.

Shulin keeps ODAs closed during delivery to cilia

Shulin notably shuts down ODA motor activity, suggesting that it is the proposed inhibitor (4) required during targeting of ODAs to the cilia. Unlike the cytoplasmic dyneins, which are auto-inhibited (15, 16), ODAs rely on Shulin to enforce inhibition. Immunostaining revealed that Shulin localized to regenerating cilia (Fig. 5, A to C, and fig. S20). This is the stage of ciliogenesis when ODAs are being actively imported and incorporated (8). By contrast, in mature cilia with stably incorporated dyneins, the amounts of Shulin appeared reduced relative to ODAs (Fig. 5, A to C). To test if Shulin's entry into cilia was ODA dependent, we used a temperature-sensitive mutant (*OADIC11*) in which ciliary entry of ODAs is blocked at the restrictive temperature of 39°C (Fig. 5, D and E). Shulin accumulated in regenerating cilia as normal at the permissive 30°C , but its entry was prevented at the restrictive temperature (Fig. 5, D and E). Thus, Shulin travels with ODAs during cilia growth until they reach their final axonemal location (Fig. 5F).

Shulin's inhibitory effect on ODAs could serve several purposes. During IFT of ODAs, Shulin may prevent aberrant interactions with axonemal microtubules, which would hinder their transport. At their final location, ODAs interact with the A-tubule via their tail domains and with the B-tubule via their motor domains (20). Shulin's inhibition could be important to allow the ODA tails to correctly dock before the motors can engage the B-tubule. Finally, as previously proposed, inhibition may also play a role in preventing any free ODAs escaping prematurely from cilia (4).

In addition to its inhibitory role during ciliary trafficking, Shulin may have other functions. First, Shulin knockdown resulted in reduced amounts of ODAs in the cell body as well as the cilia (fig. S21), suggesting that Shulin is required to prevent ODA degradation in the cytoplasm. Shulin may play a role in ODA assembly, such that in its absence, incorrectly assembled ODAs are removed. Alternatively, Shulin binding may directly shield cell body ODAs from constitutive degradation pathways. Second, Shulin is also implicated in directly targeting proteins to cilia. Its human

ortholog, C20ORF194, binds the small GTPase Arl3 in primary cilia (24). Arl3-GTP (guanosine 5'-triphosphate) exclusively localizes to cilia and regulates targeting of numerous ciliary proteins (25). Because primary cilia lack ODAs, Shulin may target other components in this context. In motile cilia, Arl3 is also important for assembly (26), which raises the possibility that the Shulin-Arl3 interaction plays a direct role in ODA delivery. In summary, our work shows that Shulin inhibits and packages ODAs and plays a key role in their targeting to cilia.

REFERENCES AND NOTES

1. I. A. Drummond, *Curr. Opin. Cell Biol.* **24**, 24–30 (2012).
2. U. W. Goodenough, J. E. Heuser, *Cell* **41**, 341–342 (1985).
3. M. W. Leigh et al., *Genet. Med.* **11**, 473–487 (2009).
4. S. M. King, *Cold Spring Harb. Perspect. Biol.* **8**, a028100 (2016).
5. M. E. Fowkes, D. R. Mitchell, The Role of Preassembled Cytoplasmic Complexes in Assembly of Flagellar Dynein Subunits, *Mol. Biol. Cell* **9**, 2337–2347 (1998).
6. N. T. Ahmed, C. Gao, B. F. Luckner, D. G. Cole, D. R. Mitchell, *J. Cell Biol.* **183**, 313–322 (2008).
7. J. Dai, F. Barbieri, D. R. Mitchell, K. F. Lechtreck, *Mol. Biol. Cell* **29**, 2553–2565 (2018).
8. J. L. Rosenbaum, K. Carlson, *J. Cell Biol.* **40**, 415–425 (1969).
9. N. E. Williams et al., *Eukaryot. Cell* **5**, 555–567 (2006).
10. C. R. Wood, R. Hard, T. M. Hennessey, *J. Cell Sci.* **120**, 3075–3085 (2007).
11. G. J. Attwell, C. S. Bricker, A. Schwandt, M. A. Gorovsky, D. G. Pennock, *J. Protozool.* **39**, 261–266 (1992).
12. M. E. Porter, K. A. Johnson, *J. Biol. Chem.* **258**, 6575–6581 (1983).
13. U. Goodenough, J. Heuser, *J. Mol. Biol.* **180**, 1083–1118 (1984).
14. B. Wickstead, K. Gull, *Traffic* **8**, 1708–1721 (2007).
15. K. Zhang et al., *Cell* **169**, 1303–1314.e18 (2017).
16. K. Toropova et al., *Nat. Struct. Mol. Biol.* **26**, 823–829 (2019).
17. H. Sakakibara, D. R. Mitchell, R. Kamiya, *J. Cell Biol.* **113**, 615–622 (1991).
18. H. Schmidt, R. Zalyte, L. Urnauvicius, A. P. Carter, *Nature* **518**, 435–438 (2015).
19. J. Lin, D. Nicastro, *Science* **360**, eaar1968 (2018).
20. S. Kubo et al., Remodeling and activation mechanisms of outer arm dynein revealed by cryo-EM, *bioRxiv* 2020.11.30.404319 [Preprint]. 30 November 2020. <https://doi.org/10.1101/2020.11.30.404319>.
21. Y. Liu et al., *Nature* **577**, 426–431 (2020).
22. A. M. Sydor et al., *Biochemistry* **52**, 1788–1801 (2013).
23. C. Lee et al., *Cell Biol. (Henderson NV)* (2020).
24. K. J. Wright et al., *Genes Dev.* **25**, 2347–2360 (2011).
25. S. Alkanderi et al., *Am. J. Hum. Genet.* **103**, 612–620 (2018).
26. A. Cuvillier et al., *J. Cell Sci.* **113**, 2065–2074 (2000).

ACKNOWLEDGMENTS

We thank B. Santhanam for help with comparative genomic analyses. We acknowledge J. Grimmett and T. Darling for scientific computing support and the MRC LMB EM Facility (G. Sharov, G. Cannone) for microscopy data acquisition time and support. We also acknowledge Diamond Light Source for access and support of the cryo-EM facilities at the UK's national Electron Bio-imaging Centre (eBIC: proposal b23268), funded by the Wellcome Trust, MRC, and BBRSC. We thank K. Nguyen and V. Chandrasekaran for microscopy time; F. Coscia for graphene oxide grid assistance; F. O'Reilly for guidance optimizing cross-linking; S. Bullock and members of the Carter lab for comments on the manuscript; S. Chaaban for sharing custom randomization and angular-distribution representation scripts; S. Chaaban, A. Fellows, and G. Manigrasso for double-blind counting of ODA conformations; C. Stone for help with figures; and S. Utekar for suggesting the name Shulin. **Funding:** This study was supported by the Medical Research Council, UK (MRC_UP_A025_1011) and Wellcome Trust (WT120711) to A.P.C., Wellcome Trust (218653/Z/19/Z) to F.A.A. and by the Deutsche Forschungsgemeinschaft under Germany's Excellence Strategy–EXC 2008/1–390540038, project no. 426290502 and Wellcome Trust (103139) to J.R. **Author contributions:** G.R.M. performed all cell biological, biochemical, and (with F.A.A.) negative-stain EM analyses. G.R.M. prepared ODA-Q22MS1 BS3 cross-linking samples and ODA-Shulin cryo-EM samples. C.K.L. collected all cryo-EM datasets and performed conservation analysis for ODA-Shulin contacts. G.R.M. determined an initial cryo-EM structure. F.A.A., with guidance from C.K.L.,

determined the higher-resolution cryo-EM structures. A.P.C., C.K.L., and F.A.A. built and refined models. J.D.H. and J.B. performed cilia beat frequency analysis. M.S. and F.B. performed MS. J.R. and Z.A.C. processed ODA-Q22MS1 cross-linked samples by MS and analyzed the data. A.P.C. and G.R.M. conceived the project. A.P.C. guided the project. A.P.C., G.R.M., C.K.L., and F.A.A. wrote the manuscript with help from all authors. **Competing interests:** The authors declare no competing interests. **Data and materials availability:** Mass spectrometry data have been deposited to ProteomeXchange (PRIDE) database under accession code PXD022396. Cross-linking mass spectrometry data have been deposited via the ProteomeXchange (JPOST) database under

accession code PXD022936. Atomic coordinates and cryo-EM maps have been deposited in the Protein Data Bank under accession codes 6ZYW (overall structure), 6ZYX (Shulin region), and 6ZYY (Dyh3 motor region) and in the Electron Microscopy Data Bank under accession codes EMD-11576 (full-length), EMD-11577 (tail), EMD-11578 (ordered tail), EMD-11579 (Shulin region), EMD-11580 (extended Shulin region), EMD-11581 (Dyh3 motor region), EMD-11582 (Dyh4 motor), EMD-11583 (Dyh5 motor), and EMD-11584 (extended Dyh5 motor).

Materials and methods and references cited therein can be found in the main article online.

SUPPLEMENTARY MATERIALS

science.sciencemag.org/content/371/6532/910/suppl/DC1
Figs. S1 to S21
Tables S1 to S5
References (27–57)
Movies S1 and S2
MDAR Reproducibility Checklist

3 August 2020; accepted 15 January 2021
10.1126/science.abe0526

CORONAVIRUS

Model-informed COVID-19 vaccine prioritization strategies by age and serostatus

Kate M. Bubar^{1,2*}, Kyle Reinholt³, Stephen M. Kissler⁴, Marc Lipsitch^{4,5}, Sarah Cobey⁶, Yonatan H. Grad⁴, Daniel B. Larremore^{3,7*}

Limited initial supply of severe acute respiratory syndrome coronavirus 2 (SARS-CoV-2) vaccine raises the question of how to prioritize available doses. We used a mathematical model to compare five age-stratified prioritization strategies. A highly effective transmission-blocking vaccine prioritized to adults ages 20 to 49 years minimized cumulative incidence, but mortality and years of life lost were minimized in most scenarios when the vaccine was prioritized to adults greater than 60 years old. Use of individual-level serological tests to redirect doses to seronegative individuals improved the marginal impact of each dose while potentially reducing existing inequities in COVID-19 impact. Although maximum impact prioritization strategies were broadly consistent across countries, transmission rates, vaccination rollout speeds, and estimates of naturally acquired immunity, this framework can be used to compare impacts of prioritization strategies across contexts.

Severe acute respiratory syndrome coronavirus 2 (SARS-CoV-2) has caused a public health and economic crisis worldwide. As of January 2021, there have been more than 85 million cases and 1.8 million deaths reported (*1*). To combat this crisis, a variety of nonpharmaceutical interventions have been implemented, including shelter-in-place orders, limited travel, and remote schooling. Although these efforts are essential to slowing transmission in the short term, long-term solutions—such as vaccines that protect from SARS-CoV-2 infection—remain urgently needed. The benefits of an effective vaccine for individuals and their communities have resulted in widespread demand, so it is critical that decision-making on vaccine distribution is well motivated, particularly in

the initial phases when vaccine availability is limited (*2*).

We used a model-informed approach to quantify the impact of COVID-19 vaccine prioritization strategies on cumulative incidence, mortality, and years of life lost. Our approach explicitly addresses variation in three areas that can influence the outcome of vaccine distribution decisions. First, we considered variation in the performance of the vaccine, including its overall efficacy, a hypothetical decrease in efficacy by age, and the vaccine's ability to block transmission. Second, we considered variation in both susceptibility to infection and the infection fatality rate by age. Third, we considered variation in the population and policy—including the age distribution, age-stratified contact rates, and initial fraction of seropositive individuals by age—and the speed and timing of the vaccine's rollout relative to transmission. Although the earliest doses of vaccines will be given to front-line health care workers under plans such as those from the COVAX initiative and the U.S. National Academies of Sciences, Engineering, and Medicine (NASEM) recommendations (*3*), our work is focused on informing the prioritization of the doses that follow. On the basis of regulatory approvals and initial vaccine rollout speeds of early 2021, our investigation focuses generally on scenarios with

a partially mitigated pandemic [reproduction number (*R*) between 1.1 and 2.0], vaccines with protective efficacy of 90%, and rollout speeds of 0.2% of the population per day.

There are two main approaches to vaccine prioritization: (i) directly vaccinate those at highest risk for severe outcomes and (ii) protect them indirectly by vaccinating those who do the most transmitting. Model-based investigations of the trade-offs between these strategies for influenza vaccination have led to recommendations that children be vaccinated because of their critical role in transmission (*4, 5*) and have shown that direct protection is superior when reproduction numbers are high but indirect protection is superior when transmission is low (*6*). Similar modeling for COVID-19 vaccination has found that the optimal balance between direct and indirect protection depends on both vaccine efficacy and supply, recommending direct vaccination of older adults for low-efficacy vaccines and for high-efficacy but supply-limited vaccines (*7*). Rather than comparing prioritization strategies, others have compared hypothetical vaccines, showing that even those with lower efficacy for direct protection may be more valuable if they also provide better indirect protection by blocking transmission (*8*). Prioritization of transmission-blocking vaccines can also be dynamically updated on the basis of the current state of the epidemic, shifting prioritization to avoid decreasing marginal returns (*9*). These efforts to prioritize and optimize doses complement other work showing that under different vaccine efficacy and durability of immunity, the economic and health benefits of COVID-19 vaccines will be large in the short and medium terms (*10*). The problem of vaccine prioritization also parallels the more general problem of optimal resource allocation to reduce transmission, such as with masks (*11*).

Evaluation of vaccine prioritization strategies

We evaluated the impact of vaccine prioritization strategies using an age-stratified SEIR model (susceptible, exposed, infectious, recovered) because age has been shown to be an important correlate of susceptibility (*12–14*), seroprevalence (*12, 15*), severity (*16–18*), and

¹Department of Applied Mathematics, University of Colorado Boulder, Boulder, CO 80309, USA. ²IQ Biology Program, University of Colorado Boulder, Boulder, CO 80303, USA.

³Department of Computer Science, University of Colorado Boulder, Boulder, CO 80309, USA. ⁴Department of Immunology and Infectious Diseases, Harvard T. H. Chan School of Public Health, Boston, MA 02115, USA. ⁵Center for Communicable Disease Dynamics, Harvard T. H. Chan School of Public Health, Boston, MA 02115, USA.

⁶Department of Ecology and Evolution, University of Chicago, Chicago, IL 60637, USA. ⁷BioFrontiers Institute, University of Colorado Boulder, Boulder, CO 80303, USA.

*Corresponding author. E-mail: kate.bubar@colorado.edu (K.M.B.); daniel.larremore@colorado.edu (D.B.L.)

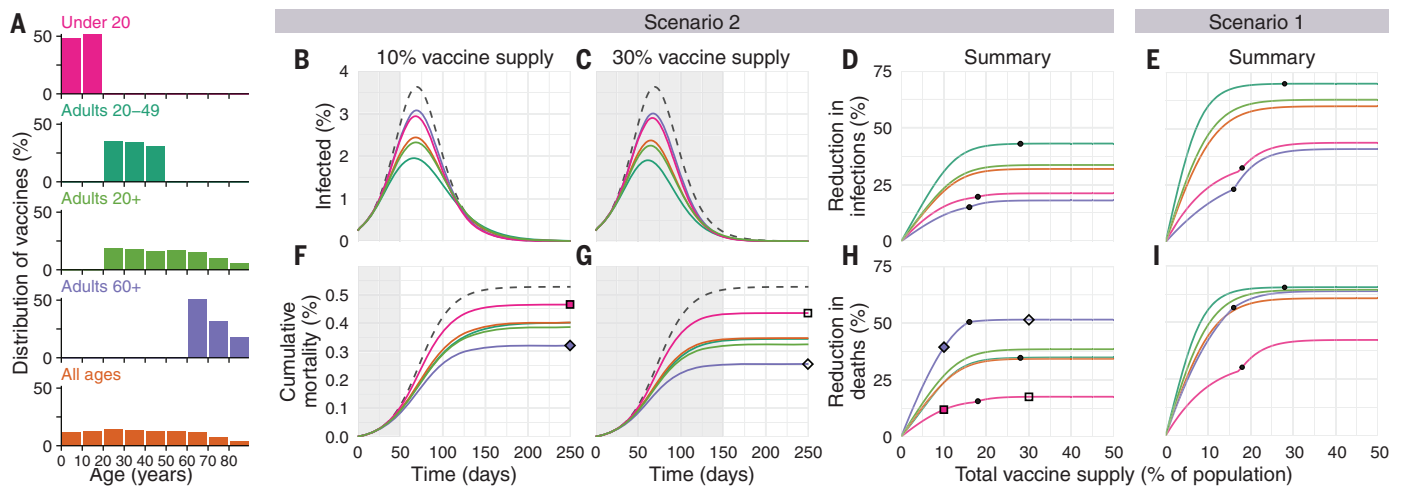


Fig. 1. Impacts of vaccine prioritization strategies on mortality and infections.

(A) Distribution of vaccines for five prioritization strategies: under 20 years, adults 20 to 49 years, adults 20+ years, adults 60+ years, and all ages. (B, C, F, and G) Example simulation curves show [(B) and (C)] percentage of the total population infected over time and [(F) and (G)] cumulative mortality for no vaccines (gray dashed lines) and for five different prioritization strategies [colored lines matching (A)], with [(B) and (F)] 10% and [(C) and (G)] 30% vaccine supply. (D, E, H, and I) Summary curves show percent reductions in [(D) and (E)] infections and [(H) and (I)] deaths in comparison to an unmitigated outbreak for vaccine

supplies between 1 and 50% after 365 days of simulation. Squares and diamonds show how the outputs from single simulations [(F) and (G)] correspond to points in summary curves (H). Gray shading indicates the period during which vaccine is being rolled out at 0.2% of total population per day. Black dots indicate break points at which prioritized demographic groups have been 70% vaccinated, after which vaccines are distributed without prioritization. These simulations assume contact patterns and demographics of the United States (38, 53) and an all-or-nothing, transmission-blocking vaccine with 90% vaccine efficacy and $R_0 = 1.5$ (scenario 2) and $R_0 = 1.15$ (scenario 1).

mortality (19, 20). This model includes an age-dependent contact matrix, susceptibility to infection, and infection fatality rate (IFR), allowing us to estimate cumulative incidence of SARS-CoV-2 infections, mortality due to infection, and years of life lost (YLL) (supplementary materials, materials and methods) by means of forward simulations of 1 year of disease dynamics. Cumulative incidence, mortality, and YLL were then used as outcomes by which to compare vaccine prioritization strategies. These comparisons may be explored by using accompanying open-source and interactive calculation tools that accompany this study (27).

We first examined the impact of five vaccine prioritization strategies for a hypothetical infection- and transmission-blocking vaccine of varying efficacy. The strategies prioritized vaccines to (i) children and teenagers, (ii) adults between ages 20 and 49 years, (iii) adults 20 years or older, (iv) adults 60 years or older, and (v) all individuals (Fig. 1A). In all strategies, once the prioritized population was vaccinated, vaccines were allocated irrespective of age—that is, in proportion to their numbers in the population. To incorporate vaccine hesitancy, at most 70% of any age group was eligible to be vaccinated (22).

We measured reductions in cumulative incidence, mortality, and YLL achieved by each strategy, varying the vaccine supply between 1 and 50% of the total population, under two scenarios. In scenario 1, vaccines were admin-

istered to 0.2% of the population per day until supply was exhausted, with basic reproduction number (R_0) = 1.15, representing highly mitigated spread during vaccine rollout. In scenario 2, vaccines were administered to 0.2% of the population per day until supply was exhausted, but with $R_0 = 1.5$, representing substantial viral growth during vaccine rollout (example model outputs are provided in Fig. 1). Results for additional scenarios in which vaccines were administered before transmission began are described in the supplementary materials, supplementary text, corresponding to countries without ongoing community spread such as South Korea and New Zealand. We considered two ways in which vaccine efficacy (ve) could be below 100%: an all-or-nothing vaccine, in which the vaccine provides perfect protection to a fraction ve of individuals who receive it, or as a leaky vaccine, in which all vaccinated individuals have reduced probability ve of infection after vaccination (supplementary materials, materials and methods).

Of the five strategies, direct vaccination of adults older than 60 years of age (60+) always reduced mortality and YLL more than the alternative strategies when transmission was high [$R_0 = 1.5$, scenario 2, 90% efficacy (Fig. 1); 30 to 100% efficacy (fig. S5)]. For lower transmission ($R_0 = 1.15$, scenario 1), vaccination of adults aged 20 to 49 years reduced mortality and YLL more than the alternative strategies, but differences between prioritization of adults

aged 20 to 49 years, 20+ years, and 60+ years were small for vaccine supplies above 25% (Fig. 1 and fig. S5). Prioritizing adults aged 20 to 49 years minimized cumulative incidence in both scenarios for all vaccine efficacies (Fig. 1 and fig. S5). Prioritizing adults aged 20 to 49 years also minimized cumulative incidence in both scenarios under alternative rollout speeds (0.05 to 1% vaccinated per day) (fig. S6). When rollout speeds were at least 0.3% per day and vaccine supply covered at least 25% of the population, the mortality-minimizing strategy shifted from prioritization of ages 20 to 49 years to adults aged 20+ or 60+ years for scenario 1; when rollout speeds were at least 0.75% per day and covered at least 24% of the population, the mortality-minimizing strategy shifted from prioritization of adults aged 60+ years to adults aged 20+ or 20 to 49 years for scenario 2 (fig. S6). Findings for mortality and YLL were only slightly changed by modeling vaccine efficacy as all or nothing (fig. S5) or leaky (fig. S7).

Impact of transmission rates, age demographics, and contact structure

To evaluate the impact of transmission rates on the strategy that most reduced mortality, we varied the basic reproductive number R_0 from 1.1 to 2.0 when considering a hypothetical infection- and transmission-blocking vaccine with 90% vaccine efficacy. We found that prioritizing adults aged 60+ years remained the best way to reduce mortality and YLL for

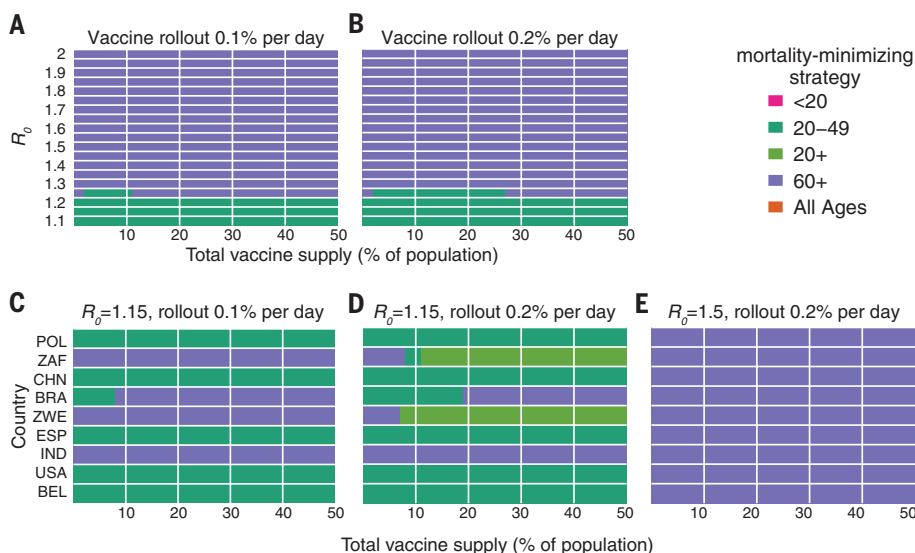


Fig. 2. Mortality-minimizing vaccine prioritization strategies across reproductive numbers R_0 and countries. (A to E) Heatmaps show the prioritization strategies that result in maximum reduction of mortality for varying values of [(A) and (B)] the basic reproductive number R_0 and [(C), (D), and (E)] across nine countries, for vaccine supplies between 1 and 50% of the total population, for an all-or-nothing and transmission-blocking vaccine, 90% vaccine efficacy. [(A) and (B)] Contact patterns and demographics of the United States (38, 53). [(C), (D), and (E)] Contact patterns and demographics of POL, Poland; ZAF, South Africa; CHN, China; BRA, Brazil; ZWE, Zimbabwe; ESP, Spain; IND, India; USA, United States of America; and BEL, Belgium, with R_0 and rollout speeds as indicated.

$R_0 \geq 1.3$, but prioritizing adults aged 20 to 49 years was superior for $R_0 \leq 1.2$ (Fig. 2, A and B, and fig. S8). Prioritizing adults aged 20 to 49 years minimized infections for all values of R_0 investigated (fig. S8).

To determine whether our findings were robust across countries, we analyzed the ranking of prioritization strategies for populations with the age distributions and modeled contact structures of the United States, Belgium, Brazil, China, India, Poland, South Africa, and Spain. Across these countries, direct vaccination of adults aged 60+ years minimized mortality for all levels of vaccine supply when transmission was high ($R_0 = 1.5$, scenario 2) (Fig. 2E) but in only some cases when transmission was lower ($R_0 = 1.15$, rollout 0.2% per day, scenario 1) (Fig. 2D). Decreasing rollout speed from 0.2% to 0.1% per day caused prioritization of adults aged 60+ years to be favored in additional scenarios (Fig. 2C). Across countries, vaccination of adults aged 20 to 49 years nearly always minimized infections, and vaccination of adults aged 60+ years nearly always minimized YLL for scenario 2, but no clear ranking of strategies emerged consistently to minimize YLL in scenario 1 (fig. S9).

Vaccines with imperfect transmission-blocking effects

We also considered whether the rankings of prioritization strategies to minimize mortality would change if a vaccine were to block

COVID-19 symptoms and mortality with 90% efficacy across age groups in preventing infection or disease, a phenomenon known to affect influenza vaccines (23–26). To understand the impact of age-dependent COVID-19 vaccine efficacy, we incorporated a hypothetical linear decrease from a baseline efficacy of 90% for those younger than 60 years to 50% in those 80 years and older (Fig. 3). As expected, this diminished the benefits of any prioritization strategy that included older adults. For example, strategies that prioritize adults aged 20 to 49 years were unaffected by decreased efficacy among adults aged 60+ years, whereas strategies prioritizing adults aged 60+ years were markedly diminished (Fig. 3). Despite these effects, prioritization of adults aged 60+ years remained superior to the alternative strategies to minimize mortality in scenario 2.

Variation in vaccine efficacy by age

COVID-19 vaccines may not be equally effective across age groups in preventing infection or disease, a phenomenon known to affect influenza vaccines (23–26). To understand the impact of age-dependent COVID-19 vaccine efficacy, we incorporated a hypothetical linear decrease from a baseline efficacy of 90% for those younger than 60 years to 50% in those 80 years and older (Fig. 3). As expected, this diminished the benefits of any prioritization strategy that included older adults. For example, strategies that prioritize adults aged 20 to 49 years were unaffected by decreased efficacy among adults aged 60+ years, whereas strategies prioritizing adults aged 60+ years were markedly diminished (Fig. 3). Despite these effects, prioritization of adults aged 60+ years remained superior to the alternative strategies to minimize mortality in scenario 2.

To test whether more substantial age-dependent vaccine effects would change which

strategy minimized mortality in scenario 2, we varied the onset age of age-dependent decreases in efficacy, the extent to which it decreased, and the baseline efficacy from which it decreased. We found that as long as the age at which efficacy began to decrease was 70 years or older and vaccine efficacy among adults aged 80+ years was at least 25%, prioritizing adults aged 60+ years remained superior in the majority of parameter combinations. This finding was robust to whether the vaccine was modeled as leaky versus all or nothing, but we observed considerable variation from country to country (fig. S11).

Incorporation of population seroprevalence and individual serological testing

Because of early indications that naturally acquired antibodies correlate with protection from reinfection (27), seroprevalence will affect vaccine prioritization in two ways. First, depending on the magnitude and age distribution of seroprevalence at the time of vaccine distribution, the ranking of strategies could change. Second, distributing vaccines to seropositive individuals would reduce the marginal benefit of vaccination per dose.

To investigate the impact of vaccinating mid-epidemic while using serology to target the vaccine to seronegative individuals, we included age-stratified seroprevalence estimates in our model by moving the data-specified proportion of seropositive individuals from susceptible to recovered status. We then simulated two approaches to vaccine distribution. In the first, vaccines were distributed according to the five prioritization strategies introduced above, regardless of any individual's serostatus. In the second, vaccines were distributed with a serological test, so that individuals with a positive serological test would not be vaccinated, allowing their dose to be given to someone else in their age group.

We included age-stratified seroprevalence estimates from New York City [August 2020; overall seroprevalence 26.9% (28)] and demographics and age-contact structure from the United States in evaluations of the previous five prioritization strategies. For this analysis, we focused on scenario 2 (0.2% rollout per day, $R_0 = 1.5$ inclusive of seropositives) and found that the ranking of strategies to minimize incidence, mortality, and YLL remained unchanged: Prioritizing adults aged 60+ years most reduced mortality, and prioritizing adults aged 20 to 49 years most reduced incidence, regardless of whether vaccination was limited to seronegative individuals (Fig. 4). These rankings were unchanged when we used lower or higher age-stratified seroprevalence estimates to test the consistency of results [Connecticut, July 2020, overall seroprevalence 3.4% (29) and synthetic, overall seroprevalence 39.5%] (figs. S12 and S13). Despite

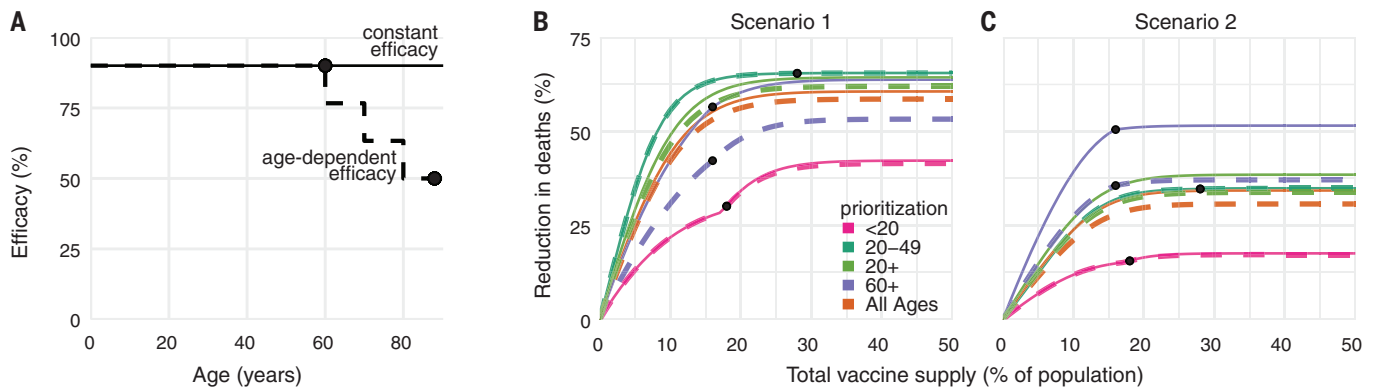


Fig. 3. Effects of age-dependent vaccine efficacy on the impacts of prioritization strategies. (A) Diagram of hypothetical age-dependent vaccine efficacy shows decrease from 90% baseline efficacy to 50% efficacy among individuals aged 80+ years, beginning at age 60 (dashed line). (B and C) Percent reduction in deaths in comparison with an unmitigated outbreak for transmission-blocking all-or-nothing vaccines with either constant 90% efficacy for all ages

groups (solid lines) or age-dependent efficacy shown in (A) (dashed lines), covering scenario 1 [0.2% rollout per day, $R_0 = 1.15$; (B)] and scenario 2 [0.2% rollout per day, $R_0 = 1.5$ (C)]. Black dots indicate break points at which prioritized demographic groups have been 70% vaccinated, after which vaccines are distributed without prioritization. Shown are contact patterns and demographics of the United States (38, 53); all-or-nothing and transmission-blocking vaccine.

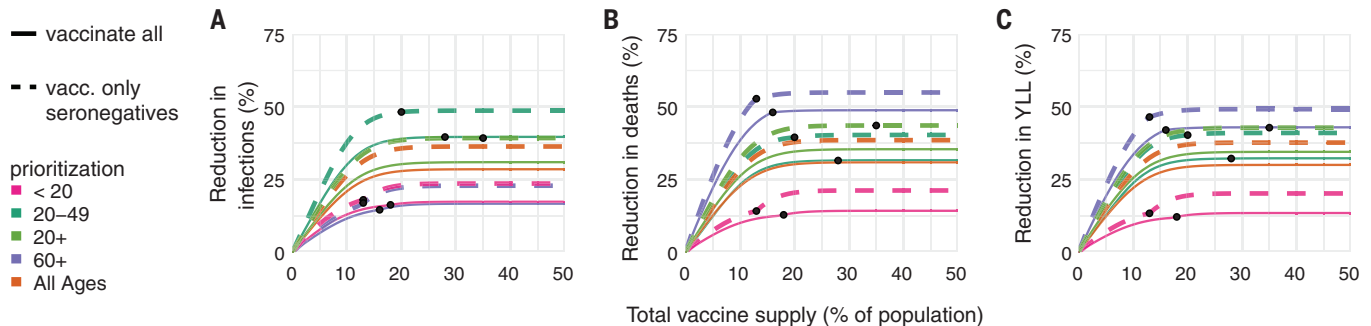


Fig. 4. Effects of existing seropositivity on the impacts of prioritization strategies. (A to C) Percent reductions in (A) infections, (B) deaths, and (C) years of life lost (YLL) for prioritization strategies when existing age-stratified seroprevalence is incorporated [August 2020 estimates for New York City; mean seroprevalence 26.9% (28)]. Plots show reductions for scenario 2 (0.2% rollout per day, $R_0 = 1.5$) when vaccines are given to all individuals (solid lines) or to only

seronegatives (dashed lines), inclusive of 96% serotest sensitivity, 99% specificity (54), and approximately 3 months of seroreversion (supplementary materials, materials and methods) (29). Shown are U.S. contact patterns and demographics (38, 53), all-or-nothing and transmission-blocking vaccine with 90% vaccine efficacy. Lower and higher seroprevalence examples are provided in figs. S12 and S13, respectively.

lowered sensitivity to detect past exposure due to seroreversion (30, 31), preferentially vaccinating seronegative individuals yielded large additional reductions in cumulative incidence and mortality in locations with higher seroprevalence (Fig. 4 and fig. S13) and modest reductions in locations with low seroprevalence (fig. S12). These results remained unchanged when statistical uncertainty, because of sample size and imperfect test sensitivity and specificity, was incorporated into the model (32).

Discussion

This study demonstrated the use of an age-stratified modeling approach to evaluate and compare vaccine prioritization strategies for SARS-CoV-2. After accounting for country-specific age structure, age-contact structure, infection fatality rates, and seroprevalence, as well as the age-varying efficacy of a hypothet-

ical vaccine, we found that across countries, those aged 60 years and older should be prioritized to minimize deaths, assuming a return to high contact rates and prepandemic behavior during or after vaccine rollout. This recommendation is robust because of the dramatic differences in IFR by age. Our model identified three general regimes in which prioritizing adults aged 20 to 49 years would provide greater mortality benefits than would prioritizing older adults. One such regime was in the presence of substantial transmission-mitigating interventions ($R_0 = 1.15$) and a vaccine with 80% or higher transmission-blocking effects. A second regime was characterized by substantial transmission-mitigating interventions ($R_0 = 1.15$) and either rollout speeds of at most 0.2% per day or vaccine supplies of at most 25% of the population. The third regime was characterized by vaccines with very low efficacy in

older adults, very high efficacy in younger adults, and declines in efficacy starting at age 59 or 69 years. The advantage of prioritizing all adults or adults aged 20 to 49 versus 60+ years was small under these conditions. Thus, we conclude that for mortality reduction, prioritization of older adults is a robust strategy that will be optimal or close to optimal to minimize mortality for virtually all plausible vaccine characteristics.

By contrast, the ranking of infection-minimizing strategies for midepidemic vaccination led to consistent recommendations to prioritize adults aged 20 to 49 years across efficacy values and countries. For pretransmission vaccination, prioritization shifted toward children and teenagers for leaky vaccine efficacies 50% and below, which is in line with prior work (7), as well as for vaccines with weak transmission-blocking properties. Because a vaccine is likely

to have properties of both leaky and all-or-nothing models, empirical data on vaccine performance could help resolve this difference in model recommendations, although data are difficult to obtain in practice [for example, (33, 34)].

It is not yet clear whether the first generation of COVID-19 vaccines will be approved everywhere for the elderly or those under 18 years of age (35–37). Although our conclusions assumed that the vaccine would be approved for all age groups, the evaluation approaches introduced here can be tailored to evaluate a subset of approaches restricted to those within the age groups for which a vaccine is licensed, by using open-source tools such as those that accompany this study. Furthermore, although we considered three possible goals of vaccination—minimizing cumulative incidence, mortality, or YLL—our framework can be adapted to consider goals such as minimizing hospitalizations, intensive care unit occupancy (7), or economic costs (10).

We demonstrated that there is value in pairing individual-level serological tests with vaccination, even when accounting for the uncertainties in seroprevalence estimates (32) and seroreversion (30). The marginal gain in effective vaccine supply, relative to no serological testing, must be weighed against the challenges of serological testing before vaccination. Serostatus itself is an imperfect indicator of protection, and the relationship of prior infection, serostatus, and protection may change over time (10, 27, 30, 31). Delays in serological test results would impair vaccine distribution, but partial seronegative-targeting effects might be realized if those with past polymerase chain reaction (PCR)-confirmed infections voluntarily deprioritized their own vaccinations.

The best-performing strategies depend on assumptions about the extent of a population's interactions. We used prepandemic contact matrices (38), reflecting the goal of a return to prepandemic routines once a vaccine is available, but more recent estimates of age-stratified contact rates could be valuable in modeling midpandemic scenarios (39, 40). Whether prepandemic or midpandemic contact estimates are representative of contact patterns during vaccine rollout remains unknown and may vary on the basis of numerous social, political, and other factors. The scenarios modeled here did not incorporate explicit nonpharmaceutical interventions, which might persist if vaccination coverage is incomplete, but are implicitly represented in scenario 1 ($R_0 = 1.15$).

Our study relies on estimates of other epidemiological parameters. In local contexts, these include age-structured seroprevalence and IFR, which vary by population (19, 20, 41). Globally, key parameters include the degree to which antibodies protect against reinfection

or severity of disease and relative infectiousness by age. From vaccine trials, we also need evidence of efficacy in groups vulnerable to severe outcomes, including the elderly. Additionally, it will be critical to measure whether a vaccine that protects against symptomatic disease also blocks infection and transmission of SARS-CoV-2 (42).

The role of children during this pandemic has been unclear. Under our assumptions about susceptibility by age, children are not the major drivers of transmission in communities, which is consistent with emerging evidence (12). Thus, our results differ from the optimal distribution for influenza vaccines, which prioritize school-age children and adults aged 30 to 39 years (5). However, the relative susceptibility and infectiousness of SARS-CoV-2 by age remain uncertain. Although it is unlikely that susceptibility to infection conditional on exposure is constant across age groups (12), we ran our model to test the sensitivity of this parameter. Under the scenario of constant susceptibility by age, vaccinating those under 20 years of age has a greater impact on reducing cumulative cases than vaccinating those aged 20 to 49 years (figs. S14 and 15).

Our study is subject to a number of limitations. First, our evaluation strategy focuses on a single country at a time, rather than on between-population allocation (43). Second, we only consider variation in disease severity by age. However, other factors correlate with disease outcomes, such as treatment and health care access and comorbidities, which may correlate with factors such as rural versus urban location, socioeconomic status, sex (44, 45), and race and ethnicity (46), which are not accounted for in this study. Inclusion of these factors in a model would be possible, but only with statistically sound measurements of their stratified infection risk, contact rates, and disease outcomes. Even in the case of age stratification, contact surveys have typically not surveyed those 80 years and older, yet it is this population that suffers dramatically more severe COVID-19 disease and higher infection fatality rates. We extrapolated contact matrices to those older than 80, but direct measurements would be superior. Last, our study focused on guiding strategy rather than providing more detailed forecasting or estimates (10). As such, we have not made detailed parameter fits to time series of cases or deaths but rather have used epidemiologic models to identify robust strategies across a range of transmission scenarios.

Our study also considers variation in disease risk only by age, through age-structured contact matrices and age-specific susceptibility, whereas many discussions around COVID-19 vaccine distribution have thus far focused on prioritizing health care or essential workers

(47, 48). Contact rates, and thus infection potential, vary greatly not only by occupation and age but also by living arrangement (such as congregate settings or dormitories), neighborhood and mobility (49–52), and whether the population has a coordinated and fundamentally effective policy to control the virus. With a better understanding of population structure during the pandemic, and risk factors of COVID-19, these limitations could be addressed. Meanwhile, the robust findings in favor of prioritizing those age groups with the highest IFR to minimize mortality could potentially be extended to prioritize those with comorbidities that predispose them to a high IFR because the strategy of prioritizing the older age groups depends on direct rather than indirect protection.

Vaccine prioritization is not solely a question of science but a question of ethics as well. Hallmarks of the COVID-19 pandemic, as with other global diseases, are inequalities and disparities. Although these modeling efforts focus on age and minimizing incidence and death within a simply structured population, other considerations are crucial, from equity in allocation between countries to disparities in access to health care, including vaccination, that vary by neighborhood. Thus, the model's simplistic representation of vulnerability (age) should be augmented by better information on the correlates of infection risk and severity. Fair vaccine prioritization should avoid further harming disadvantaged populations. We suggest that after distribution, pairing serological testing with vaccination in the hardest-hit populations is one possible equitable way to extend the benefits of vaccination in settings where vaccination might otherwise not be deemed cost effective.

REFERENCES AND NOTES

1. Johns Hopkins University Coronavirus Research Center, COVID-19 Dashboard by the Center for Systems Science and Engineering at Johns Hopkins University (2020); <https://coronavirus.jhu.edu/map.html>.
2. R. Khamsi, *Nature* **580**, 578–580 (2020).
3. National Academies of Sciences, Engineering, and Medicine, *Framework for Equitable Allocation of COVID-19 Vaccine* (National Academies Press, 2020); <https://doi.org/10.17226/25917>.
4. D. Weycker et al., *Vaccine* **23**, 1284–1293 (2005).
5. J. Medlock, A. P. Galvani, *Science* **325**, 1705–1708 (2009).
6. S. Bansal, B. Pourbohloul, L. A. Meyers, *PLOS Med.* **3**, e387 (2006).
7. L. Matrajt, J. Eaton, T. Leung, E. R. Brown, *medRxiv* 20175257 [Preprint], 15 December 2020. <https://doi.org/10.1101/2020.08.14.20175257>.
8. M. E. Gallagher et al., *medRxiv* 20170456 [Preprint], 11 August 2020. <https://doi.org/10.1101/2020.08.07.20170456>.
9. J. H. Buckner, G. Chowell, M. R. Springborn, *medRxiv* 20199174 [Preprint], 6 October 2020. <https://doi.org/10.1101/2020.09.22.20199174>.
10. F. Sandmann et al., *medRxiv* 20200857 [Preprint], 25 September 2020. <https://doi.org/10.1101/2020.09.24.20200857>.
11. C. J. Worby, H.-H. Chang, *Nat. Commun.* **11**, 4049 (2020).

12. E. Goldstein, M. Lipsitch, M. Cevik, *J. Infect. Dis.* **2020**, jiaa691 (2020).
13. N. G. Davies *et al.*, *Nat. Med.* **26**, 1205–1211 (2020).
14. J. Zhang *et al.*, *Science* **368**, 1481–1486 (2020).
15. S. Herzog *et al.*, medRxiv 20125179 [Preprint] (2020). <https://doi.org/10.1101/2020.06.08.20125179>.
16. A. L. Mueller, M. S. McNamara, D. A. Sinclair, *Aging (Albany NY)* **12**, 9959–9981 (2020).
17. Y. Liu *et al.*, *Eur. Respir. J.* **55**, 2001112 (2020).
18. J. Westmeier *et al.*, *mBio* **11**, e02243–e0240 (2020).
19. A. T. Levin *et al.*, *Eur. J. Epidemiol.* **35**, 1123–1138 (2020).
20. H. Salje *et al.*, *Science* **369**, 208–211 (2020).
21. K. M. Bubar *et al.*, *kbubar/vaccine_prioritization*: Updated code for published paper. Zenodo (2020).
22. M. Brennan, Willingness to Get COVID-19 Vaccine Ticks Up to 63% in U.S., Online (8 December 2020); <https://news.gallup.com/poll/327425/willingness-covid-vaccine-ticks.aspx>.
23. P. A. Gross, A. W. Hermogenes, H. S. Sacks, J. Lau, R. A. Levandowski, *Ann. Intern. Med.* **123**, 518–527 (1995).
24. J. K. H. Lee *et al.*, *Expert Rev. Vaccines* **17**, 435–443 (2018).
25. T. M. E. Govaert *et al.*, *JAMA* **272**, 1661–1665 (1994).
26. J. A. Lewnard, S. Cobey, *Vaccines* **6**, 28 (2018).
27. S. F. Lumley *et al.*, *N. Engl. J. Med.* 10.1056/NEJMoa2034545 (2020).
28. City of New York, COVID-19 data (2020); www1.nyc.gov/site/doh/covid/covid-19-data-testing.page.
29. K. L. Bajema *et al.*, *JAMA Intern. Med.* 10.1001/jamainternmed.2020.7976 (2020).
30. H. Ward *et al.*, medRxiv 20219725 [Preprint] 27 October 2020. <https://doi.org/10.1101/2020.10.26.20219725>.
31. J. M. Dan *et al.*, bioRxiv 383323 [Preprint] 18 December 2020. <https://doi.org/10.1101/2020.11.15.383323>.
32. D. B. Larremore *et al.*, medRxiv 20067066 [Preprint] 22 June 2020. <https://doi.org/10.1101/2020.04.15.20067066>.
33. D. Ellenberger *et al.*, *Virology* **352**, 216–225 (2006).
34. K. E. Langwig *et al.*, *mBio* **8**, e00796-17 (2017).
35. P. Span, “Older adults may be left out of some COVID-19 trials,” *The New York Times* 19 June 2020; <https://www.nytimes.com/2020/06/19/health/vaccine-trials-elderly.html>.
36. H. R. Sharpe *et al.*, *Immunology* **160**, 223–232 (2020).
37. M. Kornfield, “When will children get a coronavirus vaccine? Not in time for the new school year, experts fear,” *The Washington Post* 2 December 2020; www.washingtonpost.com/health/2020/12/02/kids-vaccine-delay.
38. K. Prem *et al.*, medRxiv 20159772 [Preprint] (2020); <https://doi.org/10.1101/2020.07.22.20159772>.
39. C. I. Jarvis *et al.*, *BMC Med.* **18**, 124 (2020).
40. J. A. Backer *et al.*, medRxiv 20101501 [Preprint] 16 October 2020. <https://doi.org/10.1101/2020.05.18.20101501>.
41. S. Ghisolfi *et al.*, “Predicted COVID-19 fatality rates based on age, sex, comorbidities, and health system capacity,” working paper (Center for Global Development, 2020).
42. M. Lipsitch, N. E. Dean, *Science* **370**, 763–765 (2020).
43. L. E. Duijzer, W. L. van Jaarsveld, J. Wallinga, R. Dekker, *Prod. Oper. Manag.* **27**, 143–159 (2018).
44. T. Takahashi *et al.*, *Nature* **588**, 315–320 (2020).
45. D. Chakravarty *et al.*, *Commun. Biol.* **3**, 374 (2020).
46. M. Webb Hooper, A. M. Nápoles, E. J. Pérez-Stable, *JAMA* **323**, 2466–2467 (2020).
47. M. Jenco, “CDC vaccine committee may prioritize health care workers for COVID-19 vaccines,” *AAP News* 27 August 2020; <https://www.aappublications.org/news/2020/08/27/covid19vaccinepriorities082620>.
48. J. Cohen, *Science* **369**, 15–16 (2020).
49. S. Mishra, J. C. Kwong, A. K. Chan, S. D. Baral, *CMAJ* **192**, E684–E685 (2020).
50. L. Hawks, S. Woolhandler, D. McCormick, *JAMA Intern. Med.* **180**, 1041–1042 (2020).
51. H. S. Badr *et al.*, *Lancet Infect. Dis.* 10.1016/S1473-3099(20)30861-6 (2020).
52. J. Ducharme, “These maps show how drastically COVID-19 risk varies by neighborhood,” *Time* 22 July 2020; <https://time.com/5870041/COVID-19-neighborhood-risk>.
53. United Nations Department of Economic and Social Affairs Population Division, World population prospects (2019); <https://population.un.org/wpp>.
54. C. H. GeurtsvanKessel *et al.*, *Nat. Commun.* **11**, 3436 (2020).

ACKNOWLEDGMENTS

The authors thank S. Herzog, M. Jit, J. Wallinga, and H. Johnson for their feedback. **Funding:** K.M.B. was supported in part by the Interdisciplinary Quantitative Biology (IQ Biology) Ph.D. program at the BioFrontiers Institute, University of Colorado Boulder. K.M.B. and D.B.L. were supported in part through the MIDAS Coordination Center (MIDASNI2020-2) by a grant from the National Institute of General Medical Science (3U24GM132013-02S2). M.L., S.M.K., and Y.H.G. were supported in part by the Morris-Singer Fund for the Center for Communicable Disease Dynamics at the Harvard T. H. Chan School of Public Health. M.L. and D.B.L. were supported in part by the SeroNet program of the National Cancer Institute (1U01CA261277-01). **Author contributions:** K.M.B., S.M.K., M.L., S.C., Y.H.G., and D.B.L. conceived of the study. K.M.B. and D.B.L. performed the analyses. K.M.B. and K.R. generated all figures. K.R. created interactive visualization tools. All authors wrote and revised the manuscript. **Competing interests:** M.L. discloses honoraria from and consulting for Merck, Affinivax, Sanofi-Pasteur, Bristol Myers Squibb, and Antigen Discovery; research funding (institutional) from Pfizer; and unpaid scientific advice to Janssen, Astra-Zeneca, and Covaxx (United Biomedical); M.L. is an honorary faculty member, Wellcome Sanger

Institute, and an associate member, Broad Institute. Y.H.G. discloses consulting for Merck and GlaxoSmithKline, and research funding from Pfizer not related to this project or topic. D.B.L. is a member of the scientific advisory board of Darwin BioSciences. **Data and materials availability:** Reproduction code is open source and provided by the authors (21). This work is licensed under a Creative Commons Attribution 4.0 International (CC BY 4.0) license, which permits unrestricted use, distribution, and reproduction in any medium, provided the original work is properly cited. To view a copy of this license, visit <https://creativecommons.org/licenses/by/4.0/>. This license does not apply to figures/photos/artwork or other content included in the article that is credited to a third party; obtain authorization from the rights holder before using such material.

SUPPLEMENTARY MATERIALS

science.sciencemag.org/content/371/6532/916/suppl/DC1
Materials and Methods
Supplementary Text
Figs. S1 to S15
Tables S1 and S2
References (55–57)
MDAR Reproducibility Checklist

8 September 2020; accepted 12 January 2021
Published online 21 January 2021
10.1126/science.abe6959

ATMOSPHERIC CHEMISTRY

Reactive uptake of N₂O₅ by atmospheric aerosol is dominated by interfacial processes

Mirza Galib¹ and David T. Limmer^{1,2,3,4*}

Nitrogen oxides are removed from the troposphere through the reactive uptake of N₂O₅ into aqueous aerosol. This process is thought to occur within the bulk of an aerosol, through solvation and subsequent hydrolysis. However, this perspective is difficult to reconcile with field measurements and cannot be verified directly because of the fast reaction kinetics of N₂O₅. Here, we use molecular simulations, including reactive potentials and importance sampling, to study the uptake of N₂O₅ into an aqueous aerosol. Rather than being mediated by the bulk, uptake is dominated by interfacial processes due to facile hydrolysis at the liquid-vapor interface and competitive reevaporation. With this molecular information, we propose an alternative interfacial reactive uptake model consistent with existing experimental observations.

The reactive uptake of N₂O₅ in the atmospheric aerosol plays a key role in establishing the oxidative power of the troposphere and is a major factor in determining air quality and climate (*1, 2*). In nighttime air, NO and NO₂ are oxidized by O₃ to form NO₃ and N₂O₅ (*3*). Between 25 and 41% of that tropospheric N₂O₅ is thought to be subsequently removed by hydrolysis to HNO₃ in aqueous aerosol (*4, 5*). Experimentally, only the overall reactive uptake of N₂O₅ gas to aqueous aerosol can be measured (*6*). However, a molecular-level understanding of that process is lacking, frustrating attempts to rationalize variations in field measurements

(*7–11*). We used state-of-the-art computational tools, including machine learning–based reactive force fields (*12, 13*) and methods of importance sampling molecular dynamics simulations, to determine that the hydrolysis of N₂O₅ in aqueous aerosol is fast and subsequently that interfacial processes dominate its reactive uptake. This finding is inconsistent with traditional models of reactive uptake, which assume reaction-limited bulk hydrolysis and equilibrium solvation (*6, 8, 10, 14*). Rather, we show with explicit simulations that reactive uptake can be understood as a result of competition between interfacial hydrolysis and evaporation. This interfacial model of N₂O₅ reactive uptake can reasonably reproduce the experimental reactive uptake coefficient on pure water droplets. This model also helps to rationalize a number of existing experimental observations, including the temperature dependence of the uptake coefficient and the

¹Department of Chemistry, University of California, Berkeley, CA, USA. ²Kavli Energy NanoScience Institute, Berkeley, CA, USA. ³Materials Science Division, Lawrence Berkeley National Laboratory, Berkeley, CA, USA. ⁴Chemical Science Division, Lawrence Berkeley National Laboratory, Berkeley, CA, USA. *Corresponding author. Email: dlimmer@berkeley.edu

similarity between the uptake coefficients on ice particles and liquid water droplets, and can be extended to consider the dependence on organic and inorganic species.

Under standard conditions, reactive uptake is determined by the uptake coefficient, γ , which is the fraction of N_2O_5 molecules that collide with an aerosol surface and are irreversibly lost through reaction. Measurements of γ in pure water vary, with $0.01 \leq \gamma \leq 0.08$ (8, 10). Uptake on pure water represents an idealized case of dilute solution conditions as might be found in fog or cloud droplets, because contributions from surface-active organics and soluble inorganic salts can change uptake in complex ways (7, 8, 15, 16). The size of γ and its dependence on solution composition and thermodynamic state is currently rationalized with simplified kinetic models (6, 10, 17). Unfortunately, the basic physical and chemical properties of N_2O_5 , like its solubility and hydrolysis rate constant, which are needed to validate assumptions made in such models are not available. Therefore, a model capable of directly interrogating the molecular dynamics that transfer an initially gaseous N_2O_5 molecule into its solution hydrolysis products is needed.

Molecular simulations can in principle be used to gain microscopic insight into the reactive uptake of atmospheric gases into solution (6). Classical force fields have been used to study the physical solvation of N_2O_5 (18, 19), where it is computationally tractable to use enhanced sampling methods and represent large inhomogeneous systems. However, existing potentials are not suitable to model chemical reactions, precluding a study of the hydrolysis reaction. Ab initio molecular dynamics has been used to study hydrolysis and halide substitution reactions of N_2O_5 in water clusters (20–24).

However, studying systems large enough to represent inhomogeneous systems (25) or to evolve systems long enough to study rare events is difficult. To overcome these limitations, we used machine learning techniques to fit a high-dimensional reactive potential to ab initio training data. The resultant potential allows us to access larger length and time scales than typical ab initio simulations, but with comparable accuracy. In so doing we are able to use advanced simulation methods to uncover a complete picture of the thermodynamics and reactive dynamics that lead to the uptake of N_2O_5 .

To simulate the hydrolysis of N_2O_5 in liquid water, we developed a reactive force field capable of describing a broad ensemble of solvation and bonding configurations. Specifically, we constructed a model using ab initio reference data fit to a flexible artificial neural network functional. We used supervised and active learning procedures on a range of condensed-phase and reactive-path structures (26). The artificial neural networks are trained on reference energies and forces computed from density functional theory (27, 28), which provides an accurate description of aqueous solution structure and thermodynamics (29–32) and which we additionally benchmarked for N_2O_5 gas-phase dissociation energies (table S1). The resultant reactive force field accurately represents the ab initio potential-energy surface of water and N_2O_5 (tables S2 and S3), but at a substantially reduced computational cost, enabling the systematic study of the thermodynamics and kinetics of solvated N_2O_5 and its hydrolysis products (figs. S1 to S8).

Thermodynamics of solvation and hydrolysis

Figure 1A shows a characteristic snapshot of N_2O_5 and its surrounding solvation environ-

ment generated from our neural network force field. The intramolecular structure of the solvated N_2O_5 is characterized by large fluctuations in the position of the center oxygen (fig. S9). These fluctuations manifest the tendency of N_2O_5 to spontaneously undergo intramolecular charge separation, localizing excess positive charge in an emergent $\text{NO}_2^{\delta+}$ moiety and excess negative charge in an $\text{NO}_3^{\delta-}$ moiety, as a transient precursor to dissociation (19, 24). Despite the transient charge separation, we find that N_2O_5 is relatively weakly solvated on average (fig. S10). Water forms less than one hydrogen bond with the outer oxygens on average and even fewer with the nitrogens and bridging oxygen, resulting in an unstructured solvation shell. This is because the localization of the charge is primarily on the nitrogens, which are sterically inaccessible.

The observed hydration structure is consistent with N_2O_5 being sparingly soluble in water. To quantify the driving force for dissolving N_2O_5 in water, we computed the solvation free energy using thermodynamic perturbation theory (tables S5 and S6). The resultant solvation free energy, $F_s = 1.3 \pm 0.5$ kcal/mol, implies a Henry's law constant of $H = 0.4 \pm 0.1$ M/atm. H is smaller than has been inferred from previous mass uptake experiments, which showed a range from 1 to 10 M/atm (33). However, the interpretation of such experiments is difficult because of the inability to separate solvation from subsequent hydrolysis. For a molecule with a dipole, this solubility is relatively low, though it is only modestly smaller than that of less-reactive nitrogen oxides (34). The low solubility reflects a subtle interplay between favorable long-range electrostatic energetics and a large unfavorable cavity formation entropy.

The hydrolysis of N_2O_5 in liquid water is thermodynamically favorable. We calculated the free energy for dissociating N_2O_5 using umbrella sampling. Specifically, we computed the free energy, $F(R)$, as a function of the intramolecular nitrogen–nitrogen distance, R . The free energy is shown in Fig. 1B and exhibits a narrow minimum at $R = 2.6$ Å and a broad plateau for $R > 4$ Å, separated by a barrier at $R = 3$ Å. The minimum at $R = 2.6$ Å reflects the intact N_2O_5 molecule, as shown in Fig. 1A, whereas the plateau for $R > 4$ Å manifests its dissociation. We find that at large R , it is thermodynamically favorable to form two equivalents of HNO_3 (Fig. 1A). The barrier region is wide, because large separations are needed to solvate the separated nitrogens. A barrier of nearly 4 kcal/mol implies that hydrolysis is a rare event and that N_2O_5 can be dynamically distinguished from its eventual hydrolysis products. The free energy difference between the reactant and product basin results in a dissociation constant of 1.3×10^4 M. The low solubility of N_2O_5 implies that nearly all solvated N_2O_5 in pure water is transformed to HNO_3 .

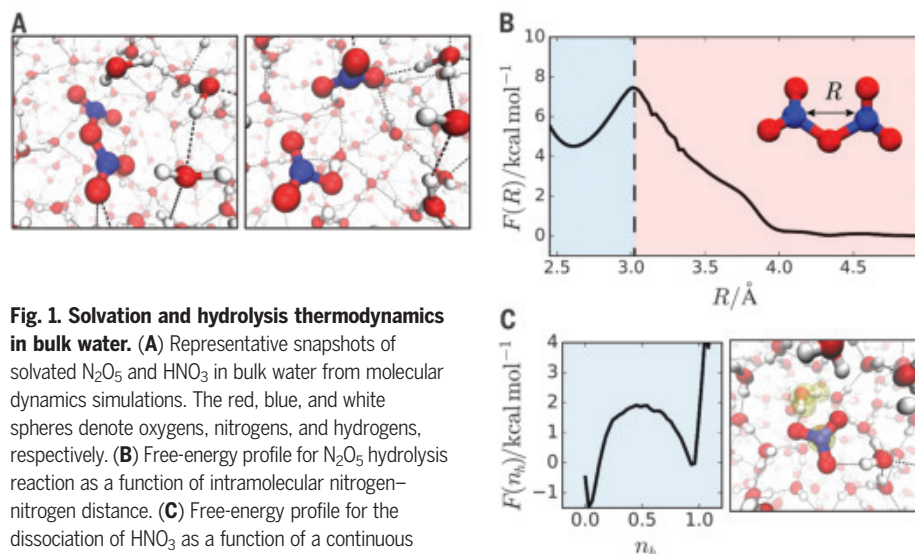
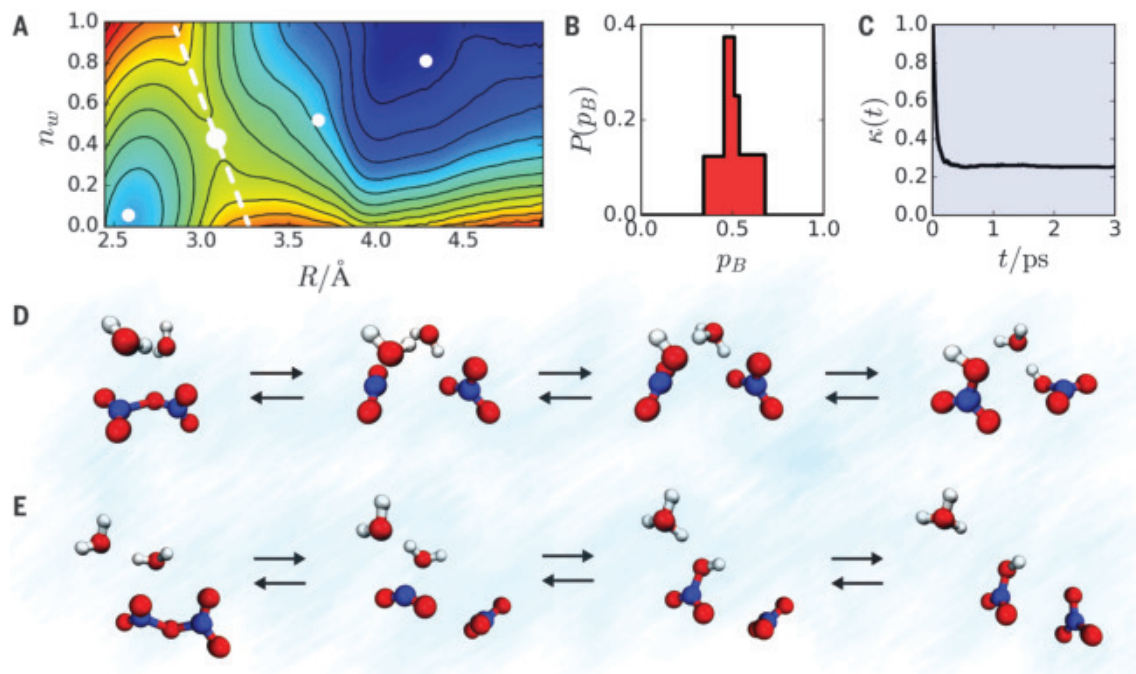


Fig. 1. Solvation and hydrolysis thermodynamics in bulk water. (A) Representative snapshots of solvated N_2O_5 and HNO_3 in bulk water from molecular dynamics simulations. The red, blue, and white spheres denote oxygens, nitrogens, and hydrogens, respectively. (B) Free-energy profile for N_2O_5 hydrolysis reaction as a function of intramolecular nitrogen–nitrogen distance. (C) Free-energy profile for the dissociation of HNO_3 as a function of a continuous coordination number between an O in the NO_3 moiety and a hydrogen, n_h (left). A characteristic snapshot of dissociated HNO_3 from molecular dynamics trajectory is shown, where the excess proton is highlighted in yellow (right).

Fig. 2. Kinetics and microscopic reaction mechanisms for the hydrolysis of N_2O_5 in bulk water. (A) Free energy as a function of the intramolecular nitrogen–nitrogen distance and a continuous water coordination number, n_w . Lines are spaced 1 kcal/mol apart, and the dashed line plots the separatrix. The circles indicate the approximate location of configurations in (D) and (E). (B) Distribution of commitment probabilities to the product basin, p_B , for configurations taken along the separatrix in (A). (C) Transmission coefficient, $\kappa(t)$, as a function of time.



(D) Representative snapshots along a molecular dynamics trajectory in which two protonated nitric acids are formed through the concerted ionization of water and addition of the OH^- to the NO_2^+ moiety, followed by proton transfer to the NO_3^- moiety. (E) Representative snapshots along a molecular dynamics trajectory in which hydrolysis of N_2O_5 into one HNO_3 and one NO_3^- proceeds through the concerted ionization of water and addition of the OH^- to the NO_2^+ moiety.

After hydrolysis, it is thermodynamically favorable for the nascent nitric acid to dissociate into an excess proton and NO_3^- . We computed the free energy to deprotonate HNO_3 by monitoring a continuous coordination number, n_h , between the oxygens on the NO_3 moiety and a hydrogen (26). The free energy, $F(n_h)$, can be estimated directly from simulations and is shown in Fig. 1C. The free energy difference for removing a proton corresponds to a $\text{p}K_a$ value of -1.1 (where K_a is the acid dissociation constant), which is reasonably close to the experimental value of -1.35 (35).

Taken together, the calculated thermodynamics of N_2O_5 solvation and subsequent hydrolysis in water are consistent with experimental observations that its accommodation into aqueous aerosol is largely irreversible (6). Though weakly soluble, in water N_2O_5 will undergo hydrolysis to form two HNO_3 , which will subsequently deprotonate. Under high nitrate concentrations, or in low-humidity droplets, this equilibrium could be shifted back toward an intact N_2O_5 . Indeed, low-water content droplets are observed to have smaller reactive uptake coefficients, and dissolved nitrate salts can reduce the reactive uptake by more than an order of magnitude (8, 34).

Kinetics of N_2O_5 hydrolysis

The mechanism of N_2O_5 hydrolysis involves an interplay between intramolecular charge

separation and stabilization from the surrounding water. To understand this interplay, we identified a reaction coordinate that encodes the microscopic details relevant to hydrolysis in solution. An appropriate reaction coordinate is one that is capable of both distinguishing the intact N_2O_5 from its dissociation products as well as characterizing the transition-state ensemble of configurations, which are those configurations that have equal probability of committing to either the reactant or product states (36). Although the nitrogen–nitrogen distance in Fig. 1B is capable of the former, it fails in the latter. Configurations taken at fixed values of R are overwhelmingly committed to either the reactant or product basins of attractions. This is because R lacks direct information about the surrounding water, which is pivotal in describing hydrolysis.

We have found that an appropriate reaction coordinate for hydrolysis is a linear combination of the nitrogen–nitrogen distance, R , and a continuous coordination number between the nitrogen atoms in N_2O_5 and the surrounding water molecules, denoted n_w (26). The coordination number acts as collective solvent coordinate and describes ion pairing and solvation dynamics in solution (37). Figure 2A shows the corresponding free energy surface, $F(n_w, R)$, computed using umbrella sampling. A line $n_w = 3R + 9.6$ defines a separatrix distinguishing the reactant and product basins. The direction orthogonal to the separatrix acts

as the reaction coordinate, ξ . For small R , the weak hydration structure of N_2O_5 is evident by the low value of n_w . The $\text{NO}_3^{\delta-}$ and $\text{NO}_2^{\delta+}$ pair generated at large R but $n_w = 0$ is not thermodynamically stable. The hydrolysis products, which are two equivalents of HNO_3 , at large R have an increased coordination number, $n_w \approx 1$, reflecting the altered bonding arrangement upon abstracting a water molecule. The saddle point of the surface, which we denote ξ^* , is located at an intermediate coordination number $n_w = 0.4$ and intermediate nitrogen–nitrogen distance $R = 3.1 \text{ \AA}$, with a free energy barrier $F(\xi^*) = 3.8 \text{ kcal/mol}$. The thermodynamically most likely reactive path follows the simultaneous increase in the nitrogen–nitrogen distance and coordination number. The increasing distance correlates with the lengthening of a N–O bond and accompanying charge reorganization, which is thermodynamically stabilized by a solvent fluctuation that alters the coordination number.

We used the Bennett-Chandler method (38) to quantify the rate constant for hydrolysis. Specifically, we computed the rate, k_h , as a product of the transition-state theory estimate and the transmission coefficient, $\kappa(t)$, where t is lag time. The transition-state theory estimate of the rate is computable from the free-energy surface. The transmission coefficient corrects transition-state theory for dynamical effects at the top of the barrier and is given by the plateau region of the flux-side

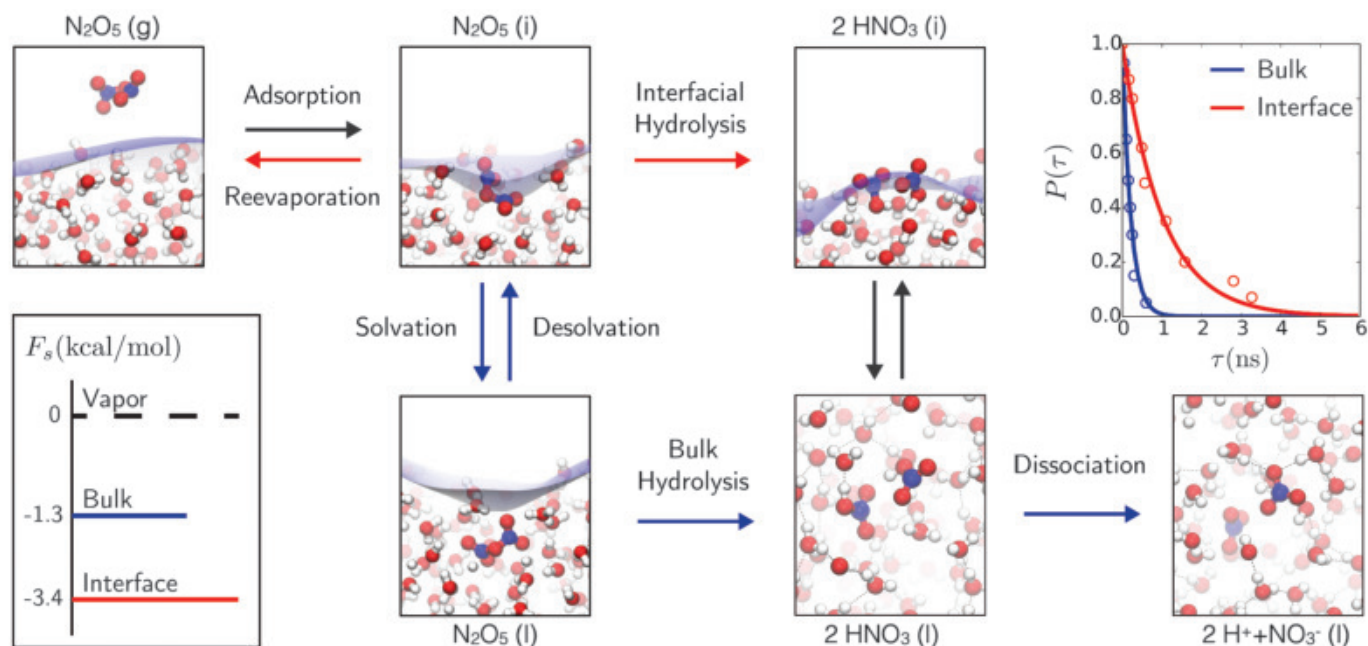


Fig. 3. Elementary physical and chemical steps involved in the reactive uptake of N_2O_5 in a pure-water droplet. Red denotes our proposed interfacial model, and blue refers to the standard bulk model. The images show an incoming N_2O_5 molecule first adsorbed at the liquid-vapor interface, which then either reacts to form HNO_3 or evaporates back into the gas phase. Diffusion into the bulk of the droplet is comparatively slow, but once in the bulk, N_2O_5 can undergo

hydrolysis. In either case, deprotonation of HNO_3 occurs after solvation into the bulk. The blue surface in the top images represents the location of the liquid-vapor interface. The probability distribution of the lifetime time of a N_2O_5 molecule, $P(\tau)$, at the air-water interface and in bulk water is shown at the top right. Solvation free energies of N_2O_5 at the air-water interface and in bulk compared with the gaseous N_2O_5 are shown at the bottom left.

correlation function. The transmission coefficient is shown in Fig. 2C. Taken together, we find the rate of hydrolysis $k_h = 4.1 \text{ ns}^{-1}$, implying an average lifetime of N_2O_5 to be nearly 240 ps. This time is in excellent agreement with that estimated from reactive trajectories propagated with direct dynamics.

Figure 2, D and E, show representative snapshots taken along typical hydrolysis pathways. Subsequent to passing through the transition state, we find that the ensemble of reactive pathways bifurcate, resulting in two different product states. In one pathway (Fig. 2D), two nitric acids are formed through the concerted ionization of water and addition of the OH^- to the NO_2^+ moiety, followed by proton transfer to the NO_3^- moiety. In the other pathway (Fig. 2E), one HNO_3 and one NO_3^- are formed. This process proceeds through the ionization of water and addition of the OH^- to the NO_2^+ ; however, the H_3O^+ generated does not have an existing hydrogen-bond wire to enable the subsequent donation of the proton to the NO_3^- . In our ensemble of trajectories, 20% of those follow the first pathway and 80% follow the latter one. These observations are similar to previous calculations for water clusters (21). During hydrolysis, we find that NO_2^+ is only formed transiently, with an average lifetime of 4 ps, and is better characterized by a hydrated H_2ONO_2^+ species. Once an HNO_3 molecule has its own independent

solvation shell, we find that dissociation occurs on average within 60 ps, or with a reaction rate of 15.4 ns^{-1} . The Grotthuss diffusion of the excess protons are well reproduced with our force field. We find a relative diffusivity of H_3O^+ to OH^- of 2.2 compared with the 1.9 measured experimentally (39).

Previous estimates of the hydrolysis rate for N_2O_5 in solution place it on the order of 10^{-3} to 10^{-4} ns^{-1} , or three to four orders of magnitude slower than our computed rate (40). However, like the solubility of N_2O_5 , this rate has been inferred indirectly from mass transfer models and has not been measured independently. The model that is most commonly invoked assumes equilibration between the vapor and bulk solution and is valid when uptake is reaction limited (6). Given the short lifetime of N_2O_5 in solution, this equilibrium assumption requires reevaluation. Indeed, the reaction diffusion length is small, defined as $l_D = \sqrt{D/k_h}$, where D is the self-diffusion constant of N_2O_5 . Within our model, $l_D \approx 1 \text{ nm}$ (table S4). As a consequence, we expect that N_2O_5 does not diffuse away from the interfacial region before reacting. This suggests that rather than being mediated by bulk solvation and subsequent reaction, reactive uptake of N_2O_5 is determined directly at the air-water interface, through a process of interfacial absorption and reaction. This is in agreement with some measurements on the particle size

dependence of reactive uptake, but not all (40, 41).

Interfacial model for N_2O_5 reactive uptake

The canonical kinetic model for the reactive uptake of N_2O_5 is the so-called resistor model (6, 14, 17, 42). This model assumes that the gas molecule is first accommodated at the surface, with probability α , and then diffuses from the surface to the bulk where the reaction takes place. The bulk reaction with rate k_h should be slow enough that an equilibrium can be established between the gas and the liquid phases, with concentrations determined by Henry's law constant H . Under these assumptions for the mass transfer kinetics, the reactive uptake coefficient, γ , can be estimated from

$$\gamma = \left(\frac{1}{\alpha} + \frac{v}{4k_B T H \sqrt{Dk_h}} \right)^{-1}$$

where v is the thermal velocity, $k_B T$ is the Boltzmann constant times temperature (T). Measurements suggest a value of $\alpha \approx 0.4$ (43); however, as discussed above, neither H nor k_h can be independently measured. Previous work has assumed the value of H to be 5.0 M/atm, which was taken from extrapolating the known solubilities of a series of other NO_x compounds (34). Inverting the expression for γ and setting it equal to 0.03, which is the middle of the range of experimental estimates,

provides an estimate of the reaction rate on the order of 10^5 s^{-1} for N_2O_5 hydrolysis. This analysis is internally consistent, because it predicts a reaction-diffusion length much larger than the width of the interface, $l_D \approx 80 \text{ nm}$, but the solubility and hydrolysis rate are dramatically different from those computed ab initio. Using our computed values of H and k_h , we arrive at $\gamma = 0.6$, which is much higher than observed.

This inconsistency can be resolved by formulating an alternative to the standard resistor model that envisions the reactive uptake of N_2O_5 as an interfacial process. Specifically, assuming all incoming N_2O_5 molecules stick to the interface and do not diffuse away, the reactive uptake is given by a competition between hydrolysis of N_2O_5 at an interface (21) and its reevaporation. If k_h^s is the reaction rate at the surface and k_e is the evaporation rate, then the reactive uptake coefficient can be computed from

$$\gamma = \frac{k_h^s}{k_h^s + k_e}$$

which, in the limit that γ is small, reduces to $\gamma = k_h^s/k_e$ (44). This competition is illustrated in Fig. 3 with accompanying simulation snapshots and contrasts it with the processes of solvation and bulk hydrolysis included in the standard resistor model. This interfacial model is analogous to an older perspective on N_2O_5 uptake (41). Using molecular dynamics simulations, we have tested the assumptions of this model and explicitly computed γ by estimating k_h^s and k_e .

We computed the reaction rate at the air-water interface to be $k_h^s = 0.95 \text{ ns}^{-1}$ from direct molecular dynamics simulations. The distribution of waiting times for hydrolysis are shown in Fig. 3. This rate is slower than the corresponding rate in the bulk by a factor of four and predominantly follows a pathway that generates two protonated HNO_3 molecules. This is consistent with previous reports of the weaker acidity of HNO_3 and HCl at the air-water interface (45, 46). We estimated the evaporation rate by first computing the free energy of adsorption to the interface from the vapor using thermodynamic perturbation theory and then assuming that evaporation is barrierless. We obtained a free energy of adsorption $F_s = 3.4 \text{ kcal/mol}$, which is lower than the corresponding solvation free energy, as shown in Fig. 3. This indicates that N_2O_5 is preferentially solvated at the interface (fig. S11), which is consistent with previous studies using empirical potentials (18, 19) and the weak hydration observed in our bulk simulations. From this, we estimate an evaporation rate $k_e = 12.5 \text{ ns}^{-1}$. The reactive uptake coefficient computable from these two rate processes yields $\gamma = 0.07$, which is on the high end of the measured experimental range (8, 10).

An interfacial model of N_2O_5 reactive uptake helps rationalize a number of existing experimental observations and opens additional questions for further examination. For example, it has been noted that the temperature dependence of N_2O_5 uptake is weakly negative (47, 48). The similar activation energies for interfacial hydrolysis and evaporation result in both processes decreasing with temperature, though the larger energy of hydrolysis is consistent with a negative temperature dependence. Further, measurements of the reactive uptake on ice particles are close to those for liquid particles (49). The importance of surface processes elucidated in our work clarifies this coincidence, as diffusion into the bulk of the solid is prohibitively slow, yet interfacial hydrolysis can still proceed. Finally, it is known that uptake can be suppressed at high nitrate concentrations (8). From additional simulations with excess nitrate, we find that the stabilization of N_2O_5 in the presence of NO_3^- results from a weakened solvation structure of N_2O_5 , which makes it difficult for water to stabilize nascent charge separation, suppressing the hydrolysis rate (fig. S12). Such a mechanism of suppression could be quite general and highlights the need for future research with more complex solutions. Suppression of the hydrolysis rate below 10^5 s^{-1} should restore the canonical bulk reaction model. To move beyond idealized compositions and conditions, we imagine our framework can be incorporated into existing reaction diffusion models where molecular mechanisms and chemical data are known. For example, the suppression of uptake by surface-active organics can be incorporated by parameterizing rates to accommodate, reevaporate, and react with surface coverage. In cases where molecular mechanisms are unknown, additional neural network-based simulations can be used. For example, to understand the origin branching ratio to nitril halides (50), models capable of the $\text{S}_\text{N}2$ reaction between Cl^- with N_2O_5 at the liquid-vapor interface can be developed and studied.

REFERENCES AND NOTES

- J. H. Seinfeld, S. N. Pandis, *Atmospheric Chemistry and Physics: From Air Pollution to Climate Change* (Wiley, 2016).
- P. J. Crutzen, *Annu. Rev. Earth Planet. Sci.* **7**, 443–472 (1979).
- S. S. Brown, J. Stutz, *Chem. Soc. Rev.* **41**, 6405–6447 (2012).
- C. D. Holmes et al., *Geophys. Res. Lett.* **46**, 4980–4990 (2019).
- B. Alexander et al., *Atmos. Chem. Phys.* **20**, 3859–3877 (2020).
- P. Davidovits, C. E. Kolb, L. R. Williams, J. T. Jayne, D. R. Worsnop, *Chem. Rev.* **106**, 1323–1354 (2006).
- J. M. Davis, P. V. Bhavne, K. M. Foley, *Atmos. Chem. Phys.* **8**, 5295–5311 (2008).
- T. Bertram, J. Thornton, *Atmos. Chem. Phys. Discuss.* **9**, 15181–15214 (2009).
- J. P. Abbatt, A. K. Lee, J. A. Thornton, *Chem. Soc. Rev.* **41**, 6555–6581 (2012).
- W. L. Chang et al., *Aerosol Sci. Technol.* **45**, 665–695 (2011).
- E. E. McDuffie et al., *J. Geophys. Res. Atmos.* **123**, 4345–4372 (2018).
- A. Singarab, J. Behler, C. Dellago, *J. Chem. Theory Comput.* **15**, 1827–1840 (2019).
- L. Zhang et al., *Adv. Neural Inf. Process. Syst.* **31**, 4436–4446 (2018).
- U. Pöschl, *Atmos. Res.* **101**, 562–573 (2011).
- S. C. Park, D. K. Burden, G. M. Nathanson, *J. Phys. Chem. A* **111**, 2921–2929 (2007).
- O. S. Ryder et al., *J. Phys. Chem. A* **119**, 11683–11692 (2015).
- H. Akimoto, *Atmospheric Reaction Chemistry* (Springer, 2016), pp. 239–284.
- W. Li, C. Y. Pak, Y. S. Tse, *J. Chem. Phys.* **148**, 164706 (2018).
- B. Hirshberg et al., *Phys. Chem. Chem. Phys.* **20**, 17961–17976 (2018).
- A. D. Hammerich, B. J. Finlayson-Pitts, R. B. Gerber, *Phys. Chem. Chem. Phys.* **17**, 19360–19370 (2015).
- E. Rossich Molina, R. B. Gerber, *J. Phys. Chem. A* **124**, 224–228 (2020).
- L. M. McCaslin, M. A. Johnson, R. B. Gerber, *Sci. Adv.* **5**, eaav6503 (2019).
- N. V. Karimova et al., *J. Phys. Chem. A* **124**, 711–720 (2020).
- J. P. McNamara, I. H. Hillier, *Phys. Chem. Chem. Phys.* **2**, 2503–2509 (2000).
- I.-F. Wu, Kuo, C. J. Mundy, *Science* **303**, 658–660 (2004).
- Methods and materials are available as supplementary materials.
- Y. Zhang, W. Yang, *Phys. Rev. Lett.* **80**, 890 (1998).
- S. Grimme, J. Antony, S. Ehrlich, H. Krieg, *J. Chem. Phys.* **132**, 154104 (2010).
- A. Bankura, A. Karmakar, V. Carnevale, A. Chandra, M. L. Klein, *J. Phys. Chem. C* **118**, 29401–29411 (2014).
- M. Galib et al., *J. Chem. Phys.* **146**, 244501 (2017).
- T. Morawietz, A. Singarab, C. Dellago, J. Behler, *Proc. Natl. Acad. Sci. U.S.A.* **113**, 8368–8373 (2016).
- O. Marsalek, T. E. Markland, *J. Phys. Chem. Lett.* **8**, 1545–1551 (2017).
- T. F. Mentel, M. Sohn, A. Wahner, *Phys. Chem. Chem. Phys.* **1**, 5451–5457 (1999).
- R. Sander, *Atmos. Chem. Phys.* **15**, 4399–4981 (2015).
- H. McKay, *Trans. Faraday Soc.* **52**, 1568–1573 (1956).
- P. L. Geissler, C. Dellago, D. Chandler, *J. Phys. Chem. B* **103**, 3706–3710 (1999).
- S. Roy, M. D. Baer, C. J. Mundy, G. K. Schenter, *JCTC* **13**, 3470–3477 (2017).
- D. Chandler, *J. Chem. Phys.* **68**, 2959–2970 (1978).
- R. Mills, V. M. Lobo, *Self-Diffusion in Electrolyte Solutions: A Critical Examination of Data Compiled from the Literature* (Elsevier, 2013).
- C. J. Gaston, J. A. Thornton, *JPC A* **120**, 1039–1045 (2016).
- A. Fried, B. E. Henry, J. G. Calvert, M. Mozurkewich, *J. Geophys. Res.* **99**, 3517–3532 (1994).
- D. R. Worsnop et al., *J. Phys. Chem.* **93**, 1159–1172 (1989).
- G. Grzinić, T. Bartels-Rausch, A. Turler, M. Ammann, *Atmos. Chem. Phys.* **17**, 6493–6502 (2017).
- D. R. Hanson, *J. Phys. Chem. B* **101**, 4998–5001 (1997).
- E. S. Shamay, V. Buch, M. Parrinello, G. L. Richmond, *J. Am. Chem. Soc.* **129**, 12910–12911 (2007).
- M. D. Baer, D. J. Tobias, C. J. Mundy, *J. Phys. Chem. C* **118**, 29412–29420 (2014).
- J. M. Van Doren et al., *J. Phys. Chem.* **94**, 3265–3269 (1990).
- C. George et al., *J. Phys. Chem. C* **98**, 8780–8784 (1994).
- R. Apodaca, D. Huff, W. Simpson, *Atmos. Chem. Phys.* **8**, 7451–7463 (2008).
- T. B. Sobrya, H. Pliszka, T. H. Bertram, G. M. Nathanson, *J. Phys. Chem. A* **123**, 8942–8953 (2019).

ACKNOWLEDGMENTS

We thank T. Bertram, B. Gerber, A. Goetz, and G. Nathanson for stimulating discussions and B. Hirshberg for initial solvated N_2O_5 configurations. **Funding:** This work was funded by the National Science Foundation through the National Science Foundation Center for Aerosol Impacts on Chemistry of the Environment (NSF-CAICE) under grant no. CHE 1801971. This research used resources of the National Energy Research Scientific Computing Center (NERSC), a U.S. Department of Energy Office of Science User Facility operated under contract no. DE-AC02-05CH1123. **Author contributions:** M.G. and D.T.L. designed the numerical simulation setup, analyzed the data, and prepared the manuscript. M.G. ran the simulations, and D.T.L. supervised the project. **Competing interests:** The authors declare no competing interests. **Data and materials availability:** All data are available in the manuscript or supplementary materials.

SUPPLEMENTARY MATERIALS

science.sciencemag.org/content/371/6532/921/suppl/DC1
Materials and Methods
Figs. S1 to S12
Tables S1 to S6
References (51–66)

10 July 2020; accepted 22 January 2021
10.1126/science.abd7716

CORONAVIRUS

Plitidepsin has potent preclinical efficacy against SARS-CoV-2 by targeting the host protein eEF1A

Kris M. White^{1,2,*†}, Romel Rosales^{1,2,*}, Soner Yildiz^{1,2}, Thomas Kehrer^{1,2}, Lisa Miorin^{1,2}, Elena Moreno^{1,2}, Sonia Jangra^{1,2}, Melissa B. Uccellini^{1,2}, Raveen Rathnasinghe^{1,2}, Lynda Coughlan³, Carles Martinez-Romero^{1,2}, Jyoti Batra^{4,5,6,7}, Ajda Rojc^{4,5,6,7}, Mehdi Bouhaddou^{4,5,6,7}, Jacqueline M. Fabius^{4,6}, Kirsten Obernier^{4,5,6,7}, Marion Dejeose⁸, María José Guillén⁹, Alejandro Losada⁹, Pablo Avilés⁹, Michael Schotsaert^{1,2}, Thomas Zwaka⁸, Marco Vignuzzi¹⁰, Kevan M. Shokat^{4,6,7,11}, Nevan J. Krogan^{1,4,5,6,7,†}, Adolfo García-Sastre^{1,2,12,13,†}

Severe acute respiratory syndrome coronavirus 2 (SARS-CoV-2) viral proteins interact with the eukaryotic translation machinery, and inhibitors of translation have potent antiviral effects. We found that the drug plitidepsin (aplidin), which has limited clinical approval, possesses antiviral activity (90% inhibitory concentration = 0.88 nM) that is more potent than remdesivir against SARS-CoV-2 in vitro by a factor of 27.5, with limited toxicity in cell culture. Through the use of a drug-resistant mutant, we show that the antiviral activity of plitidepsin against SARS-CoV-2 is mediated through inhibition of the known target eEF1A (eukaryotic translation elongation factor 1A). We demonstrate the in vivo efficacy of plitidepsin treatment in two mouse models of SARS-CoV-2 infection with a reduction of viral replication in the lungs by two orders of magnitude using prophylactic treatment. Our results indicate that plitidepsin is a promising therapeutic candidate for COVID-19.

Over the past 20 years, three novel coronaviruses have been introduced into the human population, causing substantial morbidity and mortality. The severe acute respiratory syndrome coronavirus (SARS-CoV) and Middle East respiratory syndrome coronavirus (MERS-CoV) epidemics were each limited in scope, but both are associated with severe disease and high mortality rates (1–3). The ongoing COVID-19 pandemic caused by the SARS-CoV-2 virus is the result of a zoonotic transmission event, similar to previous coronavirus epidemics (4–7). Recent studies have detected many SARS-like and MERS-like coronaviruses in natural bat reservoirs and have shown them to be capable of replication in human lung cells in vitro (8–10).

This suggests the presence of a large reservoir of coronaviruses with pandemic potential. Antiviral therapeutics are urgently needed to combat SARS-CoV-2 in the current pandemic and will be the first line of defense for the future coronavirus epidemics that appear more likely as the human population expands in close contact with animal reservoirs.

COVID-19 is a viral-induced inflammatory disease of the airways and lungs with multi-organ involvement that can cause severe respiratory and systemic issues. SARS-CoV-2 replication in the lungs leads to inflammatory, innate, and adaptive immune responses that cause substantial host tissue damage (3, 11). COVID-19 can lead to end-stage lung disease and systemic involvement with currently limited treatment options and poor prognoses. The current standards of care include oxygen therapy and ventilation, along with the antiviral remdesivir and the anti-inflammatory dexamethasone. Remdesivir (12, 13) and dexamethasone (14) have each improved patient outcomes in clinical trials and have been approved for emergency use by regulatory agencies, but remdesivir in particular has shown limited efficacy (15) and dexamethasone is a steroid that does not directly inhibit viral replication. This leaves a continued need for the development or repurposing of antiviral drugs for the treatment of COVID-19.

Our previously published SARS-CoV-2 (16) and pan-coronaviral (17) interactomes highlighted 332 host proteins that are likely to play a role in the viral life cycle of SARS-CoV-2. In that work we tested 47 existing drugs that were known to modulate these identified host proteins, with many of these drugs showing substantial antiviral activity against SARS-CoV-2 in cell culture (16). Of the inhibitors

tested, those that targeted the eukaryotic translation machinery (eIF4H interacts with SARS-CoV-2 Nsp9) demonstrated particularly potent antiviral activities. Zotatafin (18), an inhibitor of eIF4A (a partner of eIF4H), had a 90% inhibitory concentration (IC₉₀) of 154 nM, and ternatin-4 (19), an inhibitor of eEF1A that has potential interactions with multiple coronavirus proteins (17), had an IC₉₀ of 15 nM against SARS-CoV-2 in Vero E6 cells (16).

Plitidepsin is a potent inhibitor of SARS-CoV-2 in vitro

In an effort to further explore the therapeutic potential of host eEF1A as a target for the treatment of COVID-19, we evaluated the eEF1A inhibitor plitidepsin (aplidin), which has limited clinical approval for the treatment of multiple myeloma. Plitidepsin has also successfully undergone a phase I/II clinical study for the treatment of COVID-19 (20, 21) by the pharmaceutical company PharmaMar and is moving forward into a phase II/III COVID-19 study. We first tested plitidepsin inhibition of SARS-CoV-2 replication using an immunofluorescence-based antiviral screening assay in Vero E6 cells (22). Plitidepsin inhibited SARS-CoV-2 with an IC₉₀ of 1.76 nM (Fig. 1B), which was 9 times as potent as ternatin-4 and 87.5 times as potent as zotatafin in the same assay (16). We next tested plitidepsin in the same antiviral assay using a human cell line (hACE2-293T). The anti-SARS-CoV-2 activity of plitidepsin was even more potent in human cells, with an IC₉₀ of 0.88 nM (Fig. 1D), which is more potent than remdesivir tested in the same cell line by a factor of 27.5 (Fig. 1C). The cytotoxicity of plitidepsin was examined in parallel with antiviral activity; at all concentrations in both cell types, we observed a cytostatic impact on cell proliferation (Fig. 1, B and D). We had previously found the lack of a dose-response curve in our cytotoxic assay to be suggestive of a cytostatic, rather than cytotoxic, effect on cells, but further work is required to confirm this hypothesis. Finally, we tested the antiviral effect of plitidepsin in an established model of human pneumocyte-like cells (23, 24). We found that treatment with plitidepsin inhibited SARS-CoV-2 replication (Fig. 1E) with an IC₉₀ of 3.14 nM and a selectivity index of 40.4, which suggests that plitidepsin has potent antiviral activity in primary human lung cells.

In an effort to better understand the mechanism of action through which plitidepsin inhibits SARS-CoV-2 infection, we performed a time-of-addition assay in which plitidepsin or remdesivir was added to hACE2-293T cells at –2, 0, +2, or +4 hours relative to infection. In this 8-hour single-cycle infection, we found that 20 nM plitidepsin strongly inhibited nucleocapsid protein expression even when added 4 hours after infection (Fig. 1F). This is indicative of a cytoplasmic replication-stage inhibitor,

¹Department of Microbiology, Icahn School of Medicine at Mount Sinai, New York, NY, USA. ²Global Health Emerging Pathogens Institute, Icahn School of Medicine at Mount Sinai, New York, NY, USA. ³Department of Microbiology and Immunology and Center for Vaccine Development and Global Health (CVD), University of Maryland School of Medicine, Baltimore, MD, USA. ⁴Quantitative Biosciences Institute (QBI), University of California, San Francisco, CA 94158, USA. ⁵J. David Gladstone Institutes, San Francisco, CA 94158, USA. ⁶QBI Coronavirus Research Group (QCRG), San Francisco, CA 94158, USA. ⁷Department of Cellular and Molecular Pharmacology, University of California, San Francisco, CA 94158, USA. ⁸Huffington Foundation Center for Cell-Based Research in Parkinson's Disease, Department of Cell, Developmental, and Regenerative Biology, Black Family Stem Cell Institute, Icahn School of Medicine at Mount Sinai, New York, NY, USA. ⁹Research and Development Department, PharmaMar, 28770 Colmenar Viejo, Madrid, Spain. ¹⁰Viral Populations and Pathogenesis Unit, CNRS UMR 3569, Institut Pasteur, 75724 Paris Cedex 15, France. ¹¹Howard Hughes Medical Institute, University of California, San Francisco, CA 94143, USA. ¹²Department of Medicine, Division of Infectious Diseases, Icahn School of Medicine at Mount Sinai, New York, NY, USA. ¹³Tisch Cancer Institute, Icahn School of Medicine at Mount Sinai, New York, NY, USA.

*These authors contributed equally to this work.

†Corresponding author. Email: kris.white@mssm.edu (K.M.W.); nevan.krogan@ucsf.edu (N.J.K.); adolfo.garcia-sastre@mssm.edu (A.G.-S.)

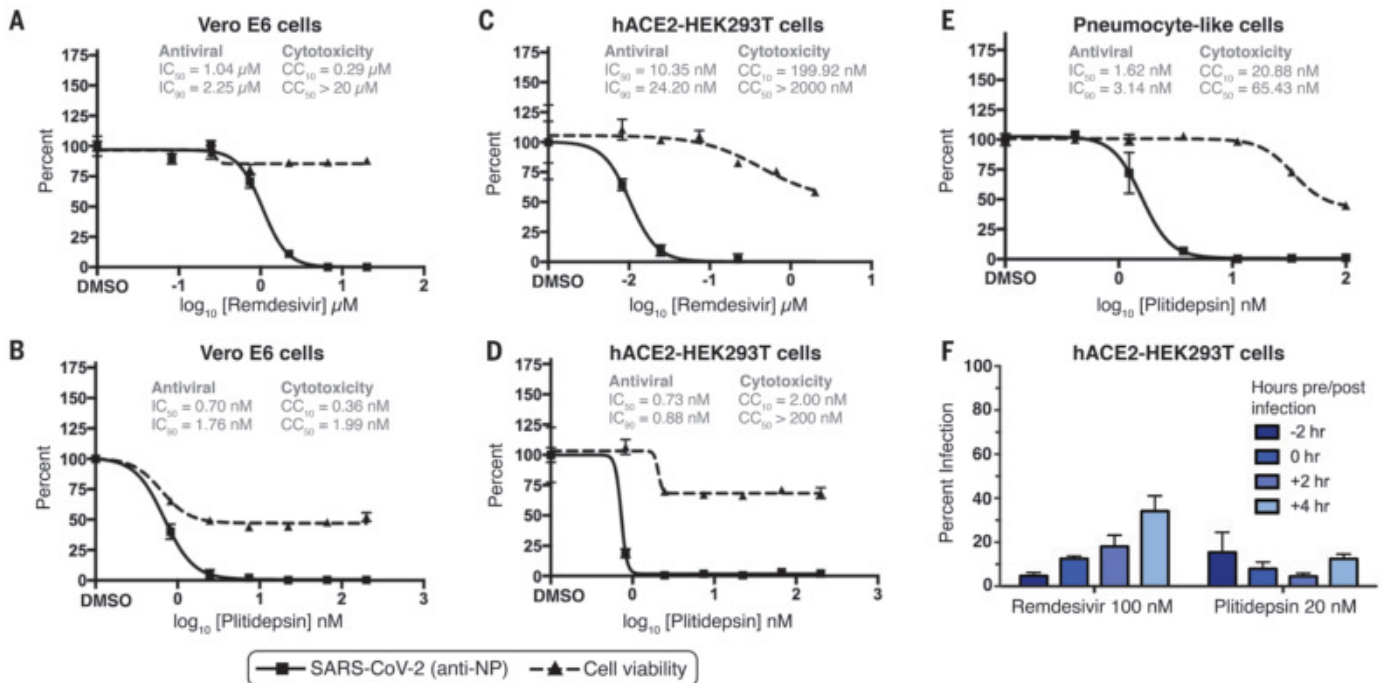


Fig. 1. Plitidepsin exhibits a strong antiviral activity in SARS-CoV-2 multiple cell lines. (A to E) Vero E6 cells [(A) and (B)], hACE2-293T cells [(C) and (D)], or pneumocyte-like cells (E) were treated with indicated doses of remdesivir [(A) and (C)] or plitidepsin [(B), (D), and (E)]. IC_{50} , IC_{90} , 50% cytotoxic concentration (CC_{50}), and CC_{10} values are indicated above the curves. All cells were pretreated for 2 hours

and the drugs were maintained in the media throughout the experiment. SARS-CoV-2 infection and cell viability were measured at 48 hours. (F) The antiviral activities of plitidepsin and remdesivir were evaluated in pretreatment and post-infection time points in hACE2-293T cells. In all panels, data are means \pm SD of three independent experiments performed in biological triplicate. DMSO, dimethyl sulfoxide.

which is consistent with the predicted antiviral mechanism of a known translation inhibitor.

Remdesivir is part of the current standard of care for the treatment of COVID-19 (25, 26). We therefore assessed the dynamics between the antiviral effects of plitidepsin and remdesivir when used together in vitro. Our analysis using the Synergyfinder (27) software suggests that plitidepsin has an additive effect with remdesivir (fig. S2) and would be a potential candidate to be considered in a combined therapy with the current standard of care.

Plitidepsin antiviral activity against SARS-CoV-2 is mediated through the inhibition of eEF1A

Plitidepsin inhibits the activity of the host factor eEF1A and is predicted to interact with the same binding site as didemnin B, which is structurally related to plitidepsin, and the structurally unrelated ternatin-4. Exogenous overexpression of an Ala³⁹⁹ \rightarrow Val (A399V) mutant of eEF1A confers resistance in cancer cells to both didemnin B (28) and ternatin-4 (29) inhibition, and we predicted that it may similarly affect plitidepsin. We examined whether this A399V mutation could mitigate the observed anti-SARS-CoV-2 activity of plitidepsin. First, we transiently cotransfected 293T cells with expression plasmids for hACE2 and either wild-type eEF1A (eEF1A-WT) or eEF1A-A399V, which were confirmed to be expressed in \sim 30% of cells by means of immuno-

fluorescent staining for the Flag epitope (fig. S1). We then measured the antiviral activity of plitidepsin against SARS-CoV-2 in these transfected 293T cells. Transfection with eEF1A-A399V, but not eEF1A-WT, increased the IC_{90} of plitidepsin by a factor of >10 (Fig. 2A). No impact from the A399V mutant transfection was observed upon plitidepsin inhibition of cell proliferation (Fig. 2D), consistent with observations of ternatin-4 (29). The differential effect of eEF1A-A399V transient transfection between the antiviral and antiproliferative impact of plitidepsin is consistent with previous findings that coronaviruses are considerably more sensitive to translation perturbations than the host cell (30, 31). We then generated an eEF1A-A399V CRISPR knock-in 293T cell line (293T-A399V) to further evaluate the role of eEF1A inhibition in the antiviral activity of plitidepsin. We found that this 293T-A399V cell line was refractory to the SARS-CoV-2 antiviral activity of plitidepsin by a factor of >12 as compared to the parental cell line (Fig. 2B) but did not have a similar impact on remdesivir inhibition (Fig. 2C). Furthermore, we found that plitidepsin antiviral activity could be almost fully restored through transient transfection of the 293T-A399V cells with wild-type, but not mutant, eEF1A (Fig. 2B). This 293T-A399V cell line was also resistant to the antiproliferative activity of plitidepsin, and this could only be partially rescued by transfec-

tion of the wild-type protein (Fig. 2E), again similar to previous results with ternatin-4 (29). Furthermore, small interfering RNA (siRNA) silencing of eEF1A protein expression during SARS-CoV-2 infection led to a large reduction in viral N protein levels but had no impact on the GAPDH control (Fig. 2F). Taken together, this evidence indicates that the antiviral activity of plitidepsin is mediated through eEF1A inhibition and confirms eEF1A as a druggable target for the inhibition of SARS-CoV-2 replication.

We next explored the impact of plitidepsin treatment on viral RNA and protein production over the course of SARS-CoV-2 infection. We analyzed the SARS-CoV-2 genomic and N subgenomic RNA content of Vero E6 cells infected with SARS-CoV-2 at a multiplicity of infection (MOI) of 1 at 4, 8, 12, and 24 hours after infection in the presence or absence of equivalent inhibitory doses of plitidepsin or remdesivir. We found that plitidepsin significantly reduced genomic RNA content at 8 and 12 hours after infection and fell just short of significance at the 24-hour time point, similar to remdesivir treatment (Fig. 3A). Interestingly, plitidepsin had a much greater impact on the accumulation of the N subgenomic RNA. Plitidepsin greatly reduced the subgenomic RNA expression as early as 4 hours after infection and maintained a significant impact throughout the time course (Fig. 3B). Remdesivir had no effect on N subgenomic RNA at 4 hours, but

Fig. 2. Antiviral mechanism of action of plitidepsin

is mediated through inhibition of eEF1A.

(A) Plitidepsin inhibition of SARS-CoV-2

replication in 293T cells transfected with eEF1A-WT or

eEF1A-A399V expression vectors. Plitidepsin inhibition is

reduced by expression of the A399V mutation, whereas virus

replication in wild-type and eEF2A-transfected mutations

remain susceptible to treatment with plitidepsin. (B and

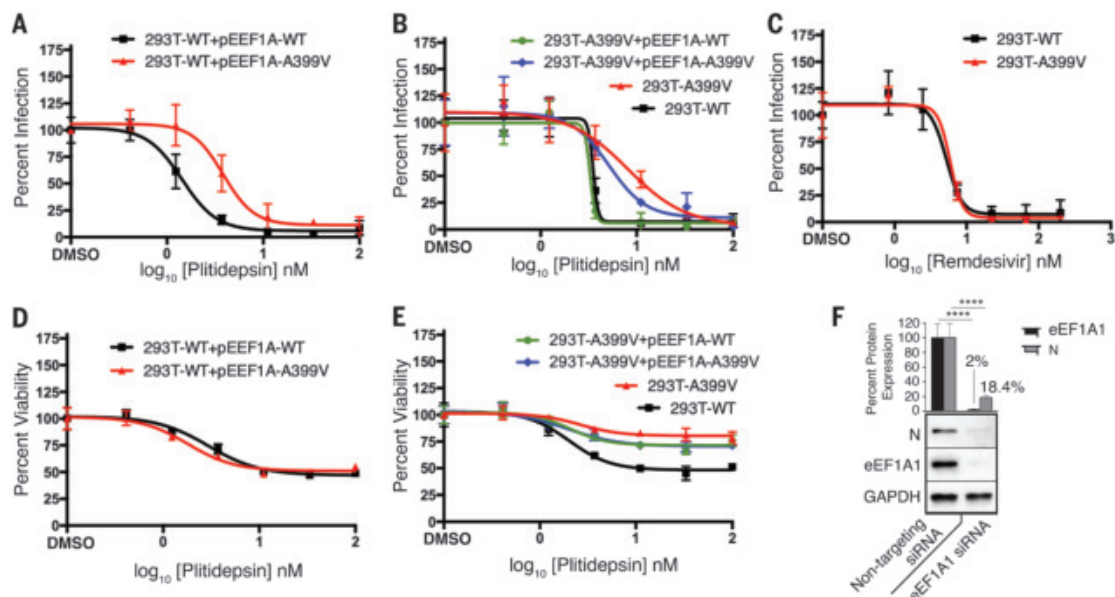
C) Plitidepsin (B) and remdesivir (C) inhibition of SARS-CoV-2

replication in a CRISPR 293T cell line carrying an A399V mutation in eEF1A.

Viral replication in wild-type eEF1A preserves susceptibility

to plitidepsin inhibition, whereas the presence of the eEF1A A399V mutation rendered the SARS-CoV-2 infection resistant to the eEF1A inhibitor. Remdesivir

inhibition of SARS-CoV-2 viral replication was not affected by the A399V mutation. (D and E) Plitidepsin inhibition of cell proliferation, as measured by (4,5-dimethylthiazol-2-yl)-2,5-diphenyltetrazolium bromide (MTT) assay, is not affected by transfection of the A399V mutant (D) but is reduced by the 293T-A399V CRISPR cell line (E). (F) siRNA silencing of eEF1A greatly reduces N protein levels. In all panels, data are means \pm SD of three independent experiments performed in biological triplicate. **** P < 0.0001.



did show a reduction at all other time points tested. We then measured the viral N protein levels in the presence and absence of plitidepsin or remdesivir treatment. Similar to RNA levels, plitidepsin had a more potent and sustained inhibition of the expression the N protein over the time course of infection relative to remdesivir (Fig. 3, C and D). This specific inhibition of N subgenomic RNA expression, particularly early in infection, is likely a result of the inhibition of viral translation by plitidepsin. It was previously shown that coronaviruses are highly sensitive to translation inhibitors (30, 31) and that negative-sense genome accumulation is more greatly affected than the positive sense (32). The current model of coronavirus discontinuous transcription (33) has been guided by evidence that subgenomic RNA formation occurs during negative strand synthesis (34). Therefore, a translation inhibitor that has a greater impact on negative-sense RNA production would also be expected to specifically reduce subgenomic RNA formation and accumulation, as we observed with plitidepsin. Furthermore, consistent with an impact of plitidepsin in protein translation, N protein levels were more greatly reduced in plitidepsin-treated cells than in remdesivir-treated cells at 24 hours after infection, when levels of N RNA were equivalent between these two treatments.

Plitidepsin shows in vivo antiviral efficacy in mouse models of SARS-CoV-2 infection

Plitidepsin has been clinically developed for the treatment of multiple myeloma with a

well-established safety profile and pharmacokinetics (35–38). Initially, plitidepsin underwent a large clinical development program in which cancer patients were treated with plitidepsin as a single agent in several phase I and II clinical trials. Results gathered from these clinical studies demonstrated that the probability of having cardiac adverse events, a concern in COVID-19 patients, was not significantly affected by plitidepsin treatment (39–41), although these events were found in other chemically related compounds that display a different mechanism of action (42, 43). It is worth highlighting that plitidepsin had a good safety profile in a phase I clinical trial (44), which administered a total of 11.4 mg spaced over 5 days of treatment. The dose level used in the COVID-19 proof-of-concept phase I study (21) had a maximum total of 7.5 mg spaced over 3 days.

On the basis of these clinical safety data and good pharmacokinetics (fig. S3A), we determined that a concentration of plitidepsin an order of magnitude greater than the demonstrated in vitro IC_{50} could be safely achieved in the lungs of mice using a single daily dose. Therefore, we tested the in vivo efficacy of plitidepsin in two different established animal models of SARS-CoV-2 infection. First, we used a human ACE2-expressing adenovirus to transduce the naturally resistant wild-type BALB/c mice and sensitize them to SARS-CoV-2 infection (Fig. 4A) (45). Five days after adenovirus transduction, mice were infected with 1×10^4 plaque-forming units (pfu) of SARS-CoV-2. As a proof-of-principle experiment, we performed prophylactic dosing with 0.3 mg/kg

or 1 mg/kg plitidepsin 2 hours before infection with SARS-CoV-2. The 0.3 mg/kg group received continued dosing once per day for 2 more days, whereas the 1 mg/kg group received only that single dose (Fig. 4B). SARS-CoV-2 lung titers were quantified from two independent experiments for the plitidepsin groups and compared to vehicle and remdesivir controls (Fig. 4C). There was a reduction of nearly 2 log units in SARS-CoV-2 viral titers in the lungs of the 0.3 mg/kg plitidepsin group relative to the vehicle control group, whereas there was a reduction of 1.5 log units observed from the single dose of 1 mg/kg plitidepsin. Note that we used a very high concentration of remdesivir in these assays (50 mg/kg) because of the known high concentration of esterases present in mouse serum that degrade remdesivir (46).

We then performed a study in the K18-hACE2 mouse model (Fig. 5A), which supports a robust SARS-CoV-2 infection (45, 47), in which the 0.3 mg/kg dosage of plitidepsin was assessed for ability to reduce viral titers and inflammation in the lung. K18-hACE2 mice were treated with one daily dose of plitidepsin for 3 days starting 2 hours before infection with SARS-CoV-2 (Fig. 5B). We found a reduction of 2 log units in viral lung titers at day 3, similar to two daily 50 mg/kg doses of remdesivir (Fig. 5C). Histopathology analysis (Fig. 5D) also showed a reduction of lung inflammation in plitidepsin-treated mice (histopathology score of 1/16) over vehicle-treated (histopathology score of 5.4/16) and remdesivir-treated (histopathology score of 2.3/16) mice

at day 3 after infection (Fig. 5E). There was no peribronchiolar inflammation noted in the plitidepsin-treated group. Taken together, these experiments show that plitidepsin treatment can reduce the replication of SARS-CoV-2 by two orders of magnitude and reduce lung inflammation in vivo, and has compelling potential for clinical efficacy for the treatment of COVID-19.

Discussion

The ongoing SARS-CoV-2 pandemic has created the immediate need for antiviral therapeutics that can be moved into the clinic within months rather than years. This led us to screen clinically approved drugs with established bioavailability, pharmacokinetics, and safety profiles. Our previous study of the SARS-CoV-2 interactome (16) led us to eEF1A as a druggable target with the potential for potent inhibition of SARS-CoV-2 in vitro. eEF1A has been previously described to be an important host factor for the replication of many viral pathogens (48–50), including influenza virus (51) and respiratory syncytial virus (52). Specifically, it has been found to be involved in transmissible gastroenteritis coronavirus replication (53) and was detected in SARS-CoV virions (54). Therefore, inhibition of eEF1A as a strategy for the treatment of viral infection may extend to other human coronaviruses and beyond to unrelated viral pathogens. This potential for broad-spectrum antiviral activity makes plitidepsin an intriguing candidate for further exploration as a treatment for viral infections with no clinically approved therapeutics. It is also important to note that a host-targeted antiviral such as plitidepsin offers protection from naturally occurring viral mutants, to which viral-targeted therapeutics and vaccines are more susceptible. In fact, plitidepsin was found to maintain nanomolar potency against the B.1.1.7 variant (55) recently discovered in the United Kingdom (56, 57).

In our animal experiments, we did detect a slight body weight loss of mice that were treated with plitidepsin daily, whereas mice that received a single 1 mg/kg dose did not lose any weight while still exhibiting reductions in viral lung titers (fig. S3B). It is unclear whether this observed toxicity is mouse-specific, and although toxicity is a concern with any host-targeted antiviral, the safety profile of plitidepsin is well established in humans. Furthermore, the dose of plitidepsin being used in an ongoing COVID-19 clinical trial is substantially lower than used in these experiments and it has been well tolerated in patients with minimal side effects. Interestingly, the most well-established and effective steroid for the treatment of COVID-19, dexamethasone (14), is also a commonly used treatment for multiple myeloma (58). This has led to plitidepsin already having an established safety profile with concurrent dexamethasone treatment

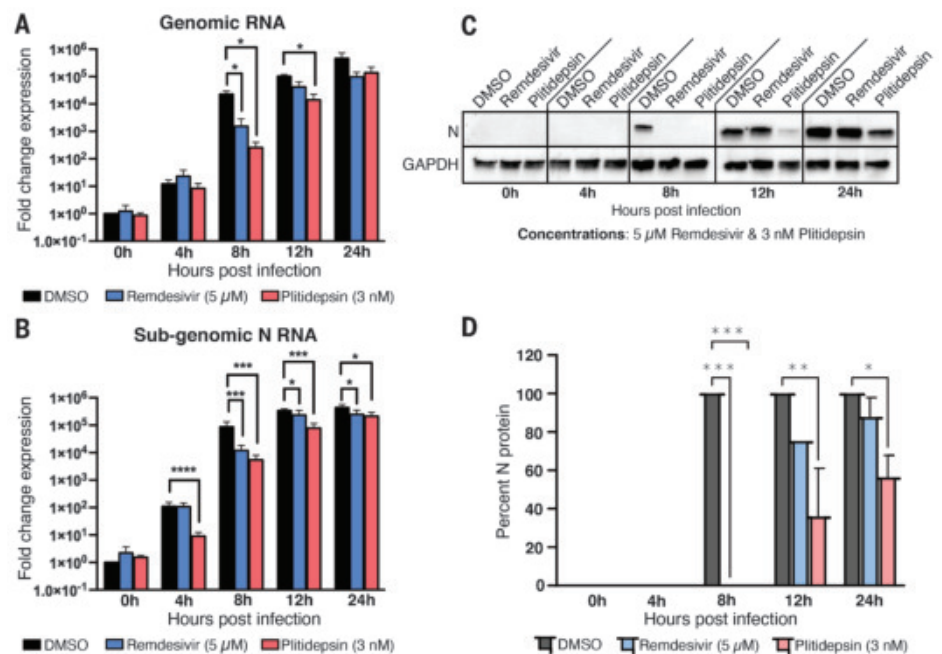


Fig. 3. Plitidepsin treatment causes a specific reduction in subgenomic RNA expression. (A to D) Vero E6 cells were infected with SARS-CoV-2 at an MOI of 1 in the presence or absence of 3 nM plitidepsin or 5 μM remdesivir and samples were taken at the indicated time points. The levels of genomic RNA (A) and subgenomic N RNA (B) were analyzed with specific reverse transcription quantitative polymerase chain reactions (RT-qPCR). (C) Cell lysates were collected at the indicated times and subjected to Western blotting. (D) Each protein band was quantified by ImageJ and normalized to GAPDH levels. Data are means ± SD of three independent experiments performed in biological triplicate. **P* < 0.05, ***P* < 0.01, ****P* < 0.001, *****P* < 0.0001.

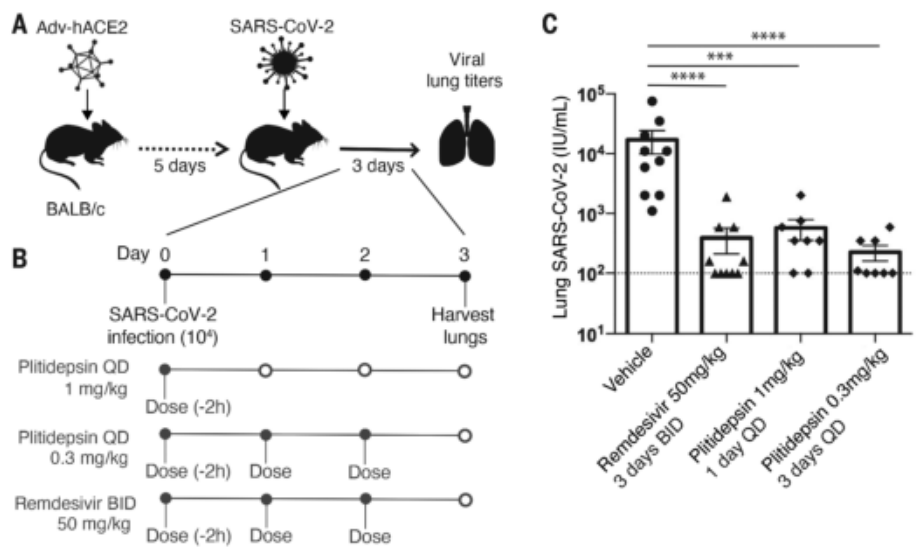


Fig. 4. Plitidepsin treatment significantly reduces SARS-CoV-2 infection in BALB/c mice expressing human ACE2. (A) Schematic of adenovirus expression of human ACE2 model of SARS-CoV-2 infection. BALB/c mice were transduced with human ACE2 expressing adenovirus. Mice were sensitized intranasally with 2.5×10^8 pfu. (B) Mice were intranasally infected with 10^4 pfu of SARS-CoV-2 and subcutaneously treated with either 0.3 mg/kg plitidepsin once daily for 3 days, a single dose of 1 mg/kg plitidepsin, or 50 mg/kg remdesivir once daily for 3 days. (C) SARS-CoV-2 lung titers in the plitidepsin-treated group relative to vehicle and remdesivir controls. Virus titers were determined in whole lung homogenates by median tissue culture infectious dose (TCID₅₀) at day 3 after infection. The limit of detection for viral titers is indicated with a dotted line. Vehicle and remdesivir, *N* = 10; plitidepsin 1 mg/kg and 0.3 mg/kg, *N* = 8. ****P* < 0.001, *****P* < 0.0001.

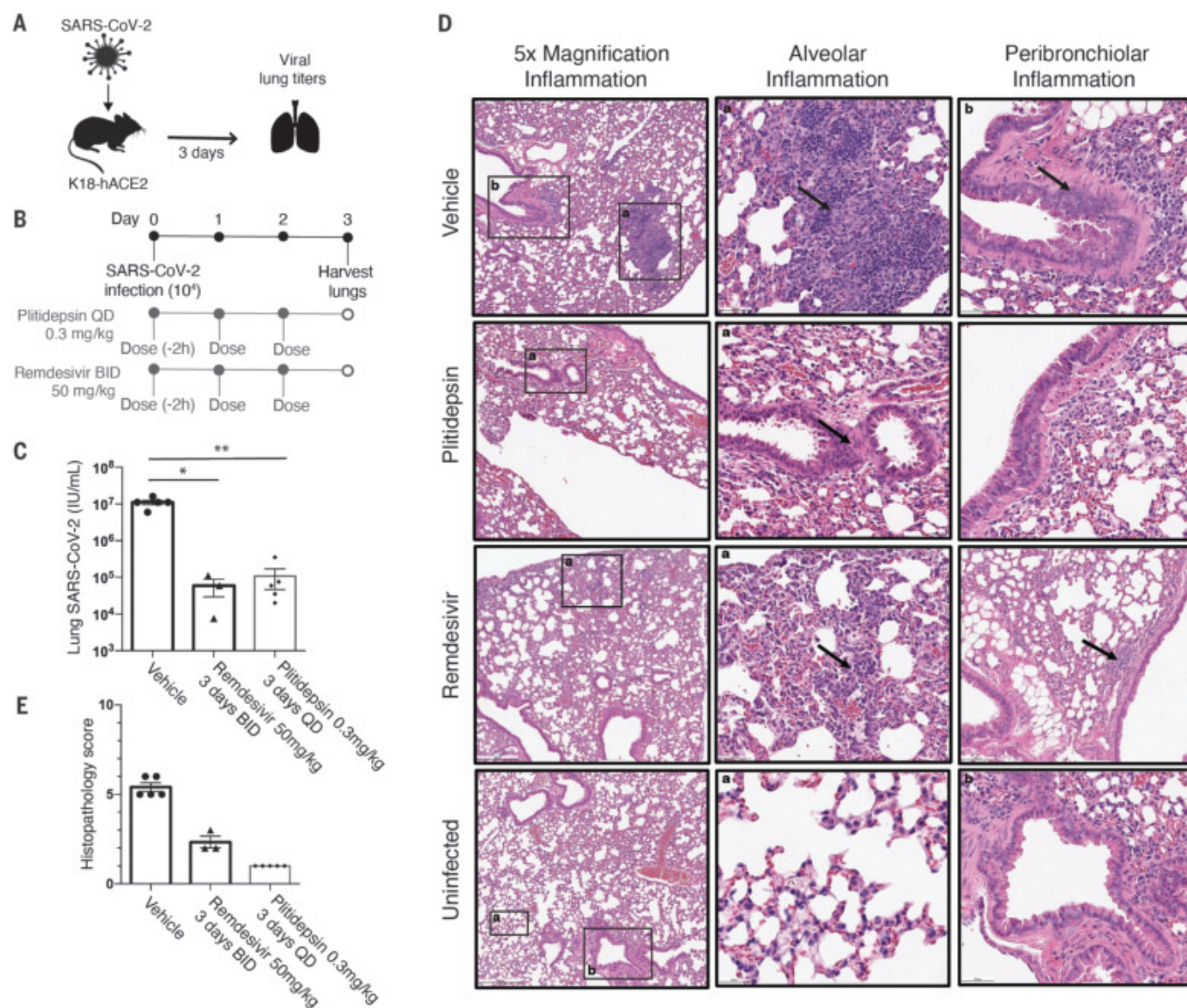


Fig. 5. Plitidepsin shows in vivo antiviral efficacy in the K18-hACE2 mouse model. (A) Schematic of the K18-hACE2 model of SARS-CoV-2 infection. (B) Mice were intranasally infected with 10^4 pfu of SARS-CoV-2 and subcutaneously treated with 0.3 mg/kg plitidepsin once daily for 3 days or with 50 mg/kg remdesivir twice daily for 3 days. (C) SARS-CoV-2 lung titers in the plitidepsin-treated group relative to vehicle and remdesivir controls. Virus titers were determined in whole lung homogenates by TCID₅₀ at day 3 after infection. Five mice were used in each group, except for the remdesivir control, which had 3. * $P < 0.05$, ** $P < 0.01$.

(D) Lungs were harvested on day 3 after infection, paraffin-embedded, and 5- μ m sections stained for hematoxylin and eosin. Regions of the lung anatomy where inflammation was assessed are highlighted by black boxes, with the corresponding higher-magnification image indicated by matching letter. Regions where inflammation was detected are indicated by arrows. (E) Pathological severity scores in infected mice. To evaluate comprehensive histological changes, lung tissue sections were scored according to pathological changes outlined in the supplementary materials.

(59, 60) and should allow for clinicians to treat with both drugs if warranted. This study establishes plitidepsin as a host-targeted anti-SARS-CoV-2 agent with in vivo efficacy. Our data and the initial positive results from PharmaMar's clinical trial suggest that plitidepsin should be strongly considered for expanded clinical trials for the treatment of COVID-19.

REFERENCES AND NOTES

- World Health Organization, "Middle East respiratory syndrome coronavirus (MERS-CoV)": www.who.int/emergencies/mers-cov/en/.
- E. de Wit, N. van Doremalen, D. Falzarano, V. J. Munster, *Nat. Rev. Microbiol.* **14**, 523–534 (2016).
- D. Wang et al., *JAMA* **323**, 1061–1069 (2020).
- Y. Z. Zhang, E. C. Holmes, *Cell* **181**, 223–227 (2020).
- K. G. Andersen, A. Rambaut, W. I. Lipkin, E. C. Holmes, R. F. Garry, *Nat. Med.* **26**, 450–452 (2020).
- B. Hu, X. Ge, L. F. Wang, Z. Shi, *Virology* **12**, 221 (2015).
- S. J. Anthony et al., *mBio* **8**, e00373-17 (2017).
- V. D. Menachery et al., *Proc. Natl. Acad. Sci. U.S.A.* **113**, 3048–3053 (2016).
- V. D. Menachery et al., *Nat. Med.* **21**, 1508–1513 (2015).
- P. C. Woo et al., *Virology* **351**, 180–187 (2006).
- Y. Liang et al., *Front. Immunol.* **11**, 1022 (2020).
- C. D. Spinner et al., *JAMA* **324**, 1048–1057 (2020).
- Y. Wang et al., *Lancet* **395**, 1569–1578 (2020).
- RECOVERY Collaborative Group, *N. Engl. J. Med.* **NEJMoA2021436** (2020).
- WHO Solidarity Trial Consortium, *N. Engl. J. Med.* **NEJMoA2023184** (2020).
- D. E. Gordon et al., *Nature* **583**, 459–468 (2020).
- D. E. Gordon et al., *Science* **370**, eabe9403 (2020).
- J. T. Ernst et al., *J. Med. Chem.* **63**, 5879–5955 (2020).
- M. Ito et al., *Peptides* **30**, 1074–1081 (2009).
- Spanish Clinical Trials Registry, 2020-001993-31: reec.aemps.es/reec/estudio/2020-001993-31.
- ClinicalTrials.gov, NCT04382066: <https://clinicaltrials.gov/ct2/show/NCT04382066?term=plitidepsin&draw=2&rank=8>.
- F. Amanat et al., *Curr. Protoc. Microbiol.* **58**, e108 (2020).
- A. Jacob et al., *Nat. Protoc.* **14**, 3303–3332 (2019).
- M. Ghaedi et al., *J. Clin. Invest.* **123**, 4950–4962 (2013).
- R. A. Siemieniuk et al., *BMJ* **370**, m2980 (2020).
- Y. Yokoyama, A. Briassoulis, H. Takagi, T. Kuno, *Virus Res.* **288**, 198137 (2020).

27. A. Ianevski, A. K. Giri, T. Aittokallio, *Nucleic Acids Res.* **48**, W488–W493 (2020).
28. P. Krastel *et al.*, *Angew. Chem. Int. Ed.* **54**, 10149–10154 (2015).
29. J. D. Carelli *et al.*, *eLife* **4**, e10222 (2015).
30. S. H. van den Worm *et al.*, *J. Virol.* **85**, 5669–5673 (2011).
31. D. Bojkova *et al.*, *Nature* **583**, 469–472 (2020).
32. S. G. Sawicki, D. L. Sawicki, *J. Virol.* **57**, 328–334 (1986).
33. S. G. Sawicki, D. L. Sawicki, S. G. Siddell, *J. Virol.* **81**, 20–29 (2007).
34. S. G. Sawicki, D. L. Sawicki, *Adv. Exp. Med. Biol.* **380**, 499–506 (1995).
35. J. Delgado-Calle *et al.*, *Oncotarget* **10**, 2709–2721 (2019).
36. L. Yao, *IDrugs* **6**, 246–250 (2003).
37. P. E. Morande *et al.*, *Invest. New Drugs* **30**, 1830–1840 (2012).
38. C. S. Mitsiades *et al.*, *Cancer Res.* **68**, 5216–5225 (2008).
39. R. Nalda-Molina *et al.*, *Cancer Chemother. Pharmacol.* **64**, 97–108 (2009).
40. A. Soto-Matos *et al.*, *Mar. Drugs* **9**, 1007–1023 (2011).
41. R. Salazar *et al.*, *Invest. New Drugs* **29**, 1406–1413 (2011).
42. R. L. Piekarz *et al.*, *Clin. Cancer Res.* **12**, 3762–3773 (2006).
43. M. H. Shah *et al.*, *Clin. Cancer Res.* **12**, 3997–4003 (2006).
44. J. A. Maroun *et al.*, *Ann. Oncol.* **17**, 1371–1378 (2006).
45. R. Rathnasinghe *et al.*, *Emerg. Microbes Infect.* **9**, 2433–2445 (2020).
46. T. P. Sheahan *et al.*, *Sci. Transl. Med.* **9**, eaa13653 (2017).
47. E. S. Winkler *et al.*, *Nat. Immunol.* **21**, 1327–1335 (2020).
48. D. Li, T. Wei, C. M. Abbott, D. Harrich, *Microbiol. Mol. Biol. Rev.* **77**, 253–266 (2013).
49. W. Abbas, A. Kumar, G. Herbein, *Front. Oncol.* **5**, 75 (2015).
50. N. S. Heaton *et al.*, *Immunity* **44**, 46–58 (2016).
51. S. Sammaibashi, S. Yamayoshi, Y. Kawaka, *Front. Microbiol.* **9**, 1446 (2018).
52. T. Wei *et al.*, *PLOS ONE* **9**, e114447 (2014).
53. X. Zhang *et al.*, *Vet. Microbiol.* **172**, 443–448 (2014).
54. B. W. Neuman *et al.*, *J. Virol.* **82**, 5279–5294 (2008).
55. A.-K. Reuschl *et al.*, *bioRxiv* 427991 [preprint], 24 January 2021.
56. S. V. Rajkumar, *Am. J. Hematol.* **95**, 548–567 (2020).
57. New and Emerging Respiratory Virus Threats Advisory Group, NERVTAG meeting on SARS-CoV-2 variant under investigation VUI-202012/01 (18 December 2020); <https://khub.net/documents/135939561/338928724/SARS-CoV-2+variant+under+investigation%2C+meeting+minutes.pdf/962e866b-161f-2fd5-1030-32b6ab467896?t=1608491166921>.
58. A. Rambaut *et al.*, Preliminary genomic characterisation of an emergent SARS-CoV-2 lineage in the UK defined by a novel set of spike mutations (18 December 2020); <https://virological.org/t/preliminary-genomic-characterisation-of-an-emergent-sars-cov-2-lineage-in-the-uk-defined-by-a-novel-set-of-spike-mutations/563>.
59. I. Spicka *et al.*, *Ann. Hematol.* **98**, 2139–2150 (2019).
60. M. Leisch, A. Egle, R. Greil, *Future Oncol.* **15**, 109–120 (2019).

ACKNOWLEDGMENTS

We thank R. Albrecht for support with the BSL3 facility and procedures at the ISMMS, R. Cadagan for technical assistance, and J. Taunton for helpful insights and assistance in regard to eF1A inhibitors. **Funding:** Supported by the Defense Advanced Research Projects Agency (HR0011-19-2-0020) (A.G.-S., N.J.K., and K.M.S.); by CRIP (Center for Research for Influenza Pathogenesis), a NIAID supported Center of Excellence for Influenza Research and Surveillance (CEIRS, contract # HHSN272201400008C); by supplements to NIAID grant U19AI135972 and DoD grant W81XWH-20-1-0270; by the generous support of the JPB Foundation and the Open Philanthropy Project [research grant 2020-215611 (5384)]; and by anonymous donors to A.G.-S. This research was also funded by the Huffington Foundation (T.Z.); NIH grants P50AI150476, U19AI135990, U19AI135972, R01AI143292, R01AI120694, P01AI1063302, and R01AI122747 (N.J.K.), R01CA221969 and R01CA244550 (K.M.S.), and F32CA239333 (M.B.); by the Excellence in Research Award (ERA) from the Laboratory for Genomics Research (LGR), a collaboration between UCSF, UCB, and GSK (grant 133122P to N.J.K.); by the Laboratoire d'Excellence "Integrative Biology of Emerging Infectious Diseases" grant ANR-10-LABX-62-IBED (M.V.); and by funding from FastGrants COVID19 grant from the Emergent Ventures program at the Mercatus Center of George Mason University, F. Hoffmann-La Roche, Vir Biotechnology, the Roddenberry Foundation, and gifts from QCRG philanthropic donors (N.J.K.). S.Y. received funding from Swiss National Foundation (SNF) Early Postdoc.Mobility fellowship (P2GEP3_184202). **Author contributions:** K.M.W., N.J.K., and A.G.-S. conceived and codirected the study; K.M.W., N.J.K., A.G.-S., R.R., S.Y., L.C., M.B., P.A., T.Z., and K.M.S. designed the experiments; K.M.W., R.R., S.Y., T.K., L.M., E.M., S.J., J.B., A.R., and M.D. performed *in vitro* experiments; K.M.W., R.R., S.Y., M.B.U., R.R., C.M.-R., M.J.G., A.L., P.A., and M.S. performed *in vivo* experiments; K.M.W., N.J.K., A.G.-S., R.R., S.Y., M.B., J.M.F., K.O., M.J.G., A.L., P.A.,

M.V., and K.M.S. interpreted the data; and K.M.W., N.J.K., A.G.-S., R.R., S.Y., S.J., M.B., M.D., P.A., and T.Z. wrote the manuscript. All authors read and accepted the manuscript. **Competing interests:** The Garcia-Sastre laboratory has received research support from Pfizer, Senhwa Biosciences, and 7Hills Pharma. A.G.-S. has consulting agreements for the following companies involving cash and/or stock: Vivaldi Biosciences, Contrafect, 7Hills Pharma, Avimex, Vaxalto, Accurius, and Esperovax. The Krogan laboratory receives funding from Roche and VIR, and N.J.K. has consulting agreements with Maze Therapeutics and Interline Therapeutics. K.M.S. has consulting agreements for the following companies involving cash and/or stock compensation: Black Diamond Therapeutics, BridGene Biosciences, Denali Therapeutics, Dice Molecules, eFFECTOR Therapeutics, Erasca, Genentech/Roche, Janssen Pharmaceuticals, Kumquat Biosciences, Kura Oncology, Merck, Mitokinin, Petra Pharma, Revolution Medicines, Type6 Therapeutics, Venthera, Wellspring Biosciences (Araxes Pharma), Turning Point Therapeutics, Ikena, Nextech. M.J.G., A.L., and P.A. are employees and shareholders of PharmaMar SA (Madrid, Spain). **Data and materials availability:** Plitidepsin is available from PharmaMar for noncommercial use under an MTA. All relevant data are included within this manuscript and all

materials other than plitidepsin are readily available upon request from the corresponding authors. This work is licensed under a Creative Commons Attribution 4.0 International (CC BY 4.0) license, which permits unrestricted use, distribution, and reproduction in any medium, provided the original work is properly cited. To view a copy of this license, visit <https://creativecommons.org/licenses/by/4.0/>. This license does not apply to figures/photos/artwork or other content included in the article that is credited to a third party; obtain authorization from the rights holder before using such material.

SUPPLEMENTARY MATERIALS

science.sciencemag.org/content/371/6532/926/suppl/DC1
Materials and Methods

Figs. S1 to S3
References (61–64)
MDAR Reproducibility Checklist

28 October 2020; accepted 20 January 2021

Published online 25 January 2021

10.1126/science.abf4058

REPORTS

GEOPHYSICS

Optical polarization-based seismic and water wave sensing on transoceanic cables

Zhongwen Zhan^{1*}, Mattia Cantono², Valey Kamalov², Antonio Mecozzi³, Rafael Müller², Shuang Yin², Jorge C. Castellanos¹

Seafloor geophysical instrumentation is challenging to deploy and maintain but critical for studying submarine earthquakes and Earth's interior. Emerging fiber-optic sensing technologies that can leverage submarine telecommunication cables present an opportunity to fill the data gap. We successfully sensed seismic and water waves over a 10,000-kilometer-long submarine cable connecting Los Angeles, California, and Valparaiso, Chile, by monitoring the polarization of regular optical telecommunication channels. We detected multiple moderate-to-large earthquakes along the cable in the 10-millihertz to 5-hertz band. We also recorded pressure signals from ocean swells in the primary microseism band, implying the potential for tsunami sensing. Our method, because it does not require specialized equipment, laser sources, or dedicated fibers, is highly scalable for converting global submarine cables into continuous real-time earthquake and tsunami observatories.

The oceans present a major gap in geophysical instrumentation, hindering fundamental research on submarine earthquakes and Earth's interior structure as well as effective earthquake and tsunami warning for offshore events. The data gap motivates many technologies, such as ocean-bottom seismic or pressure sensors, cabled geophysical observatories (1), autonomous vehicles (2), and floats with hydrophones (3). Emerging fiber-optic sensing technologies bring a different possible solution. Marra *et al.* turned a 96-km-long submarine cable into a sensitive seismic sensor using ultrastable laser interferometry of a round-trip signal (4). An-

other technology, distributed acoustic sensing (DAS), interrogates intrinsic Rayleigh back-scattering and converts tens of kilometers of dedicated fiber into thousands of seismic strainmeters on the seafloor (5–7). If a fraction of the million-kilometer submarine fiber-optic network could function as geophysical sensors, we would have a large increase in data coverage for large portions of the seafloor. Sites of interest for geophysical interrogation, such as the Hawaii or Iceland hotspots, and coastal cities next to subduction zones are often key nodes in telecommunication networks. The abundant number of fibers around them, if mobilized for geophysical research, could provide critical data for assessing geohazards and investigating seafloor and ocean processes.

Major obstacles exist on the path toward global fiber-based geophysical networks on the seafloor. Unlike their counterparts on

¹Seismological Laboratory, Division of Geological and Planetary Sciences, California Institute of Technology, Pasadena, CA, USA. ²Google LLC, Mountain View, CA, USA.

³Department of Physical and Chemical Sciences, University of L'Aquila, Coppito, Italy.

*Corresponding author. Email: zwzhan@caltech.edu

land, submarine cables are extraordinarily expensive to deploy, heavily used, and strictly regulated. As the backbone of global internet connectivity, long-haul submarine cables usually have surprisingly few fiber strands (~2 to 6 pairs). Therefore, unused strands of fiber (called dark fibers), which are currently required for DAS, are rare. Furthermore, to take full advantage of long transoceanic cables, DAS needs to both function across frequent repeaters and drastically increase its range (which is currently ~50 km) (8). Techniques that rely on sophisticated and expensive equipment, such as ultrastable laser sources (4) or repeaters with built-in geophysical sensors required specifically for geophysical sensing (9), raise cost and security concerns depending on the extent of equipment changes needed, sensitivity of collected information, and data policies. Additionally, the installation of sensing equipment in facilities where telecommunications equipment sits can raise security concerns with regard to eavesdropping and service disruption. These practical considerations make large-scale incorporation into existing or future submarine cables challenging.

We took a different approach and turned the 10,000-km submarine cable “Curie” into a geophysical instrument that detected both earthquake shaking and ocean waves. The Curie cable was deployed in 2019 by Google to connect Los Angeles, California, and Valparaíso, Chile, along the eastern edge of the Pacific Ocean (Fig. 1 and fig. S1) (10). From north to south, the cable crosses multiple faults offshore of southern California and then crosses the Eastern Pacific Rise three times onto the Cocos Plate. Most of the length of the cable

lies along the Central American and South American subduction zones at ~400 km to the ocean side of the trenches. Along the open-ocean cable section, the water depth is 4000 m on average but can be as shallow as 2000 m near the oceanic ridges and plateau and as deep as 6000 m when crossing the trench near Valparaíso. Near this path, more than 50 shallow earthquakes with a moment magnitude (M_w) larger than 7.5 have occurred since 1900 (Fig. 1, blue dots), 10 of which were larger than M_w 8.0 and posed a substantial threat of shaking and tsunami. Two events are particularly notable: The 1960 Chilean M_w 9.5 earthquake is the largest ever recorded (11), and the 1985 Mexico City M_w 8.0 earthquake devastated the city (12).

We monitored the state of polarization (SOP) of regular optical telecommunication traffic through the Curie cable (fig. S2). The SOP can be represented by the Stokes parameters and visualized on the Poincaré sphere (13) (Fig. 2A). Whereas the SOP of the transmit laser is stable over a long time scale (e.g., days), the output SOP at the receiver end is, in general, different from the input SOP and changes over time owing to various external perturbations to the fiber (10, 14, 15). For terrestrial fibers, the output SOP can be chaotic and hard to interpret owing to substantial temperature variations along cable and air flow or human-, animal-, and/or traffic-induced vibrations when integrated over the entire optical path. Extreme SOP transients with up to 5 Mrad/s anomalies were observed during lightning strikes (16). However, by making orders-of-magnitude more sensitive measurements, we found the output SOP of the Curie transcontinental sub-

marine cables to be much more stable compared with that of terrestrial cables, because the absolute majority of the path is in the deep ocean with almost constant temperature and minimal mechanical or electromagnetic perturbations (Fig. 2B). Therefore, strong seismic waves or long-period water waves produced by earthquakes close to the Curie cable can cause distinct and observable SOP anomalies (Fig. 2C).

In modern fiber-optic systems, polarization multiplexing is widely used to enhance the data transmission rate (17). The signal SOP is routinely recovered at the receivers to avoid cross-talk and ensure correct reception of the transmitted signals (18). This operation is performed by an adaptive digital equalizer implemented in application-specific integrated circuits (ASICs) (19, 20). By accessing the internal registers of the ASICs, we measured SOP at sampling rates of tens of hertz on the vast majority of commercially available optical coherent transponders (10). Therefore, our approach adds minimal burden to the installation and operation of the submarine cable systems.

Because two of the three Stokes parameters are independent given the unit length of the normalized polarization vector, we rotated the SOP measurements toward the north pole on the Poincaré sphere over a 200-s moving-window average (10). Effectively working as a high-pass filter, the rotation operation also helped reduce the effect of long-term SOP drifts of unknown origin in our experimental setup, potentially owing to temperature variations and mechanical vibrations over the short land sections of cable at both

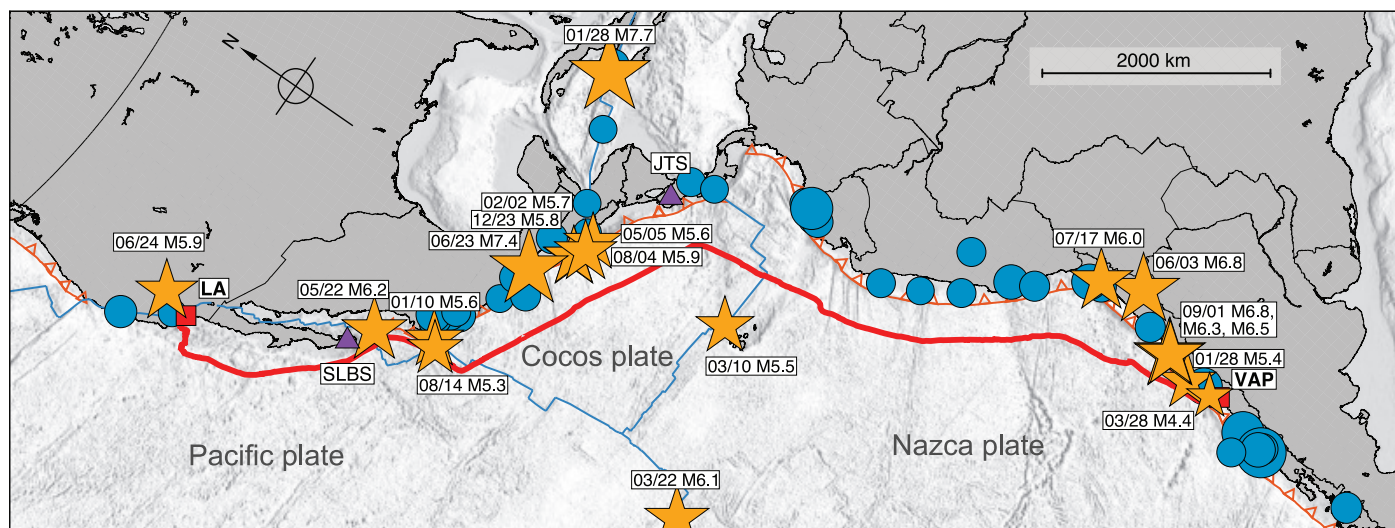


Fig. 1. Tectonics and earthquakes along the Curie cable. The Curie cable (red curve) is a 10,000-km-long submarine fiber-optic cable connecting Los Angeles (LA) and Valparaíso (VAP) along or across a series of active plate boundaries (blue and orange barbed lines). More than 50 earthquakes with a magnitude of >7.5 (blue dots) have occurred in this region since 1900. During

our initial test period of SOP sensing (December 2019 to September 2020), we detected ~20 moderate-to-large earthquakes (yellow stars labeled with date and earthquake magnitude), most of which occurred in the Central and South American subduction zones. JTS and SLBS (purple triangles) are coastal seismic stations along the Curie cable.

ends. After rotation (Fig. 2D), S1 and S2 of the Stokes parameters had values centered around zero, allowing a more straightforward spectral analysis.

During our test period from 15 December 2019 to 4 September 2020, the largest subduction zone event along the Curie cable was the 23 June Oaxaca, Mexico, magnitude 7.4 ($M_{7.4}$) earthquake. The event was ~500 km to the cable at the closest point (Fig. 1). The strong SOP perturbations caused by the shaking lasted more than 20 min (Fig. 3, A and B). In comparison, the vertical-component shaking recorded at the UNM (National Autonomous University of Mexico) seismic station in Mexico City, also ~500 km from the earthquake, lasted ~5 min. The signal durations differ because the SOP measurements reflect the integrated effects of shaking along thousands of kilometers of cable over which the light polarization is perturbed.

The integral effect of SOP along the cable complicates our picking of the primary and secondary (P and S) waves, especially for large events, such as the Oaxaca $M_{7.4}$ earthquake, that also have long rupture durations. On 3 June 2020, we detected on SOP a $M_{w6.8}$ intermediate-depth earthquake underneath Peru, 200 km landward of the coast and 680 km from the Curie cable. Because of the longer distance and the short source durations of intermediate-depth earthquakes (21), we were able to identify clearly separated P and S wave packages in the 0.8 to 3 Hz frequency band (Fig. 3, D and F). Somewhat unexpectedly, 350 s after the earthquake origin time, another package of strong but lower-frequency (0.3 to 0.8 Hz) waves arrived at the Curie cable (Fig. 3, E and F). Given the waves' slow average speed (~2 km/s) and the non-excitation of short-period surface waves from the earthquake at 97 km depth (see fig. S4 for an example of surface waves on SOP), we believe that these late waves are either ocean acoustic waves or Scholte waves converted from the direct P and S waves near bathymetric features (e.g., slopes, trench) (22, 23) and subseafloor heterogeneities (e.g., fault zones) (7). The same mechanism must have contributed to the long SOP signal durations for shallow earthquakes close to the trenches (e.g., Fig. 3A), in addition to the intrinsic integral effect of SOP measurements, as discussed earlier.

For tsunami warning, a key application of seafloor geophysics, the ability to detect water waves is critical for confirming, adjusting, or lifting the initial warnings on the basis of the faster seismic waves (24). This process is currently achieved by a sparse network of ~60 DART (Deep-ocean Assessment and Reporting of Tsunamis) buoys around the globe, mostly along subduction zones. The high cost of installing and maintaining DARTs limits sensor density. If tsunami waves could instead

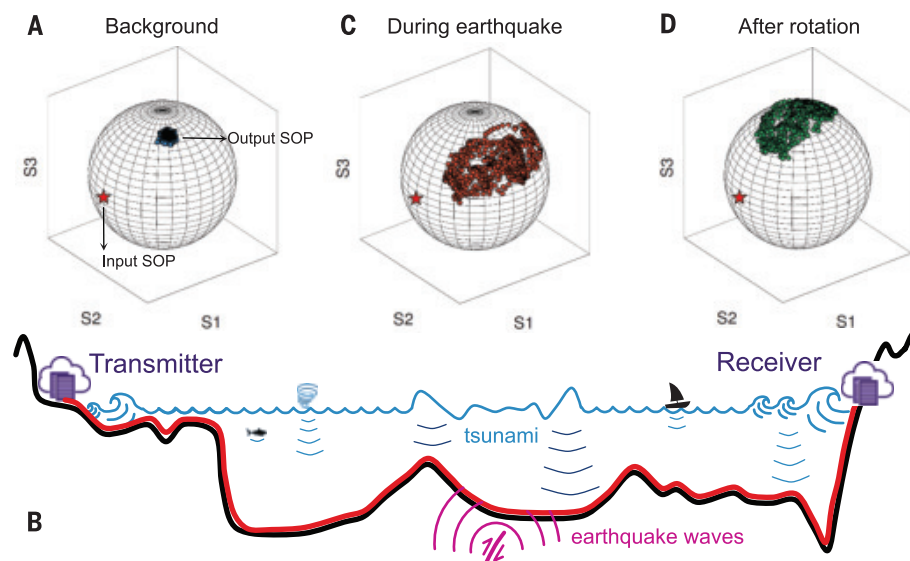


Fig. 2. Principles of polarization-based geophysical sensing. (A) The state of polarization (SOP) at the receiver is monitored routinely (blue dots on the Poincaré sphere) while the input SOP stays stable (red star). For the Curie cable, the output SOP is robust, owing to relatively minimal perturbations along most of its path in the deep ocean (B). The robustness allows us to detect earthquakes or ocean waves that produce SOP anomalies by shaking or pressuring the cable (C). Because the three Stokes parameters are normalized to 1.0, only two are independent. In this study, we rotate the Stokes parameters to the north pole of the Poincaré sphere (9) and focus on analyzing the S1 and S2 parameters after rotation (D).

be detected along submarine cables, the broader data coverage, higher sampling rate, and faster telemetry could supplement current DART systems to provide faster and more reliable tsunami warnings (25). During our test period, only the Oaxaca $M_{7.4}$ earthquake produced tsunami waves (~1 cm high in the open ocean), which were not detected by our current SOP measurement system. In this prototype, the SOP noise is higher at long periods where we expect the tsunami waves (fig. S5), potentially because of temperature variations over the 7.7-km land section of cable (10). In a well-controlled laboratory environment, the SOP noise level is substantially lower than the field observations over a broad frequency band, between 0.01 and 10 Hz (Fig. 3C).

However, in the primary microseism frequency band (~0.06 Hz), we observed multiple packages of dispersive signals from ocean swells, each of which lasted for a few days (Fig. 4A). The timing of the wave packages coincides well with the primary and secondary microseism pairs observed at coastal seismic stations located along the cable, as shown in Fig. 4, B and C, for two representative stations, SLBS (Sierra la Laguna Baja California Sur, Mexico) and JTS (Las Juntas de Abangares, Costa Rica) (station location shown in Fig. 1). Microseism signals at coastal sites are related to ocean swells produced by distant storms (26). In particular, the double-frequency secondary microseism (i.e., the seismic waves produced by wave-wave interactions) was not observed on SOP. Therefore, we suggest that

the dispersive wave packages on SOP are caused by seafloor pressure perturbations from ocean swells in shallow water, not by the passing seismic waves on the seafloor. The amplitudes of ocean swells are comparable to those of damaging tsunami waves observed in the open ocean (e.g., on the order of 1 m for the 2004 Sumatra and 2011 Tohoku earthquakes) (27, 28). Given the much longer period of tsunami waves and therefore negligible decay as a function of depth, the seafloor pressure signal of a tsunami in the open ocean would be comparable or stronger for detection on SOP than that of ocean swells. The SOP detection of tsunami waves in the open ocean is critical for effective tsunami warning.

For estimating earthquake magnitudes and forecasting tsunami wave heights, accurate SOP amplitudes of the recorded seismic and water waves are critical. Without colocated ocean-bottom seismometers or pressure sensors of similar sampling rates, calibrating the SOP amplitudes in a broad frequency band is challenging. However, we found that the amplitudes of the ocean swell events on SOP (Fig. 4A) correlate well with the strengths of the secondary microseism events at coastal seismic stations (Fig. 4, B and C) for ~30 distant storms throughout the testing period (fig. S6). Correlations may exist for the primary microseisms as well, but the data are noisy. These observations suggest that the SOP amplitude scaling has been linear and robust at least around 0.06 Hz over the 9-month observation period.

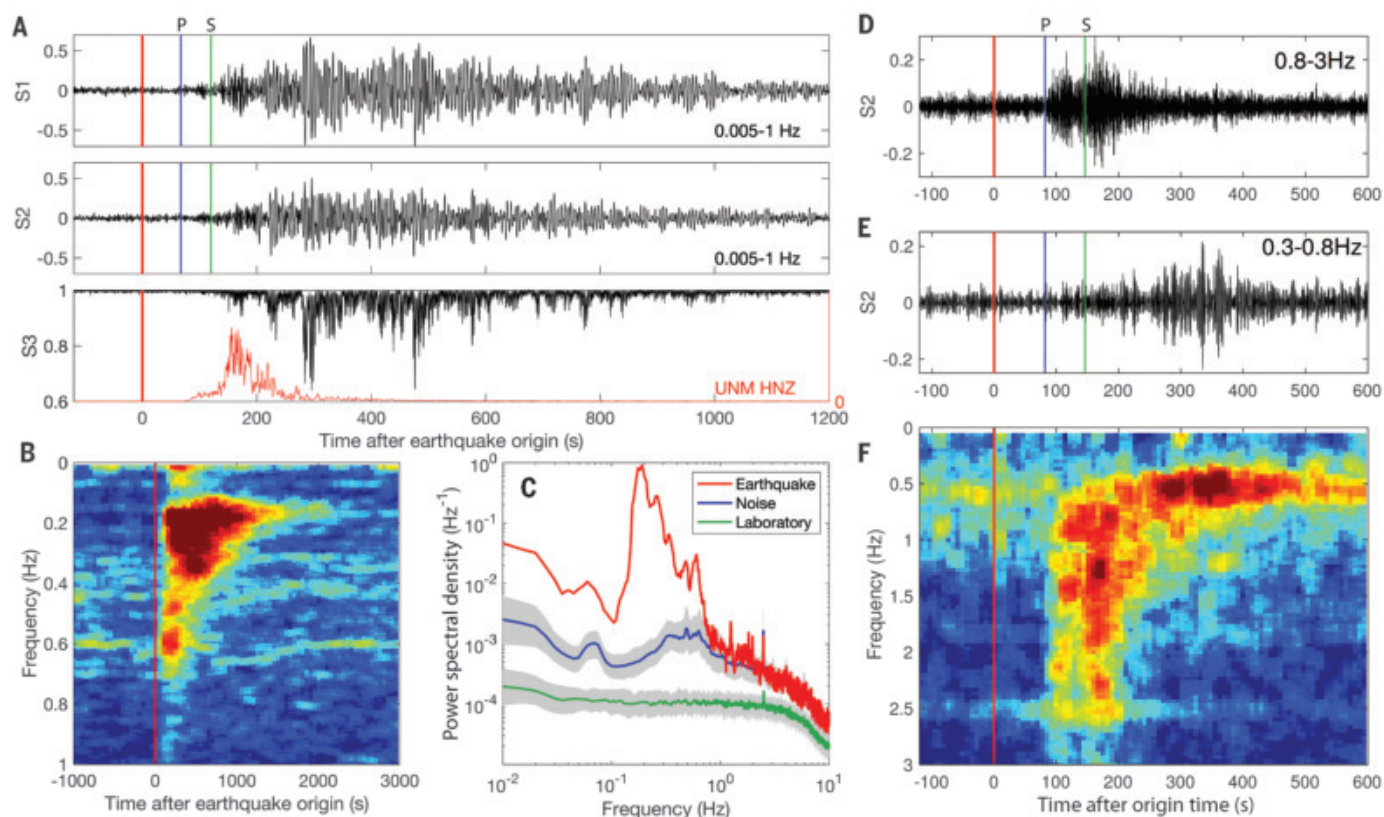


Fig. 3. Earthquake detections along the Curie cable. (A) The Curie SOP anomaly from the 23 June 2020 Oaxaca $M_{w7.4}$ earthquake (Fig. 1) lasted more than 20 min, substantially longer than the shaking duration at the UNM station in Mexico City (seismic envelope shown in red). (B) The summed spectrogram for S1 and S2 show broadband signals from 0.01 to 1 Hz, with a strong and prolonged amplification between 0.15 and 0.35 Hz, as confirmed by the power spectral density (PSD) in the first 5 min of the SOP anomaly [red curve in (C)]. The blue curve and gray band in (C) represent the median noise PSD on the same day and the 1σ confidence interval, respectively. The

PSD peak at ~ 0.06 Hz corresponds to ocean swells. The instrumental noise measured in the laboratory environment is shown as the green curve. (D to F) For a more impulsive $M_{w6.8}$ intermediate-depth earthquake on 3 June 2020, we observed distinct P and S wave packages on SOP between 0.8 and 3 Hz [(D) and (F)], and potentially ocean acoustic waves or Scholte waves at slightly lower frequencies [(E) and (F)]. The vertical red lines in all panels mark the earthquake origin time. The vertical blue and green lines in (A), (D), and (E) are theoretical earthquake P and S wave arrival times, respectively, to the closest point along the cable.

For the seismic waves, the SOP amplitude response is broadband but not flat. For example, the S1 and S2 polarization signals of the Oaxaca $M_{w7.4}$ earthquake are above the noise level between 0.01 and 1 Hz, but with the strongest peak and prolonged signals between 0.15 and 0.35 Hz (Fig. 3, B and C). The SOP earthquake signals were consistently stronger or only visible in the 0.15- to 0.35-Hz band for the nine events detected along the Central American cable section (Fig. 1), which allows us to explore amplitude scaling there. We found that the earthquakes' average SOP power spectral densities in the 0.15- to 0.35-Hz band showed an overall positive correlation with the predicted peak ground displacement in the same band, but with still unclear quantitative relations (fig. S7). We observed even more broadband SOP signals from 0.01 to 5 Hz for the 1 September $M_{w6.8}$ earthquake offshore of Vallenar, Chile (figs. S8 and S9), but with the strongest energy between 0.3 and 1.5 Hz instead. Given the consistent compo-

nents (e.g., cable, repeaters) and installation method along the Curie cable, the differences in the frequency peaks between the Mexico and Chile sections may indicate effects from water depths and site conditions. However, the consistent low-frequency sensitivity around 0.01 Hz is critical to estimating the moment magnitudes of large tsunamigenic earthquakes (29). Determining the dynamic range of SOP measurements and whether the cable-seafloor coupling plays an important role requires further observations.

Like the ultrastable laser interferometry approach (4), the SOP-based sensing integrates the mechanical perturbations over the entire optical path to produce a single SOP time series per channel. The source locations cannot be uniquely determined from a single channel. However, because the SOP approach is highly scalable with minimal modifications to existing cable systems, we expect to be able to use multiple lit cables with different paths in a given region. Once the SOP timings of the

different cables are synchronized (10), their seismic travel times could be combined to locate sources (4). For tsunami warning, the current seismic systems usually produce adequate origin times and locations promptly (25). The SOP measurements could then be jointly interpreted with the seismic and DART data to constrain earthquake magnitudes and refine tsunami forecasts. Furthermore, a suite of geophysical sensing techniques based on submarine telecommunication cables are emerging, with different levels of sensitivity, coverage, spatial resolution, and scalability (4–9). Strategic combinations of the different sensing techniques (including conventional geophysical networks) are necessary to provide the broadest coverage of the seafloor while making high-fidelity, physically interpretable measurements (e.g., locations, depth, and magnitudes).

To our knowledge, our experiment is the first direct demonstration that transcontinental submarine cables can be used for

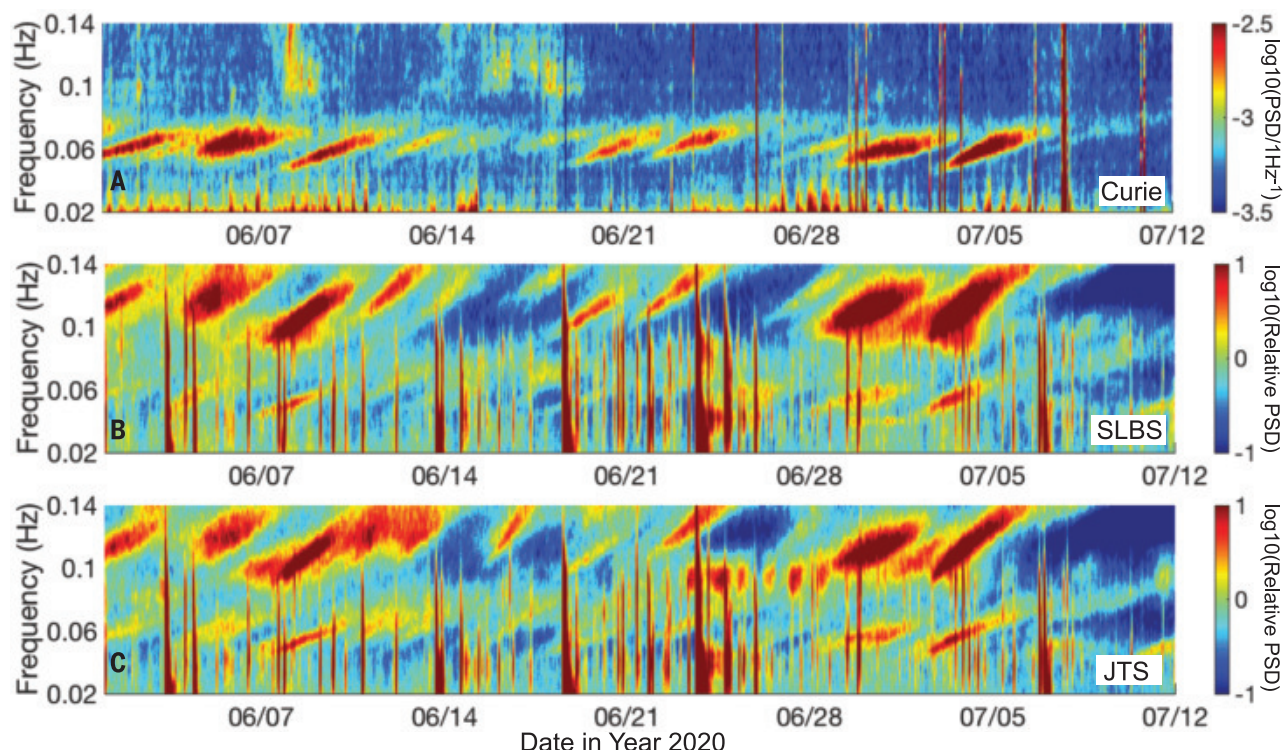


Fig. 4. SOP detection of ocean swells. (A) SOP spectrogram from 1 June 2020 to 12 July 2020. The dispersive energy packages around 0.06 Hz, in the primary microseism band, correlate well with similarly dispersive events on the relative spectrograms of coastal station (B) SLBS and (C) JTS (with

mean PSD removed; station locations shown in Fig. 1), in the primary and secondary (~0.12 Hz) microseism bands. The amplitudes of the SOP events and the microseism events are consistent overall too, which is confirmed more quantitatively in fig. S6.

environmental monitoring through sensing capabilities, in particular earthquake and ocean wave detections. The coherent subsea cable SOP detection technique showed the sensitivity level of an optical polarization interferometer (30). We find it remarkable that by monitoring the SOP of regular optical telecommunication channels via routine equipment, we detected vibrations with peak displacement as small as 0.1 mm (fig. S7) over a 10,000-km submarine cable, or 20,000 km in the round-trip channels (Fig. 1 and fig. S2). The fraction of a wavelength change in the optical path of two orthogonal polarizations implies a high relative phase to polarization stability resulting in relative optical path variation better than 10^{-14} . Substantial room exists to improve the SOP system. For example, the number of SOP channels in a single undersea cable can be the same as the number of telecommunication channels, on the order of hundreds with multiple frequencies per fiber strand (fig. S2). We expect to improve the SOP signal-to-noise ratio by combining these independent SOP measurements from multiple transponders operating on the same cable (fig. S10). Reduction of SOP noise level at high frequencies (1 to 10 Hz) would allow detection of small earthquakes that might not be detectable on terrestrial seismic networks

far away, and at low frequencies (<0.01 Hz) would enable accurate magnitude estimation for large earthquakes and direct observation of tsunami waves. With appropriate timing mechanisms (10), the SOP system would be able to sense strong seismic or ocean waves anywhere along a 10,000-km path within 30 ms of the first wave arrivals at a submarine cable, substantially faster than the closest land-based stations in many cases (e.g., fig. S11).

REFERENCES AND NOTES

1. D. Suetsugu, H. Shiobara, *Annu. Rev. Earth Planet. Sci.* **42**, 27–43 (2014).
2. R. Bürgmann, D. Chadwell, *Annu. Rev. Earth Planet. Sci.* **42**, 509–534 (2014).
3. G. Nolet et al., *Sci. Rep.* **9**, 1326 (2019).
4. G. Marra et al., *Science* **361**, 486–490 (2018).
5. E. F. Williams et al., *Nat. Commun.* **10**, 5778 (2019).
6. A. Sladen et al., *Nat. Commun.* **10**, 5777 (2019).
7. N. J. Lindsey, T. C. Dawe, J. B. Ajo-Franklin, *Science* **366**, 1103–1107 (2019).
8. Z. Zhan, *Seismol. Res. Lett.* **91**, 1–15 (2020).
9. B. M. Howe et al., *Front. Mar. Sci.* **6**, 424 (2019).
10. Materials and methods are available as supplementary materials.
11. H. Kanamori, L. Rivera, S. Lambotte, *Geophys. J. Int.* **218**, 1–32 (2019).
12. H. Eissler, L. Astiz, H. Kanamori, *Geophys. Res. Lett.* **13**, 569–572 (1986).
13. M. Born, E. Wolf, *Principles of Optics: Electromagnetic Theory of Propagation, Interference and Diffraction of Light* (Elsevier, 2013).
14. J. Wuttke, P. M. Krummrich, J. Rösch, *IEEE Photonics Technol. Lett.* **15**, 882–884 (2003).
15. P. M. Krummrich, E.-D. Schmidt, W. Weiershausen, A. Mattheus, “Field trial results on statistics of fast polarization changes

- in long haul WDM transmission systems,” *Optical Fiber Communication Conference and Exposition and The National Fiber Optic Engineers Conference Technical Digest* (paper OThT6, Optical Society of America, 2005).
16. D. Charlton et al., *Opt. Express* **25**, 9689–9696 (2017).
17. S. G. Evangelides, L. F. Mollenauer, J. P. Gordon, N. S. Bergano, *J. Lightwave Technol.* **10**, 28–35 (1992).
18. S. J. Savory, *IEEE J. Sel. Top. Quantum Electron.* **16**, 1164–1179 (2010).
19. G. Charlet et al., *J. Lightwave Technol.* **27**, 153–157 (2009).
20. C. R. S. Fludger et al., *J. Lightwave Technol.* **26**, 64–72 (2008).
21. M. Vallée, *Nat. Commun.* **4**, 2606 (2013).
22. E. A. Okal, *Adv. Geophys.* **49**, 1–65 (2008).
23. Y. Zheng, X. Fang, J. Liu, M. C. Fehler, arXiv:1306.4383 [physics.geo-ph] (18 June 2013).
24. E. Bernard, V. Titov, *Philos. Trans. R. Soc. London Ser. A* **373**, 20140371 (2015).
25. National Research Council, *Tsunami Warning and Preparedness: An Assessment of the U.S. Tsunami Program and the Nation's Preparedness Efforts* (National Academies Press, 2011).
26. R. A. Haubrich, W. H. Munk, F. E. Snodgrass, *Bull. Seismol. Soc. Am.* **53**, 27–37 (1963).
27. V. Titov, A. B. Rabinovich, H. O. Mofjeld, R. E. Thomson, F. I. González, *Science* **309**, 2045–2048 (2005).
28. M. Simons et al., *Science* **332**, 1421–1425 (2011).
29. H. Kanamori, L. Rivera, *Geophys. J. Int.* **175**, 222–238 (2008).
30. P. Grangier, R. E. Slusher, B. Yurke, A. LaPorta, *Phys. Rev. Lett.* **59**, 2153–2156 (1987).
31. Z. Zhan, Curie Data - Zhan et al., Version 1.0, CaltechDATA (2021); <https://doi.org/10.22002/D1.1668>.

ACKNOWLEDGMENTS

We thank U. Holzle for initiating the subsea-based earthquake detection project. We thank B. Koley, V. Vusirikala, M. Salsi,

M. Newland, T. Carlson, L. Bickford, S. Bhattacharya (Google LLC), M. Pan, J. Geyer (Acacia Inc.), S. Thodupunoori (Cisco Inc.), F. Santillo (Ciena Inc.), and Y. Svirko (University of Eastern Finland) for support and discussions. Earthquake information used in this study is from the U.S. Geological Survey. **Funding:** Z.Z. and J.C.C. are funded by the Gordon and Betty Moore Foundation. A.M. is partially funded by the Italian Government through the INCIPICT project. **Author contributions:** Z.Z., M.C., and V.K. designed the work. M.C., V.K., and S.Y. collected the SOP data. A.M., V.K., R.M., M.C., and S.Y. conducted the analyses in optics. Z.Z., J.C., and A.M. led

the work on earthquakes and ocean waves. All authors participated in the data interpretation. Z.Z., A.M., M.C., R.M., V.K., and S.Y. prepared the initial draft, and all authors critically revised and approved the manuscript. **Competing interests:** A U.S. patent has been filed related to this work. **Data and materials availability:** SOP data used in this study are openly available on <https://data.caltech.edu/records/1668> (31). More information about reading and processing the data files can be obtained from the authors upon request. Seismic data at the conventional stations are from the International Federation of Digital Seismograph Networks and the Global Seismic Network

and downloaded through the Incorporated Research Institutions for Seismology.

SUPPLEMENTARY MATERIALS

science.sciencemag.org/content/371/6532/931/suppl/DC1
Supplementary Text
Figs. S1 to S12
References (32–47)

13 September 2020; accepted 11 January 2021
10.1126/science.abe6648

CHEMICAL DYNAMICS

Quantum interference between spin-orbit split partial waves in the $F + HD \rightarrow HF + D$ reaction

Wentao Chen^{1*}, Ransheng Wang^{2*}, Daofu Yuan^{1*}, Hailin Zhao², Chang Luo¹, Yuxin Tan¹, Shihao Li¹, Dong H. Zhang², Xingan Wang^{1†}, Zhigang Sun^{2†}, Xueming Yang^{2,3†}

The effect of electron spin-orbit interactions on chemical reaction dynamics has been a topic of much research interest. Here we report a combined experimental and theoretical study on the effect of electron spin and orbital angular momentum in the $F + HD \rightarrow HF + D$ reaction. Using a high-resolution imaging technique, we observed a peculiar horseshoe-shaped pattern in the product rotational-state-resolved differential cross sections around the forward-scattering direction. The unusual dynamics pattern could only be explained properly by highly accurate quantum dynamics theory when full spin-orbit characteristics were considered. Theoretical analysis revealed that the horseshoe pattern was largely the result of quantum interference between spin-orbit split-partial-wave resonances with positive and negative parities, providing a distinctive example of how spin-orbit interaction can effectively influence reaction dynamics.

The discovery of electron spin by Uhlenbeck and Goudsmit in 1925 was a major breakthrough in understanding the fundamental properties of electrons and quantum systems involving electrons (1). It is well established that the couplings between electron spin with orbital angular momentum are ubiquitous in atomic, molecular, and material systems and could result in many notable phenomena, such as the splitting and shifting of atomic energy levels (2), magnetocrystalline anisotropy (3), and the quantum spin Hall effect in semiconductors (4). Electron spin has also been investigated for technological applications such as the development of electronic devices for logic operations; i.e., spintronics (5, 6).

In atomic systems, the inclusion of the coupling of electron spin (**s**) and orbital angular momenta (**l**) could lead to pronounced splitting in energy. In molecular systems, however, the situations are more complicated and

subtle because couplings between electron spin, electron orbital angular momentum, and rotational angular momentum (**j**) and orbital angular momentum (**L**) of nuclei motions are all possible. For example, in diatomic systems, couplings between electron spin, electron orbital angular momentum, and nuclei rotational angular momentum can cause fine structures, such as spin-orbit splitting and lambda doubling, in rotational states (7, 8).

In atomic and molecular collision processes, the inclusion of the coupling of electron spin and orbital angular momentum could also have a notable effect. For inelastic collisions such as that of $NO(X^2\Pi)$ with Ar, recent experimental studies have shown that differential cross sections depend sensitively on the change in total parity (9), suggesting that different spin-orbit states experience different potential interactions.

In chemical reactions involving species with unpaired electron spins with orbital angular momentum, there are at least two spin-orbit states in the low-energy range: For halogen atoms such as F and Cl, these are $^2P_{3/2}$ and $^2P_{1/2}$. The relative reactivity of these two spin-orbit states with H_2 has been a notable research topic (10–15). Owing to the breakdown of the Born-Oppenheimer approximation, which is caused mainly by the electrostatic spin-orbit coupling (SOC) between different electronic states, the excited state ($^2P_{1/2}$) was more re-

active than the ground state ($^2P_{3/2}$) at low collision energy. Attention has also been devoted to chemical reactions with lambda-doublet products (16, 17).

In addition to the electrostatic SOC between different electronic states, couplings could also occur between electron spin and the angular momentum of nuclei orbital motions in chemical reactions, which leads to the splitting of partial waves, resulting in “fine” structures of the partial waves, similar to the fine structures in the spectra of the diatomic molecules. Yet how or whether the inclusion of the partial-wave splitting in a chemical reaction can affect the dynamics remains largely unknown.

The $F + H_2 \rightarrow HF + H$ reaction is the most notable benchmark system for the study of quantum reaction resonances, which has attracted substantial attention over the past few decades. Reactive resonances were first predicted theoretically in 1973 for the $F + H_2$ reaction by using a colinear reaction model (18, 19). In 1984, a landmark crossed-molecular-beam experiment was performed on the $F + H_2$ reaction by Lee and co-workers, in which a peculiar forward-scattering peak for product $HF(v' = 3)$ was observed and attributed to reactive resonances (20). However, the dynamical origin of the forward-scattering peak remained unclarified (21, 22). In 2000, a steplike structure in the excitation function in the $F + HD \rightarrow HF + D$ reaction was observed by Liu and co-workers and was attributed to a quantum reactive resonance (23). Over the past two decades, the $F + H_2$ and $F + HD$ reactions have been extensively investigated using the high-resolution crossed-beams Rydberg H-tagging technique (24–28) and the negative-ion photodetachment spectroscopic method (29, 30), in association with accurate quantum dynamics calculations, and an accurate picture for reaction resonances in this benchmark system was established (31). The results of the molecular-crossed-beams experiment and the negative ion (FH_2^-) photodetachment study on the cold reaction resonance in the $F + H_2$ reaction were also found to be consistent (28). In all of these studies, the resonance signatures observed in the experimental results can be quite accurately accounted for by using the adiabatic theory

¹Hefei National Laboratory for Physical Sciences at the Microscale and Department of Chemical Physics, University of Science and Technology of China, Hefei, 230026, China. ²State Key Laboratory of Molecular Reaction Dynamics, Dalian Institute of Chemical Physics, Chinese Academy of Sciences, Dalian, 116023, China.

³Department of Chemistry, College of Science, Southern University of Science and Technology, Shenzhen, 518055, China.

*These authors contributed equally to this work.

†Corresponding author. Email: xawang@ustc.edu.cn (X.W.); zsun@dicp.ac.cn (Z.S.); xmyang@dicp.ac.cn (X.Y.)

without considering spin-orbit effects in these systems. Electron spin and orbital motions in these systems seemingly do not have a substantial effect on the dynamics of this resonance-mediated reaction, which occurs mostly in the adiabatic ground electronic state.

In this work, we have combined experimental and theoretical studies of the $F(^2P_{3/2}) + HD \rightarrow HF + D$ reaction at a collision energy of 2.10 kcal/mol, where the partial-wave resonances are substantial (32), to investigate the role of partial-wave splitting in the reaction by full consideration of the electron spin and orbit effects. Experimentally, we used a newly developed high-resolution velocity map imaging crossed-beams technique (33–35), in combination with near-threshold ionization of the D-atom product, to achieve the highest possible angular and translational energy resolution. This technique allowed us to accurately determine quantum-state-resolved angular distributions, which often carry the most detailed quantum dynamics information in chemical reactions. For example, this method has enabled detection of the geometric phase effect in the $H + HD \rightarrow H_2 + D$ reaction (35). Theoretically, we performed the state-to-state time-dependent quantum wave-packet calculations using an adiabatic model and a full spin-orbit-coupled model, which included all angular momentum couplings between electronic spin, electron orbital angular momentum, and nuclear orbital angular momentum in this reaction. The model was initially developed by Alexander and co-workers (11, 12, 36). Our results conclusively show that the inclusion of fine structures of partial waves has a notable effect on the dynamics of this resonance-mediated $F(^2P_{3/2}) + HD \rightarrow HF + D$ reaction.

Here we briefly describe our experimental procedures (see the supplementary materials for details; a schematic diagram of the experimental setup is provided in fig. S1). The F-atom beam was generated by discharge in the supersonic expansion of a gas mixture of 5% F_2 in helium through a pulsed valve (General Valve) with a stagnation pressure of 6 bar. The velocity (v) of the generated F-atom beam was determined to be 1.40 km/s with a speed ratio ($v/\Delta v$) of 15. To improve the beam quality, the electrode plates in the discharge area were cooled by liquid nitrogen. The HD molecular beam was produced by expanding the HD sample (97% purity) via a liquid nitrogen-cooled pulsed nozzle (Even-Lavie valve) with a stagnation pressure of 13 bar. The velocity of the HD molecular beam was 1.24 km/s with a speed ratio ($v/\Delta v$) of 30. Using the cryogenic expansion, we found that ~97% of the HD molecules in the HD molecular beam populated the ($v = 0, j = 0$) ground level. Both the pulsed F-atom beam and the HD molecular beam

were collimated by double skimmers before entering the scattering chamber; the two beams were crossed in the reaction chamber with a 160° crossing angle. The collision energy of the current experiment was 2.10 kcal/mol, with an energy spread of 0.1 kcal/mol. The D-atom products from the $F + HD \rightarrow HF + D$ reaction in the beam-crossing region were detected by a two-color (1 + 1') (vacuum ultraviolet + ultraviolet) threshold ionization method (fig. S2). In the experiment, the reaction dominantly occurred from the spin-orbit ground state $F(^2P_{3/2})$.

By means of the experimental method described above, the D-atom product velocity map image from the $F(^2P_{3/2}) + HD \rightarrow HF + D$ reaction at a collision energy of 2.10 kcal/mol (Fig. 1A) was obtained by accumulating the

signals over 2.4 million laser pulses. Using the velocity map imaging technique with near-threshold ionization, we were able to clearly resolve the rotational states of $HF(v', j')$. There are two main ring structures that correspond to the HF products in the $v' = 2$ and 3 vibrational states: The inner ring structure is due to the $HF(v' = 3)$ state product, and the well-resolved outer rings can all be assigned to individual rotational levels of the $HF(v' = 2, j')$ product. Although the $HF(v' = 3)$ product was predominantly forward scattered, the $HF(v' = 2)$ products were mainly backward scattered but with substantial forward and sideways scatterings. Notably, a peculiar horseshoe-shaped structure in the image was clearly detected in the forward-scattering direction. This structure arose from peaked angular

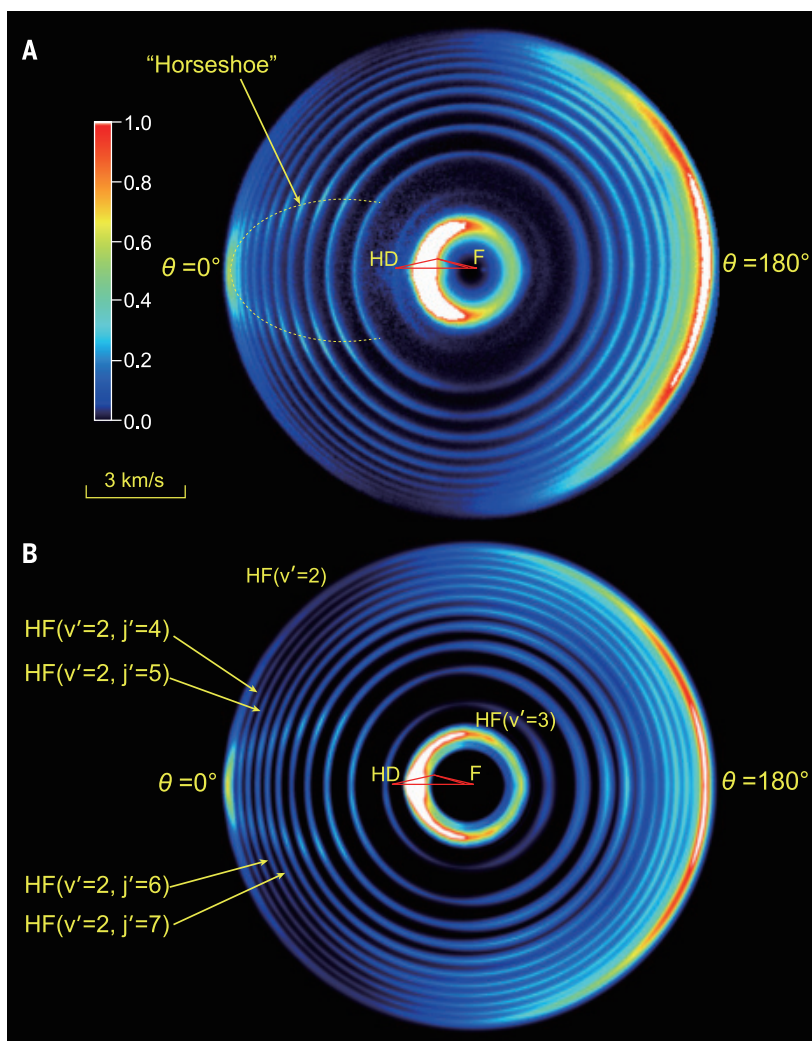


Fig. 1. The D-atom product from the $F + HD \rightarrow HF + D$ reaction at a collision energy of 2.10 kcal/mol. (A) Experimental results; (B) theoretical results. The crossing angle of the two beams is 160°. $\theta = 0^\circ$ and 180° denote the forward- and the backward-scattering direction, respectively, for the HF coproduct in the center-of-mass frame relative to the F-atom beam direction. A peculiar horseshoe-like feature in the forward-scattering direction can be clearly seen in the scattering pattern.

distributions of $\text{HF}(v' = 2)$ products in different j' states in the forward-scattering hemisphere. However, the mechanism that causes this distinctive feature in the angular distribution is not immediately clear.

From the high-resolution D-atom product image in Fig. 1A, the differential cross section

(DCS) for the HF product at different rovibrational states can be determined. For the forward-scattering direction, the rotational states of the $\text{HF}(v' = 2)$ product were clearly resolved, which allowed us to extract the rotational-state-resolved DCS with high accuracy. The experimental angular distributions

obtained for $\text{HF}(v' = 2)$ in the $j' = 3$ and 5 rotational states from Fig. 1A are shown in Fig. 2. The angular distributions for other rotational states of $\text{HF}(v' = 2)$ are plotted in fig. S4. Angular distributions for different j' states were all peaked at angles off of the exact center-of-mass forward-scattering direction ($\theta = 0^\circ$), with a double-peak structure in the full DCS. The horseshoe structure in the image was due to the double-peak structure in the DCS for different rotational states of $\text{HF}(v' = 2)$ in the forward-scattering direction (Fig. 2 and fig. S4), with increased spacing as the rotational quantum number j' increased.

To understand the dynamical origin of the horseshoe pattern in the DCS shown in Fig. 1A, we carried out theoretical investigations using different models with the time-dependent quantum reactive scattering theory. We first performed adiabatic dynamics calculations on the single potential energy surface of the lowest adiabatic electronic state (28, 37). In this adiabatic model, the F atom was regarded as a structureless atom, whose electron spin (**s**) and electron orbital angular momentum (**l**) were neglected; only rotational quantum number (**j**) and orbital angular momentum of nuclei motions (**L**) were taken into consideration. Thus, the splitting of the partial waves did not arise. The recently developed interaction-asymptotic region decomposition method was applied to extract state-to-state reactive scattering information (38).

Using the adiabatic model, we calculated the opacity function for the $\text{HF}(v' = 2, j' = 3)$ product channel (Fig. 3; blue curve with squares). The plot shows that two components—a main broad peak from $J = 0$ to 17 partial waves and a sharp peak at $J = 18$ partial waves—contributed to this product channel. Theoretical analysis indicated that the sharp peak at $J = 18$ was due to a reactive resonance via a single partial wave of $J = 18$, and the main broad peak was due to the direct reaction mechanism. The $J = 18$ partial-wave resonance was identified as the rotationally excited state of the quasi-bound (003) resonance, trapped in the $\text{HF}(v' = 3)$ -D vibrational adiabatic potential well (Fig. 4) (24). At $J = 18$, the excited resonance state, (103), did not exist anymore, and the ground resonance state, (003), was supported by a centrifugal barrier. Therefore, the resonance at $J = 18$ is a Feshbach resonance for the $\text{HF}(v' = 2)$ channel and a shape resonance for the $\text{HF}(v' = 3)$ channel (39). Theoretical results also showed that the $J = 18$ single partial-wave resonance was mostly responsible for the forward-scattering products in this reaction, and the direct reaction component was largely backward scattered (fig. S5).

We further computed the state-specific DCSs using the adiabatic model for $\text{HF}(v' = 2, j')$ in

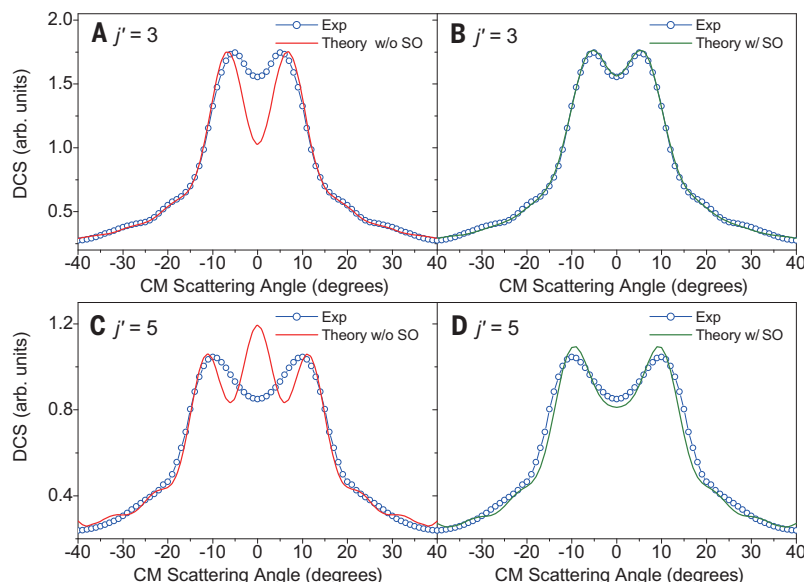


Fig. 2. Comparisons of the experimental and theoretical DCSs around the forward-scattering direction for the $\text{F} + \text{HD} \rightarrow \text{HF}(v' = 2, j' = 3 \text{ and } 5) + \text{D}$ reaction at a collision energy of 2.10 kcal/mol. (A to D) The theoretical results shown with red lines are from the adiabatic model with a structureless F atom, whereas those shown with green lines are from the model that includes full spin-orbit effects. Exp, experiment; CM, center of mass.

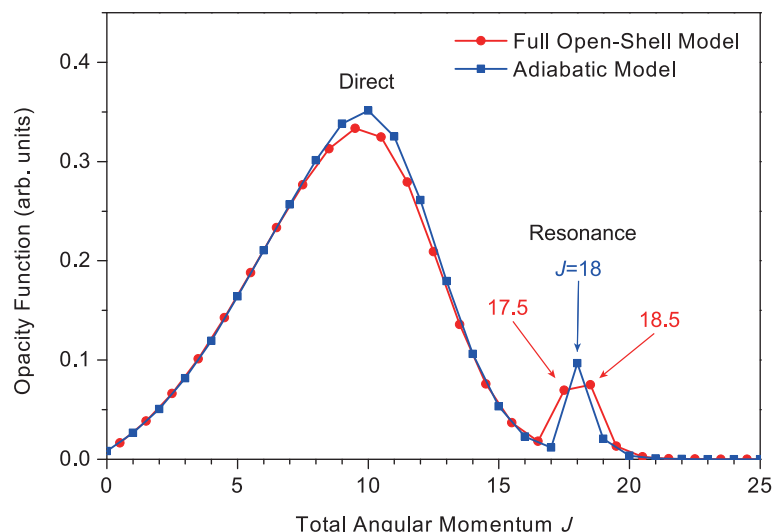


Fig. 3. Calculated opacity function for the $\text{HF}(v' = 2, j' = 3)$ product channel from the $\text{F} + \text{HD} \rightarrow \text{HF} + \text{D}$ reaction. In the adiabatic model (blue) and the full open-shell model (red), the calculated opacity function shows two different contributions: a direct reaction mechanism and a resonance-mediated reaction mechanism. In the adiabatic model, a single J partial wave is responsible for the resonance mechanism, whereas in the full open-shell model, four J partial waves contribute to the resonance mechanism.

the forward-scattering direction. The calculated adiabatic DCSs for $\text{HF}(v' = 2, j' = 3 \text{ and } 5)$ are shown in Fig. 2, A and C, respectively, for comparison with the experimental results. The adiabatic DCSs for other rotational states of $\text{HF}(v' = 2, j')$ are plotted in fig. S4, A, C, and E. For better comparison with the experiment, all of the calculated DCSs in Fig. 2 and fig. S4 have been convoluted with an estimated experimental angular resolution of 4° . No convolution was performed for the DCS with the collision energy spread. From the comparison in Fig. 2, A and C, and fig. S4, A, C, and E, we can see clearly that the adiabatic theoretical results were not in good agreement with the experimental results, especially in the exact forward-scattering direction. For the $\text{HF}(v' = 2, j' = 5)$ DCS results, the two theoretical peaks off of 0° matched quite well with the experimental ones. However, there was an extra theoretical peak at $\theta = 0^\circ$, which did not arise in the experimental results. For $\text{HF}(v' = 2, j' = 3)$, the deep dip in the adiabatic DCS shown at $\theta = 0^\circ$ was also not in good agreement with the experiment. Similarly, the adiabatic calculations were not able to reproduce the experimental findings for other j' values (fig. S4, A, C, and E). From these comparisons, it seems quite clear that the experimentally observed horseshoe pattern in the forward scattering cannot be accurately accounted for using the adiabatic dynamics model, in which the electron spin and electron orbital angular momentum cannot be included. Thus, the question becomes whether the discrepancies between the adiabatic model and the experiment were caused by neglecting the electron spin and orbital motion in the adiabatic model—i.e., caused by neglecting the fine structure of partial waves.

We then carried out the time-dependent quantum wave-packet dynamics calculations using a full six-state diabatic model (11, 12, 36), which was developed by Alexander and co-workers. This model included all angular momentum couplings between the electron spin, electron orbital angular momentum, and angular momenta of the nuclear motions. A brief description of the full six-state diabatic model can be found in the supplementary materials. The calculated DCSs for the $\text{HF}(v' = 2, j' = 3 \text{ and } 5)$ product using the full open-shell model are shown in Fig. 2, B and D, along with the experimental results. Notably, the theoretical DCSs using the full open-shell model were in near-perfect agreement with the experimental observations. The agreement for other j' states of $\text{HF}(v' = 2)$ between theory and experiment was also excellent (fig. S4, B, D, and F). These results strongly suggest that the inclusion of the electron spin and electron orbital motions in the model had a marked effect on the dynamics of the resonance-

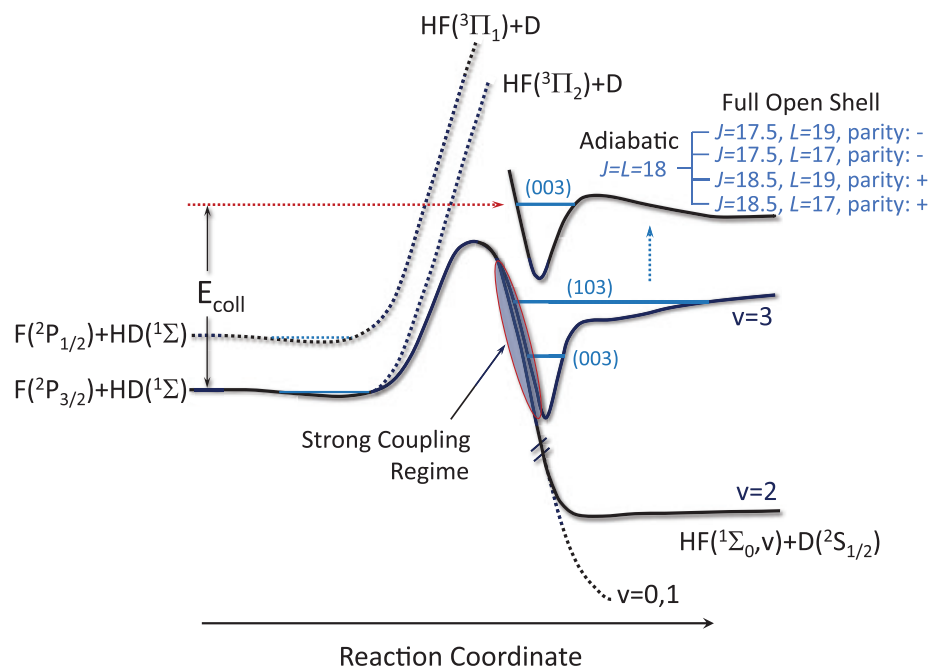


Fig. 4. Schematic of the resonance-mediated reaction mechanism. With inclusion of the full spin-orbit effects, a single $J = 18$ partial wave in the adiabatic picture is split into four partial waves (two with $J = 17.5$ of negative parity and two with $J = 18.5$ of positive parity). E_{coll} , collision energy.

mediated $\text{F} + \text{HD}$ reaction. The fine structures of partial waves in this reaction at this collision energy for reproducing the experimental DCS of such high resolution cannot be ignored.

To elucidate the underlying dynamics of this phenomenon, we also used the full six-state diabatic model to calculate the opacity functions. The opacity function for the $\text{HF}(v' = 2, j' = 3)$ product is shown in Fig. 3, in comparison with that for the adiabatic model. In contrast to the case of a single partial-wave resonance ($J = 18$) in the adiabatic model, it appears that two partial-wave resonances, $J = 17.5$ and 18.5 , were responsible for the resonance peak in the opacity function at a collision energy of 2.10 kcal/mol (Fig. 3), which refers to $\text{F}(^2\text{P}_{3/2}) + \text{HD}(v = 0, j = 0)$ at infinite separation. This finding suggests that electron spin and orbital angular momenta were coupled to the angular momentum of the nuclear motion during the chemical reaction, which split the partial waves and substantially influenced the dynamics of this reaction. More detailed analysis showed that there were actually four partial waves contributing to that peak in the opacity function at a collision energy around 2.10 kcal/mol : two with $J = 17.5$ and two with $J = 18.5$ but with different total parities (fig. S6). In addition, theoretical analysis showed that the forward-scattering products in this reaction were mainly caused by the $J = 17.5$ and 18.5 partial-wave resonances, and the direct reaction component

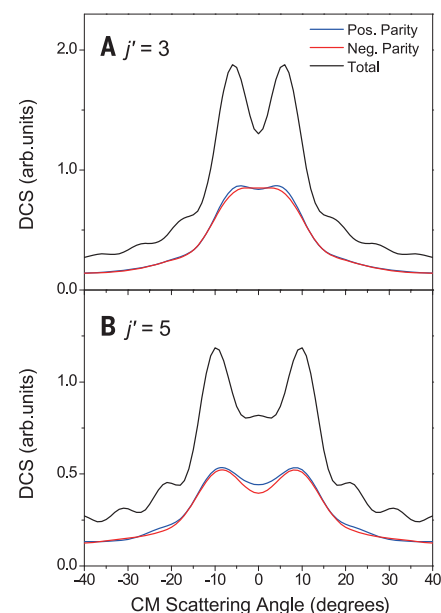


Fig. 5. Calculated DCSs for the $\text{HF}(v' = 2, j' = 3 \text{ and } 5)$ channel. (A and B) Interference between partial waves of positive and negative parities enhances the double-peak structure in the forward angular distribution and creates the slight oscillatory angular structures in the resonance-mediated $\text{F} + \text{HD} \rightarrow \text{HF} + \text{D}$ reaction. The comparison demonstrates that the double-peak structure is due to the interference between spin-orbit split-resonance partial waves of different parities.

was dominantly backward scattered (fig. S5), similar to that predicted in the adiabatic model without considering all spin-orbit interactions.

The appearance of four partial waves in the full six-state diabatic model, instead of a single partial wave in the adiabatic model, deserves more explanation. In the adiabatic model, electron spin and orbital angular momentum were neglected, and the total angular momentum \mathbf{J} was the summation of the nuclear orbital angular momentum \mathbf{L} and the diatomic rotational angular momentum \mathbf{j} (i.e., $\mathbf{J} = \mathbf{L} + \mathbf{j}$). For the reactant HD molecule in the $j = 0$ state, $J = L$. In the full six-state diabatic model, the electron spin (\mathbf{s}) and electron orbital angular momentum (\mathbf{l}) were included. The total angular momentum \mathbf{J} was thus the summation of the nuclear orbital angular momentum \mathbf{L} , the diatomic angular momentum \mathbf{j} , and the total electronic angular momentum \mathbf{j}_a (that is, $\mathbf{J} = \mathbf{L} + \mathbf{j} + \mathbf{j}_a$). Here, $\mathbf{j}_a = \mathbf{s} + \mathbf{l}$, according to Hund's case a (7). As in the experimental condition, the reactant HD molecule was in the $j = 0$ state, and we then have $\mathbf{J} = \mathbf{L} + \mathbf{j}_a$.

In the $F(2P_{3/2}) + \text{HD}$ reaction, the initial $2P_{3/2}$ state is with $s = 1/2$ and $l = 1$, and thus \mathbf{j}_a could have four different values: 1.5, 0.5, -0.5, and -1.5. Consequently, for each L quantum number, there are four J values: $L - 1.5$, $L - 0.5$, $L + 0.5$, and $L + 1.5$. For example, when $L = 18$, J can have four possible values (16.5, 17.5, 18.5, and 19.5) in the entrance channel (fig. S7). These variations imply that a single J partial wave in the adiabatic model would split into four partial waves in the full six-state diabatic model (Fig. 4) when electron spin and orbital angular momenta of both electron and nuclei motions are included.

More notably, among these four partial waves accounting for the resonances at a collision energy of ~ 2.10 kcal/mol, two of them with $J = 17.5$ are of negative total parity (-), and the other two with $J = 18.5$ are of positive parity (+). From the calculated reaction probabilities, these four spin-orbit fine-structure partial waves should have similar potential energy surfaces so that resonance states transiently trapped on these surfaces all have similar energies (fig. S6). To determine whether spin-orbit split partial waves with different parities have any effect on the reaction dynamics, we calculated the DCSs for the $\text{HF}(v' = 2, j')$ product with partial waves of pure negative or positive parity. Figure 5 displays the calculated DCS for $\text{HF}(v' = 2, j' = 3 \text{ and } 5)$ from partial waves with pure negative and positive parities. It appears that the double-peak structure in the calculated DCS for partial waves with pure negative or positive parity was substantially underestimated (Fig. 5), and the summation of these structures is

clearly not in good agreement with the experimental results. However, when all partial waves with both negative and positive parities were included, the double-peak structure in the calculated DCSs became much more pronounced and was in excellent agreement with the experiment. A similar conclusion was reached for the other rotational states of product $\text{HF}(v' = 2, j')$. These findings suggest that the enhanced forward-scattering double-peak structure, the observed horseshoe pattern, originated from quantum interference between spin-orbit split partial waves of different total parities.

With respect to previous studies (28, 32), it is noteworthy that even though the inclusion of electron spin and orbit can substantially affect the detailed structures of the DCSs for the $F + \text{HD} \rightarrow \text{HF} + \text{D}$ reaction, the picture of reactive resonances in the full six-state diabatic model is quite similar to that in the adiabatic model, except that a single adiabatic partial resonance state is now split into four spin-orbit split-partial-wave resonances. From detailed theoretical dynamics calculations, we found that the positions of the four spin-orbit split-partial-wave resonances are almost exactly the same as those in the original adiabatic partial-wave resonance state (fig. S8).

In this combined experimental and theoretical study, we have shown that electron spin and orbital angular momenta can have profound effects on the dynamics of the resonance-mediated $F + \text{HD} \rightarrow \text{HF} + \text{D}$ reaction through spin-orbit partial-wave splitting. The strong effect of spin-orbit split partial waves on chemical reactivity manifested in the state-resolved DCS is especially noteworthy, although the effect of the SOC on rotational energy levels has been well established for a long time in diatomic molecules and radicals (e.g., NO and OH). The experimental detection of the horseshoe-shaped DCS structure in the title reaction has demonstrated the power of the D-atom velocity map imaging method, in combination with threshold ionization, for accurately measuring the fine angular features in the state-resolved DCS. This finding allowed us to probe the hidden effects of spin-orbit interactions on the dynamics of this resonance-mediated chemical reaction.

REFERENCES AND NOTES

- G. E. Uhlenbeck, S. Goudsmit, *Naturwissenschaften* **13**, 953–954 (1925).
- R. Kakkar, *Atomic and Molecular Spectroscopy: Basic Concepts and Applications* (Cambridge Univ. Press, 2015).
- H. A. Dürr et al., *Science* **277**, 213–215 (1997).
- J. Wunderlich et al., *Science* **330**, 1801–1804 (2010).
- D. A. Allwood et al., *Science* **309**, 1688–1692 (2005).
- A. R. Melnik et al., *Nature* **511**, 449–451 (2014).
- R. N. Zare, A. L. Schmeltekopf, W. J. Harrop, D. L. Albritton, *J. Mol. Spectrosc.* **46**, 37–66 (1973).
- H. Lefebvre-Brion, R. W. Field, *The Spectra and Dynamics of Diatomic Molecules: Revised and Enlarged Edition* (Elsevier Academic Press, 2004).
- C. J. Eyles et al., *Nat. Chem.* **3**, 597–602 (2011).
- J. C. Tully, *J. Chem. Phys.* **60**, 3042–3050 (1974).
- M. H. Alexander, D. E. Manolopoulos, H.-J. Werner, *J. Chem. Phys.* **113**, 11084–11100 (2000).
- M. H. Alexander, G. Capecchi, H.-J. Werner, *Science* **296**, 715–718 (2002).
- L. Che et al., *Science* **317**, 1061–1064 (2007).
- X. Wang et al., *Science* **322**, 573–576 (2008).
- F. Lique, G. Li, H.-J. Werner, M. H. Alexander, *J. Chem. Phys.* **134**, 231101 (2011).
- M. H. Alexander, E. J. Rackham, D. E. Manolopoulos, *J. Chem. Phys.* **121**, 5221–5235 (2004).
- P. G. Jambrina, A. Zanchet, J. Aldegunde, M. Brouard, F. J. Aoi, *Nat. Commun.* **7**, 13439 (2016).
- G. C. Schatz, J. M. Bowman, A. Kuppermann, *J. Chem. Phys.* **58**, 4023–4025 (1973).
- S.-F. Wu, B. R. Johnson, R. D. Levine, *Mol. Phys.* **25**, 839–856 (1973).
- D. M. Neumark, A. M. Wodtke, G. N. Robinson, C. C. Hayden, Y. T. Lee, *Phys. Rev. Lett.* **53**, 226–229 (1984).
- F. J. Aoi et al., *Chem. Phys. Lett.* **223**, 215–226 (1994).
- J. F. Castillo, D. E. Manolopoulos, K. Stark, H. J. Werner, *J. Chem. Phys.* **104**, 6531–6546 (1996).
- R. T. Skodje et al., *Phys. Rev. Lett.* **85**, 1206–1209 (2000).
- M. Qiu et al., *Science* **311**, 1440–1443 (2006).
- C. Xu, D. Xie, D. H. Zhang, *Chin. J. Chem. Phys.* **19**, 96–98 (2006).
- Z. Ren et al., *Proc. Natl. Acad. Sci. U.S.A.* **105**, 12662–12666 (2008).
- D. Yu, J. Chen, S. Cong, Z. Sun, *J. Phys. Chem. A* **119**, 12193–12208 (2015).
- T. Yang et al., *Nat. Chem.* **11**, 744–749 (2019).
- D. E. Manolopoulos et al., *Science* **262**, 1852–1855 (1993).
- J. B. Kim et al., *Science* **349**, 510–513 (2015).
- T. Wang et al., *Chem. Soc. Rev.* **47**, 6744–6763 (2018).
- W. Dong et al., *Science* **327**, 1501–1502 (2010).
- S. Yu, D. Yuan, W. Chen, X. Yang, X. Wang, *J. Phys. Chem. A* **119**, 8090–8096 (2015).
- D. Yuan et al., *Nat. Chem.* **10**, 653–658 (2018).
- D. Yuan et al., *Science* **362**, 1289–1293 (2018).
- Z. Sun, D. H. Zhang, M. H. Alexander, *J. Chem. Phys.* **132**, 034308 (2010).
- J. Chen, Z. Sun, D. H. Zhang, *J. Chem. Phys.* **142**, 024303 (2015).
- H. Zhao, U. Umer, X. Hu, D. Xie, Z. Sun, *J. Chem. Phys.* **150**, 134105 (2019).
- X. Wang et al., *Proc. Natl. Acad. Sci. U.S.A.* **105**, 6227–6231 (2008).
- W. Chen et al., Quantum interference between spin-orbit split partial waves in the $F + \text{HD} \rightarrow \text{HF} + \text{D}$ reaction. *Dryad* (2021); <https://doi.org/10.5061/dryad.2547d7wpr>.

ACKNOWLEDGMENTS

Funding: This work was supported by the National Key R&D Program of China (no. 2016YFF0200500), National Natural Science Foundation of China (nos. 21688102, 21590800, 21733006, 21825303, and 21327901), Chinese Academy of Sciences (grant no. XDB 17010000), and Ministry of Science and Technology. **Author contributions:** W.C., D.Y., C.L., Y.T., S.L., X.Y., and X.W. performed the crossed-beam experiments and data analysis. R.W., H.Z., D.H.Z., and Z.S. performed the quantum dynamics calculations and data analysis. X.W., Z.S., and X.Y. designed the research. X.W., Z.S., and X.Y. wrote the manuscript. **Competing interests:** None declared. **Data and materials availability:** All data needed to evaluate the conclusions in the paper are present in the paper or the supplementary materials. All of the data have been uploaded to Dryad (40).

SUPPLEMENTARY MATERIALS

science.sciencemag.org/content/371/6532/936/suppl/DC1
Materials and Methods
Figs. S1 to S9
Tables S1 and S2
References (41–43)

25 October 2020; accepted 14 January 2021
10.1126/science.abf4205

PALEONTOLOGY

The influence of juvenile dinosaurs on community structure and diversity

Katlin Schroeder^{1*}, S. Kathleen Lyons², Felisa A. Smith¹

Despite dominating biodiversity in the Mesozoic, dinosaurs were not speciose. Oviparity constrained even gigantic dinosaurs to less than 15 kg at birth; growth through multiple morphologies led to the consumption of different resources at each stage. Such disparity between neonates and adults could have influenced the structure and diversity of dinosaur communities. Here, we quantified this effect for 43 communities across 136 million years and seven continents. We found that megatheropods (more than 1000 kg) such as tyrannosaurs had specific effects on dinosaur community structure. Although herbivores spanned the body size range, communities with megatheropods lacked carnivores weighing 100 to 1000 kg. We demonstrate that juvenile megatheropods likely filled the mesocarnivore niche, resulting in reduced overall taxonomic diversity. The consistency of this pattern suggests that ontogenetic niche shift was an important factor in generating dinosaur community structure and diversity.

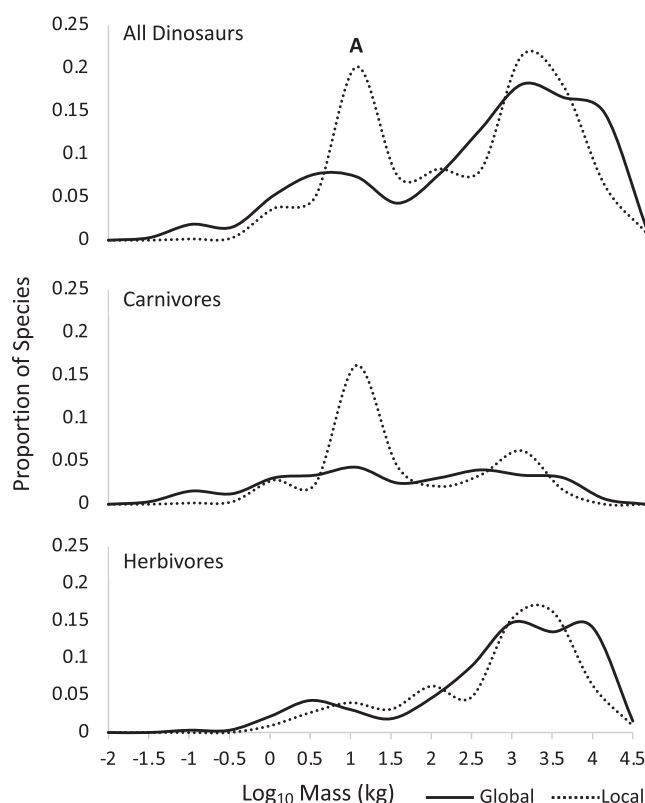
Dinosaurs were the dominant terrestrial vertebrates for >150 million years, yet their species diversity, particularly at sizes <60 kg, remained well below that of other fossil groups (1). Moreover, their overall body size distribution differed from other vertebrates. Because small-bodied vertebrates can finely partition resources and have high turnover between environments (2, 3), they typically have the highest diversity across regions. Yet curiously, large-bodied dinosaurs were the most diverse. This was particularly true for herbivorous sauropods and ornithischians, whereas the predominantly carnivorous theropods exhibited a more uniform range of sizes globally (4). Although the preponderance of large-bodied forms may be partially due to taphonomy (5), some 90% of dinosaur species <60 kg would have to be missing from the fossil record for the body mass distribution of dinosaurs to resemble that of extinct mammals, which display a pattern less skewed by size (4). Rather, dinosaurs' global body mass distribution patterns may have been linked to their physiology; as oviparous organisms, the largest dinosaurs grew from disproportionately small infants (6). Many dinosaurs exhibited marked morphological differences between juveniles and adults (7, 8), resulting in the utilization of different resources through growth and development (9–12), a relatively rare terrestrial life history strategy observed mostly in large egg-laying reptiles (13). Moreover, rapid growth combined with low adult survivorship (14–16) resulted in large populations of juvenile dinosaurs (17) that may have competed with dinosaurs that were small and medium-sized as adults.

Here, we tested whether low dinosaur species diversity and their unusual body size distribution was, at least partially, due to the large disparity between neonate and adult body size, with juveniles of larger-bodied species filling ecological niches that might have otherwise been available to other taxa. This concept of “ontogenetic niche shift” (ONS) in dinosaurs is widely assumed based on modern correlates (10, 13, 14, 18, 19). For example, based on modeling of hypothetical dinosaur communities, Codron *et al.* (9, 11) predicted that ONS led to reduced diversity of dinosaurs

weighing between 1 and 1000 kg. Despite these predictions, little work has empirically explored juveniles' influence on community structure and overall dinosaur diversity (11, 19). Thus, we examined small-scale body size patterns for evidence of competitive interactions using fossil evidence from dozens of communities representing a wide variety of environments spanning most of dinosaur evolution and evaluated the potential effects of spatial scale and trophic affiliation using well-constrained groups of biologically interacting species.

Our analyses are based on 43 dinosaur communities constructed from data extracted from the Paleobiology Database (20, 21) (table S1). From this baseline, each species' occurrence and taxonomic validity were checked individually against the literature, with taxa deemed synonymous by most experts removed and new taxa absent from the Paleobiology Database added. Masses were derived using averages from the primary literature (table S1). Wherever possible, formations were limited to smaller subsets of cooccurring species. Our dataset represents seven continents spanning 136 million years and includes >550 species. We predicted that dinosaur communities with strong local drivers would diverge from the global distribution (2, 22, 23). Because ecological interactions such as competition might not have influenced carnivorous and herbivorous dinosaurs equally (24), the shape of each carnivore and herbivore dinosaur guild within each

Fig. 1. Community divergence from global distributions. Distributions comparing 1303 global taxa with local community taxa (median). Overall, global taxa are more left skewed and communities are more bimodal. “A” indicates the largest deviation from the global distribution; the same deviation is clearly shown in the carnivore distribution.



¹Department of Biology, University of New Mexico, Albuquerque, NM 87131, USA. ²School of Biological Sciences, University of Nebraska, Lincoln, NE 68588, USA.
 *Corresponding author. Email: maguire@unm.edu

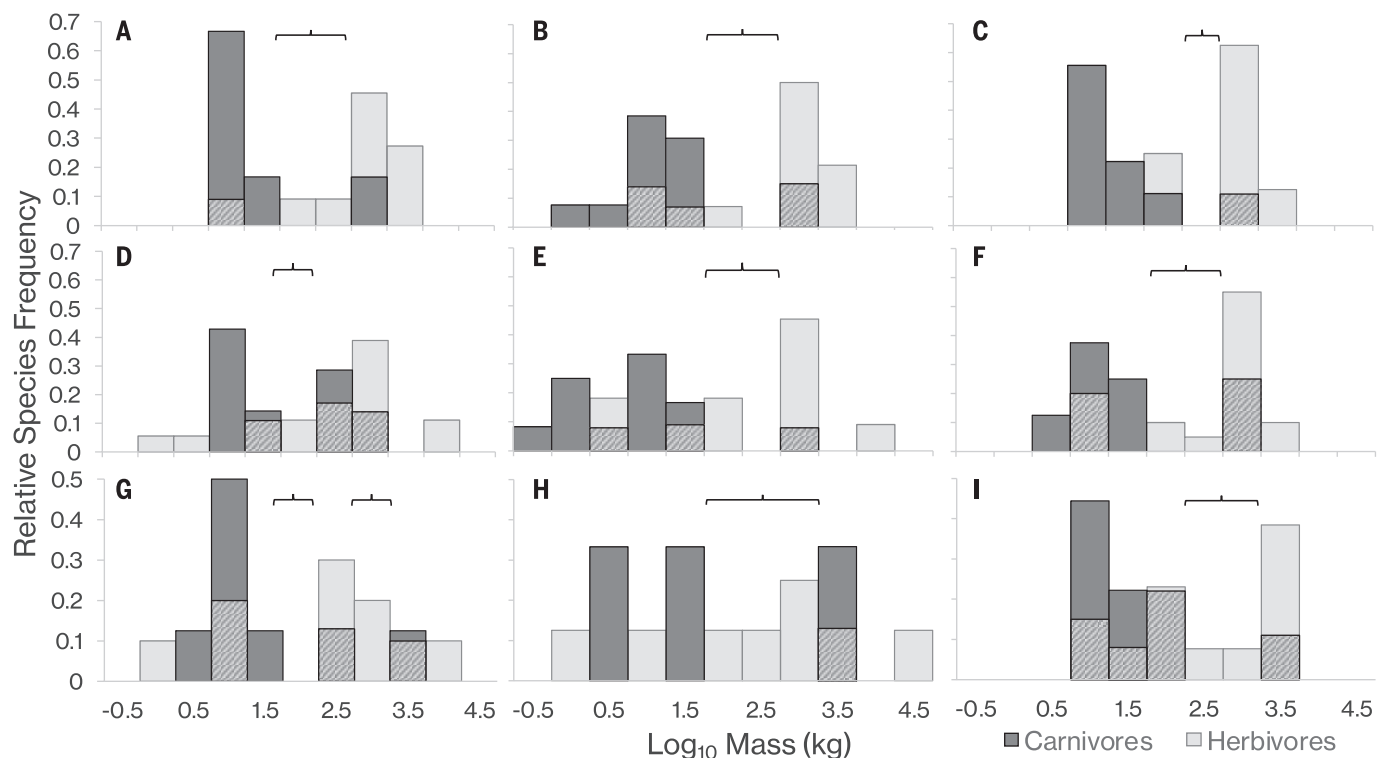


Fig. 2. Community mass-species distributions of nine formations. The formations shown are as follows: (A) Judith River, (B) Dinosaur Park, (C) Two Medicine, (D) Bayan Shireh, (E) Barun Goyot, (F) Horseshoe Canyon, (G) Cedar Mountain, (H) Cloverly, (I) Hell Creek. Brackets illustrate the gaps in carnivore distributions.

community was compared against the global distribution (4).

We found that the overall body size distributions within communities were consistently bimodal regardless of continent, taxa, and time, resulting in less-extreme skew toward large size than evidenced in the global distribution (global skew = -0.577 , community average skew = -0.365 ; table S2). The disparity between the local and global distributions was driven primarily by small (10 to 100 kg) carnivorous dinosaurs (table S4 and Fig. 1); when examined separately, local herbivore body mass distributions closely reflect their global distribution, suggesting that ecological interactions have little effect on their distribution [$P < 0.05$ in 40% of communities, Kolmogorov–Smirnov (K-S) test; table S3].

By contrast, most carnivorous guilds within communities differed from the global carnivore pattern ($P < 0.05$ for 64% of communities, K-S test; table S4), as predicted for strong local interactions. Pairwise comparisons between carnivore guild distributions were nonsignificant in 92% of tests ($\alpha = 0.05$, two-tailed t test with Bonferroni correction for multiple comparisons: $\alpha = 0.000058$ nonsignificant in 99.7%, table S7) despite differing variances, means, and sample sizes, suggesting similar underlying drivers across communities. The only exceptions are formations lacking megatheropods

(carnivores >1000 kg) (e.g., Tremp and Bissekty), those dominated by very small taxa (e.g., Yixian), or those containing multiple sauropods (e.g., Morrison and Lameta), where the availability of multiple enormous prey species may have reduced interspecific competition and allowed the coexistence of an unusually diverse assortment of carnivores.

Community distributions exhibited a persistent lack of carnivorous dinosaurs weighing between 100 and 1000 kg (Fig. 2). The least likely body size of carnivorous taxa was consistently in the 100- to 300-kg range (fig. S1). For perspective, if the modern mammal carnivore assemblage of Kruger National Park were similarly structured, there would be no carnivores between the size of an African lion (190 kg) and a bat-eared fox (4 kg) (Fig. 3). The carnivore “gap” was above the expected limit of taphonomic size bias against small dinosaurs (5), and the drivers of such bias were unlikely to have selectively affected carnivores but not herbivores, suggesting that the gap represents a true biological signal. Moreover, it is unlikely that other clades such as mammals or crocodylomorphs occupied this body size niche because no known Mesozoic mammals exceeded 15 kg (22), and crocodylomorphs were predominantly semiaquatic after the Triassic (25). Furthermore, the width of the carnivore body size gap is correlated with the size of the

largest carnivore (Kendall rank $\tau = 0.437$, $P = 0.000652$). The presence of megatheropods in the community decreased the likelihood of cooccurring species between 100 and 1000 kg even further (table S5). Formations without megatheropods, such as Yixian Lujiantun, did not exhibit body size discontinuities in their carnivorous dinosaur assemblages.

Although the overall distribution of carnivore body size was consistent, the gap itself was dynamic. From the Jurassic to the Cretaceous, the size gap in carnivore species shifted toward larger sizes, mirroring the evolutionary increase in overall dinosaur size (26), and widened from an average of 436 kg to >2060 kg. We suspect that the shift and expansion of the body size gap was caused by a number of changes from the Jurassic to the Cretaceous resulting in increased competition, including (i) decrease by half of average prey body mass, limiting the potential for size partitioning (26); (ii) the diversification of small, potentially endothermic carnivorous dinosaurs (27); and (iii) heightened ONS in Cretaceous megatheropods.

A smaller size gap was found in Jurassic communities, which were characterized by multiple large allosauroids and medium-sized ceratosaurs. Allosauroides was a morphologically diverse clade (28), which likely facilitated the cooccurrence of multiple carnivores within

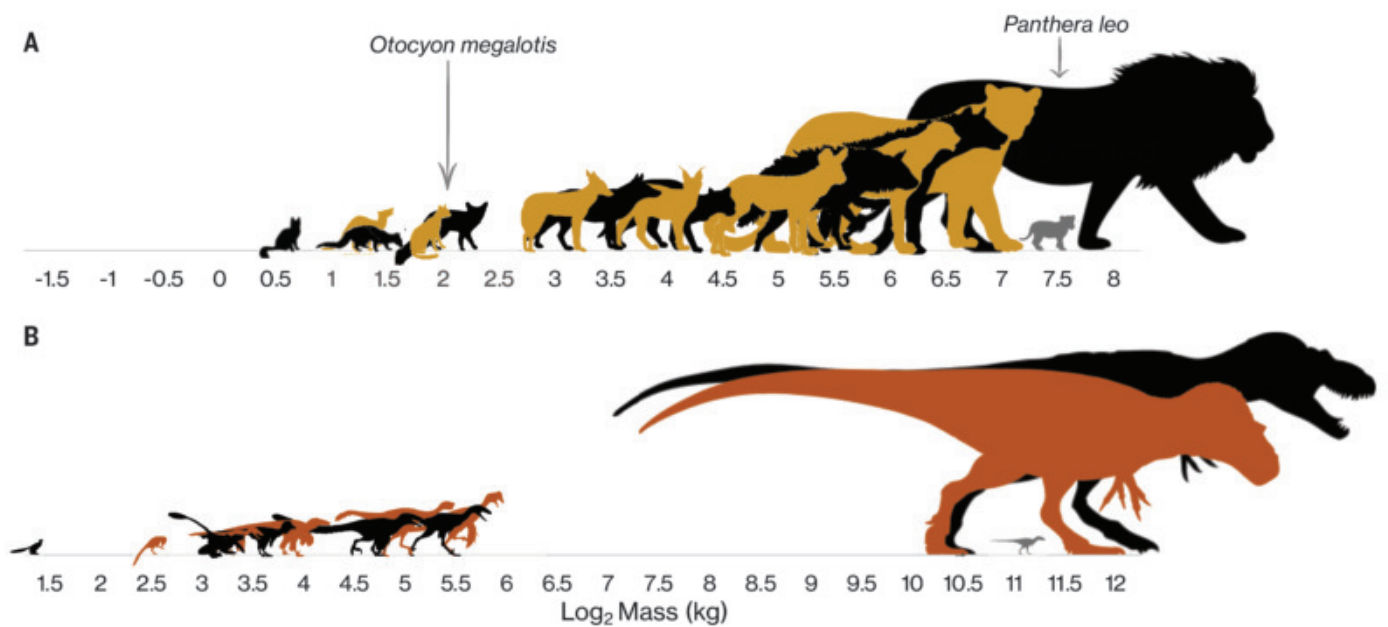


Fig. 3. The dinosaur gap versus modern carnivorous mammals. (A) Carnivorous mammals of Kruger National Park organized to scale by mass. (B) Carnivorous dinosaurs of Dinosaur Park Formation if the largest carnivore were scaled equally to the largest mammalian carnivore in Kruger. Infants (gray) of the largest species shown below adult to show relative growth requirement.

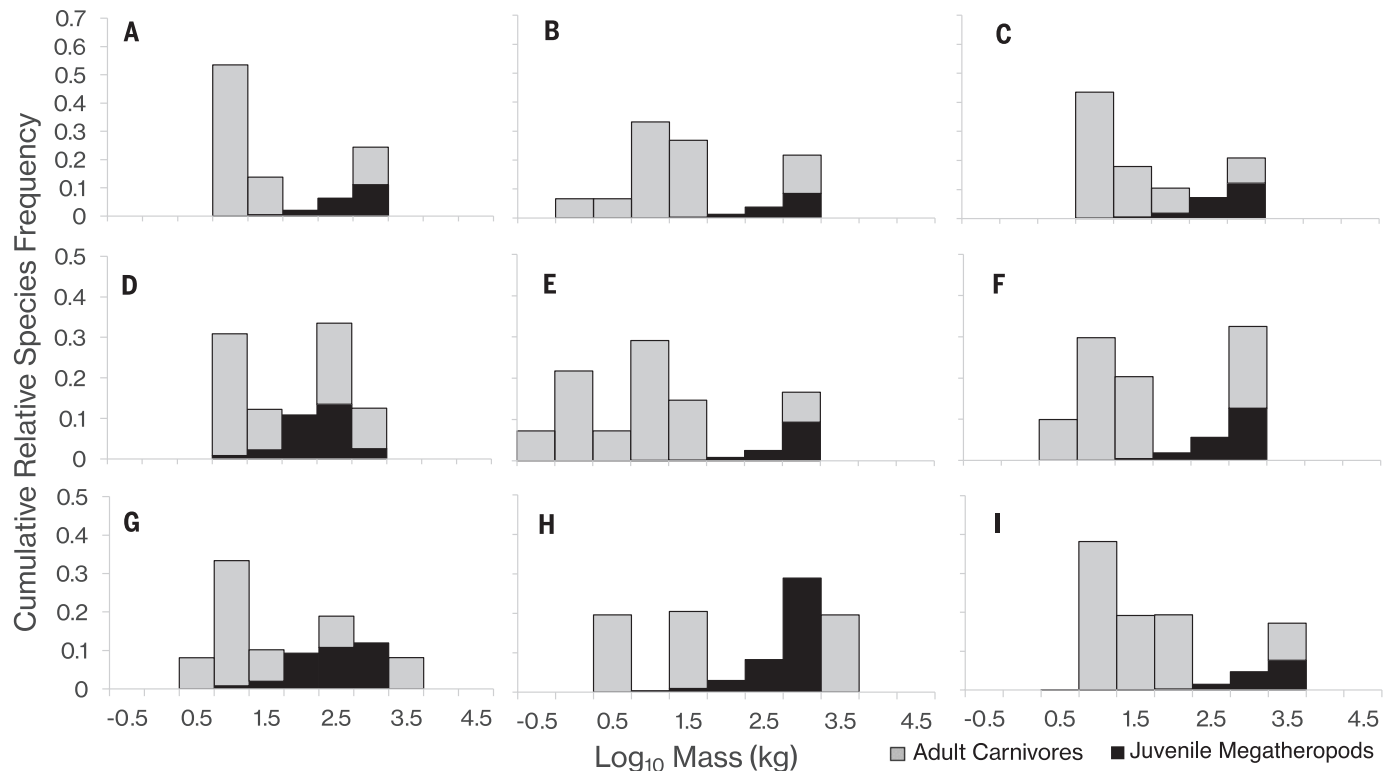


Fig. 4. Community mass-species distributions with juvenile megatheropods as morphospecies stacked with adult conspecifics. The formations shown are as follows: (A) Judith River, (B) Dinosaur Park, (C) Two Medicine, (D) Bayan Shireh, (E) Barun Goyot, (F) Horseshoe Canyon, (G) Cedar Mountain, (H) Cloverly, (I) Hell Creek. The influence of juveniles was highest within the carnivore gap and was proportional to at least 60% of adults in all measured communities. Megatheropods <3000 kg exerted the most influence, matching or outweighing their adult conspecifics in more than half of the measured formations.

communities. Juvenile allosaurs were more similar to adults than Cretaceous megatheropods (29), resulting in fewer feeding niche shifts through ontogeny. Predation on sauropods (30) may have reduced allosaurs' competition with ceratosaurs, which have been associated with piscivory or omnivory, respectively (31). This relatively high morphological differentiation and associated dietary niche partitioning combined with limited ONS in megatheropods may have allowed for the coexistence of large- and medium-sized Jurassic carnivores.

The end of the Jurassic saw a drastic reduction in the diversity of both sauropods and stegosaurs and may have led to the disappearance of many allosauroid taxa (32). Replacing the diverse megatheropod guilds of the Jurassic were Cretaceous communities dominated by a single clade: tyrannosaurs in the north and abelisaurs in the south. Both tyrannosaurs and abelisaurs have been associated with extensive morphological changes through ontogeny (7, 33). Concurrent diversification of dromaeosaurs added competitive pressure on the truncated prey base (34). The ornithischian prey that replaced sauropods likely traveled in multigenerational herds (35), limiting the possibility of predation of isolated juveniles. We suggest that competition for a limited prey source by both large and small carnivores, and the broadening of megatheropod niches, resulted in a widening of the carnivore gap.

For juvenile megatheropods to exclude smaller species from the community, they must represent a non-negligible proportion (>50%) of the biomass. Moreover, juvenile peak biomass must fall predominantly within the carnivore gap. To evaluate the effect of juveniles [<16 years of age (12, 33)] on community composition, we calculated the proportion of juvenile biomass using published growth rates derived from lines of arrested growth and survivorship curves based on relative age abundance from mass-death assemblages recorded in the fossil record (17, 36–38).

We calculated biomass through ontogeny for 1000 individual cohorts of six tyrannosaurs and four allosaurs by multiplying the mass (M_a) and survivorship (S_a) at age in years (a) such that the proportion of any species' biomass represented by juveniles (BM_J) is as follows:

$$BM_J = \sum \left(\frac{M_1 * S_1}{\sum (M_1 * S_1, M_2 * S_2 \dots M_{max} * S_{max})} \right),$$

$$\left(\frac{M_2 * S_2}{\sum (M_1 * S_1 \dots M_{max} * S_{max})} \right) \dots$$

$$\left(\frac{M_{16} * S_{16}}{\sum (M_1 * S_1 \dots M_{max} * S_{max})} \right) \quad (1)$$

We then related BM_J to the proportion of mass contained in adults, set to 1, so that relative

juvenile species proportion (RSP_J) is equal to the following:

$$RSP_J = BM_J * \left[\frac{1}{1 - BM_J} \right] \quad (2)$$

For example, if juveniles represented 60% of the biomass of *Tyrannosaurus rex*, then the juvenile “morphospecies” would be equivalent to 1.5× the taxonomic species. Tyrannosaurs and other megatheropods did not live long past somatic maturity (16), and their juvenile growth rate approached that of mammals and birds (12). This supports our finding that megatheropod biomass peaked at sexual maturity (16 to 19 years of age) and followed a log-normal distribution (fig. S2). For all 10 species examined, juvenile biomass was proportional to least 60% of adult conspecifics (table S6) and exceeded adult biomass in five tyrannosaur species. Substantial proportions of juvenile biomass, including peak biomass, fell within the range of the size gap in all communities (Fig. 4). Thus, juvenile megatheropods represented taxonomically identical but ecologically disparate morphospecies within their communities, with the greatest potential influence in the mass range of 300 to 1000 kg. Our results support the hypothesis that juvenile megatheropods effectively filled the niche of medium-sized carnivores, or mesocarnivores and therefore likely limited diversification of theropods with adult body sizes that fell within this range.

That large carnivorous dinosaurs may have filled multiple niches through ontogeny is not a new assertion (7, 9, 11, 12, 32), yet despite their morphological disparity, adults and juveniles continue to be grouped together in diversity indices, which is accurate taxonomically but not ecologically. Our analysis demonstrates the influence that juvenile megatheropods would have had as morphospecies on their community. We found a gap in the community body size distribution of carnivorous dinosaurs regardless of continent, biome, formation size, or species examined. Our analysis demonstrates that this gap was likely filled by juvenile megatheropods and suggests that low taxonomic diversity in carnivorous dinosaurs was not caused solely by taphonomy or collection bias but rather by competition for resources within and among body size niches filled by juveniles. Dinosaurs existed in a specialized terrestrial community structure, largely organized as a result of their extreme size, ovipary, and resulting ontogenetic niche shift. The “grow fast, die young” approach of megatheropods resulted in a predominance of juveniles in communities, filling the morphological and functional role of mesocarnivores, which as a result are absent from the fossil record as

individual species, artificially deflating diversity indices of dinosaurs as a whole.

REFERENCES AND NOTES

1. S. C. Wang, P. Dodson, *Proc. Natl. Acad. Sci. U.S.A.* **103**, 13601–13605 (2006).
2. J. H. Brown, P. F. Nicoletto, *Am. Nat.* **138**, 1478–1512 (1991).
3. D. A. Kelt et al., *Ecology* **77**, 746–761 (1996).
4. E. J. O'Gorman, D. W. E. Hone, *PLOS ONE* **7**, e51925 (2012).
5. C. M. Brown, D. C. Evans, N. E. Campione, L. J. O'Brien, D. A. Eberth, *Palaeogeogr. Palaeoclimatol. Palaeoecol.* **372**, 108–122 (2013).
6. R. S. Seymour, *Paleobiology* **5**, 1–11 (1979).
7. N. O. Ratsimbaholison, R. N. Felice, P. M. O'Connor, *Acta Palaeontol. Pol.* (2016).
8. T. D. Carr, *J. Vertebr. Paleontol.* **19**, 497–520 (1999).
9. D. Codron, C. Carbone, D. W. H. Müller, M. Clauss, *Biol. Lett.* **8**, 620–623 (2012).
10. E. E. Werner, J. F. Gilliam, *Annu. Rev. Ecol. Syst.* **15**, 393–425 (1984).
11. D. Codron, C. Carbone, M. Clauss, *PLOS ONE* **8**, e77110 (2013).
12. H. N. Woodward et al., *Sci. Adv.* **6**, eaax6250 (2020).
13. D. Purwandana et al., *Naturwissenschaften* **103**, 27 (2016).
14. G. M. Erickson, C. C. Rogers, S. A. Yerby, *Nature* **412**, 429–433 (2001).
15. J. R. Horner, A. De Ricqlès, K. Padian, *J. Vertebr. Paleontol.* **20**, 115–129 (2000).
16. G. M. Erickson, P. J. Currie, B. D. Inouye, A. A. Winn, *Science* **313**, 213–217 (2006).
17. G. M. Erickson, P. J. Currie, B. D. Inouye, A. A. Winn, *Can. J. Earth Sci.* **47**, 1269–1275 (2010).
18. P. Gignac, H. O'Brien, *Integr. Comp. Biol.* **56**, 449–458 (2016).
19. D. J. Varricchio, *Hist. Biol.* **23**, 91–107 (2011).
20. The Paleobiology Database (2020); <https://paleobiodb.org/>.
21. Materials and methods are available as supplementary materials.
22. F. A. Smith et al., *Science* **330**, 1216–1219 (2010).
23. J. B. Foster, *Nature* **202**, 234–235 (1964).
24. D. Codron, J. Codron, M. Sponheimer, M. Clauss, *Front. Ecol. Evol.* **4**, (2016).
25. S. L. Brusatte, M. J. Benton, M. Ruta, G. T. Lloyd, *Science* **321**, 1485–1488 (2008).
26. R. B. J. Benson, G. Hunt, M. T. Carrano, N. Campione, *Paleontology* **61**, 13–48 (2017).
27. R. B. J. Benson et al., *PLOS Biol.* **12**, e1001853 (2014).
28. K. T. Bates, R. B. J. Benson, P. L. Falkingham, *Paleobiology* **38**, 486–507 (2016).
29. C. Foth, B. P. Hedrick, M. D. Ezcurra, *PeerJ* **4**, e1589 (2016).
30. E. J. Rayfield et al., *Nature* **409**, 1033–1037 (2001).
31. R. Delcourt, *Sci. Rep.* **8**, 9730 (2018).
32. J. O. Farlow, T. R. Holtz Jr., *Paleontol. Soc. Pap.* **8**, 251–266 (2002).
33. T. D. Carr, *PeerJ* **8**, e9192 (2020).
34. A. R. Fiorillo, R. A. Gangloff, *J. Vertebr. Paleontol.* **20**, 675–682 (2001).
35. M. J. Ryan, P. J. Currie, J. D. Gardner, M. K. Vickaryous, J. M. Lavigne, *GSA* **15**, 123–133 (2000).
36. S. Wang et al., *Curr. Biol.* **27**, 144–148 (2017).
37. G. M. Erickson et al., *Nature* **430**, 772–775 (2004).
38. P. J. Bybee, A. H. Lee, E. T. Lamm, *J. Morphol.* **267**, 347–359 (2006).

ACKNOWLEDGMENTS

We thank A. Kooser and S. Schappert for their feedback on this manuscript and invaluable advice on figures. **Funding:** None. **Author contributions:** K.S., S.K.L., and F.A.S. conceived and designed the experiments and wrote the manuscript. K.S. performed the experiments, analyzed the data, and contributed reagents, materials, and analysis tools. **Competing interests:** The authors declare no competing interests. **Data and materials availability:** All data are available in the main text or supplementary materials

SUPPLEMENTARY MATERIALS

science.sciencemag.org/content/371/6532/941/suppl/DC1
Materials and Methods
Figs. S1 and S2
Tables S1 to S7
References (39–378)
MDAR Reproducibility Checklist

20 July 2020; accepted 21 January 2021
10.1126/science.abd9220

NUCLEAR ASTROPHYSICS

 ^{129}I and ^{247}Cm in meteorites constrain the last astrophysical source of solar r-process elementsBenoit Côté^{1,2,3,*}, Marius Eichler⁴, Andrés Yagüe López¹, Nicole Vassh⁵, Matthew R. Mumpower^{6,7}, Blanka Világos^{1,2}, Benjámín Soós^{1,2}, Almudena Arcones^{4,8}, Trevor M. Sprouse^{5,6}, Rebecca Surman⁵, Marco Pignatari^{9,1}, Mária K. Pető¹, Benjamin Wehmeyer^{1,10}, Thomas Rauscher^{10,11}, Maria Lugaro^{1,2,12}

The composition of the early Solar System can be inferred from meteorites. Many elements heavier than iron were formed by the rapid neutron capture process (r-process), but the astrophysical sources where this occurred remain poorly understood. We demonstrate that the near-identical half-lives (≈ 15.6 million years) of the radioactive r-process nuclei iodine-129 and curium-247 preserve their ratio, irrespective of the time between production and incorporation into the Solar System. We constrain the last r-process source by comparing the measured meteoritic ratio $^{129}\text{I}/^{247}\text{Cm} = 438 \pm 184$ with nucleosynthesis calculations based on neutron star merger and magneto-rotational supernova simulations. Moderately neutron-rich conditions, often found in merger disk ejecta simulations, are most consistent with the meteoritic value. Uncertain nuclear physics data limit our confidence in this conclusion.

The rapid neutron capture process (r-process) is the source of half of the naturally occurring elements heavier than iron (*I*), including iodine, europium, gold, platinum, and the actinides. However, the astrophysical sites where r-process elements were synthesized and the physical conditions at these sites are not well constrained.

The gravitational wave event GW170817 (2), the identification of its electromagnetic counterpart, and the inference of lanthanide elements in the ejecta (3) have shown that neutron star mergers can synthesize at least some r-process elements. GW170817 provided only limited information on the nucleosynthesis process, as only one specific element (strontium) has been identified in its spectrum (4). More detailed isotopic information for r-process nucleosynthesis is recorded in the composition of the Solar System. Analysis of primitive meteorites has produced abundance determinations for all stable isotopes (5), whereas abundances derived from stellar spectra typically provide elemental abundances only.

The Solar System's stable isotopes include contributions from multiple nucleosynthetic events (supernovae, compact binary mergers, etc.) that occurred at any time between the birth of the Milky Way and the formation of the Sun. This evolution is difficult to model but can be simplified by considering radioactive isotopes with half-lives of several million years (Myr). Analysis of meteorites has shown that such isotopes were present at the formation time of the first solids [the

calcium-aluminum-rich inclusions (CAIs)] in the early Solar System (6). Because those radioactive isotopes have all decayed over the lifetime of the Solar System, their initial abundances are inferred from excesses of the daughter isotopes they decay into. Radioactive isotopes reflect a smaller number of nucleosynthesis events than stable isotopes, specifically the events that occurred shortly before the formation of the Sun. We consider the early Solar System abundances of two radioactive isotopes with half-lives of 15.7 and 15.6 Myr, respectively: ^{129}I and the heavier actinide isotope, ^{247}Cm . We adopt abundances of these isotopes (Table 1) from previously published analyses of meteorites (7–9), where they are reported as ratios with reference isotopes $^{129}\text{I}/^{127}\text{I}$ and $^{247}\text{Cm}/^{235}\text{U}$.

The process of comparing these isotopic ratios directly with predictions from simulations and determining the nucleosynthetic

sources that enrich interstellar gas with heavy elements is highly uncertain. The abundance ratio $^{129}\text{I}/^{127}\text{I}$ has a stable isotope in the denominator, the abundance of which depends on the complete galactic enrichment history before the formation of the Solar System. This ratio is therefore affected by uncertainties in the star formation history, the amount of interstellar gas in the Milky Way, and the amount of ^{127}I removed from the interstellar gas by galactic outflows (10). The $^{247}\text{Cm}/^{235}\text{U}$ ratio is less affected by those uncertainties because ^{235}U has a half-life of 704 Myr, which is short relative to the ~ 8 to 9 billion years of galactic enrichment before the formation of the Sun. The $^{247}\text{Cm}/^{235}\text{U}$ ratio is still affected by the uncertain time interval between the synthesis of these elements and their incorporation into the early Solar System. This delay is ~ 100 to 200 Myr for r-process isotopes (11), during which ^{247}Cm and ^{235}U decay exponentially. Because their half-lives differ by a factor of 50, the $^{247}\text{Cm}/^{235}\text{U}$ abundance ratio diverges from its original value before being locked into the Solar System.

Enrichment of the interstellar gas from which the Solar System formed was not continuous but stochastic (12). It is therefore unknown how many enrichment events are recorded in the isotopic ratios derived from meteorites. Because the radioactive abundances from each event decayed for an unknown amount of time, the relative contributions are even more uncertain.

Using the $^{129}\text{I}/^{247}\text{Cm}$ abundance ratio bypasses those uncertainties because of the combination of two properties. First, ^{129}I and ^{247}Cm have the same half-life, within uncertainties, so their ratio is not strongly affected by decay over time. Second, both isotopes are short-lived compared with the average time elapsed between r-process events, so their ratio probably reflects only one event (supplementary

Table 1. Early Solar System isotopic ratios involving radioactive nuclei produced by the r-process. Column 5 provides the early Solar System ratio of each isotope listed in column 1 relative to that in column 3, with the half-lives of these isotopes (28–30) given in columns 2 and 4, respectively. All uncertainties are 2σ (11).

Short-lived radionuclide	Half-life (Myr)	Reference isotope	Half-life (Myr)	Early Solar System ratio	References
^{129}I	15.7 ± 0.8	^{127}I	Stable	$(1.28 \pm 0.03) \times 10^{-4}$	(7)
^{247}Cm	15.6 ± 1.0	^{235}U	704 ± 2	$(5.6 \pm 0.3) \times 10^{-5}$	(8, 9)
^{129}I	15.7 ± 0.8	^{247}Cm	15.6 ± 1.0	438 ± 184	See text

¹Research Centre for Astronomy and Earth Sciences, Eötvös Loránd Research Network, Konkoly Observatory, 1121 Budapest, Hungary. ²Institute of Physics, Eötvös Loránd University, 1117 Budapest, Hungary. ³National Superconducting Cyclotron Laboratory, Michigan State University, East Lansing, MI 48824, USA. ⁴Institut für Kernphysik, Technische Universität Darmstadt, 64289 Darmstadt, Germany. ⁵Department of Physics, University of Notre Dame, Notre Dame, IN 46556, USA. ⁶Theoretical Division, Los Alamos National Laboratory, Los Alamos, NM 87545, USA. ⁷Center for Theoretical Astrophysics, Los Alamos National Laboratory, Los Alamos, NM 87545, USA. ⁸GSI Helmholtzzentrum für Schwerionenforschung GmbH, 64291 Darmstadt, Germany. ⁹E.A. Milne Centre for Astrophysics, University of Hull, Hull HU6 7RX, UK. ¹⁰Centre for Astrophysics Research, University of Hertfordshire, Hatfield AL10 9AB, UK. ¹¹Department of Physics, University of Basel, 4056 Basel, Switzerland. ¹²Monash Centre for Astrophysics, School of Physics and Astronomy, Monash University, Clayton, VIC 3800, Australia.

*Corresponding author. Email: benoit.cote@csfk.org

text). Figure 1 shows a simulation of how these isotope ratios vary over time. $^{129}\text{I}/^{247}\text{Cm}$ always stays close to its production ratio, whereas $^{129}\text{I}/^{127}\text{I}$ and $^{247}\text{Cm}/^{235}\text{U}$ vary by orders of magnitude. Different astrophysical sources could have synthesized a range of $^{129}\text{I}/^{247}\text{Cm}$ abundance ratios throughout the history of the Galaxy, but only one event is likely recorded in meteorites for these isotopes. We determine the $^{129}\text{I}/^{247}\text{Cm}$ ratio in the early Solar System (Table 1) using the reported $^{129}\text{I}/^{127}\text{I}$ and $^{247}\text{Cm}/^{235}\text{U}$ ratios together with the $^{127}\text{I}/^{235}\text{U}$ ratio of 189 (5). We find $^{129}\text{I}/^{247}\text{Cm} = 438 \pm 184$, and we interpret this value as reflecting the nucleosynthesis of the last r-process event that polluted the presolar nebula.

This value relies on our adoption of solar abundances commonly used in astronomy (5). However, alternative measurements have reported an iodine abundance that is an order of magnitude lower (13), which would affect our conclusions. Adopting the lower value would make iodine less abundant than neighboring isotopes. Our nucleosynthesis calculations (see below) do not predict this feature because they generally show smoother abundance trends between neighboring species, which is more consistent with the higher abundance measurement (5). The meteoritic measurements (13) could be affected by heterogeneities on scales larger than the samples that were analyzed (the nugget effect) and by possible losses of noble gases produced from halogens such as iodine through the irradiation technique adopted for the measurements (supplementary text). We therefore prefer to adopt the higher value of the iodine abundance (5) (supplementary text).

We performed theoretical nucleosynthesis calculations to determine the $^{129}\text{I}/^{247}\text{Cm}$ abundance ratios that would be produced in the physical conditions that occur in previous hydrodynamic simulations of potential r-process sites: neutron star–neutron star (NS–NS) mergers, neutron star–black hole (NS–BH) mergers, and core-collapse supernovae (SNe) driven by strong magnetic fields and fast rotation [magneto-rotational supernovae (MR SNe)] (14). In NS–NS and NS–BH mergers, matter is ejected in two ways: (i) dynamical ejecta (15, 16) that are driven by tidal forces and shocks that occur promptly during the merger and (ii) disk ejecta (17) that are driven by heating that unbinds matter from the disk that forms around the compact central remnant left after the merger, which is either a neutron star or a black hole. Table S1 lists details of the seven simulations we considered. Because r-process nucleosynthesis predictions are affected by large uncertainties from nuclear physics (18–20), we repeated our calculations with three different sets of nuclear reaction rates and three different models for the distribution of fission fragments (11). This gen-

erated nine nucleosynthetic model predictions that were applied to each of the seven hydrodynamic simulations, for a total of 63 calculations shown in Fig. 2.

In Fig. 2, we compare our predicted $^{129}\text{I}/^{247}\text{Cm}$ ratios using different nuclear physics

input with the meteoritic ratio. The uncertainties on the meteoritic ratio include both the uncertainty in the derivation of the early Solar System ratio (Table 1) and the uncertainty in the half-lives of ^{129}I and ^{247}Cm . We include the latter to account for the slight

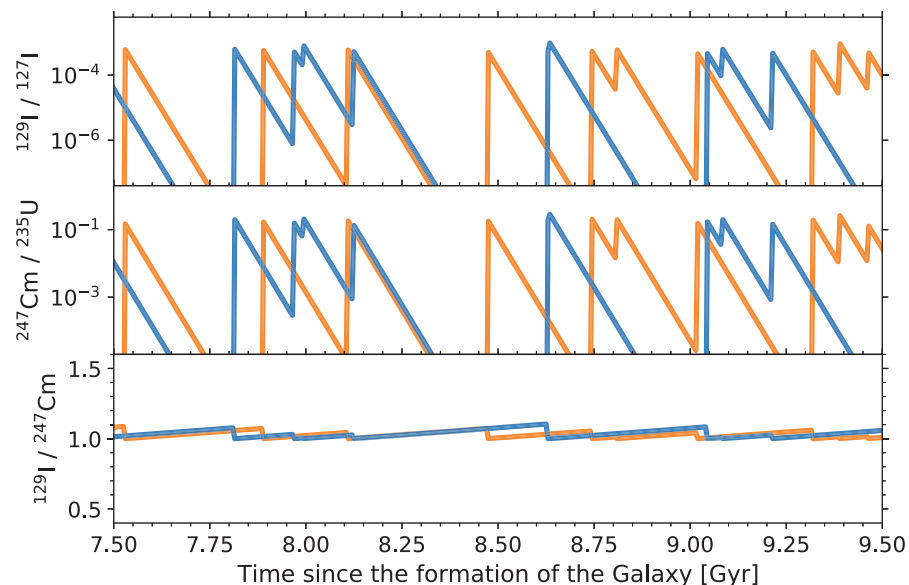


Fig. 1. Simulated evolution of the abundance ratios $^{129}\text{I}/^{127}\text{I}$, $^{247}\text{Cm}/^{235}\text{U}$, and $^{129}\text{I}/^{247}\text{Cm}$ in a parcel of Milky Way interstellar gas. The time window shown encompasses the time when the Sun formed. Each peak is produced by an additional r-process event. The blue and orange lines show two arbitrary Monte Carlo realizations for the temporal distribution of those events (27). Each event is assumed to eject the same mass of ^{129}I , ^{127}I , ^{247}Cm , and ^{235}U , such that the production ratio is equal to 1 for all three isotopic ratios. Gyr, billion years.

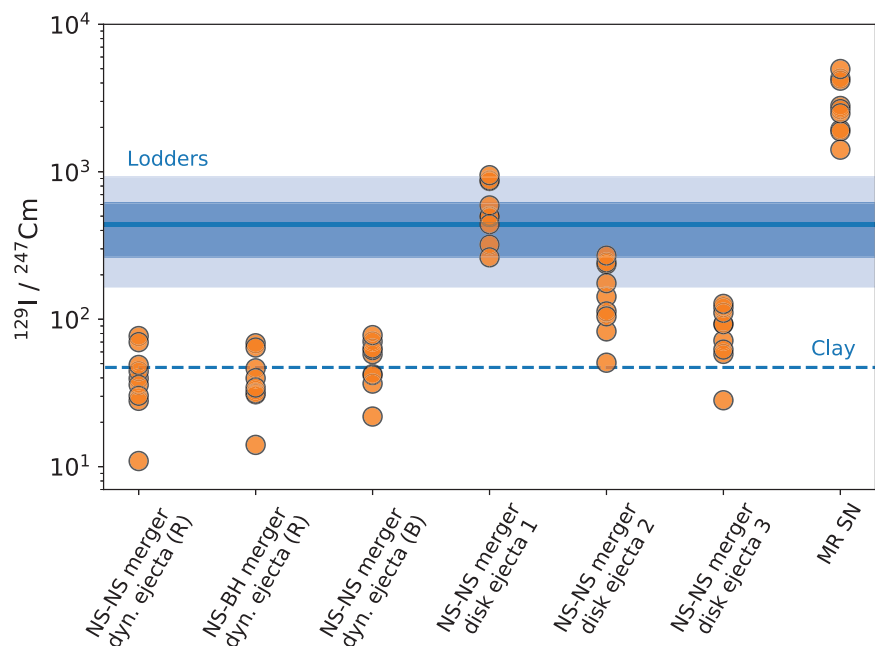


Fig. 2. $^{129}\text{I}/^{247}\text{Cm}$ abundance ratios predicted by theoretical r-process models. The dots in each model denote the use of different nuclear physics inputs (11). The horizontal blue solid line shows the meteoritic ratio, and the shaded blue bands are its 1σ and 2σ uncertainties (11). The horizontal blue dashed line shows the meteoritic ratio when adopting alternative measurements (13). dyn., dynamical; R, Rosswog; B, Bovard.

ratio variation that could have occurred during the time elapsed between the last r-process event and the condensation of the first solids in the early Solar System (17). Because ^{129}I and ^{247}Cm have substantially different atomic numbers, their relative abundances strongly depend on the physical conditions in which the r-process nucleosynthesis occurs. The predicted ratios shown in Fig. 2 vary by more than two orders of magnitude.

For the magneto-rotational supernova (MR SN) ejecta (14), the abundance ratio is always >1000 because most of the ejecta are not sufficiently neutron rich to produce enough actinides. Although other MR SN simulations may generate different results, models with alternative neutrino transport predict even lower production of actinides (21). MR SNe are expected to have occurred more often in the early Universe, because of higher stellar rotation (22), which makes MR SNe more likely to enrich very old stars than the Solar System. Collapsars are also a possible r-process site; these occur during the late evolution of some MR SNe, when a black hole surrounded by an accretion disk forms. However, their capacity to synthesize actinides (including ^{247}Cm) is debated and ranges from substantial production (23) to no production (24, 25).

For the NS-NS and NS-BH merger simulations, dynamical ejecta are dominated by very neutron-rich conditions—producing more actinides (such as ^{247}Cm) relative to lighter nuclei (^{129}I , in this case)—compared with the other r-process scenarios (see also fig. S1). As a result, the dynamical ejecta $^{129}\text{I}/^{247}\text{Cm}$ ratios are all <100 , which is below the 2σ uncertainty of the meteoritic ratio. Merger simulations predict the presence of very neutron-rich material (15, 16); however, the exact contribution of such conditions to the total ejecta is still unclear. Simulations of dynamical ejecta show a broad range of neutron richness (26).

The three NS-NS merger accretion-disk ejecta simulations give different results (Fig. 2). NS-NS disk 1 is consistent with the meteoritic value, NS-NS disk 2 partly overlaps with the 2σ uncertainty, whereas NS-NS disk 3 is below the 2σ uncertainty and therefore not compatible. Although these disk simulations represent a disk forming around an NS-NS remnant, NS-BH disk models can produce similar abundances (17).

We considered the combination of both dynamical and disk ejecta from a single binary merger (supplementary text). We found that the maximum contribution of dynamical ejecta is $\sim 50\%$ (in mass fraction) to remain within the 2σ uncertainty of the meteoritic ratio. ^{129}I and ^{247}Cm in the early Solar System were likely synthesized by only one r-process event, but if two events contributed, the meteoritic ratio could be matched by a combination of dynamical ejecta with MR SN ejecta (see Fig. 2).

However, such a mixture has an occurrence probability of $<10\%$ (supplementary text).

To test the sensitivity of these results to the input data, we performed 56 additional nucleosynthesis calculations on the dynamical ejecta (15) using a different nucleosynthesis code and a wider variety of input nuclear physics models (17). Most of these models predict $^{129}\text{I}/^{247}\text{Cm}$ ratios <100 (tables S2 and S3), which is consistent with the results presented in Fig. 2. In 4 of the 56 cases, very neutron-rich dynamical ejecta reach the meteoritic ratio. The large range in predictions is due to the nuclear physics uncertainties. Our additional calculations support our conclusion that enrichment of the presolar nebula by very neutron-rich ejecta is often inconsistent with the meteoritic data. This result applies to the last r-process event that polluted the presolar nebula with radioactive isotopes, not to the collective contribution of all previous events that built up the stable r-process solar composition.

We have shown that the $^{129}\text{I}/^{247}\text{Cm}$ abundance ratio can constrain the ejecta composition of the last r-process event that polluted the presolar nebula. This ratio is highly sensitive to the physical conditions in which ^{129}I and ^{247}Cm were synthesized. Our results suggest that moderately neutron-rich conditions are generally most consistent with the meteoritic value. However, such conclusions are limited by solar abundance determinations and current uncertainties in the available hydrodynamical and nucleosynthesis models.

REFERENCES AND NOTES

- C. J. Horowitz et al., *J. Phys. G: Nucl. Part. Phys.* **46**, 083001 (2019).
- LIGO Scientific Collaboration and Virgo Collaboration, *Phys. Rev. Lett.* **119**, 161101 (2017).
- P. S. Cowperthwaite et al., *Astrophys. J.* **848**, L17 (2017).
- D. Watson et al., *Nature* **574**, 497–500 (2019).
- K. Lodders, in *Principles and Perspectives in Cosmochemistry*, A. Goswami, B. Reddy, Eds. (Astrophysics and Space Science Proceedings, Springer, 2010), pp. 379–417.
- M. Lugaro, U. Ott, A. Kereszturi, *Prog. Part. Nucl. Phys.* **102**, 1–47 (2018).
- J. D. Gilmour, O. V. Pravdivtseva, A. Busfield, C. M. Hohenberg, *Meteorit. Planet. Sci.* **41**, 19–31 (2006).
- F. L. H. Tissot, N. Dauphas, L. Grossman, *Sci. Adv.* **2**, e1501400 (2016).
- H. Tang, M.-C. Liu, K. D. McKeegan, F. L. H. Tissot, N. Dauphas, *Geochim. Cosmochim. Acta* **207**, 1–18 (2017).
- B. Côté et al., *Astrophys. J.* **878**, 156 (2019).
- Materials and methods are available as supplementary materials.
- K. Hotokezaka, T. Piran, M. Paul, *Nat. Phys.* **11**, 1042 (2015).
- P. L. Clay et al., *Nature* **551**, 614–618 (2017).
- C. Winteler et al., *Astrophys. J.* **750**, L22 (2012).
- S. Rosswog, T. Piran, E. Nakar, *Mon. Not. R. Astron. Soc.* **430**, 2585–2604 (2013).
- L. Bovard et al., *Phys. Rev. D* **96**, 124005 (2017).
- M.-R. Wu, R. Fernández, G. Martínez-Pinedo, B. D. Metzger, *Mon. Not. R. Astron. Soc.* **463**, 2323–2334 (2016).
- M. Eichler et al., *Astrophys. J.* **808**, 30 (2015).
- M. R. Mumpower, R. Surman, G. C. McLaughlin, A. Aprahamian, *Prog. Part. Nucl. Phys.* **86**, 86–126 (2016).
- N. Vassh et al., *J. Phys. G: Nucl. Part. Phys.* **46**, 065202 (2019).
- P. Mösta et al., *Astrophys. J.* **864**, 171 (2018).
- A. Choplin, N. Tominaga, M. N. Ishigaki, *Astron. Astrophys.* **632**, A62 (2019).

- D. M. Siegel, J. Barnes, B. D. Metzger, *Nature* **569**, 241–244 (2019).
- R. Surman, G. C. McLaughlin, W. R. Hix, *Astrophys. J.* **643**, 1057 (2006).
- J. M. Miller et al., *Phys. Rev. D* **100**, 023008 (2019).
- D. Radice et al., *Astrophys. J.* **869**, 130 (2018).
- B. Côté, A. Yagüe, B. Vilagos, M. Lugaro, *Astrophys. J.* **887**, 213 (2019).
- E. Browne, J. K. Tuli, *Nuclear Data Sheets* **114**, 751–840 (2013).
- J. Timar, Z. Elekes, B. Singh, *Nuclear Data Sheets* **121**, 143–394 (2014).
- C. D. Nesaraja, E. A. McCutchan, *Nuclear Data Sheets* **121**, 695–748 (2014).
- A. Yagüe López, B. Côté, AndresYague/Stochastic_RadioNuclides: Public code for published evolution of radioisotope, version v1.0.1, Zenodo (2020); <http://doi.org/10.5281/zenodo.4321747>.
- M. Eichler, A. Arcones, Detailed abundances based on different nuclear physics for theoretical r-process scenarios [Data set], Zenodo (2021); <http://doi.org/10.5281/zenodo.4446099>.
- A. Yagüe López, bensoos, AndresYague/delta_stat_tau_code: Isolation time figure code, version v1.0.0, Zenodo (2020); <http://doi.org/10.5281/zenodo.4300334>.
- A. Yagüe López, AndresYague/IodineCurium_project_distributions: Public code for published distributions, version v1.0.0, Zenodo (2020); <http://doi.org/10.5281/zenodo.3969829>.
- N. Vassh, M. R. Mumpower, T. M. Sprouse, R. Surman, r-process abundances in neutron-rich merger ejecta given different theoretical nuclear physics inputs [Data set], Zenodo (2021); <http://doi.org/10.5281/zenodo.4456126>.
- A. Yagüe López, AndresYague/IodineCurium_project_oneEvent: Public code for published MC experiment, version v1.0.0+1, Zenodo (2020); <http://doi.org/10.5281/zenodo.3969830>.

ACKNOWLEDGMENTS

We thank K. Lodders, U. Ott, and J. Gilmour for discussions, and we thank the reviewers for improving the content of our manuscript. This work has benefited from discussions at the 2019 Frontiers in Nuclear Astrophysics Conference, supported by the JINA Center for the Evolution of the Elements, and at conferences supported by the ChETEC (Chemical Elements as Tracers of the Evolution of the Cosmos) COST Action (CA16117, European Cooperation in Science and Technology). M.P. acknowledges access to VIPER, the University of Hull High Performance Computing Facility. **Funding:** B.C., A.Y.L., B.W., M.K.P., and M.L. were supported by the ERC Consolidator Grant (Hungary) funding scheme (project RADIOSTAR, G.A. no. 724560). B.C. and M.L. were supported by the Hungarian Academy of Sciences through the Lendület project LP2014-17. B.C., M.R.M., and M.P. acknowledge support from the National Science Foundation (NSF, United States) under grant no. PHY-1430152 (JINA Center for the Evolution of the Elements). M.R.M. was supported by the U.S. Department of Energy through the Los Alamos National Laboratory and by the Laboratory Directed Research and Development program of Los Alamos National Laboratory under project no. 20190021DR. Los Alamos National Laboratory is operated by Triad National Security, LLC, for the National Nuclear Security Administration of the U.S. Department of Energy (contract no. 89233218CNA000001). M.E. and A.A. acknowledge support from the European Research Council through ERC starting grant no. 677912 EUROPIUM and Deutsche Forschungsgemeinschaft through SFB 1245. N.V. and R.S. were supported by the Fission In R-process Elements (FIRE) topical collaboration in nuclear theory, funded by the U.S. Department of Energy. A.A. was supported by the Helmholtz Forschungsakademie Hessen für FAIR. T.M.S. and R.S. were supported by the U.S. Department of Energy SciDAC collaboration TEAMS (DE-SC0018232). T.M.S. was supported by the Los Alamos National Laboratory Center for Space and Earth Science, which is funded by its Laboratory Directed Research and Development program under project no. 20180475DR. M.P. acknowledges support to NuGrid from STFC through the University of Hull's consolidated grant ST/R000840/1. **Author contributions:** B.C. developed the concept, led and coordinated the collaboration, codeveloped the statistical framework that led to Fig. 1, and participated in the writing and revising process. M.E. performed and analyzed the nucleosynthesis calculations shown in Fig. 2 and fig. S2, ran the sampling procedure shown in fig. S1, and participated in the writing and revising process. A.Y.L. performed the calculations shown in table S6, helped develop the concept, codeveloped the statistical framework that led to Fig. 1, and participated in the writing and revising process. N.V. performed and analyzed the nucleosynthesis calculations shown in tables S2 and S3 and participated in the writing and revising process. M.R.M. participated in the revising process and in the development of the PRISM code and the nuclear reaction rates

used in PRISM. B.V. calculated the probability distributions shown in figs. S4 and S5. B.S. ran the calculations shown in fig. S3. A.A., R.S., M.P., and B.W. participated in the revising process. T.M.S. participated in the development of the PRISM code. M.K.P. participated in the interpretation of meteoritic abundances and in the revising process. T.R. participated in the development of the nuclear reaction rates used in WINNET and in the revising process. M.L. calculated the early Solar System $^{129}\text{I}/^{247}\text{Sm}$ ratio shown in Table 1, helped develop the concept, and participated in the writing and revising process. **Competing interests:** We declare no conflicts of interest. **Data and materials availability:** The code used to calculate the isotopic ratios shown in Fig. 1 is available at https://github.com/AndresYague/Stochastic_RadioNuclides (31). The WINNET nucleosynthesis output and sampling code to reproduce Fig. 2 and figs. S1 and S2

are available on Zenodo (32). The code to reproduce fig. S3 is available at https://github.com/AndresYague/delta_stat_tau_code/tree/v1.0.0 (33). The Monte Carlo code used to calculate the distributions shown in figs. S4 and S5 is available at https://github.com/AndresYague/IodineCurium_project_distributions (34). The PRISM nucleosynthesis output necessary to reproduce tables S2 and S3 is available on Zenodo (35); this dataset is released under Los Alamos National Laboratory report no. LA-UR-21-20444. The Monte Carlo code to generate table S6 is available at https://github.com/AndresYague/IodineCurium_project_oneEvent (36). The trajectories of the dynamical ejecta (R) simulations were taken from https://compact-merger.astro.su.se/downloads_fluid_trajectories.html; the dynamical ejecta (B) were taken from (16); disk ejecta 1, 2, and 3 were taken from (17); and the MR SN ejecta were taken from (14). The WINNET code was developed by

C. Winteler, F. Thielemann, O. Korobkin, M. Eichler, D. Martin, J. Bliss, M. Reichert, and A. Arcones; we do not have their permission to distribute it. The PRISM code is security restricted and unavailable for public release; contact M.R.M. for details.

SUPPLEMENTARY MATERIALS

science.sciencemag.org/content/371/6532/945/suppl/DC1
Materials and Methods
Supplementary Text
Figs. S1 to S5
Tables S1 to S6
References (37–104)

7 November 2019; accepted 25 January 2021
10.1126/science.abal111

OPTOELECTRONICS

Massively parallel ultrafast random bit generation with a chip-scale laser

Kyungduk Kim¹, Stefan Bittner^{1,2}, Yongquan Zeng³, Stefano Guazzotti^{4,5}, Ortwin Hess^{4,5}, Qi Jie Wang³, Hui Cao^{1*}

Random numbers are widely used for information security, cryptography, stochastic modeling, and quantum simulations. Key technical challenges for physical random number generation are speed and scalability. We demonstrate a method for ultrafast generation of hundreds of random bit streams in parallel with a single laser diode. Spatiotemporal interference of many lasing modes in a specially designed cavity is introduced as a scheme for greatly accelerated random bit generation. Spontaneous emission, caused by quantum fluctuations, produces stochastic noise that makes the bit streams unpredictable. We achieve a total bit rate of 250 terabits per second with off-line postprocessing, which is more than two orders of magnitude higher than the current postprocessing record. Our approach is robust, compact, and energy-efficient, with potential applications in secure communication and high-performance computation.

The performance and reliability of our digital networked society are based on the ability to generate large quantities of randomness. An ever-increasing demand to improve the security of digital information has shifted the generation of random numbers from sole reliance on pseudo-random algorithms to the use of physical entropy sources. Ultrafast physical random number generators are key devices for achieving ultimate performance and reliability in communication and computation systems (1, 2). Semiconductor lasers that feature chaotic dynamics with tens-of-GHz bandwidth represent one prominent class of high-speed random number generators (3–18). Initially, 1.7 Gb/s random bit generation (RBG) was achieved with combined binary digitization of two in-

dependent chaotic laser diodes (3). Then, from a single chaotic semiconductor laser, a 12.5 Gb/s RBG was demonstrated (4), with a subsequent boost to 300 Gb/s (5). By coupling several lasers to further increase the bandwidth and using postprocessing schemes to extract more bits in analog-to-digital conversion (ADC), the total RBG rate was pushed up to 2 Tb/s (13–15, 18). However, the intrinsic time scales of lasing instabilities impose an ultimate limit on the entropy generation rate. A further increase in the RBG rate requires a different physical process with inherently faster dynamics.

Parallel RBG schemes can greatly enhance the generation rate and the scalability by producing many bit streams simultaneously. In the spatial domain, parallel generation of physical random numbers was realized by sampling two-dimensional laser speckle patterns created by a moving diffuser or a vibrating multimode fiber (19, 20). As a result of inherently long mechanical time scales, the generation rates remain low (Mb/s). Chaotic broad-area semiconductor lasers have been investigated for high-speed parallel RBG (21), but correlations of intensity fluctuations at different spatial locations impede independent parallel bit stream generation. Spectral demul-

tiplexing of amplified spontaneous emission (22, 23) or heterodyning chaotic laser emission (9) are used for parallel RBG with rates up to hundreds of Gb/s per channel. So far, such spectral-domain parallel RBG has been demonstrated with fewer than 10 channels.

We demonstrate a method that enhances the random bit rate in a single channel and also provides hundreds of channels for simultaneous generation of independent bit streams. The spatiotemporal interference of many lasing modes is used to generate picosecond-scale emission intensity fluctuations in space, so as to massively produce ultrafast random bit streams in parallel. This is achieved by tailoring the geometry of a broad-area semiconductor laser to vastly increase the number of transverse lasing modes, thereby suppressing characteristic dynamical instabilities such as filamentation. Specifically, we have designed a chip-scale laser diode to enable a large number of spatial modes lasing simultaneously with incommensurate frequency spacings, so that their interference patterns are complex and aperiodic. Spontaneous emission adds stochastic noise to make the intensity fluctuations unpredictable and nonreproducible.

A conventional broad-area edge-emitting semiconductor laser has a stripe geometry with two flat facets (Fig. 1A). Characteristically, lasing occurs only in the low-order transverse modes. Nonlinear interactions between the light field and the gain material entail irregular pulsation and filamentation (24) (Fig. 1B). The spatiotemporal correlation function of the intensity fluctuations (25, 26) $C(\Delta x, \Delta t)$ reveals nonlocal correlations in space and time (Fig. 1C). On one hand, long-range temporal correlation reflects memory, which degrades the quality of random bits generated at one spatial location. On the other hand, long-range spatial correlation means that the random bit streams generated at different locations are not completely independent, thus impeding parallel RBG (27).

To achieve massively parallel ultrafast RBG, we enhance the number of transverse lasing modes by increasing the cavity width and curving the end facets (Fig. 1D), effectively

¹Department of Applied Physics, Yale University, New Haven, CT 06520, USA. ²Chair in Photonics, LMOPS EA-4423 Laboratory, CentraleSupélec and Université de Lorraine, Metz 57070, France. ³Center for Optoelectronics and Biophotonics, School of Electrical and Electronic Engineering, School of Physical and Mathematical Science, and Photonics Institute, Nanyang Technological University, 639798 Singapore. ⁴Blackett Laboratory, Imperial College London, London SW7 2AZ, UK. ⁵School of Physics and CRANN Institute, Trinity College Dublin, Dublin 2, Ireland.
*Corresponding author. Email: hui.cao@yale.edu

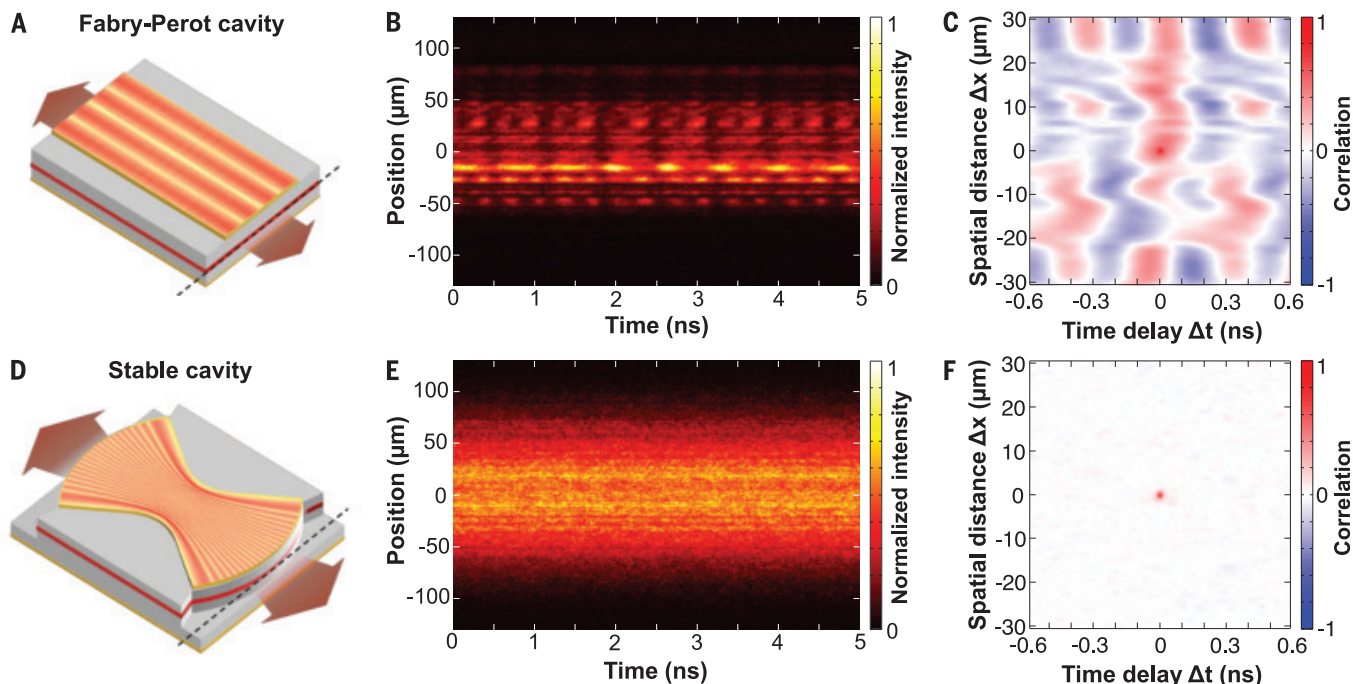


Fig. 1. Reducing spatiotemporal correlations of the lasing emission.

(A) A wide-stripe edge-emitting semiconductor laser with planar facets supports only low-order transverse modes with the typical spatial profile shown (not to scale). (B) Emission intensity $I(x, t)$ at one facet of a 100- μm -wide, 1000- μm -long GaAs quantum-well laser, measured by a streak camera, features filamentation and irregular pulsations. (C) The spatiotemporal correlation function $C(\Delta x, \Delta t)$ of the emission intensity in (B) reveals long-range spatiotemporal correlations.

(D) Our specially designed laser cavity with curved facets confines high-order transverse modes. The spatial intensity distribution of an exemplary high-order transverse mode is plotted. (E) The measured spatiotemporal trace of the lasing emission from our cavity of length 400 μm , width 282 μm and facet radius 230 μm is free of micrometer-sized filaments and GHz oscillations as seen in (B). (F) The spatiotemporal correlation function $C(\Delta x, \Delta t)$ of the emission intensity in (E) shows no long-range spatiotemporal correlations.

suppressing modulational instabilities. High-order transverse modes are well confined inside such a cavity, and their optical gain is enhanced by tailoring the top metal contact shape (26). The number of transverse lasing modes is maximized by fine-tuning the cavity geometry (27). Lasing on small length scales of transverse wavelengths of high-order modes prevents lensing and self-focusing effects (28) that would normally cause filamentation and instabilities (Fig. 1E). In turn, the absence of filaments and pulsations eliminates long-range spatiotemporal correlations in the lasing intensity (Fig. 1F). It is this shortening of the correlation lengths in space and time that paves the ground for a substantial increase in the number of independent spatial channels for parallel RBG, as well as a great enhancement of the RBG rate of every individual spatial channel.

With lasing instabilities suppressed, the dynamic variations of the emission intensity are orchestrated by the interference of lasing modes with different frequencies. The characteristic time scale of such intensity fluctuations is inversely proportional to the spectral width of the total emission, and is ~ 1 ps for the GaAs quantum-well laser (26). We show the spatiotemporal beat pattern of the intensity emitted

at one laser facet in Fig. 2A. The temporal correlation length is determined by the full width at half maximum (FWHM) of $C(\Delta x, \Delta t)$ in time (Fig. 2B). Its value of 2.8 ps is limited by the temporal resolution of our detection (26).

Thanks to the ultrafast dynamics of lasing intensity, the radio-frequency (RF) spectrum is extremely broad (Fig. 2C). Its bandwidth, which contains 80% of the entire spectrum, is 315 GHz. For comparison, the numerically simulated spectrum is even broader with a bandwidth of 632 GHz (26). After accounting for the temporal resolution of photodetection, the simulated RF spectrum matches the measured one (Fig. 2C). This agreement confirms that the ultrabroad spectrum results from the interference of many transverse and longitudinal modes.

For spatial multiplexing of RBG, the number of independent parallel channels depends on the spatial correlation length of the lasing emission. Now with nonlocal correlations removed, the local correlation length estimated from the spatial FWHM of $C(\Delta x, \Delta t)$ is 1.5 μm (Fig. 2B), which is limited by the spatial resolution of our detection. Without the finite experimental resolution, our simulation gives a correlation length of 0.5 μm (26). Thanks to this extremely short spatial correlation length,

hundreds of independent spatial channels are available for parallel RBG.

Because the transverse mode frequency spacing in our cavity design is incommensurate to the longitudinal mode spacing, the spatiotemporal interference pattern cannot repeat itself (26). Moreover, the spontaneous emission generated by quantum fluctuations constantly feeds stochastic noise into the lasing modes, making their beat pattern unpredictable and irreproducible.

To generate random bits, we divide the laser end facet into 1- μm -wide spatial channels. Because of the restricted field of view of our collection optics, only 254 spatial channels are recorded simultaneously, which is about half of the number possible with complete collection of emission. We sample the emission intensity at every spatial channel at intervals of $\tau = 1.46$ ps (sampling rate 683 GHz; Fig. 3A, left inset) (26). The emission intensity integrated over one sampling period I_n has an asymmetric probability density function (PDF), which would yield biased bits (26). We adopt the procedure from (4) to acquire the differential intensity $\Delta I_n = I_{n+4} - I_n$ which has a symmetric PDF (Fig. 3A). The differential intensity ΔI_n is digitized to 6 bits (Fig. 3A), and three least significant bits (LSBs) are used

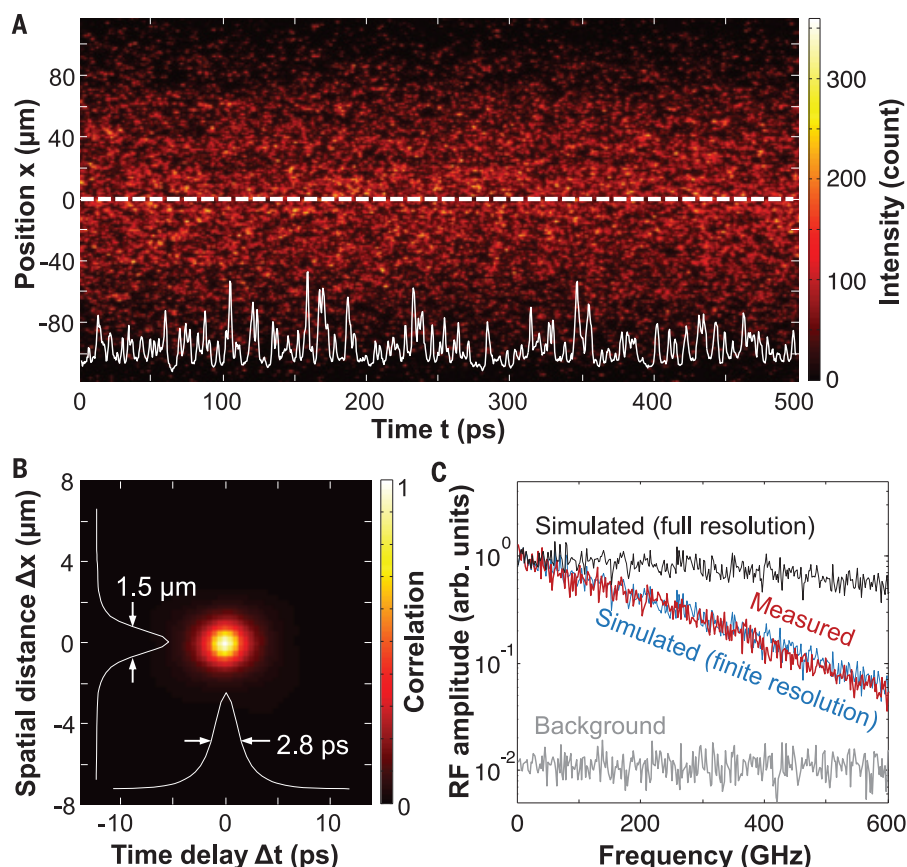


Fig. 2. Ultrafast beating of lasing modes. (A) The lasing emission at one facet of our 600-μm-long cavity exhibits a spatiotemporal interference pattern. The white solid curve is the temporal intensity fluctuation at position $x = 0$ (white dashed line). (B) The correlation function $C(\Delta x, \Delta t)$ of the measured lasing emission intensity in (A) gives the spatial and temporal correlation widths of 1.5 μm and 2.8 ps. (C) The RF spectrum (the modulus of Fourier transform) of the emission intensity in (A) at $x = 0$ (red) is much higher than the background (gray) with the laser turned off. The simulated spectrum (black) is broader but becomes narrower when the temporal resolution of our detector is taken into account (blue), in agreement with the measured one (red).

for RBG (4). All eight combinations for three LSBs have almost equal probability (Fig. 3B). We remove the residual bias by performing exclusive-OR (XOR) on two bit streams from distant spatial channels (26), which reduces the number of parallel bit streams to 127. Figure 3C reveals that the correlation between bits in a single bit stream reaches the limit $1/\sqrt{N}$ given by the bit stream length N . This leads to a single-channel bit generation rate of 2 Tb/s, which is twice the current single-channel record with off-line postprocessing (13–15).

We evaluated the quality of the generated random bits with two standard statistical test suites: NIST SP 800-22 and Diehard (26). Figure 3E provides the test results for 127 parallel bit streams; 95 of them passed all NIST tests, yielding a pass rate of 75%. Compared to the pass rates reported previously for pseudo-RBG and physical RBG, our pass rate is within the acceptable range for reliable random bit generators (16, 29). In addition, we performed the Diehard tests on all bit

streams (26). The average pass rate over 10 separate tests with different data sets is 93%, comparable to the pass rate of pseudo-RBG.

To investigate the effect of photodetection noise on RBG, we define the signal-to-noise-ratio (SNR) as the bin size s for digitization of ΔI_n divided by 2σ of the background fluctuation in a channel. With the SNR much higher than 1 for all spatial channels, the random bits are generated predominantly by the laser emission, and a numerical estimation of the noise contribution is presented in (26). Figure 3F shows that the percentage of all 188 subtests that every bit stream passes is uncorrelated with the SNR for the pair of spatial channels XOR'ed to create it, indicating that the level of detection noise does not affect the random bit quality.

To confirm the absence of correlations among the parallel bit streams, Fig. 3D shows that the mutual information (MI) between any pair of bit streams (26) is as small as the MI of uncorrelated bit streams from different

lasers. Moreover, to exclude short-term correlations, we combine odd bits from one stream and even bits from another to generate new sequences. The NIST tests of such combined bit sequences yield a pass rate of 72 to 73% (26), demonstrating that all the original parallel bit streams are truly independent.

All these test results certify the randomness of our parallel random bits generated at a cumulative rate of $2 \text{ Tb/s} \times 127 = 254 \text{ Tb/s}$. The very high RBG rate that we obtain indicates an enormous amount of entropy created by our laser. To establish its physical origin, we consider a simple model including only the interference of transverse and longitudinal lasing modes and spontaneous emission noise (26). Using the Cohen-Procaccia algorithm (1), we estimate the entropy rate h_{CP} for a bit stream generated from the simulated intensity fluctuations of a single spatial channel. Figure 4A shows the convergence of h_{CP} for different embedding dimensions d . Both the interference of a large number of lasing modes and the spontaneous emission noise contribute to entropy generation (26). As a result of stochastic intensity fluctuations, h_{CP} increases linearly with the number of digits N_{digit} . The fact that h_{CP} reaches the information theoretical limit h_0 (1, 26) indicates that the maximal possible bit rate for a single channel is achieved. This rate exceeds the experimentally obtained value because of the limited temporal resolution and dynamic range of the photodetector.

To determine how many independent spatial channels are available for parallel RBG, we investigated the effective spatial degrees of freedom (DoFs) of the emission pattern of our laser. Intuitively, the number of spatial DoFs in the total intensity pattern is expected to be $2M$, where M is the number of transverse lasing modes (26). However, as a consequence of gain competition and saturation, the mode amplitudes are not uniformly distributed, effectively reducing the spatial DoFs. Applying the Karhunen-Loeve decomposition to the intensity pattern $I(x, t)$, we compute the Shannon entropy H to obtain the complexity as a function of the number of transverse modes M (26, 30). In Fig. 4B, the number of effective DoFs 2^H grows linearly with M , but with a slope smaller than 2. By maximizing M with our cavity design, the maximal number of spatial channels is available for parallel RBG. Keeping only three LSBs after digitizing the emission intensity further reduces the spatial correlation length, and the number of independent channels is thus further increased (26).

In this proof-of-concept experiment, we have demonstrated parallel RBG in 127 independent channels with a rate of 2 Tb/s per channel. Both the single-channel bit rate and the number of spatial channels are limited by the

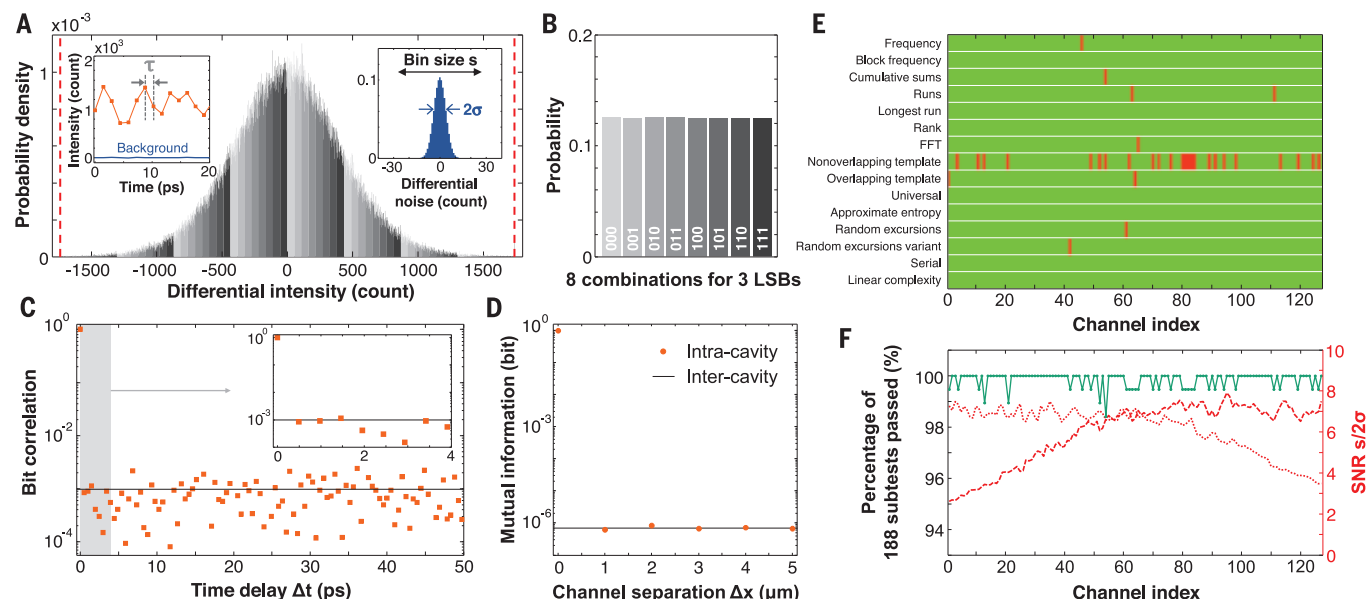


Fig. 3. Parallel random bit generation and evaluation. (A) The PDF of the differential intensity, $\Delta I_n = I_{n+4} - I_n$, which is digitized to 6 bits by binning the range $[-1740, 1740]$ counts (vertical red dashed lines) into 64 equally spaced intervals. Three LSBs are taken from each sample. The gray scale of the bars represents their eight combinations. Left inset: A segment of intensity time trace of a single spatial channel (red line), sampled at intervals $\tau = 1.46$ ps (red dots). The blue curve is the background count. Right inset: The PDF of the differential background count with a standard deviation $\sigma = 3.9$ counts, much smaller than the bin size $s = 54$ for ΔI_n . (B) The probability for all eight combinations of three LSBs is almost equal. (C) A bit stream with length $N = 2^{20}$ has a bit

correlation (red squares) around the lower limit $1/\sqrt{N}$ (black line). Inset: Close-up of short delay times. (D) The mutual information between bit streams in two channels with varying separation (Intracavity) is equal to that between the streams from two independent lasers (Intercavity). (E) The NIST SP800-22 test results include 15 kinds of statistical tests, yielding a total of 188 subtests for 127 parallel bit streams. The green color denotes one stream passing one test; conversely, red denotes test failure. Ninety-five bit streams pass all subtests, yielding a pass rate of 75%, which is considered acceptable for a reliable RBG. (F) The percentage of all 188 subtests that every bit stream passes (green) is uncorrelated with the SNR $s/2\sigma$ of the corresponding pair of spatial channels (red dashed and dotted lines).

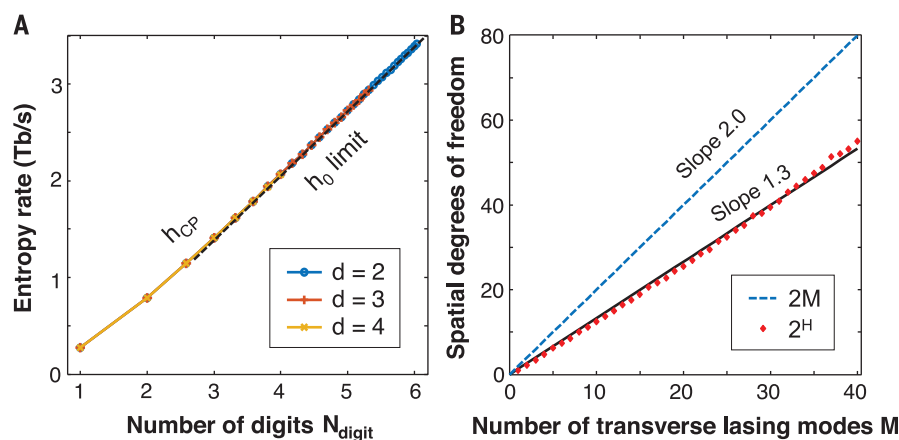


Fig. 4. Information capacity of spatiotemporal intensity pattern of simulated lasing emission. (A) The entropy rate h_{CP} in a single spatial channel converges for different embedding dimensions d and reaches the information theoretical limit h_0 (black dashed line), indicating that the maximum possible RBG rate is reached. (B) The effective number of spatial degrees of freedom 2^H in the emission pattern grows linearly with the number of transverse lasing modes M . The black solid line is a linear fit. The blue dashed line is the naively expected number of spatial degrees of freedom $2M$, which exceeds 2^H .

resolution and efficiency of our experimental apparatus. Improving the temporal resolution and the dynamic range of photodetection can double the single-channel bit rate to ~ 4 Tb/s. If all the emission is collected with finer spatial

resolution, our laser can produce ~ 500 independent bit streams (26). Then the cumulative bit rate will reach 2 Pb/s.

It is possible to create a compact parallel-RBG system by integrating fast photodetectors

with the laser in a single chip (26). Alternatively, commercially available linear arrays of photodiodes may be butt-coupled to the laser chip on both ends. Although current photodiodes are not fast enough to fully resolve the temporal intensity dynamics, spatial multiplexing with hundreds of channels alone will drastically increase the RBG rate.

Compared to existing RBG schemes, our method, based on a single laser diode without optical feedback or optical injection, is extremely simple yet highly efficient. It does not necessitate any fine-tuning of operation parameters, and its performance is robust against fabrication defects. In our current experiments, the random bit streams are generated by a computer through off-line postprocessing including XOR of bit streams from different locations. Real-time streaming of parallel random bits to a computer by conducting the postprocessing (including XOR) “on the fly” remains a major technological challenge (16, 17).

Besides the application of RBG, the extraordinary spatiotemporal complexity of our laser facilitates rich, diverse dynamical behavior, which can be finely tailored via the cavity geometry. By varying the spatial structure of cavity modes and tuning their characteristic

length scale, we could effectively manipulate their nonlinear interactions with the gain medium to create deterministic spatiotemporal structures on demand. Such an ability to control the number of active modes and their nonlinear interactions promotes our laser as a model system to study many-body phenomena and for harvesting spatiotemporal quantum fluctuations. Because our laser possesses a variety of temporal and spatial scales, it may also be useful for studying optical turbulence with high Reynolds numbers. Despite having a high-dimensional phase space with a complex landscape, our laser is compact and may be used for reservoir computing and for creating physical unclonable functions (PUFs).

REFERENCES AND NOTES

1. J. D. Hart *et al.*, *APL Photonics* **2**, 090901 (2017).
2. M. Herrero-Collantes, J. C. Garcia-Escartin, *Rev. Mod. Phys.* **89**, 015004 (2017).
3. A. Uchida *et al.*, *Nat. Photonics* **2**, 728–732 (2008).
4. I. Reidler, Y. Aviad, M. Rosenbluh, I. Kanter, *Phys. Rev. Lett.* **103**, 024102 (2009).
5. I. Kanter, Y. Aviad, I. Reidler, E. Cohen, M. Rosenbluh, *Nat. Photonics* **4**, 58–61 (2010).
6. A. Argyris, S. Deligiannidis, E. Pikasis, A. Bogris, D. Syvridis, *Opt. Express* **18**, 18763–18768 (2010).
7. K. Hirano *et al.*, *Opt. Express* **18**, 5512–5524 (2010).
8. J. Zhang *et al.*, *Opt. Express* **20**, 7496–7506 (2012).
9. X. Li, S. Chan, *IEEE J. Quantum Electron.* **49**, 829–838 (2013).
10. N. Oliver, M. C. Soriano, D. W. Sukow, I. Fischer, *IEEE J. Quantum Electron.* **49**, 910–918 (2013).
11. X. Fang *et al.*, *IEEE Trans. Circuits Syst. I* **61**, 888–901 (2014).
12. M. Virte, E. Mercier, H. Thienpont, K. Panajotov, M. Sciamanna, *Opt. Express* **22**, 17271–17280 (2014).
13. R. Sakuraba, K. Iwakawa, K. Kanno, A. Uchida, *Opt. Express* **23**, 1470–1490 (2015).
14. X. Tang *et al.*, *Opt. Express* **23**, 33130–33141 (2015).
15. T. Butler *et al.*, *Opt. Lett.* **41**, 388–391 (2016).
16. S. Shinohara, K. Arai, P. Davis, S. Sunada, T. Harayama, *Opt. Express* **25**, 6461–6474 (2017).
17. K. Ugajin *et al.*, *Opt. Express* **25**, 6511–6523 (2017).
18. S. Xiang *et al.*, *J. Lightwave Technol.* **37**, 3987–3993 (2019).
19. J. Marron, A. J. Martino, G. M. Morris, *Appl. Opt.* **25**, 26 (1986).
20. P. Lalanne *et al.*, *Opt. Commun.* **76**, 387–394 (1990).
21. M. Arahata, A. Uchida, *IEEE J. Sel. Top. Quantum Electron.* **21**, 522–530 (2015).
22. X. Li, A. B. Cohen, T. E. Murphy, R. Roy, *Opt. Lett.* **36**, 1020–1022 (2011).
23. K. Li *et al.*, *Opt. Lett.* **44**, 2446–2449 (2019).
24. O. Hess, T. Kuhn, *Prog. Quantum Electron.* **20**, 85–179 (1996).
25. I. Fischer, O. Hess, W. Elsaßer, E. Göbel, *Europhys. Lett.* **35**, 579–584 (1996).
26. See supplementary materials.
27. K. Kim *et al.*, *Appl. Phys. Lett.* **115**, 071101 (2019).
28. S. Bittner *et al.*, *Science* **361**, 1225–1231 (2018).
29. D. Lihua, Z. Yong, J. Ligang, H. Xucang, in *2014 Tenth International Conference on Computational Intelligence and Security* (IEEE, 2014), pp. 402–404.
30. A. L. Franz, R. Roy, L. B. Shaw, I. B. Schwartz, *Phys. Rev. Lett.* **99**, 053905 (2007).

ACKNOWLEDGMENTS

H.C. and K.K. thank R. Roy and M. Sciamanna for stimulating discussions. We acknowledge the computational resources provided by the Yale High Performance Computing Cluster (Yale HPC). **Funding:** Supported by NSF grant ECCS-1953959; Office of Naval Research grant N00014-21-1-2026; National Research Foundation Competitive Research Program grants NRF-CRP-18-2017-02 and NRF-CRP-19-2017-01 and A*Star AME programmatic grant A18A7b0058 for the work at Nanyang Technological University; and Science Foundation Ireland grant 18/RP/6236. **Author contributions:** K.K. conducted the experiment, analyzed data, and prepared the manuscript; S.B. built the experimental setup and guided data analysis; Y.Z. and Q.J.W. did sample fabrication; S.G. and O.H. guided the analysis of semiconductor laser dynamics; and H.C. conceived the idea, initiated the project, and supervised the research. **Competing interests:** The authors declare no competing financial interests. **Data and materials availability:** All data needed to evaluate the conclusions in the paper are present in the paper or the supplementary materials.

SUPPLEMENTARY MATERIALS

science.sciencemag.org/content/371/6532/948/suppl/DC1
Materials and Methods
Supplementary Text
Figs. S1 to S17
Table S1
References (31–47)

15 April 2020; resubmitted 28 September 2020
Accepted 11 January 2021
10.1126/science.abc2666

CHAIR AND PROFESSOR

DEPARTMENT OF PHARMACOLOGY

CASE WESTERN RESERVE UNIVERSITY SCHOOL OF MEDICINE

The School of Medicine at Case Western Reserve University (CWRU) invites applications and nominations for the position of Chair of the Department of Pharmacology. The Department has a long history of outstanding research including the work of multiple Nobel Laureates (<https://case.edu/medicine/pharmacology/>). CWRU seeks an outstanding scientist with the skills and vision necessary for developing and strengthening a department with an innovative research program that integrates basic pharmacological research with other School of Medicine (SOM) and University departments. Importantly, the candidate will have the opportunity to continue to develop and foster strong translational and disease-impacting programs in the department and with CWRU faculty at our affiliate hospital programs: University Hospitals Cleveland Medical Center, Cleveland Clinic (including the Lerner Research Institute), MetroHealth Medical Center, and the Louis Stokes Cleveland VA Medical Center. The Department has an outstanding education portfolio with graduate and medical education programs that significantly contribute to the mission and overall strength of the SOM. The department graduate training program emphasizes core competencies, diversity and career development.

The Department has strong collaborative efforts and membership in the Case Center for Synchrotron Biosciences, the Case Comprehensive Cancer Center, the Visual Sciences Research Center, the Cleveland Center for Membrane and Structural Biology, and the Cleveland Brain Health Institute (see <https://case.edu/medicine/departments-centers/centers-institutes>). Diversity and inclusive excellence is an important cornerstone for the SOM and all applicants will be expected to be a strong proponent of this SOM commitment. The Chair will be supported by a competitive recruitment package that includes substantial support for additional faculty recruitments to the Department.

The campus at CWRU encourages and facilitates collaborative interactions among scientists in the Schools of Medicine, Engineering, including Biomedical Engineering, Nursing, Dentistry, and the College of Arts and Sciences. Extensive expertise exists in protein structure, including NMR, X-ray crystallography, and Cryo-EM; drug discovery and development; metabolomics; neurodegeneration; and genomics and epigenetics. The new chair will be expected to capitalize on these and other resources to build cross-institutional collaborative research and educational programs. While it is expected that the chair will continue their commitment to research and training in their field of interest, the chair is also expected to recruit and mentor a diverse cohort of faculty who offer a breadth of perspectives and approaches to scientific interrogation that reflect this diversity, and to focus on career development for all trainees and faculty.

The SOM research mission is supported by excellent core facilities that include: high-throughput drug screening; genomics & sequencing; proteomics; metabolomics; induced pluripotent stem cell production; transgenic animal model development; behavioral testing; physiological phenotyping; human and small animal imaging; super-resolution microscopy; flow cytometry; structural biology; data management; biostatistics; and computational biology & bioinformatics.

Applicants must have a PhD and/or MD or equivalent degree, with a record of scientific achievement recognized at the national/international level by peer review and recommendations, demonstrated leadership and collaborative skills, dedication to the education and mentorship of both trainees and faculty, and a commitment to prioritizing diversity and inclusion in their leadership roles. Appointment as a Professor of Pharmacology with tenure is anticipated.

Applicants should submit a curriculum vitae, a letter of interest addressing research, educational, administrative and leadership goals, as well as a statement of your commitment to diversity and inclusion to: Walter Boron MD, PhD, Pharmacology Chair Search Committee, c/o Lesa Goodman (pharmacology-chair-search@case.edu).


In employment, as in education, Case Western Reserve University is committed to Equal Opportunity and Diversity. Women, veterans, members of underrepresented minority groups, and individuals with disabilities are encouraged to apply. Case Western Reserve University provides reasonable accommodations to applicants with disabilities. Applicants requiring a reasonable accommodation for any part of the application and hiring process should contact the Office of Inclusion, Diversity and Equal Opportunity at 216-368-8877 to request a reasonable accommodation. Determinations as to granting reasonable accommodations for any applicant will be made on a case-by-case basis.

SOMETIMES THE GRASS REALLY IS GREENER SOMEPLACE NEW.

 Find your next job at [ScienceCareers.org](https://sciencecareers.org)

There's scientific proof that when you're happy with what you do, you're better at what you do. Access career opportunities, see who's hiring and take advantage of our proprietary career-search tools. Get tailored job alerts, post your resume and manage your applications all in one place: sciencecareers.org

ScienceCareers

FROM THE JOURNAL SCIENCE  AAAS



Tenure Track Faculty Position Environmental Resource Biorecovery

at the Ecole polytechnique fédérale de Lausanne (EPFL)

The EPFL School of Architecture, Civil and Environmental Engineering (ENAC) invites applications for a tenure track Assistant Professor of Environmental Resource Biorecovery, located within the Institute of Environmental Engineering (Institut d'ingénierie de l'environnement, IIE).

Biological wastes generated from wastewater treatment, industry or agriculture are a largely untapped source for production of value-added products or energy. Their recovery utilizes biological and chemical processes that provide alternative sources for chemical feedstocks for the production of different products (e.g., plastics or other polymers, high-value chemicals, protein for animal feed, enzymes). For instance, nutrients, cellulose, volatile fatty acids, extracellular polymeric substances or proteins can be recovered from wastewater and activated sludge. Similarly, many opportunities exist for alternative energy products, e.g., bioethanol, biobutanol, biogas, biohydrogen or bioelectricity. Resource biorecovery thus supports sustainability goals by reinjecting products into the circular economy.

We welcome applications from experimentalists whose research interests include wastewater, and who employ a range of investigative tools. In particular, candidates using multi-omics approaches combined with a systems biology component are encouraged to apply. Within EPFL, the appointee will have excellent opportunities for interdisciplinary collaborations spanning microbiology, biochemistry, biosensing and biotechnology.

We seek an outstanding individual who will lead an internationally recognized research program that leverages the opportunities offered by EPFL. The professor will be committed to excellence in undergraduate and graduate level teaching, and will contribute to the Environmental Engineering program, which emphasizes basic and translational research as the foundation for environmental adaption and engineering design.

EPFL is a growing and well-funded institution fostering excellence and diversity. It is well equipped with experimental and computational infrastructure, and offers a fertile environment for interdisciplinary research collaboration. The EPFL environment is multilingual and multicultural, with English serving as a common interface. EPFL offers internationally competitive start-up resources, salaries and benefits. Besides its main Lausanne campus, EPFL operates antenna sites across Western Switzerland, in Fribourg, Geneva, Neuchâtel and Sion.

The following documents are requested in PDF format: cover letter including a statement of motivation, curriculum vitae, publication list, concise statements of research and teaching interests (up to 5 pages for each statement) as well as the names and addresses, including emails, of at least three references (may be contacted at a later stage).

Applications should be uploaded to the EPFL recruitment web site:

<https://facultyrecruiting.epfl.ch/position/28737538>

Formal evaluation of the applications will begin on **April 1, 2021**. The search will continue until the position is filled.

Further enquiries should be made to:

Prof. Tamar Kohn

Chair of the Search Committee

E-mail: searchbioresource@epfl.ch

Additional information on EPFL: www.epfl.ch/en, www.epfl.ch/schools/enac, www.epfl.ch/schools/enac/research/environmental-engineering-institute-iie, www.epfl.ch/schools/enac/education/environmental

EPFL is an equal opportunity employer and a family friendly university. It is committed to increasing the diversity of its faculty, and strongly encourages women to apply.



Paternot Faculty Chair in Interdisciplinary Cancer Research

at the Ecole polytechnique fédérale
de Lausanne (EPFL)

The School of Life Sciences of EPFL (Ecole polytechnique fédérale de Lausanne) invites applications for a Full or Associate Professor position in the field of **Interdisciplinary Cancer Research**.

This search is part of major initiatives in the Lake Geneva region to promote cancer research, which is increasingly driven by integrating research from different fields ranging from basic sciences to clinical spheres. We are primarily seeking highly accomplished mid-career candidates, although in exceptional cases more junior candidates will be considered.

The successful candidate will develop an independent internationally prominent research program in the broad domain of interdisciplinary cancer research and its potential therapeutic applications, will participate in both undergraduate and graduate teaching, and will supervise PhD students and postdoctoral fellows. Candidates may work on a wide range of cancer-specific areas including but not limited to: cancer genetics, functional genomics and genome instability, epigenetic regulation of cancer genotypes, cancer metabolism, computational cancer genetics, bioengineering of cell-based therapies and oncolytic viruses, or the chemical biology of cancer.

The successful candidate will be a part of EPFL's cancer research institute (ISREC) and is expected to perform and coordinate highly interactive biomedical research. This includes reaching out to EPFL's interdisciplinary campus (Schools of Basic Sciences, Engineering, and Information and Communication Technologies) and to Swiss Cancer Center Leman, which brings together EPFL, the Universities of Lausanne and Geneva and clinical departments of the Hospitals of Lausanne and Geneva.

This chair will be financed by the ISREC Foundation, which actively supports cancer research since 1964, most recently through the AG-ORA building which hosts the core of the Swiss Cancer Center Leman.

Applications include a cover letter, a curriculum vitae, a list of publications, a synopsis of major accomplishments, and a concise statement of future research agenda and teaching interests, along with the name, address and e-mail of at least five references. Applications should be uploaded as PDF files to the recruitment web site:

<https://facultyrecruiting.epfl.ch/position/28737541>

Formal evaluation of candidates will begin on

19 April 2021, and continue until the position is filled.

Enquiries may be sent to:

Prof. Freddy Radtke

Search Committee Chair

E-mail: cancer.research@epfl.ch

For additional information on EPFL and the Institute of Bioengineering, please consult: www.epfl.ch, sv.epfl.ch

EPFL is an equal opportunity employer and family friendly university. It is committed to increasing the diversity of its faculty. It strongly encourages women to apply.

myIDP:
A career plan customized
for you, by you.

For your career in science, there's only one

Science

Features in myIDP include:

- Exercises to help you examine your skills, interests, and values.
- A list of 20 scientific career paths with a prediction of which ones best fit your skills and interests.
- A tool for setting strategic goals for the coming year, with optional reminders to keep you on track.
- Articles and resources to guide you through the process.
- Options to save materials online and print them for further review and discussion.
- Ability to select which portion of your IDP you wish to share with advisors, mentors, or others.
- A certificate of completion for users that finish myIDP.



Visit the website and start planning today!
myIDP.sciencecareers.org

ScienceCareers In partnership with: AAAS



Who's the top employer for 2020?

Science Careers' annual survey reveals the top companies in biotech & pharma voted on by *Science* readers.

Read the article and employer profiles at sciencecareers.org/topemployers



**Science 2020
TOP EMPLOYER**



FACULTY POSITION IN DEVELOPMENTAL/REGENERATIVE BIOLOGY

The Department of Cell and Molecular Biology, one of the most highly funded departments at Tulane University (<https://sse.tulane.edu/cell>), has two major research directions: developmental biology and neuroscience. We anticipate filling a tenure-track position at the **Assistant Professor** or **Associate Professor** rank, beginning **July 1, 2021 (or January 1, 2022)**. Targeted are candidates whose research interests focus on Developmental and/or Regenerative Biology.

Applicants for the assistant professor position must have a Ph.D., at least 2 years of postdoctoral experience, a strong publication record, and show strong potential for obtaining external funding. Applicants for the associate professor position should have a strong, established research program supported by external funding. Experience in genome-wide studies is considered desirable. The successful applicant will be expected to establish a vigorous, independent research program and to participate in graduate and undergraduate teaching. Opportunities exist for research collaborations with, and participation in, the Tulane Neuroscience Program, the newly founded Tulane Brain Institute, the Tulane National Primate Research Center, the Tulane Center for Aging, and the Tulane Cancer Center.

All applicants should submit their curriculum vitae, a brief statement of research interests and three letters of recommendation via the link: **apply.interfolio.com/83783**. Application deadline is **April, 15, 2021** (or open until the position is filled).

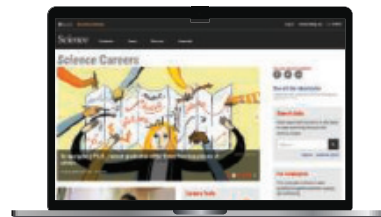
Tulane University is an Equal Opportunity/Affirmative Action/ADA Employer and encourages minority and female applicants to apply.

CAREER PLANNING

Science Careers helps you advance your career. Learn how !

- Register for a free online account on **ScienceCareers.org**.
- Search hundreds of job postings and find your perfect job.
- Sign up to receive e-mail alerts about job postings that match your criteria.
- Upload your resume into our database and connect with employers.
- Watch one of our many webinars on different career topics such as job searching, networking, and more.
- Download our career booklets, including Career Basics, Careers Beyond the Bench, and Developing Your Skills.
- Complete an interactive, personalized career plan at "my IDP"
- Visit our Employer Profiles to learn more about prospective employers.
- Read relevant career advice articles from our library of thousands.

Visit **ScienceCareers.org**
today — all resources are free



SCIENCECAREERS.ORG

Science Careers

FROM THE JOURNAL SCIENCE

By Naomi Dalchand

A perfect illusion

On the morning of my Ph.D. qualifying exam, I rolled out of bed, showered, and slid into my navy blue blazer and matching checkered pants. Next came the makeup. I brushed on a layer of foundation and drew thick black lines around my eyes—a look that signified the boldness I wanted to embody during my presentation. I put on heels and walked around my apartment, a test drive to ensure I wouldn't collapse on the floor in pain. After a few laps, I looked in the mirror. I felt confident—ready to face the members of my Ph.D. committee and answer whatever questions they threw at me. It's a strategy I developed thanks to an unlikely inspiration: Lady Gaga.

I've always struggled with being confident. As an undergraduate, my heart pounded whenever I raised my hand to answer questions posed by professors. I knew the material, but the prospect of getting the answer wrong in front of all my classmates was daunting.

Later, in graduate school, I especially feared giving presentations about my research. Beforehand, I would practice for hours on end. I knew I risked sounding rehearsed and boring, but calming my nerves was more important. The practice helped somewhat, but on presentation day, I still sounded flustered.

I pored over books to find the best ways to format and outline a presentation. If I had clear slides, I reasoned, maybe then I'd have the courage to speak with authority. I ended up with well-designed slides, but I could not present them any better.

Unlocking the key to my confidence was much more difficult than I anticipated. I realized I couldn't expect to wake up one day, look in the mirror, and say, "OK, today is the big day; today I am going to be confident." But perhaps I could find a creative solution that would work for me.

The breakthrough came during the month before my qualifying exam—a major milestone in my Ph.D. program that triggered waves of self-doubt—when I listened to a Lady Gaga album titled *Joanne*. As an avid fan, I noticed it sounded completely different from her past albums. She had switched from her usual dance-pop to soft rock and country, and her outfits—now cowgirl getups—had changed as well. I was intrigued. Lady Gaga was taking a huge professional risk, but she was confident in the music she released, confident in herself, and confident in her ability to adopt a new image.

That got me thinking: Could I do something similar before I stepped on stage? My naturally shy and quiet per-



“My naturally shy and quiet personality was not exactly ideal for public speaking.”

sonality was not exactly ideal for public speaking, so I thought about the traits and the image I wanted my professional self to possess. I pictured a steady, clear voice and a tall, commanding stance. I imagined myself as the expert in the room who wasn't afraid to say, "I'm not sure." I thought about the moments when I felt the most put together, when I wore professional clothing and highlighted my features through makeup. To me, makeup wasn't a mask. It signified boldness, femininity, and self-assurance—all traits I associated with strength and power.

I experimented with the idea during a practice presentation at home. I stood next to my laptop in professional attire, speaking loudly and fluidly—a sharp contrast to my usual practice routine, which involved sit-

ting at my desk in pajamas speaking quietly. It was a promising start. I decided to give my new presenter persona a try at my qualifying exam.

When I walked into the exam room, I was pleased to discover I had a newfound confidence. Sure, I was nervous, but an unfamiliar sense of calm rushed through me as soon as I began my talk. I was able to answer questions without a quaver in my voice, and I took ownership of the work I presented. Finally, I was the expert. At that moment, I realized that we either succumb to feelings of doubt or find innovative ways to overcome them.

In the years since, my presenter persona has given me confidence during many talks and interviews, and I've become more comfortable transforming into this role when necessary. There's no surefire way to become a confident presenter. But thanks to Lady Gaga, I now have a strategy that works. ■

Naomi Dalchand is a Ph.D. student at Northwestern University. Send your career story to SciCareerEditor@aaas.org.

CALL FOR PAPERS



Energy Material Advances

Energy Material Advances is an online-only, Open Access journal published in affiliation with **Beijing Institute of Technology (BIT)** and distributed by the **American Association for the Advancement of Science (AAAS)**. The journal publishes, research articles, review articles, short communications, perspectives, and editorials. *Energy Material Advances* covers multiple fields from cutting-edge material to energy science, investigating theoretical, technological as well as engineering aspects.

Submit your research to *Energy Material Advances* today!

Learn more at spj.sciencemag.org/energymatadv

The Science Partner Journal (SPJ) program was established by the American Association for the Advancement of Science (AAAS), the nonprofit publisher of the *Science* family of journals. The SPJ program features high-quality, online-only, Open Access publications produced in collaboration with international research institutions, foundations, funders and societies. Through these collaborations, AAAS furthers its mission to communicate science broadly and for the benefit of all people by providing top-tier international research organizations with the technology, visibility, and publishing expertise that AAAS is uniquely positioned to offer as the world's largest general science membership society. Visit us at: spj.sciencemag.org



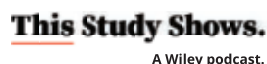
UNDERSTANDING DYNAMIC ECOSYSTEMS

AAAS | ANNUAL MEETING

AAAS, publisher of the **Science** family of journals, thanks the sponsors
of the virtual 2021 AAAS Annual Meeting:



Host University



AAAS Science & Technology Policy Fellowships, American Academy of Arts & Sciences,
American Society for Virology, AUI, Defense Threat Reduction Agency,
Food and Drug Administration, Harvard University Press, iMedRIS,
Japan Association of Communication for Science and Technology,
Japan Society for the Promotion of Science, Library of Congress: Congressional
Research Service, MIT Press, National Institute of Justice,
National Institute of Neurological Disorders and Stroke, National Science Policy Network,
Princeton University Press, Science Careers, Science Journals, Science Partner Journals,
SciLine, Sigma Xi, Society for Science & the Public, University of Washington

As of January 31, 2021

CONNECT WITH US ONLINE:

aaas.org/meetings | [#AAASmtg](https://twitter.com/AAASmtg)